



The
University
Of
Sheffield.

***Multifunctional nanocomposites for the
conservation of marine archaeological wood***

Enrique Sánchez Pérez

Submitted in partial fulfilment of the requirements for the degree of
Doctor of Philosophy

The University of Sheffield
Faculty of Engineering
Department of Chemical and Biological Engineering

Supervisor: Prof Serena A. Corr
September 2019

A mis padres Manuel y Ángela. A mi hermana Clara.

I am aware of and understand the University of Sheffield policy on plagiarism and I certify that this assignment is my own work, except as otherwise indicated, and it has not been submitted as an exercise for a degree to any other university.

Signed:

Enrique Sánchez Pérez

This thesis has been supplied on the understanding that it is copyright material and that no quotation from the thesis may be published without proper acknowledgement.

Acknowledgements

I would like to first transmit my deepest gratitude to Prof Serena A. Corr as she has been a source of motivation, knowledge and encouragement throughout the past years. When I had the smallest of the problems she always led me on the way to the solution. I am immensely grateful for her encouragement, teaching, guidance and patience. It has been an absolute pleasure working within the Corr Group.

Secondly, I would like to say thank you to Dr. Esther Aluri, a co-worker, supervisor and friend. I am extremely thankful for her patience, hard work, guidance and enormous help along these years. It has been a real pleasure working with you.

Special thanks go to Eleanor Schofield. Although she has not been present all along my stay in Glasgow and Sheffield, she has been key not only in helping putting together chemistry and archaeology, but also in helping to understand the countless, puzzling details of the conservation of the *Mary Rose*.

Thanks to Mr. Peter Chung from the School of Geographical and Earth Sciences, his know-how in electron microscopy and Raman spectroscopy have been of great help.

Thank you to Mr. Jim Gallagher for his support and humour. His help with the SEM in the School of Chemistry was invaluable, as well as his company and chat.

Special thanks to Michael Beglan. I very much appreciate his priceless advice and friendly words in the lab, in the coffee room and in the office. A good part of this work could not have been done without his help. Outside of the lab he had been the glue that kept us all together. He is very much missed in Sheffield.

Big thanks to all the guys from the Corr Group. The new and the old ones: Tom, Josefa, Marco, Beth, Lianne, Esther, Hany, Sam, Innes, Katie, Manik, Naresh, Otto, Chris, Jazz and Heather. They made long hours of work less painful and boring, and helped out in many ways, not only scientifically. Specials thanks to Marco, for his friendship, jokes and invaluable advice. (Aunque en realidad te lo he pagado con creces en paciencia, collejas y marujeos :D) Thanks also to my pals in the school of chemistry, Albane, Laura P., Alexandra, Moya, Finlay, and Jessica. They are all amazing and made me fully enjoy my time in Glasgow.

It has been a great pleasure to be a member of the GCC family. Countless evenings at the wall, great adventures in remote hills, scary icy walls, or chilled out bbq's by a loch... every minute spent with any of you felt like being in an ephemeral freezing/midge-infested dual paradise. I would not change that for anything in the world. I feel the luckiest person for getting to know the Spanish gang; they all have a special place in my heart. Their company has made these years unforgettable.

The little Foundry gang has a place in my heart too. My time in Sheffield has been short so far, but I really had fun with them at the wall, in the Peak and in the pub. Merci to Celia for her complaints and motivation to climb; to Henry, for the good laughs, chat and climbs; et merci à toi Guillaume pour les leçons de français et pour la motivation interminable pour grimper.

I would like to say a word of thanks to my parents Ángela and Manolo, and my sister Clara. I can only be proud of calling them mum, dad and sister. They are the most patient, supportive and loving family one can have (¡Qué familia!) and so I am eternally grateful for being part of it. The education and love they provided me with make them responsible for this work too (aunque no entendáis la mitad de lo que dice, no se puede tener todo).

I would also like to thank Dr Reynaldo Villalonga for his invaluable help, advice and guidance in my early years as a researcher.

I would like to thank The Leverhulme Trust and the Heritage Lottery Fund as they supported and funded this work through a Leverhulme Trust Research Project Grant (RPG-2015-134).

I would also want to thank the *Mary Rose* Trust and the University of Warwick for their invaluable support -especially Professor Rachel K. O'Reilly-, the Diamond Light Source for the use of their facilities, Dr. Giannantonio Cibirri at Diamond Light Source for his help and advice, The University of Sheffield, and the University of Glasgow for their funding and support with this project.

I am also very grateful to Prof Kirsten Jensen at the University of Copenhagen, Prof Simon Billinge at Columbia University, Dr Marco di Michel and Dr Gavin Vaughan at the ESRF for their help with obtaining absorption tomography data.

Abstract

Marine archaeological wood often suffers from acidification processes that lead to the degradation of the fibres, threatening the integrity of archaeological artefacts. Iron ions originating from corroded fixtures, nails, or other objects diffuse into the structure of waterlogged wooden artefacts over time, playing a key role in their degradation. The presence of iron ions and oxidised sulfur species in marine archaeological wood has been linked to the formation of sulfur-based acids and to the oxidative degradation of cellulose and hemicellulose.^{1,2} These processes have deleterious effects on the structural integrity of wooden artefacts and pose a major challenge in the long-term conservation of marine archaeological wood.³ This thesis describes the design, synthesis, characterisation, and preliminary tests of a series of conservation treatments aiming for the sequestration and complete removal of harmful iron species present in waterlogged wood, thus preventing the formation of acidic species. These treatments consist of magnetic nanocomposites which contain iron chelating agents and are encapsulated in a polyethylene glycol-based, thermoresponsive polymer for a safe and controlled application. The iron sequestering capability of the nanocomposites range between 39 and 80 % when tested in aqueous solution. Far IR spectroscopy studies on preliminary treatments on artificial archaeological oak and *Mary Rose* wood samples indicate that iron ions are successfully removed from the wood by the nanocomposite-laden polymer.

These conservation treatments are capable of removing harmful iron ions from marine archaeological wood, and a number of parameters in their preparation can be adjusted to meet the requirements of different artefacts to be treated. The combined magnetic and thermoresponsive properties of these materials allow for a safe and controlled application of the treatments and opens new possibilities in the design of novel non-invasive conservation strategies. While previous conservation treatments aimed to remove the iron ions or to neutralise the acidic species present in the wood, the approach presented here manages to physically remove iron ions from not only the surface, but also from the wood structure. Due to the high tunability of the systems developed, these can be applied for the conservation of many other materials such as stone, paintings, fabric, or leather.

1 G. Almkvist and I. Persson, *Holzforschung*, 2008, **62**, 694-703.

2 K. M. Wetherall, R. M. Moss, A. M. Jones, A. D. Smith, T. Skinner, D. M. Pickup, S. W. Goatham, A. V. Chadwick and R. J. Newport, *J. Archaeol. Sci.*, 2008, **35**, 1317-1328.

3 M. Sandström, F. Jalilehvand, I. Persson, U. Gelius, P. Frank and I. Hall-Roth, *Nature*, 2002, **415**, 893-897.

Table of contents

Acknowledgements	VIII
Abstract	X
Acronyms and Abbreviations	XVIII
List of Tables	XX
List of Figures	XXII
Chapter 1. Introduction	1
1.1 The <i>Mary Rose</i>	1
1.2 Conservation needs and challenges	3
1.2.1 Acidification of marine-archaeological wood: the sulfur and iron problem	7
1.2.2 Conservation strategies to date	9
1.3 Nanoparticles as conservation agents	10
1.3.1 Properties of nanoparticles	10
1.3.1.1 Magnetic materials and magnetic nanoparticles	11
1.3.2 Previous strategies for nanoparticle-based conservation treatments	15
1.3.3 Specific conservation approaches using magnetic nanoparticles	16
1.4 Synthetic approaches to magnetic nanoparticles	16
1.4.1 Co-precipitation	16
1.4.2 Thermal decomposition	18
1.4.3 Hydrothermal synthesis	19
1.4.4 Microemulsions approach	19
1.4.5 Sol-gel method	20

1.4.6 Microwave synthesis of nanoparticles	21
1.5 Functionalisation strategies for multifunctional nanoparticles	21
1.6 Polymer synthesis protocols	23
1.6.1 RAFT polymerisation	24
1.6.2 Thermoresponsive polymers	25
1.7 Chelating agents	26
1.8 Aims and objectives	30
References	33
Chapter 2. Materials and methods	41
2.1 Materials	41
2.2 Characterisation and synthetic methods	42
2.2.1 Powder X-ray diffraction (PXRD)	42
2.2.2 Scanning Electron Microscopy (SEM)	44
2.2.3 Energy-dispersive X-ray spectroscopy (EDS)	45
2.2.4 Transmission Electron Microscopy (TEM)	46
2.2.5 UV-visible spectroscopy	46
2.2.6 Fluorescence spectroscopy	48
2.2.7 Dynamic Light Scattering	49
2.2.8 Fourier-transform infrared spectroscopy (FTIR)	50
2.2.9 Raman spectroscopy	51
2.2.10 Thermal Gravimetric Analysis (TGA)	52
2.2.11 Atomic Absorption spectroscopy (AAS)	53
2.2.12 Nuclear Magnetic Resonance (NMR)	54
2.2.13 Microwave synthesis	55
2.3 Experimental	56
2.3.1 Preparation of Fe ₃ O ₄ nanoparticles by co-precipitation	56
2.3.1.1 Preparation of Fe ₃ O ₄ nanoparticles by microwave-assisted co-precipitation	57

2.3.1.2 Functionalisation of iron oxide nanoparticles	57
2.3.1.2.1 Functionalisation with Protoporphyrin IX	58
2.3.1.2.2 Functionalisation with DTPA	59
2.3.2 Synthesis of thermoresponsive polymer p(DEGMA ₄₅ -CO-MMA ₅)	60
2.3.3 Synthesis of Fe ₃ O ₄ -VTES-polymer-porphyrin (multifunctional nanocomposite)	60
2.3.4 Protocol for application of PPIX/PEG 200 functionalised nanoparticles on wood samples	62
2.3.5 Inclusion of functionalised nanoparticles in thermoresponsive polymer	63
2.3.6 Protocol for treatment of wood samples with functionalised nanoparticle-thermoresponsive polymer	63
References	65
Chapter 3. Porphyrin/PEG-functionalised magnetic nanoparticles	69
3.1 Introduction	69
3.2 Results and discussion	70
3.2.1 Synthesis of magnetic nanoparticles	70
3.2.1.1 Characterisation of magnetic nanoparticles	72
3.2.2 Functionalisation of Fe ₃ O ₄ with PPIX and PEG 200	74
3.2.2.1 Strategies for functionalisation	74
3.2.2.2 Synthesis of APTES-PPIX	75
3.2.2.2.1 Characterisation of APTES-PPIX	76
3.2.2.3 Synthesis of APTES-PEG 200	79
3.2.2.3.1 Characterisation of APTES-PEG 200	80
3.2.3 Coating magnetic nanoparticles with APTES-PPIX and APTES-PEG 200	83
3.2.3.1 Characterisation of the nanocomposite Fe ₃ O ₄ -APTES-PEG 200/PPIX	83
3.2.4 Application of Fe ₃ O ₄ -APTES-PEG 200/PPIX for iron chelation	88
3.2.4.1 Evaluation of iron sequestration in aqueous solution	88
3.3 Conclusions	90
References	93

Chapter 4. Thermoresponsive magnetic nanocomposite for marine archaeological wood conservation	95
4.1 Application of Fe ₃ O ₄ -APTES-PEG 200/PPIX nanocomposite on test wood samples	95
4.1.1 Development of a PEG-based thermoresponsive polymer	98
4.2 Synthesis and characterisation of thermoresponsive polymer p(DEGMA ₄₅ -co-MMA ₅)	99
4.3 Preparation of polymer-mixed-nanocomposite	103
4.4 Treatment of artificial archaeological wood with polymer-mixed-nanocomposite and characterisation	103
4.4.1 Preparation of artificial archaeological wood samples	103
4.4.2 Treatment of artificial archaeological wood with polymer-mixed-nanocomposite	103
4.4.3 Evaluation of the iron sequestration properties of polymer-mixed-nanocomposite	104
4.5 Design of multifunctional nanocomposite Fe ₃ O ₄ -p(DEGMA ₄₅ -co-MMA ₅)-porphyrin (Fe ₃ O ₄ -VTES-polymer-porphyrin)	106
4.5.1 Preparation and characterisation of Fe ₃ O ₄ -VTES-polymer-porphyrin multifunctional nanocomposite	107
4.5.1.1 Preparation and characterisation of Fe ₃ O ₄ -VTES	107
4.5.1.2 Preparation of porphyrin-p(DEGMA ₄₅ -co-MMA ₅) (porphyrin-polymerthiol)	108
4.5.1.3 Grafting porphyrin-polymerthiol onto Fe ₃ O ₄ -VTES	113
4.5.2 Characterisation of the multifunctional nanocomposite Fe ₃ O ₄ -VTES-polymer-porphyrin	113
4.6 Evaluation of iron chelation of Fe ₃ O ₄ -VTES-polymer-porphyrin	120
4.6.1 Evaluation of iron chelation in solution	121
4.6.2 Evaluation of iron chelation in artificial archaeological oak and <i>Mary Rose</i> wood	123
4.6.2.1 Preparation of the multifunctional nanocomposite-laden thermoresponsive polymer (nanocomposite-laden polymer)	123
4.6.2.2 Application of the nanocomposite-laden polymer on artificial archaeological wood	124
4.6.2.3 Application of the nanocomposite-laden polymer on <i>Mary Rose</i> wood and evaluation of its iron sequestration properties	125

4.6.2.4 Evaluation of the iron sequestration properties of the nanocomposite-laden polymer	126
4.7 Conclusions	128
References	131
Chapter 5. Thermoresponsive polymer-mixed DTPA-functionalised nanocomposite for marine archaeological wood conservation	133
5.1 Introduction	133
5.2 Results and discussion	136
5.2.1 Preparation of Fe ₃ O ₄ -APTES-DTPA (DTPA-nanocomposite)	136
5.2.1.1 Strategies for functionalisation	136
5.2.1.2 Synthesis and characterisation of DTPA-nanocomposite	136
5.2.2 Evaluation of iron chelation of the DTPA-nanocomposite	142
5.2.2.1 Evaluation of iron chelation in solution	142
5.2.2.2 Evaluation of iron chelation in wood	144
5.2.2.2.1 Preparation of thermoresponsive polymer-mixed DTPA-functionalised nanocomposite (polymer-mixed DTPA-nanocomposite)	144
5.2.2.2.2 Application of polymer-mixed DTPA-nanocomposite on artificial archaeological oak	145
5.2.2.2.3 Evaluation of the iron sequestration properties of polymer-mixed DTPA-nanocomposite	146
5.3 Conclusions	147
References	149
Chapter 6. Conclusions and future work	151
6.1 Conclusions	151
6.2 Future work	153
Appendices	155

Acronyms and abbreviations

^1H NMR	Proton nuclear magnetic resonance spectroscopy
AAS	Atomic Absorption Spectroscopy
AIBN	Azobis(isobutyronitrile)
APCAs	Aminopolycarboxylic acids
APTES	(3-Aminopropyl) triethoxysilane
ATR	Attenuated total reflectance
CDCl_3	Deuterated chloroform
CTA	Chain transfer agent
DCM	Dichloromethane
DEGMA	Di(ethylene glycol) methyl ether methacrylate
DLS	Dynamic light scattering
DMAP	4-dimethylaminopyridine
DMF	Dimethylformamide
DMSO	Dimethyl sulfoxide
DMSO-d_6	Deuterated dimethylsulfoxide
DTAPA - da	Diethylenetriamine pentaacetic dianhydride
DTPA	Diethylenetriamine pentaacetic acid, pentetic acid
EDC	(3-dimethylaminopropyl)-N'-ethylcarbodiimide
EDS/EDX	Energy dispersive X-ray spectroscopy
EDTA	Ethylenediaminetetraacetic acid
$\text{Fe}(\text{acac})_3$	Iron(III) acetylacetonate
FTIR	Fourier-transform infrared spectroscopy
HR SEM	High-resolution scanning electron microscopy
HR TEM	High-resolution transmission electron microscopy
IDA	Iminodiacetic acid
LCST	Lower critical solution temperature
MMA	Methyl methacrylate
MW co-precipitation	Microwave-assisted co-precipitation
NHS	N-Hydrosuccinimide
NTA	Nitrilotriacetic acid
PEG	Polyethylene glycol
PPIX	Protoporphyrin IX
RAFT	Reversible addition-fragmentation chain transfer
SAED	Selected area electron diffraction
TCEP·HCl	Tris(2-carboxyethyl)phosphine hydrochloride
TEA	Triethylamine
TGA	Thermogravimetric analysis
THF	Tetrahydrofuran
UCST	Upper critical solution temperature
VTES	Vinyltriethoxysilane
XRD	X-ray diffraction

List of Tables

Table	Caption	Page
3.1	Average crystallite sizes from Scherrer broadening for Fe ₃ O ₄ nanoparticles synthesised by traditional and MW co-precipitation.	73
3.2	Nanoparticles average sizes and polydispersity index (PDI) values for iron oxide nanoparticles prepared by MW assisted co-precipitation and by traditional co-precipitation.	73
3.3	Average crystallite sizes for magnetite nanoparticles synthesised by MW co-precipitation, and for magnetite functionalised with APTES-PPIX and APTES-PEG 200, estimated with the Scherrer equation.	87

List of Figures

Figure	Caption	Page
1.1	Schematic showing a sequence model of erosion and sedimentation at the <i>Mary Rose</i> wreck site. (a) The port side remained exposed to currents and consequently was quickly eroded. (b) The wreck was then covered by silt and eelgrass, and (c) over the years further layers of sediments were deposited. ⁴	2
1.2	(a) Painting of the <i>Mary Rose</i> donated to the <i>Mary Rose</i> Trust by Geoff Hunt. (b) The hull of the <i>Mary Rose</i> being risen from the seabed on 11 th October 1982. (c) The hull in its current state at the <i>Mary Rose</i> Museum. (d) The <i>Mary Rose</i> museum, built around the <i>Mary Rose</i> in a dry dock at the Historic Dockyards in Portsmouth, UK.	3
1.3	Small sized metal and wooden objects under treatment with a solution of sodium sesquicarbonate to remove concretions during the active conservation stage. (Images obtained from https://maryrose.org).	6
1.4	(a) The <i>Mary Rose</i> hull during the early spraying stages inside the sealed 'hotbox', and (b) during the temperature and humidity controlled drying stage, surrounded by ventilation ducts. (c) Wooden artefacts being immersed in an aqueous solution of PEG, and (d) next to the six metres long freeze dryer used at the <i>Mary Rose</i> Museum facilities. (Images obtained from https://maryrose.org)	7
1.5	(Scheme) Fenton-type reaction where iron (II) and iron (III) catalyse the formation of hydroxyl radicals that cause the degradation of organic matter.	8
1.6	(Scheme) Oxidation reaction of iron sulphide into iron sulfate in the presence of molecular oxygen and water. Sulfuric acid is generated as a side product.	9
1.7	(a) Representation of the alignment of spins in paramagnets (non-aligned), ferromagnets (parallel), antiferromagnets (antiparallel) and ferrimagnets (antiparallel spins in different sublattices). (b) Schematic of the variation of magnetic susceptibility with temperature.	12

Above the Curie point, ferro- and ferrimagnetic materials can no longer maintain spin alignment and exhibit a paramagnetic behaviour; thermal motion also competes with spin alignment in antiferromagnets and causes them to become paramagnetic above the Néel point.

- 1.8 (a) Hysteresis cycle of a ferromagnetic material showing the multi-domain microstructure under zero field ①, spins are aligned at points of saturation magnetisation ① and ④, value of remnant magnetisation (M_r) ② and value of the coercive field (H_c) ③. (b) Schematic representation of M-H curves for i) paramagnets, ii) ferromagnets, iii) superparamagnets and iv) diamagnetic materials. 13
- 1.9 (a) Schematic showing the coercivity (H_c) behaviour of a magnetic particle as a function of its diameter. As particle size decreases the domain walls disappear, resulting in an increase in H_c until the particle size reaches D_s (transition from multi domain to single domain). When the particle size further decreases, the thermal agitation energy overcomes magnetic anisotropy energy and, as a result, the particle enters the superparamagnetic regime, D_p , where coercivity is zero.⁶⁸ (b) Magnetite crystallises in an inverse spinel structure (AB_2O_4). Here O^{2-} ions (red) are arranged in a face-centred cubic system. Fe^{2+} ions (gold) sit in octahedral sites while one half of Fe^{3+} ions (brown) occupy octahedral sites and the other half occupy tetrahedral sites. Magnetite can be represented as: $(Fe_{tet}^{3+})(Fe_{oct}^{2+})(Fe_{oct}^{3+})O_4$. 14
- 1.10 The La Mer model is generally accepted to describe particle formation mechanisms in colloidal solutions. The concentration of monomers (or ions) in solution is increased beyond a critical supersaturation level (C_{min}). Nuclei start to form rapidly (burst nucleation) which causes the concentration of monomers in solution to drop below the self-nucleation level, marking the end of the nucleation stage. Growth then occurs due to the diffusion of remaining monomers in solution to the already formed particles surfaces. A rapid nucleation and a slow growth are ideal for obtaining a narrow size distribution; if nucleation lasts too long, then heterogeneous nucleation/growth will take place yielding polydisperse particles.^{84,85} 17

- 1.11 (a) Schematic illustration of the synthesis of iron oxide nanocrystals (NCs) through the decomposition of $\text{Fe}(\text{acac})_3$ in the presence of oleic acid, oleylamine and akanediol; (b) typical TEM image of the as synthesised nanoparticles; (c) HR TEM image of the 16 nm Fe_3O_4 nanocrystals.⁹¹ 18
- 1.12 Schematic of attachment of alkoxy silane molecules onto a metal oxide nanoparticle. The covalent bonds Si-O-Fe are formed by the condensation between the hydroxyl groups, naturally present on metal oxide surfaces, and the alkoxide moieties. 23
- 1.13 Phase diagrams of a polymer-solvent system, representing temperature (T) vs. polymer volume fraction (ϕ). These diagrams show (a) lower critical solution temperature (LCST) behaviour, and (b) upper critical solution temperature (UCST) behaviour.¹³¹ 26
- 1.14 Examples of common metalloporphyrin structures. Porphyrins can form stable chelates with metals through the lone pairs of electrons on the four nitrogens. This structure is especially stable for transition metals with +2 or +3 oxidation states. The metallic centres can also be coordinated with other donor ligands or side chains in the porphyrin ring, resulting in coordination complexes where the metal forms bonds with up to six donor atoms. 28
- 1.15 Selection of common APCAs (a) iminodiacetic acid, (b) nitrilotriacetic acid, (c) ethylenediaminetetraacetic acid, (d) diethylenetriaminepentaacetic acid and (e) 1,4,7,10-tetraazacyclododecane-1,4,7,10-tetraacetic acid. The denticity of the complex formed is given by the structure of the ligand and the number of donor atoms. 29
- 1.16 The treatment, consisting of functionalised nanoparticles encapsulated in a thermoresponsive polymer, is cooled down (a) and applied onto the wood (b). After the incubation period, the temperature is increased and the treatment is peeled off the surface of the wood (c) thus removing the harmful iron species. 31

- 2.1 Schematic representation of two waves being diffracted in phase, satisfying Bragg's law. The angle of diffraction is twice the angle of incidence (θ) whilst the wavelength remains constant. 43
- 2.2 (a) UV-visible spectrum of a porphyrin derivative featuring the Soret band (B band) and Q bands. (b) Schematic representation of the energy levels of the four orbitals described by Gouterman. The degenerate e_g orbitals are responsible for the Soret band and Q bands.⁴ 47
- 2.3 (a) Individual dipoles rotating and (b) charged species oscillating upon application of microwave radiation. (c) Temperature gradient in a vessel due to conductive heating, compared to (d) uniform heating provided by microwave radiation. 56
- 2.4 Schematic of (A) the application of suspensions of bare nanoparticles and PPIX/PEG 200 - functionalised nanoparticles on a fresh oak sample with a micropipette, and (B) the sectioning of the oak sample to study its cross section by electron microscopy. The nanoparticle suspensions were applied on the face in line with the wood vessels and grain to ensure the diffusion rate was comparable among different samples. Sterile steel scalpel blades were used to cut the wood samples apart. 63
- 3.1 Schematic of the prepared nanocomposite. PPIX, a metal chelating agent, is anchored onto magnetite cores using APTES as a linker. Similarly, PEG 200 is also attached onto the nanoparticles. While PPIX can sequester harmful iron ions from the wood structure, the magnetic nature of the magnetite cores could play a key role in the handling and application of the nanocomposite to the artefact. PEG 200 may facilitate the diffusion of the nanocomposite into the archaeological wood, which has been treated with PEG for almost two decades. 71
- 3.2 Reaction schematic for the MW co-precipitation of Fe_3O_4 nanoparticles in aqueous solution. The nucleation is initiated by the addition of ammonia, followed by a short ageing stage under microwave radiation, to finally obtain magnetite nanoparticles. 71
- 3.3 Schematic of the traditional co-precipitation of Fe_3O_4 nanoparticles in aqueous solution. The nucleation is initiated by adding dropwise an 70

acidic solution of the iron chloride salts onto a solution of NaOH. The precipitated Fe₃O₄ nanoparticles were grown at 80 °C for 1 hour.

- 3.4 Powder XRD patterns of magnetite nanoparticles synthesised by MW co-precipitation and by traditional co-precipitation. **Orange**: Fe₃O₄ prepared by traditional co-precipitation; **Blue**: Fe₃O₄ synthesised by MW co-precipitation⁵; **Black**: ICSD standard of Fe₃O₄ (cubic inverse spinel, space group: *Fd $\bar{3}m$*). 72
- 3.5 High-resolution TEM micrographs of Fe₃O₄ nanoparticles prepared by (A), (C) microwave-assisted co-precipitation and (B), (D) traditional co-precipitation. Insets in micrographs (A) and (B) show the size distribution histograms obtained for each method. 74
- 3.6 Preparation of the APTES-PPIX moiety by a two-step amide coupling reaction, carried out under inert atmosphere and in the dark. In the first step a carbodiimide and N-Hydroxysuccinimide were used to obtain an intermediate (PPIX-succinimide) that will readily react with a primary amine. In the second step the primary amine in APTES reacts with the succinimide groups to form PPIX-APTES. 76
- 3.7 FTIR spectra of PPIX and APTES-PPIX. The band at 1065 cm⁻¹ corresponds to the Si-O bond in APTES, while the peaks at 1550 and 1639 cm⁻¹ are the amide I and amide II bands characteristic of amides. This suggests the successful formation of an amide bond between APTES and PPIX. 77
- 3.8 ¹H NMR spectra of APTES-PPIX obtained in DMSO-*d*₆. The signals **a**, **b**, **e** and **f** are contributions from PPIX, as described in the insets. The triplet **d** is attributed to the -SiOCH₂CH₃ protons in APTES. The multiplet **c** is a contribution from the -SiOCH₂CH₃ proton. 78
- 3.9 Preparation of the APTES-PEG 200 moiety *via* a two-step process under inert atmosphere. First, PEG 200 is reacted with succinic anhydride to form PEG 200-acid in alkaline medium. Then, an amide coupling between the primary amine in APTES and one of the carboxyl groups in PEG 200-acid yields APTES-PEG 200. 79

- 3.10 FTIR spectra of APTES-PEG 200 and a PEG 200 standard. The signals at 1070, 1200, and 1730 cm^{-1} can be attributed to the O-C-C stretch, the C-C-O stretch and the C=O stretch from the ester group. The band at 2800 cm^{-1} corresponds to aliphatic C-H stretches. The bands at 1544 and 1649 cm^{-1} are the amide I and amide II bands from the amide bond between APTES and PEG 200. The expected peak from Si-O in APTES is likely to be overlapped by the O-C-C and C-O stretches around 1070 cm^{-1} . 80
- 3.11 ^1H NMR spectrum from the synthesised APTES-PEG 200 obtained in CDCl_3 . The signals **c** is characteristic from $-\text{[O-CH}_2\text{-CH}_2\text{]}-$ protons in the polyethylene glycol structure. Signals **b** and **d** correspond to contributions from the protons in $-\text{COO-CH}_2-$ and $-\text{CH}_2\text{-COOH}$, respectively. The peak **a** is attributed to the protons in $-\text{SiOCH}_2\text{CH}_3$, characteristic of APTES. The signals **e** and **f** result from the contribution of the $-\text{NHCO-CH}_2-$ and $-\text{CH}_2\text{-NHCO-}$ protons, respectively, and indicate the presence of an amide bond between APTES and PEG 200. 82
- 3.12 Coating of magnetite nanoparticles with APTES-PPIX and APTES-PEG 200, synthesised previously. Magnetite nanoparticles were dispersed in ethanol with the help of ultrasounds. Solutions of APTES-PPIX and APTES-PEG 200 were added to the nanoparticles dispersion, and reacted in the dark and at room temperature for 48 hours. 83
- 3.13 FTIR spectra of bare Fe_3O_4 nanoparticles (red) and iron Fe_3O_4 nanoparticles coated with APTES-PEG 200 and APTES-PPIX (blue). The intense stretch at 550 cm^{-1} is due to the Fe-O bond, and the broad band at 1070 cm^{-1} is associated to the Si-O bond in APTES. The bands at 1389 and 1730 cm^{-1} correspond to the C-O stretch from the ester in PEG 200, and the C=O stretch associated with PPIX and PEG 200. The stretches at 1545 and 1630 cm^{-1} are the amide I (C=O) and amide II (C-N) bands from the amide in the APTES-PPIX and APTES-PEG 200 moieties. 84
- 3.14 Absorbance and emission spectra of a colloidal suspension of PPIX-coated magnetite nanoparticles (0.33 mg/mL in ethanol) and a PPIX standard. The absorbance band at 404 nm confirms the presence of PPIX attached onto the iron oxide nanoparticles. The emission band at 85

632 nm ($\lambda_{\text{exc}} = 404$ nm) also indicates that optical properties of the PPIX contained in the nanocomposite have been preserved, and its fluorescence has not been quenched.

- 3.15 TGA curves of the bare iron oxide nanoparticles and the nanoparticles coated with APTES-PPIX and APTES-PEG 200. The marked mass loss of the nanocomposite of about 30 % confirms the presence of an organic coating attached to the magnetic cores. 86
- 3.16 Powder XRD patterns of bare magnetite and magnetite coated with APTES-PPIX and APTES-PEG 200. **Red**: Fe_3O_4 functionalised with APTES-PPIX and APTES-PEG 200; **Blue**: bare Fe_3O_4 synthesised by MW co-precipitation; **Black**: ICSD standard of Fe_3O_4 (cubic inverse spinel, space group: $Fd\bar{3}m$) 87
- 3.17 UV-vis spectroscopic studies of an ethanolic solution of $\text{FeCl}_3 \cdot 6\text{H}_2\text{O}$ (0.2 mM) treated with the nanocomposite (0.6 mg/mL, additions of 20 μL) to assess the chelation properties of the later. **(A)** Absorption spectra from an Fe (III) solution treated with the nanocomposite were recorded showing a progressive decrease in absorbance upon increase of nanocomposite concentration. **(B)** Absorption intensity of an ethanolic solution of Fe(III) recorded at 246 nm. The decrease of intensity upon addition of the nanocomposite indicates a decrease in the concentration of free Fe(III) due to the formation of the complex Fe-PPIX. 89
- 3.18 Variation of free Fe(II) in aqueous solution with time upon treatment with the magnetic nanocomposite, measured with atomic absorption spectroscopy. The treatment with the nanocomposite bearing PPIX was able to chelate up to 85 % of free iron from a solution in 6-7 hours. 90
- 4.1 X-ray absorption tomography data for (A) fresh oak, cut across the grain of the wood; *Mary Rose* wood (B) 6 mm into the keelson plan and (C) 2 mm into the keelson wood (data collected by collaborator Prof. Kirsten M. Ø. Jensen). Image (A) displays large vessels separated by walls, and a denser area with smaller vessels. Images of degraded wood from the *Mary Rose* (B) and (C) show an increased amount of voids caused by the collapse of vessel walls. 95

- 4.2 Backscattered SEM images of the cross-section of four fresh oak samples treated with 1 mL of an aqueous suspension of (A and B) bare Fe₃O₄ nanoparticles and (B and C) PPIX/PEG 200-functionalised nanoparticles (0.6 mg/mL). The diffusion of bare and functionalised Fe₃O₄ within the wood structure was studied (A and C) in the absence and (B and D) in the presence of a 1.3 Tesla magnetic field. The bright areas indicate the depth reached by the nanoparticles under different conditions. 97
- 4.3 Preparation of the thermoresponsive polymer gel p(DEGMA₄₅-co-MMA₅) by RAFT polymerisation. Monomers DEGMA and MMA (45:5 molar ratio) were dissolved in 1,4-dioxane under inert atmosphere. AIBN and the CTA were added to the solution, and this was degassed by 4 freeze-thaw cycles. The mixture was stirred at 65 °C for 8 hours. The reaction was stopped by rapid cooling, the product was dialysed against deionised water for 5 days, and finally freeze dried for 24 hours to eliminate the residual water. 99
- 4.4 ¹H NMR spectrum of p(DEGMA₄₅-co-MMA₅) obtained in CDCl₃. The bands labelled a (0.88-1.42 ppm) and b (1.81 ppm) correspond to the -CH₃ and -CH₂- protons on the backbone of the polymer. The bands e (3.56-3.68 ppm) and d (3.40 ppm) are attributed to the -OCH₃ and -OCH₂- protons in DEGMA and MMA monomers. The triplets at 7.36, 7.52 and 7.87 ppm correspond to the *o*-, *p*- and *m*- =CH- protons, respectively, in the dithiobenzene end-group. 101
- 4.5 Variable-temperature UV-visible spectroscopy of p(DEGMA₄₅-co-MMA₅), showing its thermoresponsive behaviour. The abrupt transition in optical transmittance observed indicates that the value of the LCST is 26 °C. Below this temperature the polymer chains are hydrated and form a clear solution. Above the LCST the polymer chains expel the water molecules as they become gradually more hydrophobic, turning the solution opaque. 102
- 4.6 Images of (A) artificial archaeological wood and (B) fresh oak being treated with the polymer-mixed-nanocomposite placed onto a 1.3 Tesla permanent magnet. Image (C) shows a plastic spatula containing polymer-mixed-nanocomposite removed after the treatment. 104

- 4.7 Far IR spectroscopy of polymer-mixed-nanocomposite after treating (B) artificial archaeological oak and (C) fresh oak. Also included are the spectra of (A) the thermoresponsive polymer and (D) the PPIX/PEG 200 functionalised nanoparticles. The bands observed at 548 and 438 cm^{-1} are attributed to the stretches of Fe-O bonds in magnetite and to the rotation of the pyrrole rings in the porphyrin, respectively. The band at 363 cm^{-1} can be assigned to the oop bending of C=O bonds in the thermoresponsive polymer. Finally, the weak peak at 318 cm^{-1} in the polymer-mixed-nanocomposite applied on artificial archaeological oak could be assigned to the stretching of Fe-N bonds in the porphyrin moiety. 105
- 4.8 Schematic of Fe_3O_4 -VTES-p(DEGMA₄₅-co-MMA₅)-porphyrin nanocomposite. Here, the role of p(DEGMA₄₅-co-MMA₅) is two-fold: linking the porphyrin-amine to the magnetic nanoparticle, and providing means for electrostatic interactions with the thermoresponsive polymer. Iron oxide nanoparticles are coated with VTES in order to anchor p(DEGMA₄₅-co-MMA₅)-porphyrin *via* a thiol-ene reaction. 107
- 4.9 Schematic of the preparation of the multifunctional nanocomposite Fe_3O_4 -VTES-p(DEGMA₄₅-co-MMA₅)-porphyrin. (A) Fe_3O_4 nanoparticles were synthesised by MW assisted co-precipitation, as described in Section 3.2.1, and further functionalised with vinyltriethoxysilane (VTES). (B)(i) Porphyrin-amine is anchored to the carboxylic group of p(DEGMA₄₅-co-MMA₅) *via* a conventional amide coupling. (ii) The porphyrin-polymerdithioester is reduced to porphyrin-polymerthiol, and (iii) this is anchored onto the VTES coated Fe_3O_4 nanoparticles *via* thiol-ene click chemistry. 108
- 4.10 ^1H NMR spectra of porphyrin-p(DEGMA₄₅-co-MMA₅) obtained in DMSO- d_6 . The signals **a**, **b**, **d**, **e** and **f** are contributions from the thermoresponsive polymer backbone. The signals **h** and **k** correspond to the -CH= protons in the pyrrole rings and the -CH= protons in amino phenyl groups in the porphyrin rings, respectively. The singlets **g** and **i** can be attributed to the -NH₂ protons in the aminophenyl groups, and the -NH- protons in 110

the pyrrole rings of in the porphyrin, respectively. Finally, the singlet at 8.45 ppm (labelled as j) can be attributed to the -CONH- proton in the amide group, and the two triplets at 7.48 and 7.64 ppm (labelled as c) correspond to the -CH= protons in the dithiobenzene end of the polymer.

- 4.11 ¹H NMR spectrum of porphyrin-polymerthiol. The peaks labelled **a**, **b**, **d**, **e** and **f** are attributed to the -CH₃, -CH₂-, -OCH₃, -OCH₂- and -COOCH₂- protons, respectively, present in the backbone of p(DEGMA₄₅-co-MMA₅). The signals **g**, **h**, **i**, and **k** are the fingerprint of the porphyrin-amine, and correspond to the -NH₂, -CH= (pyrrole ring), -NH- and -CH= (aminophenyl group), respectively. The singlet **j** (8.50 ppm) is attributed to the -CONH- proton in the amide bond. The signal **c*** could be attributed to the -SH proton. The absence of the doublets characteristic of -CH= protons in the dithiobenzene end group (7.4-7.6 ppm) suggests the reduction of this to a thiol. 112
- 4.12 Powder XRD patterns from dry precipitates of Fe₃O₄ (blue), Fe₃O₄-VTES (red) and Fe₃O₄-VTES-polymer-porphyrin (orange). The three patterns are in excellent agreement with the standard of cubic inverse spinel magnetite (Fe₃O₄, JCPDS index card no. 19-629), showing that the morphology of the magnetite nanoparticles does not change through the successive functionalisation steps. The broad diffraction peaks observed are typical from nanostructures, and the average crystallite size obtained with the Scherrer equation is in the order of 14 nm. 114
- 4.13 TGA curves of Fe₃O₄, VTES functionalised Fe₃O₄ and Fe₃O₄-VTES-polymer-porphyrin. While the mass loss of the bare Fe₃O₄ is 0.5 %, the mass loss of the particles coated with VTES and with VTES-polymer-porphyrin 16.3 % and 20.6 %, respectively. This confirms the presence of organic compounds successively grafted onto the Fe₃O₄ nanoparticles. 115
- 4.14 FTIR spectra of Fe₃O₄, Fe₃O₄-VTES and Fe₃O₄-VTES-polymer-porphyrin. The intense stretch at 540 cm⁻¹ is due to the Fe-O bond, the broad bands at 754, 1005 and 1099 cm⁻¹ are attributed to the vibrations of the Si-O bond, and the band at 959 cm⁻¹ is due to the Si-O-Fe stretches. 116

Also, the bands at 1406 and 1597 cm^{-1} correspond to the $=\text{CH}_2$ and $\text{C}=\text{C}$ stretches, respectively in VTES. This confirms the successful binding of VTES onto the magnetite. The bands at 1450 and 1720 cm^{-1} correspond to the stretches of the $\text{C}=\text{O}$ bond in the amide and the $\text{C}=\text{O}$ bond from the ester groups in the porphyrin-polymer, respectively, confirming its presence onto the Fe_3O_4 nanoparticles.

- 4.15 Absorbance and emission spectra of porphyrin-polymerdithioester, porphyrin-polymerthiol and Fe_3O_4 -VTES-polymer-porphyrin obtained in ethanol. The absorbance band at 425 nm, corresponding to the porphyrin moiety can be observed in the three stages of the synthesis. The intense background and incline in the Fe_3O_4 -VTES-polymer-porphyrin spectrum is due to the scattering of the light by the magnetic nanoparticles. The emission bands, obtained at $\lambda_{\text{exc}} = 425$ nm, also confirm the presence of the fluorophore onto the Fe_3O_4 nanoparticles. 118
- 4.16 Variable-temperature UV-visible spectroscopy of porphyrin-polymerdithioester showing its thermoresponsive behaviour. The LCST observed (23 °C) is lower than the one obtained for the thermoresponsive polymer. This change in the LCST can be explained by the hydrophobic nature of the porphyrin moiety added. 119
- 4.17 (A) Temperature-dependent dynamic light scattering of Fe_3O_4 -VTES-polymer-porphyrin obtained in aqueous suspension between 20 and 40 °C. The average hydrodynamic diameter of the multifunctional nanocomposite decreases from 220 nm to 180 nm when the temperature is raised above 23 °C. (B) Representation of the disposition of the polymer chains in Fe_3O_4 -VTES-polymer-porphyrin in aqueous suspension. Low temperatures favour the adsorption of water molecules and the unfurling of the polymer chains, while high temperatures lead to the cleavage of hydrogen bonds favouring a hydrophobic behaviour and the collapse of the polymer chains. 120
- 4.18 Performance tests on chelation of free iron ions solution. (A) UV-Visible absorption spectra of an ethanolic solution of $\text{Fe}_2(\text{SO}_4)_3 \cdot 7\text{H}_2\text{O}$ (0.2 mM) treated with consecutive additions of a suspension of Fe_3O_4 -VTES-polymer-porphyrin in ethanol (0.25 mg/mL, additions of 20 μL). A 122

decrease in the intensity of the absorbance band is observed upon addition of porphyrin functionalised nanoparticles. (B) Absorption intensity of an ethanolic solution of $\text{Fe}_2(\text{SO}_4)_3 \cdot 7\text{H}_2\text{O}$ treated with functionalised nanoparticles recorded at 283 nm. Successive additions of functionalised nanoparticles lead to a decrease of the absorption intensity of Fe(III).

- 4.19 The concentration of Fe(III) in an aqueous solution of $\text{Fe}_2(\text{SO}_4)_3 \cdot 7\text{H}_2\text{O}$ was monitored by AAS during the treatment with Fe_3O_4 -VTES-polymer-porphyrin. The multifunctional nanocomposite was able to chelate 39 % of the free Fe(III) form solution after 5-6 hours. 123
- 4.20 Stages of the preparation of the nanocomposite-laden polymer. The Fe_3O_4 -VTES-polymer-porphyrin (A) is added to an ethanolic solution of thermoresponsive polymer, yielding a dark gel (D). The thermoresponsive polymer gel is shown at temperatures (B) below and (C) above the LCST. 124
- 4.21 Multifunctional nanocomposite-laden polymer was applied on (A) Blank wood and (B) artificial archaeological wood, and incubated for 4 weeks at 5 °C atop a 1.3 Tesla neodymium magnet. After the incubation period the wood samples were wrapped in transparent film (C and D), and the magnetic field was applied in the opposite direction. (E) After one week the nanocomposite-laden polymer was peeled off the wood surface. 125
- 4.22 (A) Image of a core sample obtained from the keel of the *Mary Rose*. The more degraded, darker region corresponds to the section of the core close to the surface of the wood (B) SEM-EDS micrograph showing sulfur and iron present in the core, and (C) core sample being treated with a patch of polymer gel loaded with Fe_3O_4 -VTES-polymer-porphyrin. 126
- 4.23 Far IR spectroscopy of nanocomposite-laden polymer after treating (C) *Mary Rose* wood, (D) artificial archaeological oak and (E) fresh oak. For comparison, the spectra of (A) thermoresponsive polymer, (B) porphyrin-amine and (F) multifunctional nanocomposite are included. The bands observed at 552 and 440 cm^{-1} correspond to the Fe-O stretches in magnetite, and the rotation of the pyrrole rings in the 127

porphyrin moiety, respectively. The characteristic band at 362 cm^{-1} can be associated to the oop angle bends of the C=O bonds in the thermoresponsive polymer. The band at 393 cm^{-1} can be assigned to Fe-N in plane core vibrations, while the band at 316 cm^{-1} can be attributed to the stretching of Fe-N in the porphyrin moiety.

- 5.1 Schematic of the DTPA functionalised nanoparticles. APTES is used to attach the chelating agent DTPA to the surface of the magnetic nanoparticles. These DTPA functionalised nanoparticles have been devised to chelate iron ions by means of the DTPA moieties and to be manipulated with external magnetic fields. It can also be encapsulated in a thermoresponsive polymer for a magnetically and temperature controlled application. 135
- 5.2 Schematic of the one-pot synthesis of DTPA functionalised nanoparticles (Fe_3O_4 -APTES-DTPA). (i) Highly crystalline iron oxide nanoparticles were prepared by microwave-assisted co-precipitation in aqueous media. (ii) The iron oxide nanoparticles were coated with (3-aminopropyl) triethoxysilane (APTES), which provided a convenient coating with amine groups. (iii) DTPA-da was finally anchored to the amino-coated nanoparticles *via* an amide bond between the amide and anhydride group. 138
- 5.3 Powder XRD patterns obtained from Fe_3O_4 (blue), Fe_3O_4 -APTES (red) and Fe_3O_4 -APTES-DTPA (orange). The three patterns are in good agreement with the standard of inverse spinel magnetite (Fe_3O_4 , JCPDS index card no.19-629), plotted in black. This indicates that the morphology of the magnetite nanoparticles was not affected by the functionalisation with APTES and DTPA. The broad diffraction peaks observed are characteristic of nanostructured materials. The average crystallite size calculated with the Scherrer equation is 14 nm. 139
- 5.4 FTIR spectra of Fe_3O_4 , Fe_3O_4 -APTES and Fe_3O_4 -APTES-DTPA. The intense band at 539 cm^{-1} corresponds to the stretches of the Fe-O bond. The broad band at 991 cm^{-1} is due to the stretches of the Si-O-Fe bond. The intense band at 1632 cm^{-1} is attributed to the vibrations of the C=O bonds present in the DTPA moiety. Finally, the weak band at 1389 cm^{-1} 140

can be assigned to the amide II band. These signals confirm the successful attachment of APTES and DTPA onto the iron oxide nanoparticles.

- 5.5 TGA curves of from Fe_3O_4 (blue), Fe_3O_4 -APTES (red) and Fe_3O_4 -APTES-DTPA (orange) obtained between 25 and 700 °C in N_2 atmosphere. The mass loss of 1.5 % in Fe_3O_4 can be explained by the loss of water molecules physisorbed and. Fe_3O_4 -APTES and Fe_3O_4 -APTES-DTPA show a mass loss of 4 % and 10 % at 550 °C, respectively, which indicates the attachment of the organic layers onto the magnetic nanoparticles. The slight gain in mass of Fe_3O_4 -APTES after this temperature can be explained by the oxidation of the degraded silane. 142
- 5.6 Evaluation of chelation of free iron in solution with UV-visible spectroscopy. (A) UV-visible absorption spectra of an ethanolic solution of $\text{Fe}_2(\text{SO}_4)_3 \cdot 7\text{H}_2\text{O}$ (0.2 mM) treated with a suspension of Fe_3O_4 -APTES-DTPA in ethanol (0.6 mg/mL, additions of 20 μL). The absorbance at 284 nm decreases upon addition of DTPA functionalised nanoparticles. (B) Absorbance of an ethanolic solution of $\text{Fe}_2(\text{SO}_4)_3 \cdot 7\text{H}_2\text{O}$, obtained at a fixed excitation wavelength ($\lambda_{\text{exc}} = 284 \text{ nm}$). The absorbance decreases upon addition of DTPA functionalised nanoparticles. 143
- 5.7 Atomic absorption spectroscopy was used to monitor the concentration of Fe(II) of an aqueous solution being treated with DTPA-functionalised nanoparticles. Results show that Fe_3O_4 -APTES-DTPA was able to reduce the initial concentration of free Fe(II) (4.84 mg/mL) by 50 % within 30 minutes. 144
- 5.8 Polymer-mixed DTPA-nanocomposite was applied onto (A) fresh oak and (B) artificial archaeological oak. These samples were placed atop a 1.3 Tesla permanent magnet, and incubated for 4 weeks at 5 °C. After the incubation period, the treated wood samples (C and D) were protected by transparent film and placed upside down onto the permanent magnet for one week at 5 °C. Finally, the samples were 146

brought to room temperature and the polymer mixed DTPA-nanocomposite was peeled off the surface of the oak samples.

- 5.9 Far IR spectroscopy of polymer-mixed-DTPA nanocomposite after treating (B) artificial archaeological and (C) fresh oak. The spectrum of (A) the thermoresponsive polymer is also included for comparison. The broad band at 560 cm^{-1} is attributed to the stretches of the Fe-O bonds in the iron oxide nanoparticles, and the band at 362 cm^{-1} can be assigned to the C=O bonds in the thermoresponsive polymer. Bands at 393 and 317 cm^{-1} have been previously related to the stretching and out-of-plane vibrations of Fe-N bonds. In this case, however, the intensity of those signals is not significantly different between the blank sample and the artificial archaeological wood. Bands around $316\text{--}320\text{ cm}^{-1}$ could be related to the three Fe-N bonds in DTPA-Fe. 147
- A3.1 ^1H NMR spectrum of APTES obtained in $\text{DMSO-}d_6$ 155
- A3.2 ^1H NMR spectrum of PPIX obtained in $\text{DMSO-}d_6$ 155
- A3.3 ^1H NMR spectrum of PEG obtained in CDCl_3 156
- A4.1 Temperature variable ^1H NMR spectra of $p(\text{DEGMA}_{45}\text{-co-MMA}_5)$ obtained between 20 and $40\text{ }^\circ\text{C}$. The figure on the bottom-right corner shows the variation of relative intensity with temperature, measured for the $\text{-OCH}_2\text{-}$ proton. 157
- A4.2 Raman spectrum obtained from magnetite nanoparticles. The peak at 670 cm^{-1} is characteristic of magnetite. No evidence of other phases such as maghemite ($\gamma\text{-Fe}_2\text{O}_3$) or haematite ($\alpha\text{-Fe}_2\text{O}_3$) is observed. 158

Chapter 1 - Introduction

1.1 The *Mary Rose*

The *Mary Rose* was the flagship of King Henry VIII of England's naval fleet. It was a grand warship constructed with four masts, two gun decks and two high castles, and was built between 1509 and 1511 together with her smaller sister vessel the *Peter Pomegranate*. Despite the popular belief that the *Mary Rose* was named after Mary Tudor, Henry VIII's sister, there is no evidence for this. Instead, it is more likely she was named after the Virgin Mary, also known at the time as 'The Mystic Rose'.¹ Among other historical events, she led the English fleet during the three French wars (1512-1514, 1525-1542 and 1543-1546). It has been found that during the second French war, the *Mary Rose* was kept in reserve and underwent refitting and, although the exact nature of the work performed on her is unclear, it is believed that these modifications included the addition of extra bracing to the structure of the ship and the opening of extra gunports. On the 19th July of 1545, during the Battle of the Solent, the *Mary Rose* sank, taking the lives of hundreds of men aboard and leaving approximately 34 survivors. The reasons for her sinking have been long studied and debated and still remain uncertain. Although the French claimed they holed the hull of the *Mary Rose* during action, it is believed there were political motivations for these asseverations. Alternatively, contemporary observers reported that a sudden gust of wind caught the sails of the vessel while making a turn. This caused the ship to keel over, water entered through the open lower gunports, and led to a rapid capsizing.^{2,3}

The *Mary Rose* lay on the sea bed for nearly 450 years, during which time a number of attempts to salvage the ship were made. Initial resurfacing efforts were done in the weeks after the sinking, but failed, seemingly due to the limited technical resources at the time. The vessel quickly became covered in the upper sediments of the seabed, leaving the port side exposed to erosion from marine currents. Over the centuries the wreck site was fully covered in hard clay, sealing the ship off from further erosion, albeit making its future relocation difficult. **Figure 1.1** shows a model of the erosion and sedimentation of the shipwreck in a sequence of three images depicting the stages of erosion and burial of the hull.

In 1836 John and Charles Deane, pioneer divers and inventors, were hired along with William Edwards to help remove fisherman nets caught on protruding woods on the seabed. These timbers happened to be the *Mary Rose* wreck site and, after the controversial use of explosives in the excavation, several cannons, guns and other objects were recovered.⁴ It was not until 1971 when the *Mary Rose* wreck site was rediscovered

by Alexander McKee and the British Sub-Aqua Club after a search initiated in 1964. Modern excavations during the 1970s led to the recovery of more than 19000 artefacts of diverse nature. Ultimately, the hull of the *Mary Rose* was finally raised on the 11th October 1982 following a complex operation that was carried out over several months.⁵

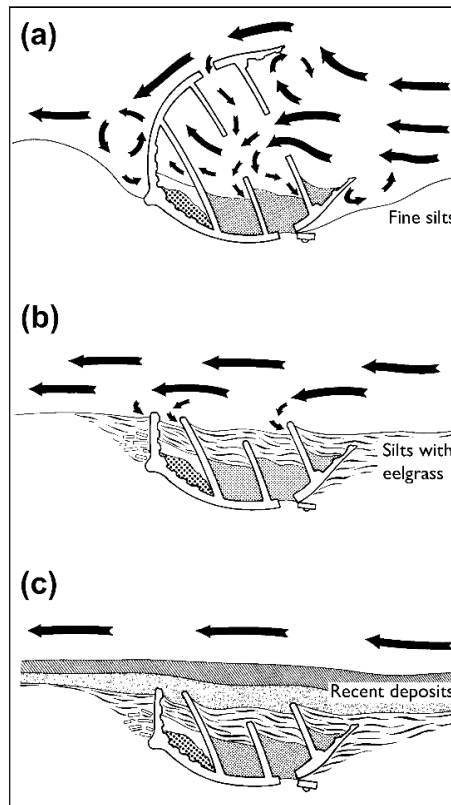


Figure 1.1. Schematic showing a sequence model of erosion and sedimentation at the *Mary Rose* wreck site. (a) The port side remained exposed to currents and consequently was quickly eroded. (b) The wreck was then covered by silt and eelgrass, and (c) over the years further layers of sediments were deposited.⁶

Further archaeological works were performed between 2003 and 2005 on the wreck site, during which more artefacts and parts of the ship structure were discovered. An anchor and the stem of the ship were then recovered. Other sections, like the forecastle, were not excavated or were reburied and still remain at the original wreck site protected under the sea floor. Since then, the salvaged hull and artefacts have been kept in the purpose-built, state-of-the-art *Mary Rose* Museum at the Portsmouth Historic Dockyard, where conservation works take place and are exhibited to the public. The nature of the findings and their degradation state were so varied that a range of new conservation methods and treatments had to be devised and tested. **Figure 1.2** shows (a) a painting of the *Mary Rose*, (b) the hull being recovered in 1982 and (c) the hull in its current location

at the *Mary Rose* Museum, (d) the *Mary Rose* Museum, at the Historic Dockyards in Portsmouth.

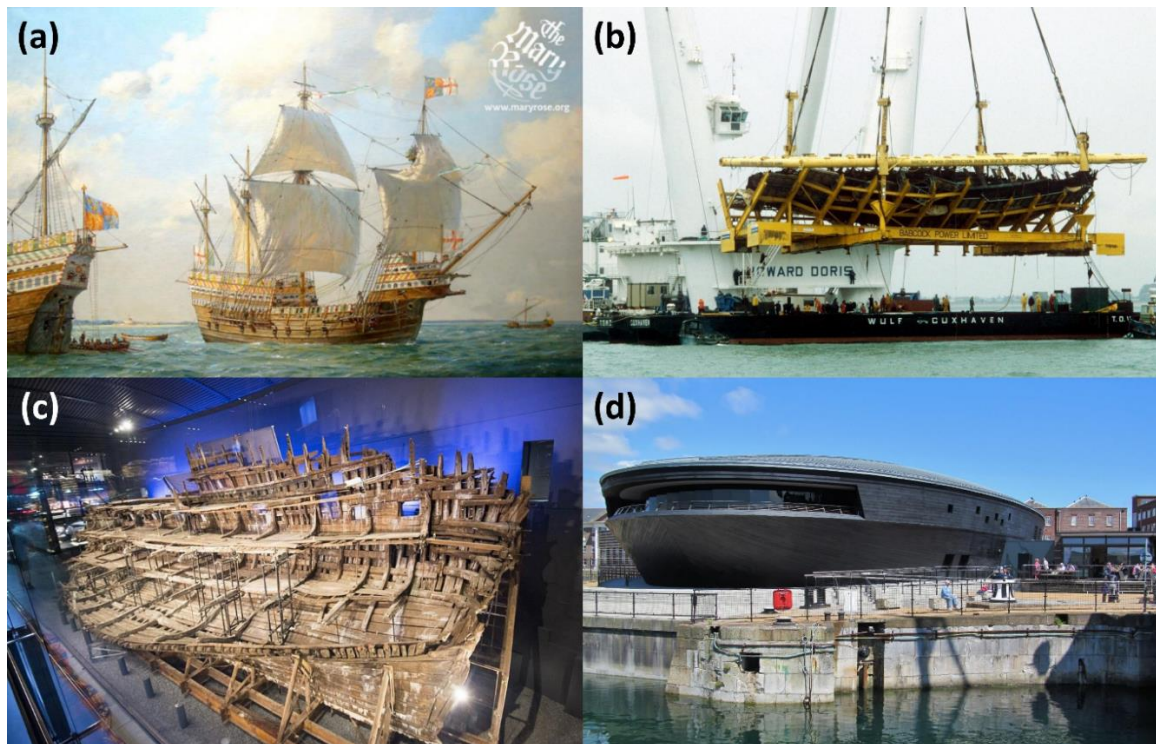


Figure 1.2. (a) Painting of the *Mary Rose* donated to the *Mary Rose* Trust by Geoff Hunt. (b) The hull of the *Mary Rose* being risen from the seabed on 11th October 1982. (c) The hull in its current state at the *Mary Rose* Museum. (d) The *Mary Rose* museum, built around the *Mary Rose* in a dry dock at the Historic Dockyards in Portsmouth, UK. (Images obtained from <https://maryrose.org>)

1.2 Conservation needs and challenges

From the moment the recovered timbers of the *Mary Rose* and artefacts were surfaced, a number of cleaning and storage strategies were meticulously studied, developed and applied.⁵ Soon after the recovered timbers were surfaced, they were transferred to a large pond of fresh water for periods ranging from 12 to 24 months. Initial conservation steps consisted of immersing recovered artefacts in tanks of fresh water, which was normally enough to remove the remaining marine sediments and desalinate. However, gentle brushing, water streams, and even warm water (up to 30 °C) or ultrasonic baths were occasionally needed to remove the most resistant deposits. For practical reasons the hull and other large structures were washed by hand, using water hoses. A common occurrence in the recovered timbers of the *Mary Rose* was the appearance of a series of iron compounds on the surface. About half of the wooden objects recovered

showed rusty orange and red-brown deposits. To remove these iron deposits, the artefacts were soaked in a 5 % (m/v) solution of the disodium salt of ethylenediaminetetraacetic acid (EDTA) in water for periods ranging from one day to three months allowing for the dissolution of the majority of iron deposits. The most resistant deposits were removed in short immersion periods of 24-36 hours in a 5 % (m/v) solution of oxalic acid in water. To complement these treatments, timbers were also temporarily stored in polyethylene sealed bags in anaerobic conditions. This anaerobic storage is known to be of much help for the further removal of iron compounds, since it prevents the formation of highly insoluble iron hydroxides and oxides. Water-based treatments and storage not only allowed wood to be cleaned from sediments, but also prevented the wood from drying out. Waterlogged archaeological wood can be severely and irreversibly damaged if allowed to dry in uncontrolled conditions, including warping, shrinking, distortion, or collapse caused by the shrinkage of wood cells.⁷

The difference in size between the artefacts recovered and the hull itself required careful approaches for treatment and passive storage. The hull was sprayed with cold fresh water between 2 and 5 °C and placed in a building made of a double layer of PVC, a so-called ‘hotbox’, which provided conveniently controlled thermal and vapour insulation and allowed for public display. Recycled, refrigerated, filtered fresh water was constantly sprayed on the hull for 12 years, and biocide treatments were applied to control localised growth of microbial slimes and fungi colonies. Alternatively, artefacts and individual timbers were submerged in purpose-built polypropylene or polyethylene tanks containing fresh water, which was renewed periodically. These objects were kept in the dark, but it was not possible to maintain a controlled temperature. The use of chilled fresh water (either spraying or immersion) was safe, non-toxic, economical, and compatible with future conservation treatment processes.

Later, during passive storage, some artefacts and individual timbers were also treated with gamma radiation to control bacteria, fungi and insects. This technique, widely used for sterilisation in biomedical applications during the 1980s and 1990s, yielded satisfactory results in preliminary studies.⁸ Therefore, since 1998 a range of doses from 20 to 100 KGy, considered safe for the wood, were used depending on the thickness and the degradation state of the objects under treatment.^{9,10} The hull, however, could not be treated due to logistical limitations in transportation. Gamma irradiation proved to be a preferable alternative to cold and wet storage strategies as it was more economical and did not pose any toxicological threat to conservators, as opposed to biocides.

While the passive storage was taking place, the team of conservators at the *Mary Rose* Museum investigated strategies to dry the hull and wooden artefacts whilst avoiding

damage to the wood structure. Among others, specialists and conservators from the 17th century Swedish ship *Vasa* (recovered two decades earlier from the bottom of the Stockholm harbour) were consulted.¹¹ The conservation programme had a number of clear objectives. First, bulking treatments were needed to permanently replace water within the wood structure. This would prevent wood cell walls from drying and shrinking, ultimately leading to structural collapse. Bulking chemicals were chosen whereby hydrogen bonds are formed with the cellulose in the wood cells and, in theory, can therefore be easily removed from the wood structure. Secondly, filling voids, lumen and intercellular spaces was also necessary to improve the mechanical properties of the recovered timbers. For this, aqueous solutions of polymers are generally employed. Finally, recovered timbers must be coated to preserve their surface quality and improve mechanical properties. Polyethylene glycol (PEG) was found to be the most suitable polymer for void filling and surface coating.

Polyethylene glycols were the selected candidates as they are safe, non-toxic, relatively inexpensive and highly soluble in water (100 mg/mL and 55 mg/mL for PEG 200 and PEG 4000, respectively). PEGs with low molecular weight are clear, viscous liquids 100 % soluble in water. Higher molecular weight PEGs are white waxy solids also soluble in water to concentrations of 50-55 % (w/v). These characteristics make PEG one of the most commonly used materials for waterlogged wood conservation, in spite of the long treatment times needed and the increasing hygroscopicity of PEG with decreasing molecular weight. PEG was considered a standard method ever since it was used by conservators on the *Vasa* in the 1960s.¹² Indeed, in the 1970s and 1980s, polyethylene glycols with molecular weights around 1500 g/mol were used to treat ancient wood, and PEG 4000 was regularly used as consolidant to preserve highly degraded marine archaeological wood.^{13,14,15,16} In addition to its use in wood conservation, PEG was also used in the 1990s for the consolidation of the polychromy of the 2200-years-old Terracotta warriors. A treatment based on PEG was successfully used to prevent the flaking and detachment of the lacquered paint from the statues by partially replacing water from the qi-lacquer structure.¹⁷

A two-step PEG treatment was developed by conservators in the *Mary Rose* trust to stabilise the size and shape of the ship's hull after several years of research with samples and actual hull timbers. In 1994 the first step of the active conservation programme started with the application of low molecular weight PEG. For over a decade, the hull of the *Mary Rose* was sprayed with low concentration aqueous solutions of PEG 200. Due to its low molecular weight this polymer could enter the cell walls, replacing water and stabilising the cell walls by means of hydrogen bonds with the cellulose. This kept the cell

walls saturated, preventing shrinkage and subsequent collapse. The second phase started in 2006 when the spray was changed to a higher molecular weight PEG. Aqueous solutions of PEG 2000 were sprayed onto the surface of the hull, which helped to fill in the permanent voids on the outer timber surface and sealed in the low grade PEG. The surface of more degraded timbers was finally treated with PEG 4000. The use of high grade PEGs was key in the preservation of the rigidity of the timbers and surface features. In contrast with the hull, the wooden artefacts and smaller timbers were submerged in aqueous solutions of PEG. This approach and the smaller size of the objects allowed for a faster diffusion of the polymer through the wood structure, therefore requiring shorter treatment times. Before being treated, the timbers were analysed microscopically to determine the degradation state of the wood. Each timber was then categorised in three classes, so specially designed treatments could be used according to the type of wood, size, and degradation state.^{18,19,20} **Figure 1.3** shows timbers and metal artefacts being treated with a solution of sodium sesquicarbonate to remove concretions.



Figure 1.3. Small sized metal and wooden objects under treatment with a solution of sodium sesquicarbonate to remove concretions during the active conservation stage. (Images obtained from <https://maryrose.org>)

After the artefacts, timbers and hull were treated with PEG they all underwent a drying stage. The majority of the objects were freeze dried for periods of weeks to months, depending on size and amount of water, while a few were instead slowly air dried. A final surface treatment with PEG 6000 was applied to some objects. The sprayers installed over the hull of the *Mary Rose* were finally switched off on 29th April 2013, bringing the PEG treatment stage to an end. The drying phase began while the hull was kept under tightly controlled temperature (18-20 °C) and humidity (50-58 % RH) conditions. In July 2016, after nearly three years, the ship was sufficiently dry, which allowed the removal of the wall and windows separating her and the visitors of the museum. **Figure 1.4** shows the *Mary Rose* hull and wooden artefacts during the PEG treatment stage and during the drying stage.

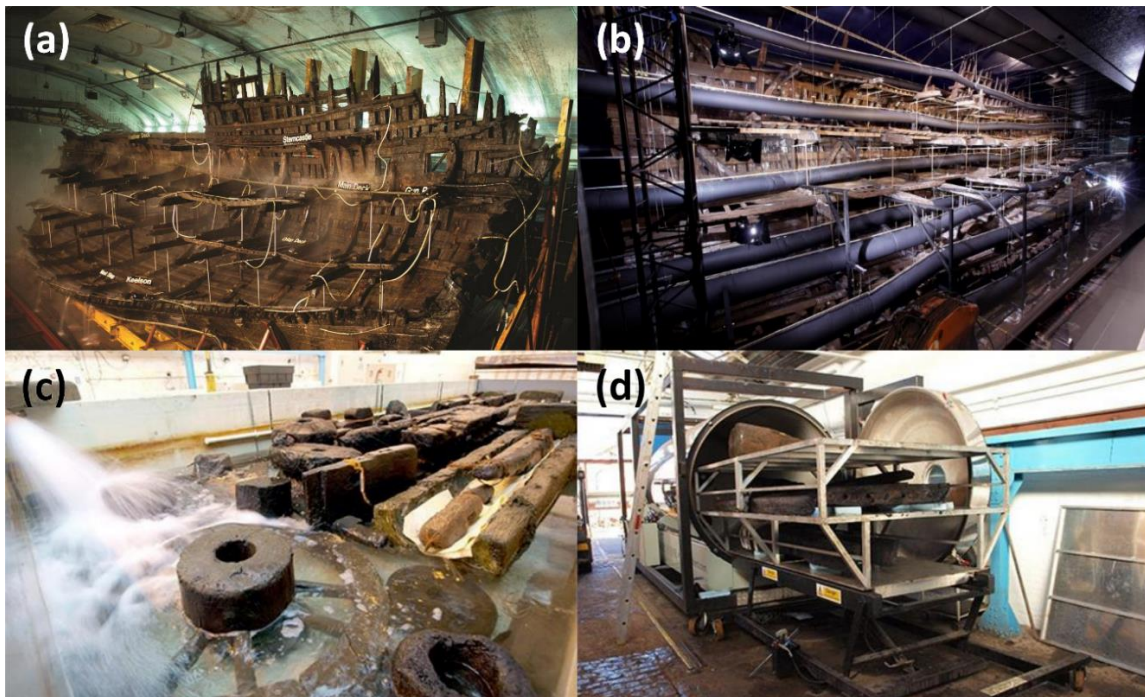


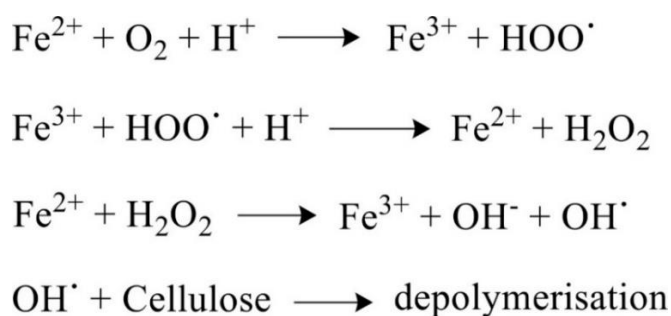
Figure 1.4. (a) The *Mary Rose* hull during the early spraying stages inside the sealed ‘hotbox’, and (b) during the temperature and humidity controlled drying stage, surrounded by ventilation ducts. (c) Wooden artefacts being immersed in an aqueous solution of PEG, and (d) next to the six metres long freeze dryer used at the *Mary Rose* Museum facilities. (Images obtained from <https://maryrose.org>)

1.2.1 Acidification of marine archaeological wood: the sulfur and iron problem

During the conservation of the *Vasa*, researchers observed degradation processes in which wood polymers, cellulose and hemicellulose, as well as the PEG used in the conservation, were broken down into lower molecular weight organic acids. This

occurrence appeared to be connected to higher concentrations of iron and low concentrations of sulfur in the wood. These findings were also correlated with a pH gradient in the wood: lower values were recorded in areas of higher degradation of polymers and higher concentration of iron. The conservators elaborated a hypothesis where the degradation processes have an oxidative nature and have been initiated by iron compounds in Fenton-type reactions. Additionally, reduced organic sulfur compounds may have a role in quenching these reactions.^{21,22} Similarly, sulfur and iron deposits were found in the timbers and wooden artefacts from the *Mary Rose*, showing that she was also exposed to similar iron-catalysed degradation processes.^{23,24} While sulfur compounds occur naturally in sea water in different oxidation states (H_2S , FeS_2 , SO_4^{2-} , SO_2 or S), it is believed that iron diffused into the wood structure from corroded fixtures, nails and other iron objects during the time on the seabed.

In Fenton reactions, iron ions can be combined with hydrogen peroxide to form hydroxyl radicals, which can react with organic matter, leading to its degradation *via* oxidation processes. In the case of archaeological wood, iron ions lodged in the wood structure pose no harm to its integrity in anaerobic conditions (*i.e.* submerged in water). However, when the wood is exposed to the atmosphere, iron can react with molecular oxygen, yielding hydrogen peroxide, therefore triggering a Fenton-type reaction described above. This sequence of reactions is described in **Scheme 1.5**.



Scheme 1.5. Fenton-type reaction where iron (II) and iron (III) catalyse the formation of hydroxyl radicals that cause the degradation of organic matter.

In anaerobic conditions, the more common forms of sulfur in marine archaeological wood are elemental sulfur, hydrogen sulphide and, when iron is present, iron sulphide. When exposed to atmospheric oxygen, iron sulphide can be oxidised in the presence of water, to form iron sulfate and sulfuric acid.²⁵ **Scheme 1.6** shows a simplified overall reaction for this process. This suggests that the oxidation of sulfur, catalysed by iron, is

one of the causes of the acidification and subsequent long term threat of degradation to marine archaeological wood.



Scheme 1.6. Oxidation reaction of iron sulphide into iron sulfate in the presence of molecular oxygen and water. Sulfuric acid is generated as a side product.

The formation of highly oxidant substances, such as hydroxyl radicals, and sulfur-based acids has a deleterious effect on the structural integrity of marine archaeological wood. These substances cause the degradation of the cellulose and hemicellulose in the wood, as well as the breakdown of the PEG used in the conservation stages. These acidification processes pose a long-term threat to the conservation of the artefacts and have been the object of significant research in relation to the conservation of the *Vasa* and the *Mary Rose*.^{21,23,24,26}

1.2.2 Conservation strategies to date

There have been a number of conservation strategies and treatments developed over the years to address the acidification and the degradation problem of marine archaeological wood, mainly focusing on the neutralisation of the sulfur and iron present in the artefacts. In the mid 2000's, Giorgi, Chelazzi, and Baglioni explored the use of alkaline earth hydroxides for the de-acidification of the *Vasa*. Suspensions of $\text{Mg}(\text{OH})_2$ and $\text{Ca}(\text{OH})_2$ nanoparticles in 2-propanol were used to treat wood samples. These treatments were successful in de-acidifying the wood, and also had the advantage over other methods of facile diffusion into the artefacts due to their small size.^{27,28,29}

More recently, Schofield, Chadwick and co-workers developed a series of methods to neutralise the free acid and the sulfur species present in the wood in order to stop the identified degradation processes. These treatments were based on SrCO_3 nanoparticles, which were applied to wood samples in the form of a suspension in 2-propanol and water. SrCO_3 was chosen as a weak base and because Sr^{2+} has a large affinity for sulfate ions. SrCO_3 nanoparticles were found to diffuse more effectively into wood samples when they had not previously been treated with PEG. Also, aqueous suspensions of these particles provided deeper penetration into wood than those in 2-propanol. Analyses with X-ray absorption spectroscopy (XAS) showed that SrCO_3 nanoparticles were effective in reacting with the iron sulfate present. This resulted in the stabilisation of iron and sulfur in the

form of siderite (FeCO_3), goethite ($\text{FeO}(\text{OH})$) and other insoluble, benign compounds, preventing further oxidation into sulfuric acid.^{30,31,32,33} Other alkaline earth carbonates, such as BaCO_3 and CaCO_3 , were later investigated. Fine aqueous dispersions of these compounds were applied to dried and PEG treated wooden artefacts from the *Mary Rose*. These studies showed that the carbonate reagents successfully dissociated and neutralised acid, and accelerated the oxidation of pyrite (FeS_2) into neutral, insoluble sulfate salts. Particularly, CaCO_3 seemed to be a more sensible option for further scale up, since it is less toxic and more environmentally friendly than its strontium and barium based counterparts.³⁴

Berko *et al.*³⁵ took a different approach to tackle the acidification problem. Their efforts were focused exclusively on neutralising the iron ions responsible for the formation of sulfur-based acids within the wood structure. Aqueous solutions of several chelating agents, namely calcium phytate, EDTA, diethylenetriaminepentaacetic acid (DTPA) and citric acid, were applied as treatments for wood samples from the *Mary Rose*. The effects of these treatments were studied with XAS. The results obtained revealed varying degrees of success in removing Fe(II) and Fe(III). Treatments with DTPA were able to remove between 50 and 90 % of the iron present in the samples, depending on the initial concentration of the iron contamination.

In 2014, Walsh *et al.*³⁶ designed a supramolecular polymer network based on host-guest interactions. This network contained different ratios of catechol and naphthol functionalities, able to form metal-ligand complexes with iron. Small angle X-ray scattering (SAXS), IR imaging, and rheological analyses performed on samples of archaeological wood treated with this functional polymer showed a significant decrease in iron content on their surface. A 1:1 ratio (catechol:naphthol) was found to be more effective in the removal of iron from the surface of the wooden samples, as opposed to polymer networks functionalised with only one of the ligands.

1.3 Nanoparticles as conservation agents

1.3.1 Properties of nanoparticles

The use of nanostructured materials has rapidly increased in recent years as a result of extensive research in a variety of fields such as solid state chemistry, colloids and surface chemistry, and polymer synthesis. The advances in synthetic methods and characterisation techniques have made possible the detailed study of matter on the nanometre scale and an increase in the understanding of the physical, chemical and optical properties of nanostructures. Nowadays nanomaterials have been at the heart of advances in biomedicine, energy storage and conversion, food technology and

electronics.^{37,38,39,40,41,42,43,44} Nanosized materials can often take on unique properties compared to their bulk counterparts, owing to their high surface areas and small sizes. Nanoporous materials, for example, can be used for molecular separation, water purification, or gas adsorption or separation thanks to their large surface-area-to-volume ratios and the possibility to control the pore size and geometry.^{45,46,47} Quantum dots, for example, are a class of materials where precise modification of the size of the nanomaterials results in a tuneable variation in the colour through quantum confinement effects.⁴⁸ Another example of a set of materials where changes in size can drive large changes in functional properties are magnetic materials, which may represent an excellent platform for the design of targeted conservation treatments.

1.3.1.1 Magnetic materials and magnetic nanoparticles

Magnetic materials may be characterised by their response to an external magnetic field. Depending on the observed behaviour, they can be classified as paramagnetic, diamagnetic, ferromagnetic, or ferrimagnetic. In paramagnetic materials for example, atoms contain unpaired electrons whose spin magnetic moments define the overall magnetic moment. In the presence of an external magnetic field, these spins can align parallel to the applied field leading to a net attraction. In the case of diamagnetic materials, the electron spins are all paired resulting in an overall zero magnetic moment. When an external magnetic field is applied, a weak magnetic dipole is induced in the opposite direction to the field. As a consequence, diamagnets are, therefore, slightly repelled from a magnetic field.⁴⁹

Materials may also exhibit spontaneous magnetisation in the absence of an applied field. Under certain conditions unpaired electrons from partially filled 3d orbitals may be coupled *via* an exchange interaction which tends to align them, reaching a more stable state. This exchange interaction can also occur between neighbouring atoms in some materials, giving rise to long-range magnetic ordering of the unpaired electrons leading to an overall net magnetic moment. Materials exhibiting this type of magnetisation are called ferromagnets. Above a certain temperature, called the Curie temperature (T_c), thermal energy outweighs the tendency of spins to stay aligned, meaning ferromagnetic materials can no longer maintain spontaneous magnetisation and instead exhibit paramagnetic behaviour. In other cases, the exchange interaction may lead adjacent spins to align antiparallel to each other. In this instance, the identical magnetic moments cancel each other out and as a result there is no net spontaneous magnetisation. These materials are called antiferromagnets and exhibit such behaviour below a characteristic

temperature known as the Néel temperature (T_N). If moments are aligned in an antiparallel manner, but the magnetisation of one sublattice is greater than that of the other sublattice, then the spins are only partially cancelled and there remains an overall spontaneous magnetisation. These are called ferrimagnetic materials and, similar to ferromagnets, only show such behaviour below the Curie temperature.^{50,51} **Figure 1.7(a)** shows how spin moments arrange in different materials with spontaneous magnetisation. **Figure 1.7(b)** shows how magnetic susceptibility of ferromagnets and antiferromagnets varies with temperature.

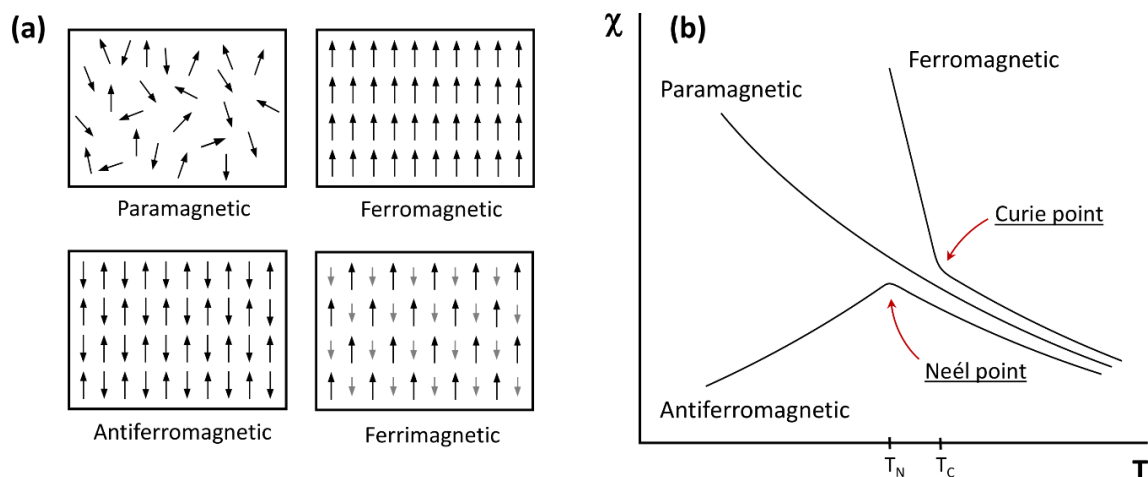


Figure 1.7. (a) Representation of the alignment of spins in paramagnets (non-aligned), ferromagnets (parallel), antiferromagnets (antiparallel) and ferrimagnets (antiparallel spins in different sublattices). (b) Schematic of the variation of magnetic susceptibility with temperature. Above the Curie point, ferro- and ferrimagnetic materials can no longer maintain spin alignment and exhibit a paramagnetic behaviour; thermal motion also competes with spin alignment in antiferromagnets and causes them to become paramagnetic above the Néel point.

The microstructure of magnetic materials is divided into small domains where spins can be aligned in the same direction. Magnetic domains are distributed within the structure so that their spins may be aligned in different directions to those of other domains. Upon application of an external magnetic field (H), magnetic domains tend to align parallel to the field showing an induced magnetisation (M). At sufficiently intense magnetic fields, the material reaches a point of saturation magnetisation.⁴⁹ **Figure 1.8(a)** shows the characteristic sigmoidal M - H curve of a magnetic material, which for ferro- and ferrimagnets usually features a hysteresis loop. When a non-magnetised bulk material (0) is subjected to an external magnetic field, its magnetisation increases following the dashed line until it reaches a saturation magnetisation point (1). If the magnetic field is

subsequently removed, there will remain a residual magnetisation within the substance (2). This remnant magnetisation can be cancelled by applying a reverse magnetic field of a specific strength, called coercive force (3). If the magnetic field is reversed enough the material can be magnetised in the opposite direction (4).

Sufficiently small particles can be single-domain as their magnetisation does not vary across the particle (i.e. all spins are aligned in the same direction and no domain walls are observed). Also, under certain size and temperature conditions, single-domain ferro- and ferrimagnets can exhibit a property called superparamagnetism.⁵² In sufficiently small single-domain particles (typical sizes between 5 and 150 nm, although this is dependent on the material and temperature), the magnetic anisotropic energy barrier between the two antiparallel orientations of the spins can be overcome by thermal energy, causing the spins to rotate coherently from one direction to the other.^{53,54,55} When the temperature increases above a certain value (blocking temperature, T_B) the magnetisation is reversed spontaneously and the relaxation times between the different directions of magnetisation shorten. Such magnetic fluctuations result in an observed net magnetic moment of zero for each individual particle, and this behaviour is known as superparamagnetism. **Figure 1.8(b)** shows how particles that transition from a blocked state (ferro- or ferrimagnetic) to a superparamagnetic state show no remanence (M_r) or coercivity (H_c). They do not exhibit any hysteresis in their M-H curve, but maintain high saturation magnetisation.⁵⁶

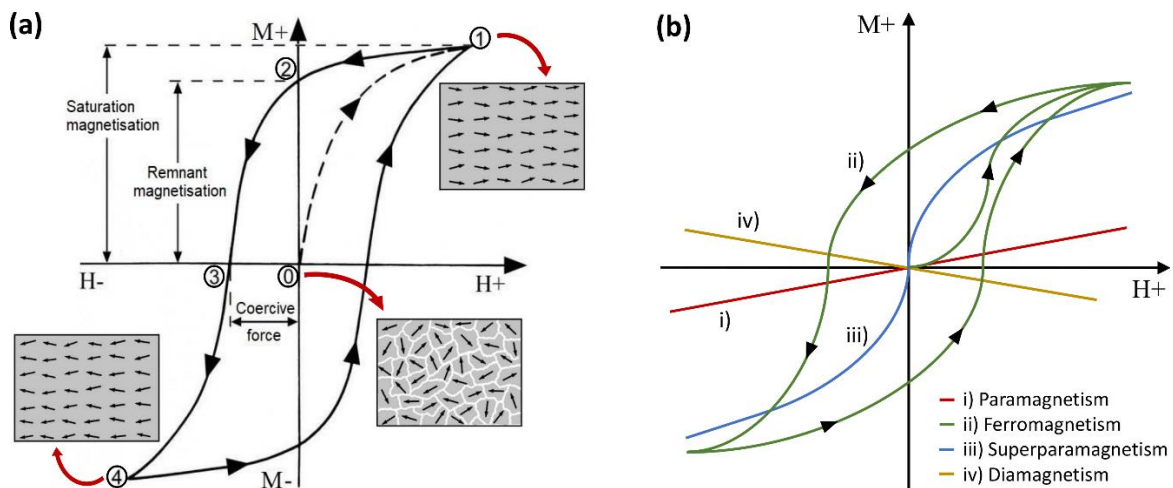


Figure 1.8. (a) Hysteresis cycle of a ferromagnetic material showing the multi-domain microstructure under zero field ①, spins are aligned at points of saturation magnetisation ① and ④, value of remnant magnetisation (M_r) ② and value of the coercive field (H_c) ③. (b) Schematic representation of M-H curves for i) paramagnets, ii) ferromagnets, iii) superparamagnets and iv) diamagnetic materials.

An example of a ferrimagnetic material is magnetite (Fe_3O_4), whose magnetic properties have seen it find applications across biomedicine, drug delivery, sensing technology, catalysis, magnetic recording and wastewater treatment.^{53,57,58,59,60,61} Magnetite has an inverse spinel structure, crystallising in the $Fd\bar{3}m$ space group. Its chemical composition may be thought of as $\text{Fe}^{2+}\text{Fe}_2^{3+}\text{O}_4^{2-}$, where the O^{2-} ions form a face-centered cubic lattice with half of the Fe^{3+} ions occupying tetrahedral sites and octahedral sites are occupied by Fe^{2+} ions and the other half of the Fe^{3+} ions. Magnetite may show superparamagnetic behaviour when the particle size is below 20 nm (critical diameter, D_P), displaying values for M_r and H_C of zero.^{62,61,63} The saturation magnetisation (M_s) value for bulk magnetite is 90 emu/g, while single crystal magnetite nanoparticles generally show values 10 to 30 % lower.^{64,65,48} Superparamagnetism, therefore, is observed when the size of the nanoparticles is below the critical diameter (D_P) and the temperature is above the blocking temperature (T_B). **Figure 1.9(a)** shows the magnetic behaviour of magnetite particles in relation to particle size. **Figure 1.9(b)** displays the crystal structure of magnetite (Fe_3O_4).

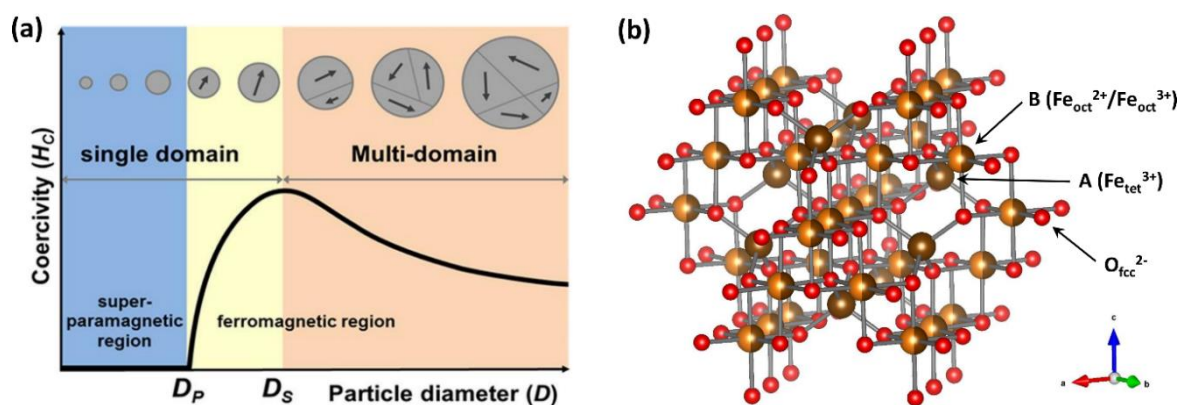


Figure 1.9. (a) Schematic showing the coercivity (H_C) behaviour of a magnetic particle as a function of its diameter. As particle size decreases the domain walls disappear, resulting in an increase in H_C until the particle size reaches D_S (transition from multi domain to single domain). When the particle size further decreases, the thermal agitation energy overcomes magnetic anisotropy energy and, as a result, the particle enters the superparamagnetic regime, D_P , where the coercivity exhibited is zero.⁶⁶ (b) Magnetite crystallises in an inverse spinel structure (AB_2O_4). Here O^{2-} ions (red) are arranged in a face-centred cubic system. Fe^{2+} ions (gold) sit in octahedral sites while one half of Fe^{3+} ions (brown) occupy octahedral sites and the other half occupy tetrahedral sites. Magnetite can be represented as: $(\text{Fe}_{\text{tet}}^{3+})(\text{Fe}_{\text{oct}}^{2+})(\text{Fe}_{\text{oct}}^{3+})\text{O}_4$.

1.3.2 Previous strategies for nanoparticle-based conservation treatments

Despite the long history of advances in the development and application of nanostructured materials, the use of nanotechnology in the conservation of cultural heritage has only been approached relatively recently for less than two decades. Amongst the earliest records of the use of technology in conservation of cultural heritage there are patented treatments in the early 20th century in which ‘silicic ether’ was used as a consolidant for stone, although they were dismissed soon after due to poor efficacy.^{67,68} Later, a combination of biocides with ‘silicic acid ester’ was designed for masonry preservation.⁶⁹ After half a century of slow but steady progress, the 1980s and 1990s saw a blossoming of techniques for stone conservation, most of them based in the use of sol-gel chemistry and alkoxysilanes as consolidants.⁷⁰ However, the first use of nanoscience in the conservation of art and artefacts dates back to the 1980s during the restoration of Renaissance paintings in the Brancacci Chapel in Florence.⁷¹ Wax, originating from candles, that had deposited on the wall paintings over the centuries, was successfully removed using microemulsions of SDS/dodecane/n-butanol/H₂O. Polymers and resins, widely used to consolidate wall paintings in the past, often degrade over time and exhibit poor treatment reversibility.^{72,73}

The use of nanoparticles in conservation has gradually increased over the last decades. For example, Giorgi *et al.*⁷⁴ successfully used suspensions of calcium and barium hydroxide nanoparticles to consolidate Mesoamerican wall paintings. More recently, Munafò *et al.*⁷⁵ used the photocatalytic properties of TiO₂ nanoparticles in the conservation of stone which had been exposed to volatile organics, microorganisms or other contaminants in urban environments. Travertine stone samples were spray-coated with colloidal suspensions of TiO₂ nanoparticles, and indoor laboratory tests showed promising self-cleaning properties from this treatment. Nanoparticles have also been used for the protection and conservation of wood. Mahltig *et al.*⁷⁶ improved the mechanical properties of various types of wood and endowed it with fire retardant, water repellent and antimicrobial properties upon application of modified silica nanosols in aqueous solution. In the 2000’s, alkaline earth hydroxide [Mg(OH)₂ and Ca(OH)₂] and carbonate [SrCO₃, BaCO₃ and CaCO₃] nanoparticles were introduced for the deacidification of decaying paper, canvas and wood.^{27,29,30,77} Although submicron sized particles had been used previously in paper conservation, these more recent approaches have pioneered the use of nanoparticles to preserve paper, canvas and wood since they used non-aqueous dispersions. This was a significant improvement since aqueous dispersions, used for example in the Bookkeepers method, contribute to the degradation of cellulose in the long term.⁷⁸

1.3.3 Specific conservation approaches using magnetic nanoparticles

The majority of materials utilised for the preparation of nanoparticles for conservation treatments are alkaline earth hydroxides and alkaline earth carbonates, as mentioned previously. However, Bonini *et al.*⁷⁹ designed a so-called ‘nanomagnetic sponge’ aimed at removing resins from the surface of wall paintings. Such sponges were comprised of cobalt-ferrite nanoparticles cross-linked through a polymer network based on PEG and acrylamide. The sponges could be loaded with solvents, microemulsions or micellar systems and applied on the surface to be treated. The magnetic responsiveness of the sponge facilitated its removal from the surface of the artwork with a permanent magnet. The magnetism of the sponges not only helped to preserve the integrity of the surfaces treated by minimising the use of tools on it but also allowed for the manipulation of the sponge to load and unload solvents. To date, there have not been attempts to apply magnetic nanoparticle based treatments to waterlogged wooden artefacts.

1.4 Synthetic approaches to magnetic nanoparticles

The variety of the existing synthetic methods allows for the preparation of magnetic particles of different sizes, shapes, size distributions, and crystallinities. Magnetite nanoparticles may be coated during their synthesis for an improved physical or chemical stability, as preparation for further functionalisation or to gain control over the growth of the nanoparticles. Thus, while some methods offer high control over size and shape with low yields, other strategies are inexpensive, easily scalable and yield particles with wider size distributions. Popular synthetic pathways for the preparation of magnetic nanoparticles, including co-precipitation, thermal decomposition, hydrothermal synthesis, and microemulsions are discussed below.

1.4.1 Co-precipitation

Co-precipitation is a facile and convenient method to synthesise iron oxide nanoparticles as it is easy to scale-up, can be carried out at relatively low temperatures, and particles are precipitated from aqueous solutions, avoiding the use of large amounts of organic solvents. However, this method tends to yield particles with a broad size distribution which can lead to non-ideal magnetic behaviour. In co-precipitation the stages of nucleation, growth, and aggregation occur quasi-simultaneously. Briefly, nucleation occurs when the concentration of the precursors reaches the maximum critical concentration, or supersaturation, and nuclei start to form. In order to obtain highly

monodisperse nanoparticles, a short burst of nucleation should cause a decrease in concentration and the rapid interruption of nuclei formation. This would be followed by a longer period of growth of the nuclei in which solutes diffuse from the solution and incorporate onto the particle surface. In non-ideal conditions, nucleation and growth stages overlap, causing new nuclei to form while those already formed continue growing. Inevitably, this gives the particles a wider size distribution.^{80,81} **Figure 1.10** shows a La Mer diagram describing the fundamental stages of particle formation in colloidal solution.

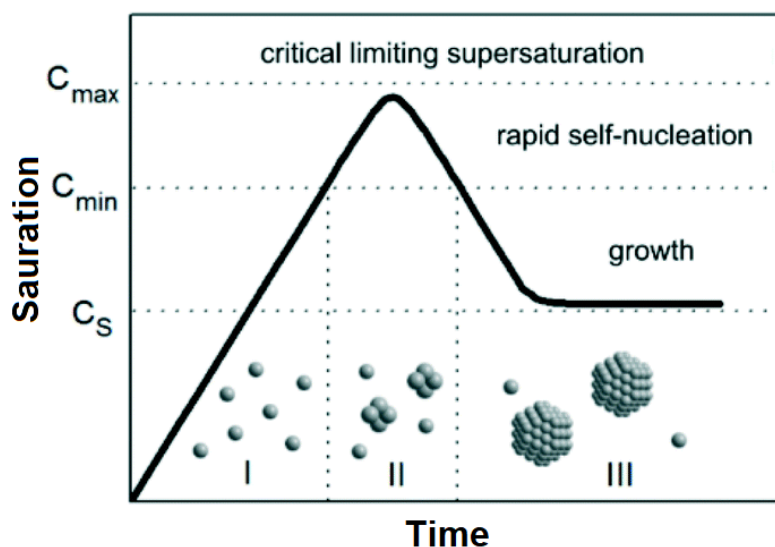


Figure 1.10. The La Mer model is generally accepted to describe particle formation mechanisms in colloidal solutions. The concentration of monomers (or ions) in solution is increased beyond a critical supersaturation level (C_{min}). Nuclei start to form rapidly (burst nucleation) which causes the concentration of monomers in solution to drop below the self-nucleation level, marking the end of the nucleation stage. Growth then occurs due to the diffusion of remaining monomers in solution to the already formed particles surfaces. A rapid nucleation and a slow growth are ideal for obtaining a narrow size distribution; if nucleation lasts too long, then heterogeneous nucleation/growth will take place yielding polydisperse particles.^{82,83}

Nonetheless, a certain degree of monodispersity can still be achieved as smaller, newly formed nuclei may adhere to larger particles reaching a more thermodynamically stable state where the surface area to volume ratio is minimised. This phenomenon is known as Ostwald ripening and causes the size distribution of the nanoparticles to narrow.⁸⁴ René Massart first developed a method for the preparation of aqueous magnetic liquids, and reported the preparation of monodisperse magnetic nanoparticles.^{85,86} Variations of this method exist nowadays, including ultrasonic- and microwave-assisted procedures, which allow for shorter reaction times, lower temperatures, more

homogeneous heating, and better monodispersity and crystallinity of the material synthesised.^{87,88}

1.4.2 Thermal decomposition

Highly monodisperse magnetite nanoparticles can be prepared by thermal decomposition of organometallic precursors in high-boiling organic solvents and in the presence of stabilising surfactants. The organometallic compounds generally used include iron acetylacetonate [$\text{Fe}(\text{acac})_3$], iron carbonyl [$\text{Fe}(\text{CO})_5$], or iron oleate. Common surfactants employed are oleylamine, hexadecylamine, or fatty acids such as oleic acid. In this method the ratios of the starting compounds, surfactants, and solvents used are crucial parameters for the control over the size and shape of the nanoparticles. The reaction time and temperature must also be controlled to achieve nanoparticles of a desired morphology and size. Lee *et al.*⁸⁹ have prepared Fe_3O_4 nanoparticles of various sizes, from 4 to 160 nm. They found that the boiling point of the solvent chosen had an impact on the resulting particle size. For example, [$\text{Fe}(\text{acac})_3$] was used to obtain 4 nm magnetite particles in diphenyl ether (bp 265 °C), in the presence of oleic acid. Similarly, 6 nm particles were obtained in benzyl ether (bp 300 °C), in the presence of oleylamine. Furthermore, Fe_3O_4 particles of 4 nm could be used subsequently as seeds to obtain larger nanoparticles, up to 20 nm. The single crystalline particles were found to be ferrimagnetic at 10 K and superparamagnetic at room temperature. Finally, Fe_3O_4 particles of 16 nm produced through thermal decomposition had a saturation magnetisation (M_s) of 83 emu/g Fe_3O_4 , very close to that of bulk magnetite (90 emu/g Fe_3O_4). **Figure 1.11** shows (a) the schematic of the preparation of oleate stabilised magnetite nanoparticles, and (b and c) electronic microscopy images of the as synthesised nanoparticles.

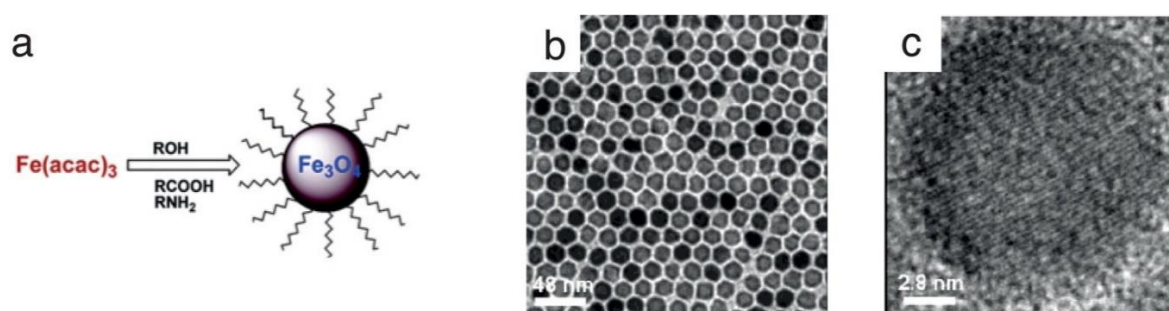


Figure 1.11. (a) Schematic illustration of the synthesis of iron oxide nanocrystals (NCs) through the decomposition of $\text{Fe}(\text{acac})_3$ in the presence of oleic acid, oleylamine and akanediol; (b) typical TEM image of the as synthesised nanoparticles; (c) HR TEM image of the 16 nm Fe_3O_4 nanocrystals.⁸⁹

Thermal decomposition allows for the preparation of highly crystalline nanoparticles of a wide range of sizes and with various surfactant coatings. However, there are some disadvantages: high temperatures are required, as well as long reaction times and the use of organic solvents, which make it difficult to scale up the synthetic processes.^{81,90}

1.4.3 Hydrothermal Synthesis

Magnetite nanoparticles may be grown from aqueous solutions of Fe(II) and Fe(III) salts at high temperatures and high vapour pressures in Teflon-lined stainless steel autoclaves. Daou *et al.*⁹¹ reported the synthesis of monodisperse, highly crystalline Fe₃O₄ nanoparticles with an average size of 12 ± 2 nm, by means of co-precipitation of ferrous and ferric ions. Interestingly, subsequent hydrothermal treatment of these particles (250 °C, 24 hours) yielded monodisperse, highly crystalline Fe₃O₄ nanoparticles of 39 ± 5 nm in diameter, with saturation magnetisation of 82.5 emu/g, close to that of bulk magnetite. Dhage *et al.*⁹² explored the use of a microwave treatment to assist the hydrothermal stage in the preparation of magnetite nanoparticles. Using identical conditions to the conventional hydrothermal method (190 °C, 154 psi) the reaction times were shortened to 30 min. Although the microwave-assisted hydrothermal method resulted in much shorter reaction times, the particles prepared often ranged 100 to 500 nm in size. This resulted in polydisperse samples.

1.4.4 Microemulsion approach

Micelles are spherical supramolecular assemblies formed in aqueous media consisting of surfactant molecules aggregated with their hydrophilic end in contact with the solvent and the hydrophobic tail towards the centre. In organic solvents, the orientation of the surfactant molecules is inverted, forming reverse micelles. Here, the polar heads are oriented towards the inside of the sphere, and the hydrophobic tails are in contact with the solvent. When oil is mixed with water in the presence of surfactants, micelles or reverse micelles may be formed giving rise to a stable system called an emulsion. Reverse micelles are often used as micro reactors to grow nanoparticles inside them. For this, a small amount of water containing the precursors for the reaction is dispersed in a non-polar continuous phase in the presence of a surfactant. A microemulsion is formed, containing nanometre-sized water droplets. Typically, the nucleation stage occurs within certain micelles, followed by growth *via* the exchange of nuclei during micellar collisions upon stirring.⁹³ In many procedures the inverse micelle size varies linearly with the water

to surfactant ratio (ω_o). This parameter is also associated with the remarkable control of particle size control in the microemulsion method. The choice of surfactant, cosurfactant, and nature of continuous phase can influence the interchange dynamics of the micelle by modifying the rigidity of the aqueous-oil interface. These conditions can be adjusted to control the particle growth towards a certain shape or crystalline phase.⁹⁴ Pileni *et al.*^{95,96} first introduced the use of colloidal self-assemblies for the synthesis of a variety of ferrites and cobalt metal nanocrystals, for which both regular and reverse micelles were used. The main limitations of the microemulsion approach are the large amount of solvent needed and the low yields obtained.

1.4.5 Sol-gel method

In sol-gel synthesis the starting point is an aqueous solution (*sol*) of the precursors, typically metal alkoxides or metal chlorides. These precursors generally undergo a series of hydrolytic and polycondensation processes to form a suspension of nanoparticles. The *sol* evolves in an inorganic network within a liquid phase, the *gel* phase, and the liquid phase is then removed *via* a drying process. The sol-gel method is inexpensive and yields highly crystalline and monodisperse nanoparticles. The main drawback of this method is the need for a purification treatment after the synthesis, since the presence of reaction by-products is common and must be removed to avoid contamination.⁹⁷ However, there are opportunities for tuning the sol-gel approach. For example, Biddlecombe *et al.*⁹⁸ prepared iron oxide nanoparticles from a metallorganic iron (II) alkoxide precursor $[\text{Fe}(\text{O}i\text{Bu})_2(\text{THF})_2]$ using an ultrasound-assisted thermal treatment in THF. Depending on the reaction conditions used, the nanoparticles obtained were identified as superparamagnetic γ -maghemite (9 nm) or magnetite (19 nm), and were found to aggregate in needle-like and plate-like assemblies, respectively. In 2012, Lemine *et al.*⁹⁹ prepared highly crystalline magnetite using a sol-gel method in supercritical conditions. The 8 nm nanoparticles were obtained by bringing an ethanolic solution of iron (III) acetylacetonate to supercritical conditions in an autoclave. Sol-gel methods require low reaction temperatures to yield products of high purity. However, the reaction times needed are often long and the precursors used are relatively expensive.

1.4.6 Microwave synthesis of nanoparticles

Microwave-assisted synthetic methods employ microwave radiation to induce an intrinsic heating of the precursors. The use of microwaves for the synthesis of nanomaterials has several advantages over conventional heating methods, namely reduction of reaction time, improved reproducibility, reduction of side reactions, and a significant improvement in the control over reaction conditions. This results in an improved control of the morphology, phase, particle size and particle size distribution of the nanomaterials, and therefore greater control of their intrinsic properties.^{100,101} For example, ZnSe alloyed quantum dots (QDs) can be prepared *via* a microwave-assisted aqueous synthesis.¹⁰² Precise control over the reaction time and temperature is key to obtain QDs that exhibit improved photoluminescent high quantum yields up to 17 % compared with organometallic methods or hydrothermal synthesis. Microwave radiation has also been used for the preparation of cathode materials for lithium batteries. For instance, Yang *et al.* synthesised LiV_3O_8 *via* a microwave solid-state route.¹⁰³ This material showed enhanced ionic conductivity, discharge capacity and cycle performance due to the creation of two-dimensional Li^+ diffusion channels created between the nanosheet-shaped structures obtained with this synthetic route. Microwaves have been recently incorporated and further developed by the Corr group by introducing a microwave-assisted growth stage into co-precipitation and hydrothermal routes, or inducing heating stages in solid state routes with microwave furnaces.^{104,105} Particularly, for iron oxide nanoparticles, the use of microwaves has been found to substantially decrease the reaction times and ageing periods of Fe_3O_4 nanocrystals preparation.⁸⁷ It also provides precise control over the growth of highly crystalline and monodisperse nanoparticles in solution due to the homogeneity of the microwave heating.¹⁰⁶ This resulted in superparamagnetic Fe_3O_4 nanoparticles with a saturation magnetisation of $67.6 \text{ emu}\cdot\text{g}^{-1}$. Additionally, this method is robust, very reproducible and easily scalable.

1.5 Functionalisation strategies for multifunctional nanoparticles

Bare magnetite nanoparticles, as with the majority of other uncoated nanoparticles, when dispersed in a solvent tend to agglomerate and form precipitates, mainly through dipolar interactions with each other. This is, generally, an undesirable effect, but can be addressed by providing the nanoparticles with a stabilising coating. Coatings can have favourable wetting properties with the solvent medium to improve the particle solubility and the volume of the protective coating also provides steric hindrance between particles. Also the coatings can be tailored to provide functional groups containing, for

example, a charged species, therefore enabling electrostatic repulsion to avoid particle agglomeration or aggregation. The types of coatings can be classified into organic and inorganic shells.

Organic coatings often consist of surfactants or polymers. These are used to passivate the surface of the particles, during or after their synthesis, to avoid aggregation and favour colloidal stability. This is particularly important in ferrofluids, in which the surface properties of the magnetic particles determine their colloidal stability.^{107,108} For example, species containing phosphates, sulfates, amines or carboxyl groups can be used to coat the surface of iron oxide nanoparticles, which can enable electrostatic interactions. Polyanilines, polyesters, polyethylene glycols, dextran, chitosan, oleic acid or citrate are common species used as stabilisers during or after the preparation of the iron oxide nanoparticles. Organic coatings generally offer good biocompatibility, which is key in the synthesis of magnetic nanoparticles, but often can be unstable at high temperatures.^{109,110,111,112}

Iron oxide nanoparticles can also be coated with a variety of inorganic compounds. Silica shells are a common way to protect the cores and to provide a priming for further attachment of additional layers. Silica coatings are easily tuneable, can increase stability in aqueous conditions and facilitate further surface functionalisation.¹¹³ Other inorganic coatings include precious metals such as Au and Ag. These coatings can protect the magnetic cores against oxidation, enhance colloidal stability and enhance biocompatibility, but are commonly used for more specific purposes, like providing electrical conductivity or specific optical properties.^{114,115} Both organic and inorganic coatings have effects on the resulting magnetism of nanoparticles. The addition of non-magnetic components can result in a significant decrease in saturation magnetisation.⁸¹

Molecules bearing silane, hydroxyl and carboxyl groups are the main species used to bind to the surface of the magnetic nanoparticles.^{116,117,118} Silica coatings on iron oxide nanoparticles can be used to facilitate further functionalisation, whereby covalent links of the incoming moiety to the silica shell can be formed. These groups can easily react with the -OH groups present on the surface of bare iron oxide nanoparticles *via* direct condensation to form strong covalent bonds Fe-O-Si (**Figure 1.12**).^{119,120,121} The advantages of this approach include scalability, control over silica shell thickness and a choice of terminating functional groups.

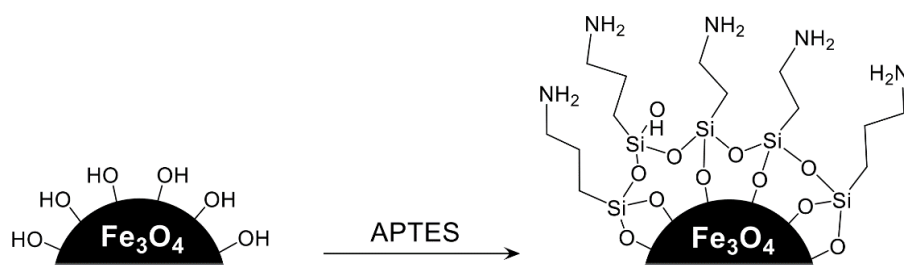


Figure 1.12. Schematic of attachment of alkoxy silane molecules onto a metal oxide nanoparticle. The covalent bonds Si-O-Fe are formed by the condensation between the hydroxyl groups, naturally present on metal oxide surfaces, and the alkoxide moieties.

Alkoxy silanes are widely used as linkers or spacers in the functionalisation of surfaces with substances such as dyes or ligands. They can form covalent bonds with the surface of iron oxide nanoparticles through condensation and can be synthesised with a variety of functional groups on the opposite end of the carbon chain to the silane groups. This enables the choice of a specific linker with a desired functional end group, depending on the nature of the substance to be attached. With the application of magnetic nanoparticles comes the additional consideration how proximity of a chemical species to the particle surface may have undesirable effects on the resulting physicochemical properties. Optically active molecules, for instance, need to be separated from the magnetic nanoparticle, since a direct attachment to the surface often results in quenched luminescence due to interactions with the unpaired electrons that give rise to the magnetism of the core particle.¹²² The affinity in biospecific interactions, like in the system biotin-streptavidin, can be affected by the steric hindrance when one of the components is immobilised on a surface. Among other parameters, the length of the spacer arm can determine the grade of valency of the system and, therefore, the affinity between protein and ligand.^{123,124} The application of silica spacers with tail functional groups allows for the design of more complex nanocomposites, for example the inclusion of polymer networks or sequestering molecules for artefact application and treatment, respectively.

1.6 Polymer synthesis protocols

Polymers are large molecules that are made of repeating, smaller units called monomers. The type, nature, number and variety of the monomers are responsible for the physicochemical properties of the polymer. Because of the enormous variety of monomers, polymeric materials can be designed with specific properties in mind.^{125,126,127}

Existing polymerisation methods can be classified as step-reaction polymerisation (generally condensation polymerisation processes) or chain-reaction polymerisation (normally addition polymerisations). In step-reaction polymerisation methods, the monomers react with each other through typical organic reactions such as esterification or acylation. The chain growth is initiated by one of these reactions, and repeated until all the monomers have formed low molecular weight species called oligomers. These oligomers then further react to form longer chains of moderate molecular weight. Step-reaction polymerisations have high activation energies and therefore require long reaction times and high temperatures. Chain-reaction polymerisations are free-radical reactions, whose mechanism consists of three distinct steps: initiation, propagation and termination. This type of polymerisation is significantly faster than step-reaction polymerisation and generally does not require high reaction temperatures. Two or more monomers can be employed in this process, yielding a so called copolymer with substantially different properties. The chains obtained can be linear, branched or cross-linked systems, generally reaching high molecular weights.¹²⁸ Step-reaction polymerisation is useful when synthesising controlled, low molecular weight structures, as the molecular weight increases slowly at the beginning of the reaction. Chain-reaction polymerisation is favourable for high molecular weight structures or denser, branched or cross-linked structures and yields chains of narrower size distribution.

1.6.1 RAFT polymerisation

Reversible addition-fragmentation chain-transfer (RAFT) polymerisation is a type of chain-reaction polymerisation, which utilises a conventional free radical initiator, and whose mechanism is mediated by a chain-transfer agent (CTA) or RAFT agent. After the initiation and propagation stages, the RAFT agent generates an equilibrium between all of the growing chains, giving them equal growth opportunities. The RAFT agent provides a narrow molecular weight distribution and determines the molar mass of the final product. RAFT mediated polymerisation is known for its simplicity to implement, its compatibility with a wide range of monomers, and its control over molecular weight distribution.^{129,130,131} Depending on the design of the polymer monomers, it is possible to introduce specific physicochemical properties in the final polymer product. One such example is the response of the polymer to external temperature fluctuations.

1.6.2 Thermoresponsive polymers

Thermoresponsive polymers show swift changes in their physical properties upon variations in temperature. According to their response to temperature, thermoresponsive polymers can be classified into two main categories: LCST- and UCST-type polymers. Some polymers become insoluble upon heating, undergoing a sharp and reversible phase transition. They present a so-called lower critical solution temperature (LCST) point, below which they are miscible with the solvent. Other polymers show the opposite behaviour and instead become soluble when heated. These are less common in aqueous media, and present an upper critical solution temperature (UCST) point. Above the UCST, the polymer is miscible with the solvent phase. Phase changes in UCST-type polymers are not as sharp as for LCST-type thermoresponsive polymers. In compounds exhibiting LCST-type behaviour, phase separation is more stable at higher temperatures, since it is an entropically driven effect. Temperatures below the LCST favour the adsorption of water molecules and the dissolution of the polymer. **Figure 1.13** provides generic examples of the phase transition for a binary solution of an LCST- or UCST-type polymer. An increase in temperature leads to the cleavage of hydrogen bonds between hydrophobic segments in the polymer and the water molecules. This increases the overall hydrophobic behaviour of the polymer, turning a clear solution into a cloudy one. This behaviour can be fine-tuned by adjusting the hydrophilic-to-hydrophobic ratio of the sections of the polymer. A UCST-type phase transition, however, is an enthalpically driven effect, hence phase separation is more stable when the temperature is lowered. These species are generally markedly hydrophilic and, upon cooling, become insoluble due to strong hydrophobic interchain (polymer-polymer) attractions.^{132,133} Since the temperature is an external stimulus which can be easily applied, the use of thermoresponsive polymers is growing in areas of biotechnology such as drug and gene delivery or tissue engineering.^{134,135,136}

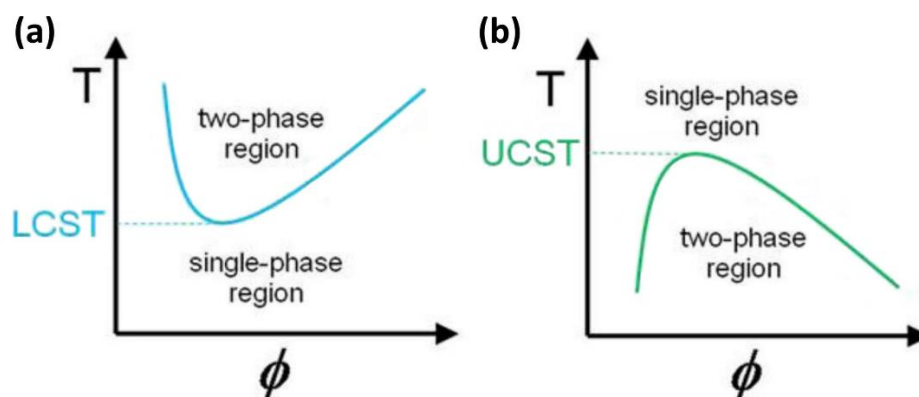


Figure 1.13. Phase diagrams of a polymer-solvent system, representing temperature (T) vs. polymer volume fraction (ϕ). These diagrams show (a) lower critical solution temperature (LCST)-type behaviour, and (b) upper critical solution temperature (UCST)-type behaviour.¹³⁶

1.7 Chelating agents

The word ‘chelate’ comes from Modern Latin *chela* (‘claw’ of a crab or a lobster) and is used in zoology to define specimens ‘having pincer-like claws’. In chemistry, a chelating agent is defined as a compound able to coordinate with a metal ion forming two or more bonds, resulting in a stable complex. From the point of view of coordination chemistry, chelating agents are multidentate ligands, and can bind metal cations *via* specific atoms with lone pairs of electrons. These electron donor atoms are, generally, nitrogen and oxygen present in functionalities such as amines, amides, carboxylic acids or oximes. Consequently, in the majority of cases, chelating agents are linear, branched or cyclic hydrocarbon chains that contain some of the aforementioned functionalities. In this work, two types of chelating agents have been used, namely porphyrins and aminopolycarboxylic acids (APCA’s), as a strategy to bind to unwanted iron ions that catalyse degradation of *Mary Rose* timbers.

Porphyrins are macrocycles consisting of four pyrrole units linked by four bridging carbons in a planar conformation. This forms an aromatic and highly conjugated 18- π electron system, which is responsible for the unique electronic and optical properties of the porphyrin derivatives. Porphyrins and metalloporphyrins can be found in nature, for example, in various types of chlorophyll and heme structures. In some chlorophylls, magnesium-containing metalloporphyrins play a key role in light harvesting and electron transport.^{137,138} Heme is a metal-ligand complex formed by iron and Protoporphyrin IX and is an essential component in the transport and storage of oxygen, drug and steroid metabolism, and signal transduction in cells.^{139,140} Porphyrins are very valued species,

used as photosensitizers in organic photovoltaic cells, photodynamic therapy and conductive organic materials, and also as bioimaging probes or antimicrobials.^{141,142,143,144,145} For some applications, porphyrins and metalloporphyrins are often immobilised on a variety of materials. For instance, Fernandez *et al.*¹⁴⁶ have reported the successful functionalisation of gold surfaces with Protoporphyrin IX (PPIX). The porphyrin units were bonded directly to an Au (111) surface, or to an amine terminated self-assembled monolayer (SAM) grown on Au (111), in order to study the metalation of PPIX molecules at the solid-liquid interface. Surface-enhanced Raman spectroscopy and X-ray absorption near edge structure (NEXAFS) measurements showed that PPIX molecules bonded to the SAM with a tilted molecular plane, while on naked Au (111) PPIX molecules lay horizontally forming multilayers. This resulted in an optimal metalation temperature of 350 K for the PPIX-SAM system whereas, when deposited onto naked Au (111), PPIX was successfully metalated at room temperature. Karousis *et al.*¹⁴⁷ functionalised graphene oxide with an aminoporphyrin derivative. The porphyrin moiety was covalently grafted onto the graphene oxide sheet by forming an amide bond between the primary amine in the porphyrin unit and the carboxyl groups present on graphene oxide. The photoelectrochemical properties exhibited by this material are of great interest in the development of optoelectronic devices. Nowostawska *et al.*¹⁴⁸ prepared magnetic fluorescent nanocomposites by covalently attaching porphyrin moieties onto silica-coated magnetite nanoparticles. A carboxylic acid porphyrin was reacted with an alkoxysilane ((3-Aminopropyl)triethoxysilane, APTES), and this was further attached onto silica-coated iron oxide nanoparticles. This fluorescent magnetic nanocomposite showed promising results as a multimodal platform, with potential simultaneous application in *in vitro* biological imaging and therapeutic treatments. Fluorophores have been found to be significantly quenched when attached to magnetic cores. This process is believed to result from the contact of the fluorescent molecules with the magnetic core, leading to a charge transfer process, previously reported by Mandal *et al.*¹⁴⁹ In this work, the authors studied an emulsion in water of an oil containing iron oxide nanoparticles and tri-*n*-octylphosphine stabilised CdSe/ZnS core-shell quantum dots. The increase of iron oxide content originated a decrease in fluorescence intensity of the emulsification. The authors indicated that the quenching can be partially avoided by introducing a shell before adding the fluorescent molecule or by adding a spacer between the fluorophore and the magnetic core. Additionally, fluorophores can suffer from self-quenching at high concentrations, for example, when nanoparticles are loaded with large amounts of fluorescent molecules. In the case of porphyrin derivatives, self-quenching can occur through π - π stacking aggregation.^{150,151} **Figure 1.14** shows some examples of porphyrins chelating metal

cations. Often, other ligands or donor groups present in side chains participate in the coordination complex.

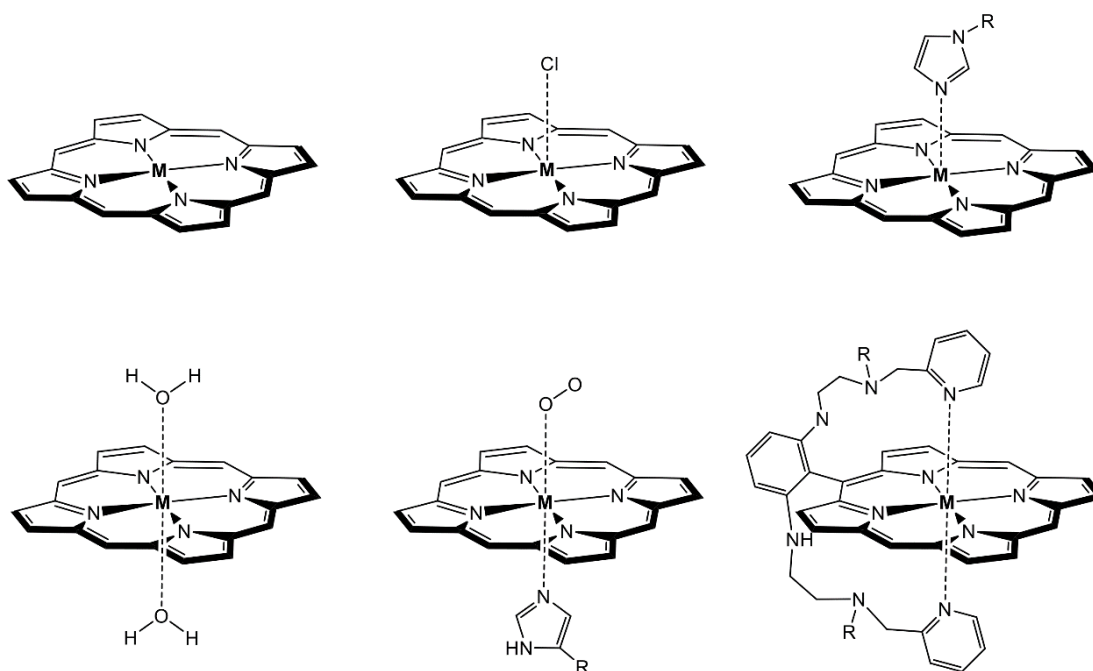


Figure 1.14. Examples of common metalloporphyrin structures. Porphyrins can form stable chelates with metals through the lone pairs of electrons on the four nitrogens. This structure is especially stable for transition metals with +2 or +3 oxidation states. The metallic centres can also be coordinated with other donor ligands or side chains in the porphyrin ring, resulting in coordination complexes where the metal forms bonds with up to six donor atoms.

Aminopolycarboxylic acids (APCAs) consist of linear or cyclic hydrocarbon chains bearing one or more primary, secondary or tertiary amines and carboxyl groups. As in the example of porphyrins described above, carboxyl groups and nitrogen centres within the APCAs have lone pairs of electrons that coordinate with the metal ions to form complexes. Therefore, there exists a wide variety of APCAs able to chelate metal ions in different geometries and with different denticity, depending on the number of aforementioned functionalities. APCAs have been used for decades in a variety of fields such as environmental chemistry, medicine or molecular biology. For instance, iminodiacetic acid, nitrilotriacetic acid, EDTA or DTPA which have been largely studied during the late 1990's and 2000's for the removal of heavy metals from water. Despite being commercially available, their application on an industrial scale has not been successful, mainly due to the cost and complexity of the preparation methods.¹⁵² Some APCAs have also been studied for their use in the inhibition and activation of metal cation dependent enzymes.¹⁵³ Coordination complexes formed by DTPA and derivatives with isotopes such

as Gd-93, Gd-95 or In-111 have been widely employed as MRI contrast agents.^{154,155} DTPA is also used for the chelation of plutonium and uranium in the early stages of treatment after an accidental exposure to these radioactive metals.¹⁵⁶

Of specific relevance to this work, EDTA and DTPA have previously been used for the removal of iron corrosion products from archaeological artefacts due to their strong iron chelating properties.^{35,157,158} They are effective species for this application: EDTA is a hexadentate ligand forming a stable, octahedral environment upon chelation of divalent or trivalent metals with its four carboxylic acids and its two amino groups; DTPA consists of an ethyleneamine backbone with three amines and five carboxyl groups, and is potentially an octadentate ligand. It can also coordinate with metals in an octahedral geometry leaving two free carboxyl groups. These extra carboxyl groups make a significant difference with EDTA in that they can be used for further attachment of DTPA onto a substrate. **Figure 1.15** shows some examples of APCAs of different denticity coordinating a metal ion. The number and arrangement of the donor groups within the structure give rise to a vast range of chelating agents capable of coordinating multiple metal ions with different geometries.

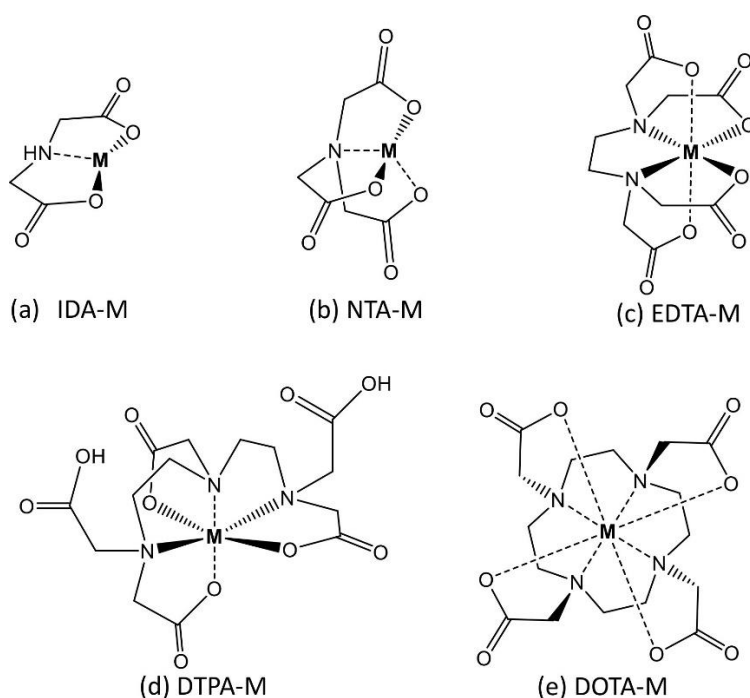


Figure 1.15. Selection of common APCAs (a) iminodiacetic acid, (b) nitrilotriacetic acid, (c) ethylenediaminetetraacetic acid, (d) diethylenetriaminepentaacetic acid and (e) 1,4,7,10-tetraazacyclododecane-1,4,7,10-tetraacetic acid. The denticity of the complex formed is given by the structure of the ligand and the number of donor atoms.

1.8 Aims and objectives

The specific aims of this work are to address the conservation problems faced by marine archaeological wood in general, and the *Mary Rose* in particular due to chemical degradation processes. As described in **Section 1.2.2**, one of the main threats to the integrity of marine archaeological wood is the formation of harmful acidic substances within the wood structure. Conservators of the *Vasa* and the *Mary Rose* have detected iron and sulfur deposits within the wood structure and found that iron can catalyse acidification processes under atmospheric conditions: iron sulphides can be oxidised in the presence of oxygen and water to form iron sulfate and sulfuric acid. The sulfuric acid produced then has a deleterious effect through corrosion of the wood structure. Iron ions also play a key role in Fenton-type reactions where the hydroxyl radicals formed can degrade lignin, cellulose and hemicellulose, main components of wood.

The treatments suggested to date are able to neutralise the iron ions with different degrees of success. However, none of the strategies consider the subsequent extraction of the iron from the wood to completely eliminate the threat to the *Mary Rose* timbers. The complete removal of the iron ions is a necessary condition for the successful long term conservation of these artefacts, yet this must be achieved in a way that does not cause any harm to the underlying artefact.

This research focuses on the design, synthesis, characterisation and evaluation of a series of tuneable tools for the safe neutralisation, sequestration and removal of harmful iron ions from marine archaeological wood. The nanocomposites presented here are based on magnetic nanoparticles functionalised with a metal chelating agent, and are further embedded in a thermoresponsive polymer. **Figure 1.16** shows a schematic of the proposed design for the treatment of waterlogged wood. Magnetic nanoparticles functionalised with chelating agents are embedded in a thermoresponsive polymer (a). This system is cooled down and applied on wood where high amounts of harmful iron ions have been detected (b). The nanoparticles penetrate in the wood structure upon application of an external magnetic field. After the incubation period, during which the chelating agents have sequestered the iron ions, the treatment is heated up mildly and peeled off the surface of the treated artefact (c).

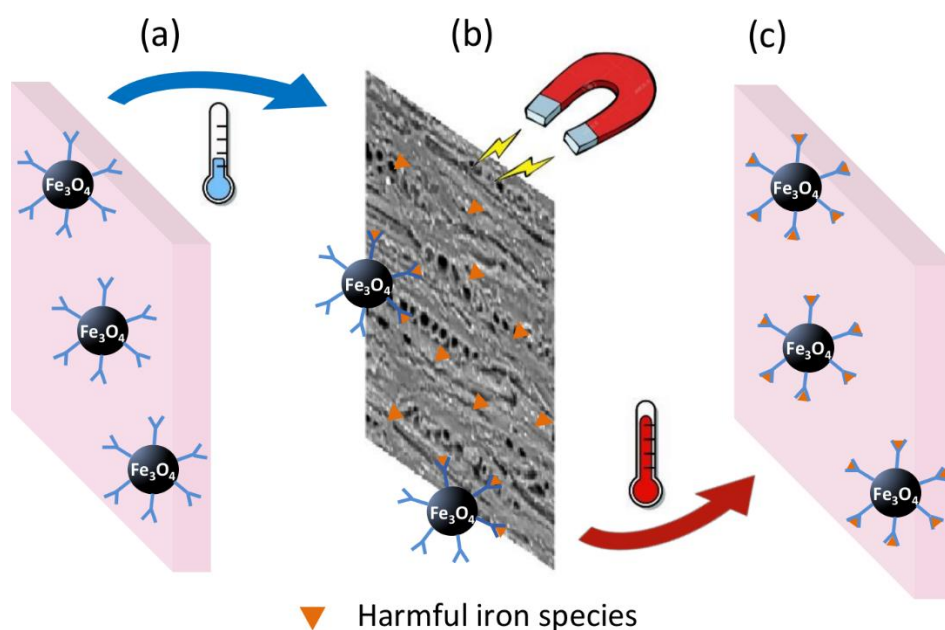


Figure 1.16. The treatment, consisting of functionalised nanoparticles encapsulated in a thermoresponsive polymer, is cooled down (a) and applied onto the wood (b). After the incubation period, the temperature is increased and the treatment is peeled off the surface of the wood (c) thus removing the harmful iron species.

Iron oxide nanoparticles prepared by microwave-assisted co-precipitation methods have allowed for short reaction times and yield highly crystalline nanoparticles and will be employed in this work.⁸⁷ A series of chelating agents are investigated, specifically two porphyrin derivatives, Protoporphyrin IX (PPIX) and 5,10,15,20-tetrakis (4-aminophenyl) porphyrin (porphyrin-amine), and an aminopolycarboxylic acid, diethylenetriamine pentaacetic acid (DTPA). A detailed examination of anchoring of these moieties to the iron oxide nanoparticle surface is undertaken. The use of a thermoresponsive polymer is proposed, based on di(ethyleneglycol) methyl ether methacrylate (DEGMA) and methyl methacrylate (MMA), which can be prepared by reversible addition-fragmentation chain-transfer (RAFT) polymerisation.^{159,160,161} The purpose of this polymer is to act as a delivery mechanism for the iron oxide nanoparticles, allowing the release of the functionalised nanoparticles with the simple addition of a heating step. To optimise the interactions of the nanocomposite with the PEG already present in the *Mary Rose* wood from previous conservation measures, the inclusion of PEG functionalities on the particles will also be examined.

The synthetic process of each nanocomposite has been monitored with a complete range of characterisation techniques. The purity, crystalline nature and polydispersity of the magnetic nanoparticles have been studied by powder X-ray diffraction (PXRD) and

high resolution transmission electron microscopy (HR TEM). The preparation of linkers, polymers and chelating agents has been monitored by proton nuclear magnetic resonance spectroscopy (^1H NMR) to confirm the identity of the intermediate and final products. The thermoresponsive nature of the polymer was confirmed by dynamic light scattering (DLS) and temperature dependent UV-visible spectroscopy. The functionalisation of the magnetic nanoparticles with the different chelating agents was confirmed with Fourier-transform infrared spectroscopy (FTIR), UV-visible spectroscopy, fluorescence spectroscopy and thermogravimetric analysis (TGA). Finally, the iron chelating abilities of the prepared nanocomposites were tested in aqueous and ethanolic solutions, on artificially aged oak (chemically modified), and on wood samples of the *Mary Rose*. The chelation of iron in solution was evaluated by atomic absorption spectroscopy (AAS) and UV-visible spectroscopy, while the iron chelation in wood was studied by far IR spectroscopy.

The magnetic and thermoresponsive nature of these multifunctional nanocomposites can be a valuable advantage in the application of these treatments onto wooden artefacts. The three independent constituents of these treatments can be substituted by alternative materials, making these tools highly tunable, with adjustable properties for each specific case. Consequently, the design of these multifunctional nanocomposites can be potentially extrapolated for the treatment and conservation of a broad range of archaeological findings.

References

- 1 P. Marsden, *Mary Rose, your noblest shippe: anatomy of a Tudor warship. The archaeology of the Mary Rose*, The Mary Rose Trust Ltd, 2009.
- 2 A. Stirland, *Raising the Dead: The Skeleton Crew of Henry VIII's Great Ship, the Mary Rose*, Wiley, 2000.
- 3 L. S. Bell, J. A. Lee Thorp and A. Elkerton, *J. Archaeol. Sci.*, 2009, **36**, 166-173.
- 4 M. Rule, *The Mary Rose: the excavation and raising of Henry VIII's flagship*, Conway Maritime Press, 1983.
- 5 M. Jones and Mary Rose Trust, *For future generations: conservation of a Tudor maritime collection*, Mary Rose Trust, 2003.
- 6 J. Gardiner, M. J. Allen, M. A. Alburger and Mary Rose Trust., *Before the mast: life and death aboard the Mary Rose*, Mary Rose Trust, 2005.
- 7 C. Pearson, *Conservation of marine archaeological objects*, Butterworths, 1987.
- 8 R. M. Brinston and B. K. Wilson, *Med. Device Technol.*, 1993, **4**, 18-22.
- 9 S. B. Pointing, University of Portsmouth, 1995.
- 10 S. B. Pointing, E. B. Gareth Jones and M. Jones, *Mycoscience*, 1996, **37**, 455-458.
- 11 B. Håfors, *Conservation of the Swedish warship Vasa from 1628*, Stockholm, 2001.
- 12 E. Hocker, G. Almkvist and M. Sahlstedt, *J. Cult. Herit.* **13S**, 2012, 175-182.
- 13 S. Keene, in *Proceedings of the ICOM waterlogged wood working group conference. Ottawa, 15-18 September 1981*, 1982.
- 14 B. B. Christensen, *The conservation of waterlogged wood in the National Museum of Denmark.*, National Museum of Denmark, Copenhagen, 1970.
- 15 C. W. Gregson, in *Problems of the Conservation of Waterlogged Wood*, ed. W. A. Oddy, Greenwich: National Maritime Museum, Maritime Monographs and Reports n.16, London, 1975, pp. 113-114.
- 16 M. Sawada, in *2nd ICOM Waterlogged Wood Working Group conference*, eds. R. Ramiere and M. Colardelle, Grenoble, 1984, pp. 117-124.
- 17 H. Langhals and D. Bathelt, *Angew. Chemie - Int. Ed.*, 2003, **42**, 5676-5681.
- 18 J. de Jong, in *Biodeterioration investigation techniques*, ed. Arthur Harry Walters, Applied Science, 1977, pp. 295-338.
- 19 J. de Jong, in *The conservation of shipwrecks*, Zagreb, 1978, p. 667.
- 20 J. de Jong, W. Eenkhoorn and A. J. M. Wevers, in *Controlled drying as an approach to the conservation of shipwrecks*, Ottawa, 1981, p. 58.
- 21 G. Almkvist and I. Persson, *Holzforschung*, 2008, **62**, 694-703.
- 22 M. Sandström, F. Jalilehvand, I. Persson, U. Gelius, P. Frank and I. Hall-Roth, *Nature*, 2002, **415**, 893-897.

- 23 M. Sandström, F. Jalilehvand, E. Damian, Y. Fors, U. Gelius, M. Jones and M. Salomé, *Proc. Natl. Acad. Sci. U. S. A.*, 2005, **102**, 14165-70.
- 24 K. M. Wetherall, R. M. Moss, A. M. Jones, A. D. Smith, T. Skinner, D. M. Pickup, S. W. Goatham, A. V. Chadwick and R. J. Newport, *J. Archaeol. Sci.*, 2008, **35**, 1317-1328.
- 25 C. O. Moses, D. Kirk Nordstrom, J. S. Herman and A. L. Mills, *Geochim. Cosmochim. Acta*, 1987, **51**, 1561-1571.
- 26 G. Almkvist and I. Persson, *Holzforschung*, 2008, **62**, 704-708.
- 27 R. Giorgi, D. Chelazzi and P. Baglioni, *Langmuir*, 2005, **21**, 10743-10748.
- 28 R. Giorgi, D. Chelazzi and P. Baglioni, *Appl. Phys. A*, 2006, **83**, 567-571.
- 29 D. Chelazzi, R. Giorgi and P. Baglioni, *Macromol. Symp.*, 2006, **238**, 30-36.
- 30 E. J. Schofield, R. Sarangi, A. Mehta, A. M. Jones, F. J. W. Mosselmans and A. V. Chadwick, *Mater. Today*, 2011, **14**, 354-358.
- 31 A. V. Chadwick, E. J. Schofield, A. M. Jones, G. Cibir and J. F. W. Mosselmans, *Solid State Ionics*, 2012, **225**, 742-746.
- 32 A. V. Chadwick, K. Howland, M. J. Went, E. J. Schofield and A. M. Jones, *Macromol. Symp.*, 2014, **337**, 74-79.
- 33 E. J. Schofield, R. Sarangi, A. Mehta, A. M. Jones, A. Smith, J. F. W. Mosselmans and A. V. Chadwick, *J. Cult. Herit.*, 2016, **18**, 306-312.
- 34 E. J. Schofield, C. Delaveris and R. Sarangi, *J. Archaeol. Sci. Reports*, 2015, **4**, 427-433.
- 35 A. Berko, A. D. Smith, A. M. Jones, E. J. Schofield, J. F. W. Mosselmans and A. V. Chadwick, *J. Phys. Conf. Ser.*, 2009, **190**, 012147.
- 36 Z. Walsh, E.-R. Janeček, J. T. Hodgkinson, J. Sedlmair, A. Koutsioubas, D. R. Spring, M. Welch, C. J. Hirschmugl, C. Toprakcioglu, J. R. Nitschke, M. Jones and O. A. Scherman, *Proc. Natl. Acad. Sci. U. S. A.*, 2014, **111**, 17743-8.
- 37 R. Farr, D. S. Choi and S.-W. Lee, *Acta Biomater.*, 2014, **10**, 1741-1750.
- 38 G. De Crozals, R. Bonnet, C. Farre and C. Chaix, *Nano Today*, 2016, **11**, 435-463.
- 39 M. S. Whittingham, *Dalt. Trans.*, 2008, 5424.
- 40 A. Manthiram, A. Vadivel Murugan, A. Sarkar and T. Muraliganth, *Energy Environ. Sci.*, 2008, **1**, 621.
- 41 T. Singh, S. Shukla, P. Kumar, V. Wahla, V. K. Bajpai and I. A. Rather, *Front. Microbiol.*, 2017, **8**, 1501.
- 42 W. Lu and C. M. Lieber, *Nat. Mater.*, 2007, **6**, 841-850.
- 43 D. S. Hecht, L. Hu and G. Irvin, *Adv. Mater.*, 2011, **23**, 1482-1513.
- 44 A. D. Franklin, *Science*, 2015, **349**, 704-714.
- 45 D. P. Broom and K. M. Thomas, *MRS Bull.*, 2013, **38**, 412-421.

- 46 Z. Wang, A. Knebel, S. Grosjean, D. Wagner, S. Bräse, C. Wöll, J. Caro and L. Heinke, *Nat. Commun.*, 2016, **7**, 13872.
- 47 C. Sun, B. Wen and B. Bai, *Sci. Bull.*, 2015, **60**, 1807-1823.
- 48 B. Bhushan, D. Luo, S. R. Schricker, W. Sigmund and S. Zauscher, Eds., *Handbook of Nanomaterials Properties*, Springer Berlin Heidelberg, Berlin, Heidelberg, 2014.
- 49 A. A. Kaufman and R. O. Hansen, in *Methods in Geochemistry and Geophysics*, Elsevier, 2008, vol. 42, pp. 207-254.
- 50 A. J. Dekker, in *Solid State Physics*, Macmillan Education UK, London, 1981, pp. 464-497.
- 51 N. A. Spaldin, *Magnetic materials: fundamentals and applications*, Cambridge University Press, Cambridge (NY), 2011.
- 52 Y. L. Raikher and V. I. Stepanov, *J. Magn. Magn. Mater.*, 2007, **316**, 417-421.
- 53 C. Corot, P. Robert, J.-M. Idée and M. Port, *Adv. Drug Deliv. Rev.*, 2006, **58**, 1471-1504.
- 54 V. Marghussian, in *Nano-Glass Ceramics. Processing, Properties and Applications*, William Andrew Publishing, 2015, pp. 181-223.
- 55 T. D. Clemons, R. H. Kerr and A. Joos, *Compr. Nanosci. Nanotechnol.*, 2019, 193-210.
- 56 R. V. Kumar, Y. Koltypin, Y. S. Cohen, Y. Cohen, D. Aurbach, O. Palchik, I. Felner and A. Gedanken, *J. Mater. Chem.*, 2000, **10**, 1125-1129.
- 57 S. A. Corr, Y. P. Rakovich and Y. K. Gun'ko, *Nanoscale Res. Lett.*, 2008, **3**, 87-104.
- 58 W. Zhang, X. Li, R. Zou, H. Wu, H. Shi, S. Yu and Y. Liu, *Sci. Rep.*, 2015, **5**, 11129.
- 59 S. Nie, E. Starodub, M. Monti, D. A. Siegel, L. Vergara, F. El Gabaly, N. C. Bartelt, J. de la Figuera and K. F. McCarty, *J. Am. Chem. Soc.*, 2013, **135**, 10091-10098.
- 60 R. John, M. Berritta, D. Hinzke, C. Müller, T. Santos, H. Ulrichs, P. Nieves, J. Walowski, R. Mondal, O. Chubykalo-Fesenko, J. McCord, P. M. Oppeneer, U. Nowak and M. Münzenberg, *Sci. Rep.*, 2017, **7**, 4114.
- 61 C. T. Yavuz, J. T. Mayo, W. W. Yu, A. Prakash, J. C. Falkner, S. Yean, L. Cong, H. J. Shipley, A. Kan, M. Tomson, D. Natelson and V. L. Colvin, *Science*, 2006, **314**, 964-7.
- 62 H.-U. Worm, *Geophys. J. Int.*, 1998, **133**, 201-206.
- 63 Q. Li, C. W. Kartikowati, S. Horie, T. Ogi, T. Iwaki and K. Okuyama, *Sci. Rep.*, 2017, **7**, 9894.
- 64 A. Demortière, P. Panissod, B. P. Pichon, G. Pourroy, D. Guillon, B. Donnio and S. B. Egin-Colin, *Nanoscale*, 2011, **3**, 225.
- 65 P. Dutta, S. Pal, M. S. Seehra, N. Shah and G. P. Huffman, *J. Appl. Phys.*, 2009,

- 105, 07B501.
- 66 J. Sung Lee, J. Myung Cha, H. Young Yoon, J.-K. Lee and Y. Keun Kim, *Sci. Rep.*, 2015, **5**, 12135.
- 67 A. Laurie, pat. no: 203042, 1923.
- 68 A. Laurie, pat. no: 1561988, 1925.
- 69 G. King, A. Warnes, pat. no: 513366, 1939.
- 70 G. Wheeler, *Alkoxysilanes and the consolidation of stone*, Getty Publications, Los Angeles, 2005.
- 71 P. G. De Gennes and C. Taupin, *J. Phys. Chem.*, 1982, **86**, 2294-2304.
- 72 P. Mora, L. Mora and P. Philippot, *Conservation of wall paintings*, Butterworths, London, Boston, 1984.
- 73 C. V. Horie, *Materials for conservation: organic consolidants, adhesives, and coatings*, Butterworths, 1987.
- 74 R. Giorgi, M. Ambrosi, N. Toccafondi and P. Baglioni, *Chem. - A Eur. J.*, 2010, **16**, 9374-9382.
- 75 P. Munafò, E. Quagliarini, G. B. Goffredo, F. Bondioli and A. Licciulli, *Constr. Build. Mater.*, 2014, **65**, 218-231.
- 76 B. Mahltig, C. Swaboda, A. Roessler and H. Böttcher, *J. Mater. Chem.*, 2008, **18**, 3180-3192.
- 77 R. Giorgi, L. Dei, M. Ceccato, C. Schettino, P. Baglioni and S. Stefano, *Langmuir*, 2002, **18**, 8198-8203.
- 78 H. A. Carter, *J. Chem. Educ.*, 1996, **73**, 417.
- 79 M. Bonini, S. Lenz, E. Falletta, F. Ridi, E. Carretti, E. Fratini, A. Wiedenmann and P. Baglioni, *Langmuir*, 2008, **24**, 12644-12650.
- 80 T. Ahn, J. H. Kim, H.-M. Yang, J. W. Lee and J.-D. Kim, *J. Phys. Chem. C*, 2012, **116**, 6069-6076.
- 81 A.-H. Lu, E. L. Salabas and F. Schüth, *Angew. Chemie Int. Ed.*, 2007, **46**, 1222-1244.
- 82 V. K. La Mer, *Ind. Eng. Chem.*, 1952, **44**, 1270-1277.
- 83 J. Polte, *CrystEngComm*, 2015, **17**, 6809-6830.
- 84 T. Tadros, in *Encyclopedia of Colloid and Interface Science*, Springer Berlin Heidelberg, Berlin, Heidelberg, 2013, pp. 820-820.
- 85 R. Massart, *IEEE Trans. Magn.*, 1981, **17**, 1247-1248.
- 86 R. Massart, E. Dubois, V. Cabuil and E. Hasmonay, *J. Magn. Magn. Mater.*, 1995, **149**, 1-5.
- 87 M. J. Williams, E. Sánchez-Pérez, E. R. Aluri, F. J. Douglas, D. A. Maclaren, O. M. Collins, E. J. Cussen, J. D. Budge, L. C. Sanders, M. Michaelis, C. M. Smales, J.

- Cinatl, S. Lorrio, D. Krueger, R. T. M. De Rosales and S. A. Corr, *RSC Adv.*, 2016, **6**, 83520-83528.
- 88 D. N. F. Muche, F. L. Souza and R. H. R. Castro, *React. Chem. Eng.*, 2018, **3**, 244.
- 89 J. Lee, S. Zhang and S. Sun, *Chem. Mater.*, 2013, **25**, 1293-1304.
- 90 L. Wu, A. Mendoza-Garcia, Q. Li and S. Sun, *Chem. Rev.*, 2016, **116**, 10473-10512.
- 91 T. J. Daou, G. Pourroy, S. Bégin-Colin, J. M. Grenèche, C. Ulhaq-Bouillet, P. Legaré, P. Bernhardt, C. Leuvrey and G. Rogez, *Chem. Mater.*, 2006, **18**, 4399-4404.
- 92 S. R. Dhage, Y. B. Kholam, H. S. Potdar, S. B. Deshpande, P. P. Bakare, S. R. Sainkar and S. K. Date, *Mater. Lett.*, 2002, **57**, 457-462.
- 93 M. Ethayaraja, K. Dutta, D. Muthukumaran and R. Bandyopadhyaya, *Langmuir*, 2007, **23**, 3418-3423.
- 94 G. Granata, F. Pagnanelli, D. Nishio-Hamane and T. Sasaki, *Appl. Surf. Sci.*, 2015, **331**, 463-471.
- 95 M. P. Pileni, *J. Phys. Chem.*, 1993, **97**, 6961-6973.
- 96 M. P. Pileni, *Langmuir*, 1997, **13**, 3266-3276.
- 97 A. Chiolerio, A. Chiodoni, P. Allia and P. Martino, in *Handbook of Nanomaterials Properties*, Springer Berlin Heidelberg, Berlin, Heidelberg, 2014, pp. 213-246.
- 98 G. B. Biddlecombe, Y. K. Gun'ko, J. M. Kelly, S. C. Pillai, J. Michael, D. Coey, M. Venkatesan and A. P. Douvalis, *J. Mater. Chem.*, 2001, **11**, 2937-2939.
- 99 O. M. Lemine, K. Omri, B. Zhang, L. El Mir, M. Sajieddine, A. Alyamani and M. Bououdina, *Superlattices Microstruct.*, 2012, **52**, 793-799.
- 100 G. B. Dudley, R. Richert and A. E. Stiegman, *Chem. Sci.*, 2015, **6**, 2144-2152.
- 101 C. O. Kappe, *Angew. Chemie Int. Ed.*, 2004, **43**, 6250-6284.
- 102 H. Qian, X. Qiu, L. Li and J. Ren, *J. Phys. Chem. B*, 2006, **110**, 9034-9040.
- 103 G. Yang, G. Wang and W. How, *J. Phys. Chem. B*, 2005, **109**, 11186-11196.
- 104 T. E. Ashton, J. V. Laveda, D. A. MacLaren, P. J. Baker, A. Porch, M. O. Jones and S. A. Corr, *J. Mater. Chem. A*, 2014, **2**, 6238-6245.
- 105 M. Amores, T. E. Ashton, P. J. Baker, E. J. Cussen and S. A. Corr, *J. Mater. Chem. A*, 2016, **4**, 1729-1736.
- 106 J. A. Gerbec, D. Magana, A. Washington and G. F. Strouse, *J. Am. Chem. Soc.*, 2005, **127**, 15791-15800.
- 107 V. Ervithayasuporn and Y. Kawakami, *J. Colloid Interface Sci.*, 2009, **332**, 389-393.
- 108 S. García-Jimeno and J. Estelrich, *Colloids Surfaces A Physicochem. Eng. Asp.*, 2013, **420**, 74-81.

- 109 C. Yang, J. Du, Q. Peng, R. Qiao, W. Chen, C. Xu, Z. Shuai and M. Gao, *J. Phys. Chem. B*, 2009, **113**, 5052-5058.
- 110 A. Mukhopadhyay, N. Joshi, K. Chattopadhyay and G. De, *ACS Appl. Mater. Interfaces*, 2012, **4**, 142-149.
- 111 R. Y. Hong, B. Feng, L. L. Chen, G. H. Liu, H. Z. Li, Y. Zheng and D. G. Wei, *Biochem. Eng. J.*, 2008, **42**, 290-300.
- 112 Y.-C. Chang and D.-H. Chen, *J. Colloid Interface Sci.*, 2005, **283**, 446-451.
- 113 H. L. Ding, Y. X. Zhang, S. Wang, J. M. Xu, S. C. Xu and G. H. Li, *Chem. Mater.*, 2012, **24**, 4572-4580.
- 114 P. M. Paulus, H. Bönemann, A. M. van der Kraan, F. Luis, J. Sinzig and L. J. de Jongh, *Eur. Phys. J. D*, 1999, **9**, 501-504.
- 115 S. Moraes Silva, R. Tavallaie, L. Sandiford, R. D. Tilley and J. J. Gooding, *Chem. Commun.*, 2016, **52**, 7528-7540.
- 116 I. J. Bruce and T. Sen, *Langmuir*, 2005, **21**, 7029-7035.
- 117 S. Mumtaz, L.-S. Wang, S. Z. Hussain, M. Abdullah, Z. Huma, Z. Iqbal, B. Creran, V. M. Rotello and I. Hussain, *Chem. Commun.*, 2017, **53**, 12306-12308.
- 118 S. P. Schwaminger, P. F. García, G. K. Merck, F. A. Bodensteiner, S. Heissler, S. Günther and S. Berensmeier, *J. Phys. Chem. C*, 2015, **119**, 23032-23041.
- 119 R. A. Bini, R. F. C. Marques, F. J. Santos, J. A. Chaker and M. Jafelicci, *J. Magn. Magn. Mater.*, 2012, **324**, 534-539.
- 120 D. K. Kim, M. Mikhaylova, Y. Zhang and M. Mamoun, *Chem. Mater.*, 2003, **15**, 1617-1627.
- 121 R. De Palma, S. Peeters, M. J. Van Bael, H. Van den Rul, K. Bonroy, W. Laureyn, J. Mullens, G. Borghs and M. Guido, *Chem. Mater.*, 2007, **19**, 1821-1831.
- 122 Q. Zhang, R. Su, J.-P. Wang and Q. Zhang, *J. Nanosci. Nanotechnol.*, 2016, **16**, 7427-7432.
- 123 L. G. Lis, M. A. Smart, A. Luchniak, M. L. Gupta, and V. J. Gurchich, *ACS Med. Chem. Lett.*, 2012, **3**, 745-748.
- 124 G. V Dubacheva, C. Araya-Callis, A. Geert Volbeda, M. Fairhead, J. Codeé, M. Howarth and R. P. Richter, *J. Am. Chem. Soc.*, 2017, **139**, 4157-4167.
- 125 K. Modjarrad and S. Ebnesajjad, *Handbook of polymer applications in medicine and medical devices*, William Andrew, 2014.
- 126 M. E. Abdelhamid, A. P. O'Mullane and G. A. Snook, *RSC Adv.*, 2015, **5**, 11611-11626.
- 127 H. Peng, X. Sun, W. Weng and X. Fang, in *Polymer Materials for Energy and Electronic Applications*, Academic Press, 2017, pp. 151-196.
- 128 R. J. Ouellette and J. D. Rawn, in *Organic Chemistry Study Guide*, Elsevier, 2015, pp. 587-601.

- 129 G. Moad, E. Rizzardo and S. H. Thang, *Aust. J. Chem.*, 2005, **58**, 379.
- 130 G. Moad, E. Rizzardo and S. H. Thang, *Polymer (Guildf)*., 2008, **49**, 1079-1131.
- 131 S. Perrier and P. Takolpuckdee, *J. Polym. Sci. Part A Polym. Chem.*, 2005, **43**, 5347-5393.
- 132 Y. Zhu, R. Batchelor, A. B. Lowe and P. J. Roth, *Macromolecules*, 2016, **49**, 672-680.
- 133 A. K. Kulshreshtha and C. Vasile, *Handbook of polymer blends and composites*, Rapra Technology, Shrewsbury, UK, 2002.
- 134 R. Duncan, H. Ringsdorf and R. Satchi-Fainaro, in *Polymer Therapeutics I*, Springer-Verlag, Berlin/Heidelberg, 2005, pp. 1-8.
- 135 K. Shimizu, H. Fujita and E. Nagamori, *Biotechnol. Bioeng.*, 2010, **106**, n/a-n/a.
- 136 M. A. Ward and T. K. Georgiou, *Polymers (Basel)*., 2011, **3**, 1215-1242.
- 137 J. M. Berg, J. L. Tymoczko and L. Stryer, in *Biochemistry*, W.H. Freeman, New York, 5th edn., 2002.
- 138 H. Lodish, A. Berk, S. L. Zipursky, P. Matsudaira, D. Baltimore and J. Darnell, in *Molecular Cell Biology*, ed. W. H. Freeman, John Wiley & Sons, Inc., New York, 4th edn., 2000.
- 139 P. Krishnamurthy, T. Xie and J. D. Schuetz, *Pharmacol. Ther.*, 2007, **114**, 345-358.
- 140 P. Ponka, *Am. J. Med. Sci.*, 1999, **318**, 241-256.
- 141 A. Mahmood, J.-Y. Hu, B. Xiao, A. Tang, X. Wang and E. Zhou, *J. Mater. Chem. A*, 2018, **6**, 16769-16797.
- 142 S. B. Brown, E. A. Brown and I. Walker, *Lancet Oncol.*, 2004, **5**, 497-508.
- 143 D. H. Yoon, S. B. Lee, K.-H. Yoo, J. Kim, J. K. Lim, N. Aratani, A. Tsuda, A. Osuka and D. Kim*, *J. Am. Chem. Soc.*, 2003, **125**, 11062-11064.
- 144 Y. Ding, Y. Tang, W. Zhu and Y. Xie, *Chem. Soc. Rev*, 2015, **44**, 1101-1112.
- 145 I. Stojiljkovic, B. D. Evavold and V. Kumar, *Expert Opin. Investig. Drugs*, 2001, **10**, 309-320.
- 146 C. C. Fernández, C. Spedalieri, D. H. Murgida and F. J. Williams, *J. Phys. Chem. C*, 2017, **121**, 21324-21332.
- 147 N. Karousis, A. S. D. Sandanayaka, T. Hasobe, S. P. Economopoulos, E. Sarantopoulou and N. Tagmatarchis, *J. Mater. Chem.*, 2011, **21**, 109-117.
- 148 M. Nowostawska, S. A. Corr, S. J. Byrne, J. Conroy, Y. Volkov and Y. K. Gun'ko, *J. Nanobiotechnology*, 2011, **9**, 13.
- 149 S. K. Mandal, N. Lequeux, B. Rotenberg, M. Tramier, J. Fattaccioli, J. Bibette and B. Dubertret, *Langmuir*, 2005, **21**, 4175-4179.
- 150 C. A. Hunter and J. K. M. Sanders, *J. Am. Chem. Soc.*, 1990, **112**, 5525-5534.

- 151 U. Siggel, U. Bindig, C. Endisch, T. Komatsu, E. Tsuchida, J. Voigt and J.-H. Fuhrhop, *Berichte der Bunsengesellschaft für Phys. Chemie*, 1996, **100**, 2070-2075.
- 152 E. Repo, J. K. Warchoł, A. Bhatnagar, A. Mudhoo and M. Sillanpää, *Water Res.*, 2013, **47**, 4812-4832.
- 153 A. R. Whisnant and S. D. Gilman, *Anal. Biochem.*, 2002, **307**, 226-234.
- 154 E. E. van der van der Wall, P. R. van van Dijkman, A. de Roos, J. Doornbos, A. van der Laarse, V. M. Cats, A. E. van Voorthuisen, N. A. Matheijssen and A. V Brusckke, *Br. Heart J.*, 1990, **63**, 12.
- 155 Y. Arano, T. Uezono, H. Akizawa, M. Ono, K. Wakisaka, M. Nakayama, H. Sakahara, J. Konishi and A. Yokoyama, *J. Medicinal Chem.*, 1996, **39**, 3451-3460.
- 156 S. Fukuda, *Curr. Med. Chem.*, 2005, **12**, 2765-70.
- 157 C. Pelé, E. Guilminot, S. Labroche, G. Lemoine and G. Baron, *Stud. Conserv.*, 2015, **60**, 155-171.
- 158 L. Selwyn, C. Cook, W. R. Mckinnon, R. Fairman and S. Labroche, *Iron Stain Removal from Archaeological Composite Artifacts made of Wood and Iron*, Ottawa, 2013, vol. 38.
- 159 N. S. leong, K. Brebis, L. E. Daniel, R. K. O'Reilly and M. I. Gibson, *Chem. Commun.*, 2011, **47**, 11627.
- 160 N. S. leong, M. Hasan, D. J. Phillips, Y. Saaka, R. K. O'Reilly and M. I. Gibson, *Polym. Chem.*, 2012, **3**, 794.
- 161 M. I. Gibson, D. Paripovic and H.-A. Klok, *Adv. Mater.*, 2010, **22**, 4721-4725.

Chapter 2 - Materials and methods

2.1 Materials

The following chemicals and solvents were purchased and used without further purification: $\text{FeCl}_3 \cdot 6\text{H}_2\text{O}$, $\text{FeCl}_2 \cdot 4\text{H}_2\text{O}$, $\text{FeSO}_4 \cdot 7\text{H}_2\text{O}$, $\text{Fe}_2(\text{SO}_4)_3 \cdot 7\text{H}_2\text{O}$, (3-aminopropyl)triethoxysilane (APTES, 99 %), vinyltriethoxysilane (VTES, 97 %), polyethylene glycol 200, Protoporphyrin IX (PPIX, ≥ 95 %), sodium hydroxide (NaOH, ≥ 98 %), tetrahydrofuran (THF, ≥ 99.9 %), methanol (99.8 %), dimethylformamide (DMF, 99.8 %), diethyl ether (≥ 99.0 %), triethylamine (TEA, ≥ 99.5 %), octylamine (99 %), azobis(isobutyronitrile) (AIBN, 98 %), 4-cyano-4-(phenylcarbonothioylthio) pentanoic acid, calcium oxide (CaO, ≥ 99.99 %), tris(2-carboxyethyl)phosphine hydrochloride (TCEP, ≥ 98 %), 1,4-dioxane (99.8 %), succinic anhydride (≥ 99.0 %), diethylenetriamine pentaacetic acid dianhydride (DTPA-da, 98 %), deuterated dimethylsulfoxide (DMSO-d_6 , 99.9 atom % D), deuterated chloroform (CDCl_3 , 99.8 % atom D), 1-ethyl-3-(3-dimethylaminopropyl) carbodiimide (EDC, ≥ 98.0 %), N-Hydroxysuccinimide (NHS, 98 %) and 4-dimethylaminopyridine (DMAP, 99 %) were purchased from Sigma Aldrich. Ethanol (>99.8 %) and acetone (>99.5 %) were obtained from VWR Chemicals. Dimethylsulfoxide (DMSO , ≥ 99.7 %) was purchased from Acros Organics. Molecular sieves (3 Å), ammonium hydroxide (28-30 %), hydrochloric acid (HCl, 37 %) and dichloromethane (DCM, ≥ 99 %) were obtained from Alfa Aesar. 5,10,15,20-tetrakis(4-aminophenyl) porphyrin (porphyrin-amine, >95 %) was provided by Tokio Chemical Industry Co., Ltd (TCI). Argon (99.998 %) was provided by BOC. The magnets used for decantation of magnetic nanoparticles and wood treatment were Neodymium N42 grade, with an associated magnetic field of 1.3 Tesla, and were purchased from www.first4magnets.com.¹

Dry ethanol was prepared immediately before being used. Ethanol (>99.8 %) was distilled and collected in a sealed flask with activated 3 Å molecular sieves (ca. 20 % w/w of solvent). Before its use, dry ethanol was filtered with filter paper to remove any dust from molecular sieves. Molecular sieves were previously activated in a vacuum oven at 80 °C overnight. The monomers di(ethylene glycol) methyl ether methacrylate (DEGMA, 95 %) and methyl methacrylate (MMA, 99 %) were purchased from Sigma Aldrich and were eluted through an aluminium oxide column before use in order to remove the inhibitor. SnakeSkin Dialysis Tubing (regenerated cellulose, 3.5 K MWCO), purchased from Thermo Fisher Scientific, was washed and pre-hydrated for 3-4 hours in distilled water. Nylon membrane filters (0.2 μm pore size) were purchased from Whatman. Azobis(isobutyronitrile) (AIBN, 98 %) was recrystallised from ethanol. Deoxygenated water was obtained by boiling distilled water, while bubbling argon, for 3-4 hours.

All procedures performed under inert atmosphere have been carried out using a Schlenck line with argon as the inert gas, fitted with a high vacuum rotary-vane pump.

2.2 Characterisation and synthetic methods

The preparation of the materials presented in this thesis involved a range of synthetic techniques, from microwave-assisted synthesis and co-precipitation of metal oxide nanoparticles, to surface functionalisation and RAFT polymerisation. Also, a varied range of characterisation techniques was used to evaluate these materials. These techniques aimed to study the structure and properties of each of the constituents of the nanocomposites prepared, as well as to understand the properties of the nanocomposites as a whole.

2.2.1 Powder X-ray diffraction (PXRD)

X-ray diffraction (XRD) is a non-destructive technique which allows the identification of the phase and the elucidation of the cell parameters of a crystalline material. It is extensively used in a diverse range of fields such as geology, materials, forensic, and biomedical sciences. In powder X-ray diffraction (PXRD), samples are finely ground to ensure a random orientation of the crystal domains, and data is obtained from the average bulk composition. Contrary to this, in single crystal XRD the data are collected from only one crystal. Single-crystal XRD provides more detailed information including bond lengths, bond angles, and information about site ordering. However, some limitations like the need of a crystal size under 100 atoms in the asymmetric unit or the time consuming single-crystal culture makes PXRD a more versatile and therefore widely used technique.²

X-rays are a type of electromagnetic radiation with a wavelength between 10^{-7} and 10^{-11} m, and energy in the order of 10 keV. In X-ray diffractometers, polychromatic X-rays are generally generated within a tube under vacuum by the application of a current between 15-60 kV. Electrons generated in the cathode, normally a tungsten filament, collide with the anode at the other end of the tube, generally made of Cu, Fe, Co, Cr, or Mo, thus emitting X-rays. Copper is commonly used as the material for the anode in X-ray diffraction due to its high thermal conductivity, which facilitates the refrigeration of the anode. Copper also emits two different strong radiations, K_{α} and K_{β} , due to different decay processes from 2p and 3p orbitals to 1s orbitals. K_{β} is often filtered, letting K_{α} be the wavelength used at 1.5406 Å, which is a similar value to the distance between atoms in a unit cell. Samples containing iron show intense fluorescence when using copper anodes, since the energy of Cu K_{α} is larger than the Fe K-edge. This causes an intense

background signal and poor peak resolution. To resolve this issue, Fe, Co, or Cr radiation sources can be used in combination with a secondary monochromator in the diffracted beam.

X-rays generated in the source are filtered and collimated yielding a monochromatic beam, which is finely focused on the sample. X-ray diffraction (coherent and elastic scattering of a wave) occurs when a beam of a wavelength similar to the value of atomic distances interacts with periodically aligned atoms of a crystalline substance. The incident radiation reaches the sample at varying angles (θ) but it is diffracted only at specific incident angles. At these specific angles, the diffracted radiation undergoes constructive interference and is amplified and collected by the detector. This results in a characteristic line in the diffraction pattern that can be further assigned to a certain lattice plane. A schematic description of the diffraction phenomenon is shown in **Figure 2.1**.

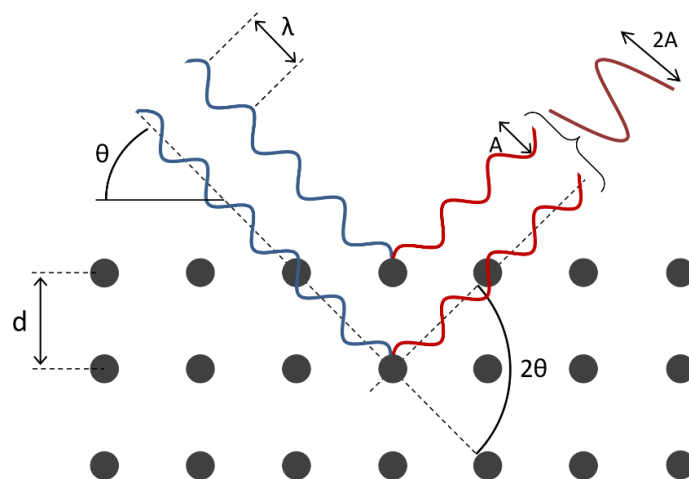


Figure 2.1. Schematic representation of two waves being diffracted in phase, satisfying Bragg's law. The angle of diffraction is twice the angle of incidence (θ) whilst the wavelength remains constant.

This phenomenon is described by Bragg's law (**Equation 2.1**), which correlates the distance between atoms within the crystal (d) and the incidence angle (θ) with the radiation wavelength (λ):

$$n \cdot \lambda = 2d \cdot \sin \theta \quad (2.1)$$

Thus, the aforementioned constructive interference occurs at angles where the path difference between waves, $2d \cdot \sin(\theta)$, is equal to the λ or an integer multiple of it. A diffraction pattern represents the intensity of the signal produced from diffracted X-rays with respect to the angle of diffraction (2θ). When Bragg's law is satisfied (i.e. the waves are diffracted in phase, leading to constructive interference), peaks can be observed at certain angles (θ or 2θ).^{3,4} Each of these peaks correspond to a family of planes which can be identified typically by comparing the diffractogram obtained with reference diffraction patterns.

Diffraction patterns may also allow for the estimation of the size of the crystalline domain using the Scherrer equation (**Equation 2.2**). This expression relates the average crystallite size to the broadening of a peak in the diffractogram, generally to the highest intensity peak. Here, τ is the average crystallite size; K is a dimensionless shape factor with a value between 0.7-1.7. For simplicity the value of 0.9, corresponding to that of a sphere, is generally taken; λ is the radiation wavelength; β is the full width at half maximum (FWHM) in radians; θ is the Bragg angle.⁵

$$\tau = \frac{K \cdot \lambda}{\beta \cdot \cos \theta} \quad (2.2)$$

In this thesis all samples were characterised using a PANalytical X' Pert powder diffractometer using Cu K_{α} radiation operated at 40 keV and 40 mA in the 2θ range of 10° to 80° , in step sizes of 0.017° (2θ), and with an integration time of 90 seconds per step. Samples were mounted in the bracket stage on a glass slide.

2.2.2 Scanning Electron Microscopy (SEM)

Scanning electron microscopy (SEM) is a widely used imaging technique in which a beam of accelerated electrons is projected onto the sample. Because the associated wavelength of electrons is 10^4 - 10^5 times shorter than that of photons used in optical microscopy, electron microscopes have higher resolution power, down to tens of nanometres depending on the mode (back-scattered electrons, secondary electrons, x-ray emission). The signal obtained with scanning electron microscopy contains information not only about the topography of the sample, but also its composition.⁶

Typically, the electron beam is emitted by an electron gun fitted with a tungsten filament cathode and its energy ranges between 1 and 40 keV. The energy used depends

on the nature of the sample; sensitive biological samples or non-conductive samples are normally characterised at low voltages to avoid damage, while inorganic samples can be studied at higher energies, and better resolution can be obtained due to the use of shorter wavelengths. Samples that are poorly conducting or non-conducting must be sputter-coated with a fine layer of metal, typically gold, platinum, or a thin layer of carbon. Several condenser lenses and an objective lens focus the beam to a spot of 0.4-5 nm, which is moved over the sample to scan it. The system is enclosed in a high vacuum chamber to avoid the electron beam being scattered by atmospheric gases. When the beam hits the sample, several interactions between the electrons and the atoms of the sample can be observed. Back-scattered electrons are elastically reflected from the sample. Heavier atoms scatter electrons more strongly producing brighter images, whilst lighter atoms scatter less strongly creating darker areas. This phenomenon can be used to differentiate regions on the sample with different chemical composition. Some electrons do not interact elastically with the sample and lose energy in the process. Due to this transmission of energy, low energy secondary electrons are ejected from the atoms in the sample and can be collected by a detector with the help of a bias voltage that attracts them. Another larger bias is used to accelerate these electrons towards the detector. Secondary electrons are responsible for the 3D-like images obtained by SEM. The samples studied in this work were deposited on aluminium stubs fitted with carbon tape and were characterised using two different electron microscopes: FEI Quanta 200 SEM and Zeiss Sigma variable pressure SEM. The operating voltage used was between 10 and 20 kV and the samples were studied in back-scattered mode.

2.2.3 Energy-dispersive X-ray spectroscopy (EDS)

Also known as EDX, energy-dispersive X-ray spectroscopy (EDS) can be used as an elemental analysis technique. It relies on the interaction of a beam of electrons with the atoms in the sample. Electrons from an inner shell of the atoms in the sample may be excited and ejected leaving an “electron hole”. This hole can be subsequently occupied by another electron from an outer, more energetic shell, emitting an X-ray in the process. The energy associated with the emitted radiation is equivalent to the difference in energy between the mentioned outer and inner shells, and is characteristic of the emitting element. This allows for the determination of the elemental composition of the sample. EDS is commonly fitted in scanning electron microscopes, in which case the electron beam is the source of excitation for the electrons in the sample. When coupled with SEM, EDS is very useful for the detailed topographic study of samples.^{6,7} EDS studies in this thesis

were carried out with an Oxford Instruments Microanalysis coupled to a Zeiss Sigma variable pressure SEM.

2.2.4 Transmission Electron Microscopy (TEM)

As with SEM, the magnification capability of TEM gives a resolution power in the nanometre range. The set-up resembles that of SEM with an electron gun emitting an electron beam which is focused into a thin and coherent beam before reaching the sample. Contrary to SEM, the detector is placed behind the sample in order to detect the electrons transmitted through the sample. The transmitted radiation is focused by several magnetic objective lenses onto a fluorescent screen, generating a visible image. Darker areas correspond to regions where fewer electrons are transmitted, and brighter areas indicate a higher transmission of electrons. Samples must be thin layers or particles in the nanometre range, thin enough to transmit enough electrons to form an adequate image. This technique allows analysts to observe features such as crystal structures, dislocations, and grain boundaries in the sample.⁸ It also allows differentiation of distinct components of a composite material, such as inorganic particles embedded in organic matrices.

The spacing between atoms is about two orders of magnitude larger than the associated wavelength of the electrons. This can cause the scattering of some electrons when the beam is focused on a single crystal and yields diffraction patterns consisting of a series of spots, which satisfy the conditions of the crystal structure. Selected area electron diffraction (SAED) is a technique frequently used in TEM which generates patterns corresponding to the reciprocal lattice, allowing for identification of crystal structures in the sample. Patterns obtained from single crystals are sharp diffraction spots, whereas polycrystalline samples give ring patterns.⁶ The samples studied in this work were characterised using a Tecnai T20 transmission electron microscope and the micrographs obtained were analysed with ImageJ.

2.2.5 UV-visible spectroscopy

UV-visible spectroscopy, also called absorption spectroscopy, is routinely used in analytical and organic chemistry for qualitative and quantitative determination of transition metals, highly conjugated organic molecules, and biological macromolecules. Although samples in solid gaseous phases can be studied, analytes are more often studied in solution. In UV-visible spectroscopy, samples are radiated with monochromatic light with wavelengths in the ultraviolet and visible spectral region, generally 100 to 800 nm.

The light can be absorbed by transition metal ions or other species present in the sample, particularly aromatic compounds and α,β -unsaturated carboxylic acids. The absorption of this radiation results in the excitation and subsequent transitions of non-bonding electrons and π -electrons to anti-bonding molecular orbitals levels, higher in energy.⁹ As an example, porphyrins have a highly conjugated π -electron system and have a very characteristic UV-visible fingerprint featuring two distinct regions. Their absorption spectrum was explained by Gouterman in the 1960s with his ‘four-orbital’ model, which has since been accepted.^{10,11} According to this model, the absorption bands in porphyrin derivatives spectra arise from transitions between two HOMO orbitals (a_{1u} and a_{2u}) and two LUMO orbitals (two degenerate e_g). The transitions between these orbitals give rise to two excited states, creating two types of signal. An intense band between 380-500 nm results from the transition from the ground state to the second excited level ($S_0 \rightarrow S_2$) and it is called the Soret band or B band. Four smaller bands caused by the weaker transition to the first excited level ($S_0 \rightarrow S_1$) can be found in the range 500-750 nm and are called the Q bands. These spectroscopic features are due to the conjugation of the 18 π -electrons and allow for easy characterisation of porphyrin derivatives by means of UV-visible spectroscopy.^{12,13} **Figure 2.2** shows (a) a generic absorbance spectrum of a porphyrin derivative displaying the characteristic Soret band and the Q bands. (b) Representation of the four orbital model by Gouterman, used to explain the spectrum of porphyrins.

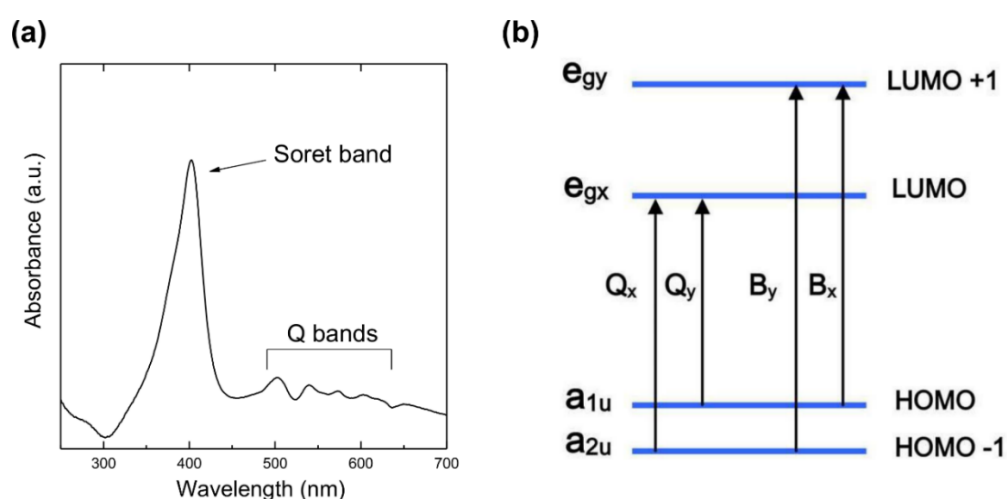


Figure 2.2. (a) UV-visible spectrum of a porphyrin derivative featuring the Soret band (B band) and Q bands. (b) Schematic representation of the energy levels of the four orbitals described by Gouterman. The degenerate e_g orbitals are responsible for the Soret band and Q bands.¹³

Absorption spectra are recorded by comparing the intensity of the incident beam (I_0) to the intensity of the remaining radiation after interacting with the sample (I), obtaining a value for the transmittance (T), as shown in **Equation 2.3**:

$$T = (I_0/I) \quad (2.3)$$

The absorbance (A) is more frequently used over the transmittance (T) due to its linear relation with the concentration of the sample, as described by the Beer-Lambert law (**Equation 2.4**):

$$\log_{10}(1/T) = A = \varepsilon \cdot c \cdot l \quad (2.4)$$

The Beer-Lambert law is the linear relationship between the properties of a substance and the attenuation of light passing through it. For a substance in solution, such attenuation depends on three parameters: the concentration of the substance (c), its absorptivity (ε), and the light path (l), which is given by the width of the cuvette containing the sample. The absorptivity, or molar extinction coefficient, is an intrinsic property of a substance and indicates how strongly it attenuates light at a given wavelength. As ε and l are generally constant throughout measurements of the same substance, the Beer-Lambert law shows how the absorbance is directly proportional to the concentration.¹⁴

UV-visible spectrometers generally have three basic experimental modes: a scanning mode, where absorbance is recorded over a predetermined range of excitation wavelengths; a photometric mode, used for quantitative analyses, where absorbance is registered at single wavelengths; and a kinetics mode, where absorbance is measured at a particular wavelength over time. These modes can be combined, therefore increasing the versatility of UV-visible spectrometry as a characterisation technique. In this research work, samples were analysed in a quartz cuvette with a light path of 1 cm and the instruments used were a Perkin Elmer Lambda 40 UV Vis spectrometer and a Shimadzu UV-2101 PC UV-Vis scanning spectrophotometer.

2.2.6 Fluorescence spectroscopy

Fluorescence spectroscopy (or fluorometry) is a technique that measures the light emitted by decaying electrons which have been previously excited by incoming radiation. It is a well-established technique for fingerprinting organic compounds and it is often used as a complement to UV-visible spectroscopic measurements. In fluorometry, the

molecules of the sample are excited to one of the vibrational states in the excited electronic state by incident radiation at a fixed wavelength. The promoted electrons then undergo a non-radiative vibrational relaxation to a lower energy vibrational state in the same excited level due to collisions with other molecules, followed by a radiative relaxation process to one of the vibrational levels in the ground electronic state. The relaxation of the electrons during this second stage results in an emission of light (fluorescence) generally in the visible region. The occurrence of a non-radiative loss of energy prior to the fluorescence causes the emitted light to be of lower energy than the absorbed radiation. This results in a shift between the absorption band and the emission band of a species, being the emission band at longer wavelengths. This difference is called Stokes shift.^{14,15}

Fluorescence spectroscopy is extensively used for qualitative and quantitative studies of porphyrins. Porphyrins, however, often suffer from self-quenching of fluorescence at high concentrations, or when anchored to certain substrates.^{16,17} Self-quenching can occur when two fluorescent molecules in close proximity aggregate and form ground state complexes or may quench through energy transfer. To avoid this phenomenon, these fluorophores can be substituted with bulky moieties, with linker chains, or can be loaded onto nanostructures in order to create space between them.^{18,19,20}

While in absorption spectroscopy the detector is placed at an angle of 180° from the incident beam to detect the difference in intensity between the incident and the transmitted beam. In emission spectroscopy the detector is placed at 90° to avoid interference from the excitation radiation. Fluorescence spectra show the emission intensity of the sample, collected at a certain wavelength, with respect to the wavelength of the emitted light. All measurements presented in this work were performed using a quartz cell with a light path of 1 cm and a Shimadzu RF-5301PC Spectrofluorophotometer.

2.2.7 Dynamic Light Scattering (DLS)

Also known as photon correlation spectroscopy (PCS), dynamic light scattering (DLS) is a very commonly used tool for the study of the diffusion of macromolecules in solution and particles in suspension, as well as their size and size distribution. When a beam of light is passed through a suspension of particles or a solution of macromolecules, it is scattered in all directions as a function of the size and shape of the scattering entities. The scattered light can interfere either constructively or destructively generating a scattering pattern with light and dark regions. Scattering patterns are recorded in short time intervals and projected on screen, where these light and dark regions can be studied.

The diffusion coefficient of the particles can be obtained from the study of the variations in the intensity of scattering spots over time, which are due to Brownian motion of the particles. Such motion is very dependent on the size of particles, temperature and viscosity of the solvent. Therefore, an accurate control of temperature in DLS is key in the acquisition of data. In the study of particles in the sub-micron range, DLS can complement the information obtained by TEM. While TEM yields values for core particles in dry samples, DLS measures allows for the determination of the hydrodynamic radius of particles in solution. Thus, the thickness of polymeric coatings on particles can be estimated by combining these two techniques. Normally, the sample contained in a glass or quartz cuvette is irradiated with a coherent and monochromatic beam of light (a laser) previously filtered by a polariser. After the light is scattered, it goes through a second polariser and is collected by a photomultiplier. The scattering pattern obtained, a speckle pattern, is then projected onto a screen. There are several modes of detection of the scattered light, depending on the type of sample, possible impurities, or the information required. DLS detectors are commonly placed at 90° , or at 158° and 173° in case of backscattered detection systems. High detection angles are often used for neglecting the contributions of rotational diffusion effects and for avoiding the multiple scattering phenomenon in highly concentrated samples. DLS measurements can also be taken as a function of incident angle. This allows for the study of particles and macromolecules without making any assumptions about their mass or shape during calculations.²¹ In this thesis, DLS measurements were conducted by Dr Ester Rani Aluri with a Zetasizer Malvern Instruments with an incident light of 633 nm (4 mW). The fluctuating scattering intensities were recorded using an avalanche photodiode detector at 90° to the incident light.

2.2.8 Fourier-transform infrared spectroscopy (FTIR)

Fourier transform infrared (FTIR) spectroscopy is based on the absorption of infrared radiation by samples in solid, liquid, or gaseous state. This technique relies on the fact that molecules absorb radiation of a certain frequency (resonant frequencies of covalent bonds) resulting in characteristic bands in the absorption spectrum for a specific molecular bond. These resonant frequencies are closely related to the strength of the bonds and the nature of the atoms at each end. The absorption of energy causes rotations and, more importantly, vibrations in the molecules, leading to changes in molecular dipoles. Some vibrational modes are active in IR as they lead to changes in the dipole moment. Vibrations can be described as changes in bond length (stretching) or changes in bond angle (bending), and can be symmetric or asymmetric. According to this, there

are six types of vibrational modes: symmetric and asymmetric stretching, scissoring, rocking, wagging and twisting. The molecular dipole of a symmetrical molecule will be less affected upon vibration of its atoms than the molecular dipole of an asymmetric molecule. This is because different atoms, with different mass and electronegativity, will contribute more strongly to variations in molecular dipole than identical atoms. Because of this, symmetric vibrations are generally weaker than asymmetric vibrations as the former lead to a smaller change in dipole moment. A molecule containing N -atoms has $3N$ degrees of freedom. The number of vibrational modes is calculated by subtracting the number of possible rotations and translations of the molecule, leaving $3N-6$ degrees of vibrational freedom ($3N-5$ if the molecule is linear). This allows for the theoretical calculation of the number of fundamental vibrations expected for a certain molecule. Symmetrical diatomic molecules, like N_2 , are not active in IR as their only possible vibration mode, stretching, does not cause a change in the dipole moment. Asymmetrical diatomic molecules have one vibrational band as they have one bond ($3 \times 2 - 5$). Larger molecules generally have more absorption bands and therefore more complex and unique IR spectra, often referred to as their fingerprints.

FTIR spectra commonly display the intensity of the radiation transmitted through the sample, transmittance (%), as a function of the reciprocal wavelength, frequency or wavenumber (cm^{-1}). Although the infrared region of the electromagnetic spectrum is approximately between 14000 and 10 cm^{-1} , the range of frequencies often used in fundamental vibration studies is $4000-400 \text{ cm}^{-1}$, with far IR spectroscopy in the region from 500 to 10 cm^{-1} .²² FTIR spectra shown in this thesis were obtained using a Shimadzu IR affinity spectrometer fitted with an attenuated total reflectance (ATR) stage, which allows for the study of solid or liquid samples without further sample preparation. Far IR spectra were obtained by Dr Ester Rani Aluri using a dry-air purged Bruker Vertex70 spectrometer equipped with a mercury arc lamp, a DLaTGS detector and a silicon solid-state beam splitter.

2.2.9 Raman spectroscopy

Raman spectroscopy is a spectroscopic technique which studies the inelastic scattering of monochromatic light with solid, liquid, and gaseous matter. It is typically used as a characterisation technique to identify species using their structural fingerprint arising from the unique vibrational frequencies of their molecules. Raman spectroscopy is based on the interaction of radiation, generally a laser, with polarised molecules placed in an electric field. The energy of the incident photons may be shifted up or down upon scattering, giving information about the vibrational and rotational transitions in these

molecules once the photon is detected. Elastic scattering is the interaction between photons and molecules with no exchange of energy, and is also referred to as Rayleigh scattering. If there is a net exchange of energy between the photon and the molecule, it is described as inelastic scattering and can also be referred to as Raman scattering or Raman effect. Raman scattering can be classified into two types: if a molecule in a basic vibrational state interacts with a photon and part of the energy is transferred to the Raman-active mode, then the frequency of the scattered light will be lower than the initial frequency; this is called Stokes scattering. If the Raman-active molecule is already in an excited vibrational mode, then the scattered photon may experience an increase in energy and will therefore be of higher frequency than the excitation radiation. This is called anti-Stokes scattering. The majority of photons undergo Rayleigh scattering which is not useful in molecular characterisation. The signals of Stokes and anti-Stokes inelastic scattering in Raman are about 0.001 % of the incident light, and therefore 0.001 % of the Rayleigh signal. Due to this difference, to discriminate Raman scattering from Rayleigh scattering, Raman spectrometers are fitted with notch filters, tuneable filters, edge pass filters, and band pass filters. These components retain Rayleigh radiation, of the same wavelength as the excitation wavelength, allowing the rest of the light to reach the detector. To be active in Raman spectroscopy, a molecule must experience changes in polarisability upon interaction with a photon. Alternatively, to be active in IR, a molecule must undergo a change in the dipole moment. For this reason, Raman and IR spectroscopies are often combined to obtain complementary information about a molecule. Raman spectra show the intensity of the scattered radiation with respect to the Raman shift, expressed in wavenumbers (cm^{-1}).^{14,23} Raman spectroscopy measurements presented in this thesis were obtained with a Horiba Jobin Yvon LabRAM HR Raman spectrometer. The samples were excited by the 532 nm line from a Ventus 532 laser system, at 1 mW.

2.2.10 Thermal Gravimetric Analysis (TGA)

The thermal gravimetric analysis (TGA) technique consists of the precise measurement of changes in the weight of a sample under a controlled atmosphere and with controlled temperature variations. It is commonly used in the characterisation of polymers, composites, fibres, and paints among other substances. Studied materials undergo processes such as desorption of volatiles, decomposition, oxidation, or reduction when heated in a range of temperatures of 20-1000 °C. These processes cause a variation in weight which is recorded as a function of temperature or as a function of time (constant

temperature or constant heating rate), thus obtaining a mass vs. temperature (or time) curve. Sharp changes in mass indicate the occurrence of one or more of the mentioned processes. The first derivative of the TGA curve, the DTG, is often calculated for further thermodynamic studies of the material. TGA and DTG curves from samples can be compared with curves obtained from reference materials for characterisation and identification purposes. Thermogravimetric analysers consist of a precision balance located inside a furnace. The atmosphere inside the furnace can be controlled by introducing air or a variety of gases (inert, oxidising/reducing, carburising, *etc.*), creating vacuum or a high pressure atmosphere. Samples are placed on sample pans which are generally made of aluminium, alumina, ceramic, or platinum and can be open or closed to the atmosphere. The use of thermal gravimetric analysis instruments coupled to infrared spectrometers (TG-FTIR) and mass spectrometers (TG-MS) has spread in the last few decades, allowing for precise characterisation of decomposition products.^{24,25} In this work, the samples were studied at a constant heating rate of 10 °C/min, between room temperature and 900 °C, in a 100 % N₂ atmosphere using platinum pans in a TA-instruments TGAQ500. The amount of sample used was 5-10 mg, and was kept constant between measurements.

2.2.11 Atomic absorption spectroscopy (AAS)

Atomic absorption spectroscopy (AAS) is a technique used for the quantitative determination of chemical elements based on the absorption of radiation of free atoms in the gaseous state. It is a well-established technique for the characterisation of trace metals in a wide variety of samples such as water, blood, urine, muscle, food, or sediments. Samples must be in solution and, in order to be analysed, they must be first atomised for which flame or electrothermal atomisers can be used. Flame atomisers are based on the thermal energy of a flame produced with a mixture of combustion gases, commonly air and acetylene. The sample is first converted into a fine aerosol, then is swept to the burner by the combustion gases where it is desolvated, resulting in small solid particles. These are volatilised by the flame and the resulting molecules, atoms and ions are then exposed to the radiation. Flame atomisers are simple and inexpensive, and are typically used for the determination of metals in liquid samples, generally in the mg/L range. Electrothermal atomisers provide more robust, sensitive measurements and can be used for solid, liquid or gaseous samples. The use of the resistive heating of a graphite tube instead of the traditional flame provides these atomisers with greater sensitivity, down to the µg/L range. An element-specific lamp irradiates the atomised species in the

flame, promoting electrons from the ground state to high energy orbitals. Subsequently, these electrons relax emitting radiation in the process. This radiation is separated from the background radiation (from the lamp) by a monochromator and finally measured by a detector. Due to the use of element-specific lamps, this technique is highly selective. Since the measured property is the absorbance, this technique is based on the Beer-Lambert-Beer law and requires the use of standard solutions of known concentration of the analyte for quantitative studies. The linear range in which analytes can be precisely determined is highly dependent on the method and analyte. For flame AAS it varies between 0.05 and 100 mg/L depending on the elements, and is typically 0.25-15 mg/L for iron.²⁶

In this work, samples were studied with a Perkin Elmer AAnalyst 400 atomic absorption spectrometer fitted with a flame atomiser and a Fe Hollow Cathode Lamp from Cathodeon ($\lambda = 248.3$ nm; max. current = 30 mA). This set-up had an estimated linear range of 0.5-5 mg/mL.

2.2.12 Nuclear magnetic resonance (NMR)

Nuclear magnetic resonance (NMR) is a characterisation technique based on spectroscopic measurements of local induced magnetic fields around atomic nuclei. It is one of the most powerful techniques used for structure elucidation. Samples are placed in a magnetic field where individual atomic nuclei absorb and re-emit radio waves at a certain frequency, resulting in nuclear magnetic resonance. This resonance frequency is dependent of local atomic magnetic fields in a molecule, which are characteristic of individual compounds. Thus, changes in these intramolecular magnetic fields give information about the electronic structure of a molecule, its dynamics, reaction state, and chemical environment. The most commonly studied nuclei are ^1H and ^{13}C , although many other isotopes such as ^2H , ^6Li , ^{10}B , ^{11}B , ^{14}N , ^{15}N , ^{17}O , or ^{19}F can also be studied by high field NMR spectroscopy. NMR spectra are unique and often predictable for small molecules and functional groups. The same functional groups in a molecule can be distinguished if they have different neighbouring atoms as chemical environments influence the NMR signal. In NMR spectroscopy, samples are dissolved in organic solvents and introduced in a glass tube which is spun during the measurement to average magnetic field variations and any glass imperfections. As most of the nuclei present in such solutions will belong to the solvent, deuterated solvents are used in ^1H NMR to avoid signals from protons in the solvent. The sample is excited with a radio frequency pulse (60-100 MHz) through a radio frequency emitter, and a receiver coil surrounding the sample tube monitors the re-emitted radiation. The signal obtained is then analysed and processed

with a Fourier transform, yielding an NMR spectrum.^{27,28} In this thesis, ¹H NMR spectra were obtained with a Bruker AVIII 400 MHz and a Bruker AVIII 500 MHz spectrometer. Deuterated dimethyl sulfoxide (DMSO-d₆) and deuterated chloroform (CDCl₃) were used as solvents.

2.2.13 Microwave synthesis

In traditional heating methods, the energy is transmitted from the heating source to the sample by either conduction or convection. The heat distribution within the volume of a sample is inherently heterogeneous in these forms of heat transfer, since the heat is transferred from the source to the recipient, and then from the recipient to the solution. Therefore, gradients of temperature are created between different parts of the sample which can lead to the presence of impurities, low yields, and low reproducibility. In contrast with this, the electromagnetic energy delivered by microwave dielectric heating can allow for uniform heating. Additionally, microwave heating offers a number of advantages over conventional heating methods, such as: high heating rates, precise control of reaction parameters, higher yields, better selectivity due to reduced side reactions, and better reproducibility. The main limitations in the use of microwave heating are the relatively high cost of the reactors, and the low penetration depth of microwave radiation which can limit the scale-up.²⁹ Microwave radiation is comprised of an electric field and a magnetic field. The electric field is the principal responsible for the generation of heat by means of two different phenomena: dipolar rotation and ionic conduction. Dipolar rotation refers to the rotation or oscillation that individual dipoles undergo to align with an oscillating electric field. The friction between these molecules causes the heating. In ionic conduction, the electric field causes charged species to move back and forth harmonically to align with a changing electric field. This movement produces heat due to the collisions between the molecules. Highly polar and/or ionic species have more efficient heating generation. At high temperatures the friction between oscillating dipoles diminishes and therefore dipolar rotation has less impact on the heating of a substance. **Figure 2.3** Shows schematics of the effect of microwaves on (a) dipolar and (b) charged species, and the temperature gradient obtained with (c) conductive heating compared to uniform heating through (d) microwave radiation.

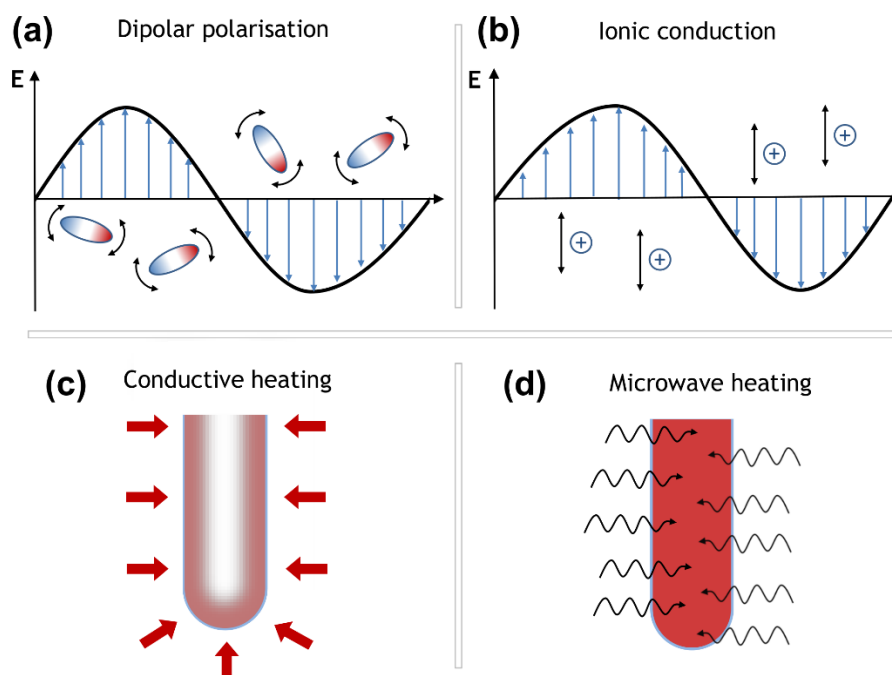


Figure 2.3. (a) Individual dipoles rotating and (b) charged species oscillating upon application of microwave radiation. (c) Temperature gradient in a vessel due to conductive heating, compared to (d) uniform heating provided by microwave radiation.

The dielectric constant (ϵ') and the dielectric loss factor (ϵ'') define the capacity of a substance to store electromagnetic energy *via* polarisation and its ability to convert that energy into heat, respectively. These parameters are used to determine the heating behaviour of a material upon radiation with microwaves, and can be quantified by means of the dielectric loss, δ . However, the loss tangent ($\tan \delta$) (Equation 2.5) is more often used:

$$\tan \delta = \epsilon'' / \epsilon' \quad (2.5)$$

In general, materials with high $\tan \delta$ values display high absorption of microwave radiation and, therefore, high heating efficiency.³⁰

2.3 Experimental

2.3.1 Preparation of Fe_3O_4 nanoparticles by co-precipitation

Co-precipitation refers to the process in which solid particles are precipitated from a solution under controlled parameters. Adjusting the pH, temperature, ionic strength,

and the choice of specific precursors allows for the control of the nucleation and growth of the nuclei, and therefore the size, shape, dispersity, and crystallinity of the particles obtained.

In this thesis, the preparation of Fe₃O₄ nanoparticles by co-precipitation was carried out as described by McCarthy *et al.*³¹ For this, FeCl₂·4H₂O (2.48 g, 12 mmol) and FeCl₃·6H₂O (6.56 g, 24 mmol) were dissolved in 25 mL of a degassed aqueous solution of 0.4 M HCl and stirred for 15 minutes. The iron solution was added dropwise to 250 mL of a degassed solution of 0.5 M NaOH heated at 40 °C under inert atmosphere. After the addition, the solution was heated to 80 °C and stirred for 1 hour under inert atmosphere. Fe₃O₄ nanoparticles were left to cool and then precipitated with a 1.3 Tesla magnet and the reaction mixture decanted. The particles were washed 6 times by dispersing them in deionised water (3 x 50 mL) and ethanol (3 x 50 mL) with sonication for 10 min. Finally, the product was dried in a rotary evaporator (45 °C, 1-2 h) and characterised by PXRD, FTIR, TGA, and TEM.

2.3.1.1 Preparation of Fe₃O₄ nanoparticles by microwave-assisted co-precipitation

The proposed synthesis strategy consists on the co-precipitation of iron oxide nanoparticles followed by a microwave-assisted growth stage, following the method described by Williams *et al.*³⁴ For this, FeCl₂·4H₂O (0.99 g, 5 mmol) and FeCl₃·6H₂O (2.70 g, 10 mmol) were dissolved in 10 mL of degassed and deoxygenated water, under inert atmosphere. The solution was then heated to 80 °C in an oil bath. Ammonium hydroxide (10 mL, 30 %) was slowly added to the solution and stirred for 20 minutes. The black precipitate was transferred to a microwave reactor and irradiated for 20 minutes at 150 °C. The product was left to cool down, decanted with a 1.3 Tesla magnet, and washed by dispersing the nanoparticles in deionised water (5 x 20 mL) with the help of an ultrasound bath. The black precipitate was dried in a rotary evaporator and characterised by PXRD, FTIR, TGA, and TEM.

2.3.1.2 Functionalisation of iron oxide nanoparticles

Fe₃O₄ nanoparticles have been functionalised with two different chelating agents: a porphyrin derivative and diethylenetriaminepentaacetic acid (DTPA). In the case of magnetite nanoparticles functionalised with porphyrin, two different approaches were taken. Firstly, Protoporphyrin IX (PPIX) was used as the chelating agent and attached onto the magnetic nanoparticles along with PEG 200. The aim of these polyethylene glycol moieties was to facilitate the electrostatic interactions between the nanoparticles and

the PEG already present in the wood of the *Mary Rose*, and with an ethylene glycol-based polymer used in subsequent stages of the project. In the second approach, 5,10,15,20-tetrakis(4-aminophenyl) (porphyrin-amine) was used as the metal chelator. In this case no additional polyethylene glycol moieties were included in the functionalisation, since the linker used between the porphyrin and the nanoparticle contained several ethylene glycol units. The DTPA-functionalised nanoparticles did not include any ethylene glycol moieties. The multiple carboxyl groups in DTPA were considered to provide sufficient electrostatic interactions with the PEG in the wood of the *Mary Rose*, and with the aforementioned polymer.

2.3.1.2.1 Functionalisation with Protoporphyrin IX

The functionalisation of iron oxide nanoparticles with PPIX and polyethylene glycol consists of three stages. PPIX and PEG 200 were both modified by adding an alkoxy silane end to each of them in separate procedures, and then attaching them to the iron oxide nanoparticle surface.

Preparation of Protoporphyrin IX-alkoxysilane

Following the amide coupling described by Vivero-Escoto *et al.*, PPIX was attached to (3-aminopropyl)triethoxysilane (APTES) in a two-step synthesis process.³⁶ In the first step, PPIX (PPIX, 370 mg, 0.66 mmol), N-hydroxysuccinimide (NHS, 170 mg, 1.5 mmol), 1-ethyl-3-(3-dimethylaminopropyl) carbodiimide (EDC, 232 mg, 1.21 mmol) and 4-(dimethylamino)pyridine (DMAP, 81 mg, 0.66 mmol) were dissolved in a mixture of dichloromethane and dimethylsulfoxide (40 mL, DCM:DMSO 1:1) under inert atmosphere and stirred for 48 h at room temperature in the absence of light. The product was purified by precipitation by adding ca. 50 mL of an ethanolic solution (20 % in water). After brief stirring (5 minutes), the precipitate was vacuum filtered with a nylon filter membrane (0.2 µm pore size) and then washed with the ethanolic solution (20 % in water). The product was lyophilised for 12 hours to eliminate traces of solvent and water, then stored at -20 °C.

In the second step of the synthesis, PPIX-succinimide (125 mg, 0.164 mmol), APTES (38 µL, 0.163 mmol) and trimethylamine (TEA, 25 µL, 0.175 mmol) were dissolved in 5 mL of DMSO under inert atmosphere at room temperature and stirred for 72 h in the absence of light. The product was purified by precipitation by adding ca. 50 mL of ethanol (20 % in water). After brief stirring, the precipitate was vacuum filtered with a nylon filter (0.2 µm pore size) and then washed with the same ethanolic solution. The dark brown powder was finally lyophilised and stored at -20 °C.

Preparation of PEG 200-alkoxysilane

Polyethylene glycol (200 g/mol) (PEG-200) was attached to APTES *via* a two-step amide coupling process inspired by the work reported by Feng *et al.*³⁷ For this, a PEG 200-acid was first synthesised, and later a PEG 200-alkoxysilane was prepared through amide coupling with APTES. In the first step, succinic anhydride (12.0 g, 120 mmol) and DMAP (1.46 g, 120 mmol) were dissolved in 30 mL of dry tetrahydrofuran (THF) under inert atmosphere and stirred for 30 minutes at 0 °C. PEG-200 (21.5 mL, 120 mmol) and TEA (1.6 mL, 12 mmol) were dissolved in 30 mL of THF, transferred to the previous solution under inert atmosphere and stirred for 2 hours at 0 °C. The solvent was removed on a rotary evaporator and the product was dissolved in DCM (30 mL). Then the solution was washed with 1 M HCl (2 x 30 mL) and the solvent was eliminated under vacuum.

In the second step, EDC (1.29 g, 6.76 mmol) was added to a solution of the previously obtained PEG 200-acid (2.0 g, 3.37 mmol) in 40 mL of dry DCM under inert atmosphere and stirred for 30 minutes at 0 °C. APTES (0.899 g, 3.41 mmol) and NHS (0.815 g, 7.08 mmol) were dissolved in dry DCM (20 mL) under inert atmosphere, added to the previous solution, and stirred for 2 hours at 0 °C, then stirred overnight at room temperature. The obtained transparent liquid was washed with 1 M HCl (2 x 30 mL) and the DCM was eliminated under vacuum.

Coating of Fe₃O₄ nanoparticles with PEG-alkoxysilane and Protoporphyrin IX-alkoxysilane

Fe₃O₄ nanoparticles (300 mg) were dispersed in ca. 30 mL of dry ethanol and placed in a sonication bath for 10 minutes. PPIX-alkoxysilane (0.137 g, 0.178 mmol) was dissolved in a mixture of dimethylsulfoxide and ethanol (10 mL, DMSO:EtOH 1:1), PEG 200-alkoxysilane (0.084 g, 0.177 mmol) was dissolved in ethanol (2 mL) and was added to the Fe₃O₄ nanoparticles suspension along with the PPIX-alkoxysilane solution. The mixture was stirred for 48 hours at room temperature in the dark (flask covered in aluminium foil). The product was decanted with a 1.3 Tesla magnet, washed first with deionised water (4 x 20 mL), then ethanol (4 x 20 mL), and finally dried under vacuum for 45-60 minutes.

2.3.1.2.2 Functionalisation of nanoparticles with DTPA

The procedure for functionalising the iron oxide nanoparticles with DTPA differs from the one used for PPIX/PEG 200. Here a one-pot, three-step procedure was developed in which APTES was anchored to the iron oxide nanoparticle, and DTPA was linked to APTES in subsequent steps. Firstly, iron oxide nanoparticles were prepared by microwave-

assisted co-precipitation, following the work by Williams *et al.* and described in **Section 2.3.1.1**.³⁴ The black precipitate obtained after the microwave treatment was decanted with a 1.3 Tesla magnet, and washed with deionised water (4 x 20 mL) and ethanol (2 x 20 mL). The drying stage was omitted and, following an adapted method by Yong *et al.*³⁸, the magnetite nanoparticles (500 mg) were dispersed in 30 mL of dry ethanol, under inert atmosphere, by sonication for 30 minutes at room temperature. Ammonia (8 mL) was added, and the solution was stirred for 10 minutes. APTES (3 mL) was added dropwise, and the reaction mixture was stirred overnight at 50 °C under inert atmosphere. The product was decanted magnetically, thoroughly washed with ethanol (4 x 20 mL), water (2 x 20 mL) and DMF (1 x 20 mL). DTPA was immobilised onto the iron oxide nanoparticles following a procedure adapted from Yang *et al.*³⁹ For this, 50 mg of the prepared APTES-coated Fe₃O₄ nanoparticles were dispersed in DMF (25 mL) by sonication for 10 minutes, and TEA (0.45 mL) was subsequently added. An excess of diethylenetriaminepentaacetic acid dianhydride (DTPA-da, 100 mg, 0.280 mmol) was added to the suspension, then stirred at 80 °C under reflux conditions for 30 minutes, and further stirred at room temperature under inert atmosphere overnight. The product was magnetically decanted and washed with TEA 1 % in DMF (2 x 20 mL), H₂O (2 x 20 mL) and acetone (2 x 20 mL). The final product was dried under vacuum at 40 °C for 1-2h.

2.3.2 Synthesis of thermoresponsive polymer p(DEGMA₄₅-co-MMA₅)

The thermoresponsive polymer was prepared using a method inspired by the work of leong *et al.*^{40,41} For this, a solution of di(ethylene glycol) methyl ether methacrylate (DEGMA, 1.888 g, 45 eq.) and methyl methacrylate (MMA, 0.1116 g, 5 eq.) in 3 mL of 1,4-dioxane was added into a Schlenk flask, previously purged by 3 vacuum-argon cycles. A solution of azobis(isobutyronitrile) (AIBN, 0.0037 g, 0.2 eq.) and 4-cyano-4-(phenylcarbonothioylthio) pentanoic acid (0.00621 g, 1 eq.) in 1 mL of 1,4-dioxane was also added to the Schlenk flask. The mixture was degassed by 4 freeze-pump-thaw cycles, backfilled with argon and stirred at 65 °C for 8 hours under inert atmosphere. The reaction product was rapidly cooled in an ice-water bath, and dialysed (MWCO: 3.5 kD) against deionised water for 5 days. The polymer solution was freeze dried for 48 hours.

2.3.3 Synthesis of Fe₃O₄-VTES-polymer-porphyrin (multifunctional nanocomposite)

The preparation of Fe₃O₄-VTES-polymer-porphyrin consists of five stages. In the first step, the thermoresponsive polymer p(DEGMA₄₅-co-MMA₅) is synthesised, as described previously in **Section 2.3.2**. In the second step, a porphyrin moiety is added to the polymer structure. Then, the dithioester end group in the polymer is reduced to a thiol. Meanwhile, magnetite nanoparticles are coated with vinyl triethoxysilane. Finally, the porphyrin-polymer-thiol is anchored onto the coated magnetite nanoparticles *via* a thiol-ene click reaction.

Preparation of Fe₃O₄-VTES

Following Yong *et al.*³⁸ 500 mg of magnetite nanoparticles (prepared as described in **Section 2.3.1.1**) were dispersed in 30 mL of dry ethanol and sonicated for 30 minutes at room temperature. Ammonia (8 mL) was added under inert atmosphere and stirred for 10 minutes before vinyltriethoxysilane (VTES, 1.5 mL, 5 % v/v) was added dropwise. The mixture was stirred overnight at 50 °C under inert atmosphere. The product was decanted magnetically, washed with ethanol (5 x 20 mL), dried under vacuum at 45 °C for 1-2 hours, and stored at 5 °C.

Preparation of porphyrin-polymerdithioester

This procedure consists of an amide coupling between p(DEGMA-co-MMA) and a porphyrin unit. For this, the polymer p(DEGMA₄₅-co-MMA₅) (0.1581 g, 1.5 eq.), prepared as per **Section 2.3.2**, was dissolved in 8 mL of DMF, along with EDC (0.0133 g, 4 eq.), and NHS (0.0068 g, 4 eq.) under inert atmosphere, and were stirred for 10 minutes at room temperature. A catalytic amount of DMAP (0.0004 g, 0.2 eq.) was also added to the solution. Next, 5,10,15,20-tetrakis(4-aminophenyl) porphyrin (porphyrin-amine, 0.0100 g, 1 eq.) and TEA (100 µL) were dissolved in 1 mL of DMF, and added to the solution. This was stirred for 72 hours in the dark, at room temperature and under inert atmosphere. After the reaction, the solution was dialysed (MWCO: 3.5 kD) in the dark, against a mixture of deionised water and methanol of varying ratios: (V_W:V_{MeOH} = 70:30, 85:15, 90:10, 100:0). These ratios were changed every 6 hours. The porphyrin-polymer solution was freeze dried for 48 hours.

Reduction of porphyrin-polymerdithioester to porphyrin-polymerthiol

In this step, the dithioester end of the polymer was reduced to thiol. For this, the previously synthesised porphyrin-polymerdithioester (0.1659 g, 1 eq.), tris(2-carboxyethyl)phosphine hydrochloride (TCEP·HCl, 0.001 g, 0.1 eq.) and octylamine

(0.5 mL, 1 eq.) were dissolved in THF (5 mL) under inert atmosphere. This reaction mixture was stirred for 4 hours in the dark at room temperature. The solvent was eliminated under vacuum and the product was precipitated with cold diethyl ether. The gel obtained was decanted, dried under vacuum at room temperature, and stored at 5 °C.

Grafting porphyrin-polymerthiol onto Fe₃O₄-VTES

The porphyrin-polymerthiol was anchored onto the VTES coated magnetite nanoparticles *via* thiol-ene click chemistry between the thiol and the vinyl groups in the polymer and nanoparticles, respectively.^{42,43,44} For this, porphyrin-polymerthiol (0.0974 g, 1 eq.) was dissolved in acetonitrile (10 mL) under inert atmosphere, and AIBN (0.0200 g, 10 eq.) was added to the solution. A suspension of Fe₃O₄-VTES nanoparticles (0.0372 g) in acetonitrile (2 mL) was added to the solution. The reaction mixture was stirred overnight, in the dark, at 70 °C and under a flow of inert gas. The product was magnetically decanted, washed with ethanol (5 x 15 mL), and dried under vacuum at room temperature.

2.3.4 Protocol for application of PPIX/PEG 200 functionalised nanoparticles on wood samples.

Bare magnetite nanoparticles and PPIX/PEG 200 functionalised nanoparticles were applied on fresh wood samples (oak cubes, side length 1.5 cm) in the form of aqueous suspensions (1 mL, 0.6 mg/mL of particles in deionised water). The nanoparticle suspensions were applied in the direction of the wood grain to ensure a consistent diffusion between samples. The wood samples were then placed atop a 1.3 Tesla permanent magnet. Another set of fresh oak samples were treated with the same suspensions and in the same manner, but were not exposed to any external magnetic field. The wood samples were incubated for 24 hours in the dark and at room temperature. After this period, the samples were cut in half along the wood grain and the direction of diffusion of the applied nanoparticle suspensions in order to perform electron microscopy studies. This procedure and the subsequent studies are discussed in **Section 4.1**. **Figure 2.4** shows a schematic of (A) the application of the nanocomposite suspension on the face perpendicular to the wood grain, and (B) a fresh oak sample being sectioned along the wood grain to study the profile of the diffused nanoparticles.

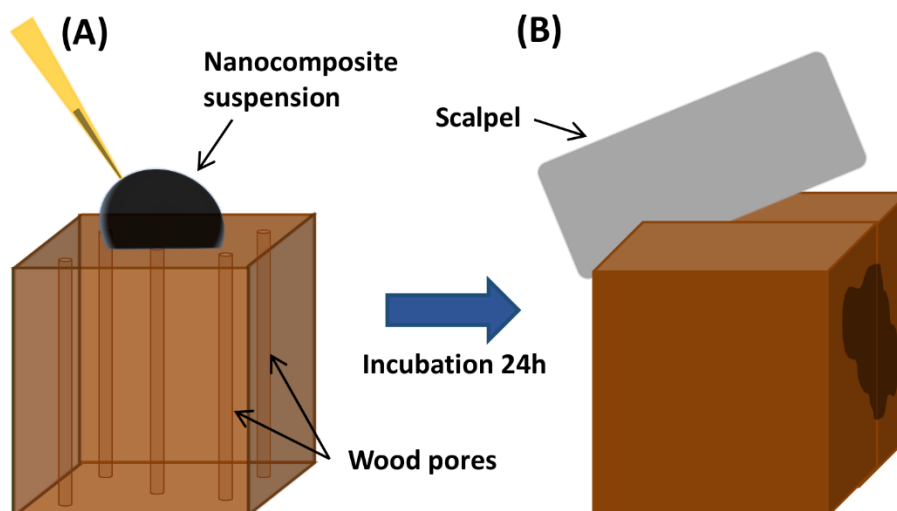


Figure 2.4. Schematic of (A) the application of suspensions of bare nanoparticles and PPIX/PEG 200 - functionalised nanoparticles on a fresh oak sample with a micropipette, and (B) the sectioning of the oak sample to study its cross section by electron microscopy. The nanoparticle suspensions were applied on the face in line with the wood vessels and grain to ensure the diffusion rate was comparable among different samples. Sterile steel scalpel blades were used to cut the wood samples apart.

2.3.5 Inclusion of functionalised nanoparticles in thermoresponsive polymer

This procedure applies to the preparation of a polymer-mixed-nanocomposite, a nanocomposite-laden polymer, and a polymer-mixed DTPA-nanocomposite, discussed in **Section 4.3**, **Section 4.6.2.1** and **Section 5.2.2.2.1**, respectively. The incorporation of functionalised magnetic nanoparticles onto the thermoresponsive polymer was carried out by dissolving 100 mg of polymer in 0.3 mL of ethanol and sonicating for 5 minutes to ensure its solubilisation. Then, 20 mg of functionalised nanoparticles (1:5 mass ratio with respect to polymer) were added to the solution, this was sonicated for 1-2 minutes until fully dispersed, and stirred for 5 minutes. The solvent was removed carefully under vacuum at room temperature for at least 30 minutes. The product was stored under inert atmosphere at 5 °C.

2.3.6 Protocol for treatment of wood samples with functionalised nanoparticle-thermoresponsive polymer.

This protocol was applied for the treatment of fresh and artificial archaeological wood samples, and *Mary Rose* samples with a polymer-mixed-nanocomposite, a nanocomposite-laden polymer, and a polymer-mixed DTPA-nanocomposite, discussed in

Section 4.4.2, Sections 4.6.2.2 and 4.6.2.3, and Section 5.2.2.2, respectively. For this, the thermoresponsive polymer containing the functionalised nanoparticles was cooled down in a fridge at 5 °C for a minimum of 3 hours, and then a portion of approximately 20 mg was applied onto the surface of the wood sample. This portion was carefully spread with a plastic spatula to form an even, thin layer. The wood sample was fixed atop a 1.3 Tesla neodymium magnet, and kept in the dark, at 5 °C for a period of four weeks. The treatment with polymer-mixed nanocomposite was carried out under the same conditions, and was incubated for 6 months. After these incubation periods, the wood samples were wrapped in transparent film, and placed upside down atop a 1.3 Tesla neodymium magnet in the dark, at 5 °C for one week. Finally, the wood samples were brought to room temperature, and the functionalised nanoparticle-thermoresponsive polymer was carefully peeled off their surface with a plastic spatula for further analysis.

References

- 1 N42 Neodymium Pot Magnet - (25 x 8 x 5mm) - 26kg Pull, https://www.first4magnets.com/pot-clamping-c43/25mm-dia-x-8mm-thick-x-5mm-c-sink-n42-neodymium-pot-magnet-26kg-pull-p3477#ps_1-1553.
- 2 D. W. Bennett, *Understanding single-crystal x-ray crystallography*, Wiley-VCH, 2010.
- 3 V. K. Pecharsky and P. Y. Zavalij, *Fundamentals of powder diffraction and structural characterization of materials*, Springer, 2009.
- 4 R. E. Dinnebier and S. J. L. Billinge, Eds., *Powder Diffraction: theory and practice*, Royal Society of Chemistry, Cambridge, 2008.
- 5 A. L. Patterson, *Phys. Rev.*, 1939, **56**, 978-982.
- 6 R. F. Egerton, *Physical principles of electron microscopy: an introduction to TEM, SEM, and AEM.*, SPRINGER, New York, 2005.
- 7 G. Friedbacher and H. Bubern, *Surface and thin film analysis : a compendium of principles, instrumentation, and applications*, Wiley-VCH, 2011.
- 8 D. B. Williams and C. B. Carter, *Transmission electron microscopy : a textbook for materials science*, Springer, 2009.
- 9 H.-H. Perkampus, *UV-VIS spectroscopy and its applications*, Springer-Verlag, Berlin, New York, 1992.
- 10 M. Gouterman, *J. Mol. Spectrosc.*, 1961, **6**, 138-163.
- 11 M. Gouterman, G. H. Wagnière and L. C. Snyder, *J. Mol. Spectrosc.*, 1963, **11**, 108-127.
- 12 K. M. Kadish, K. M. Smith and R. Guilard, *The porphyrin handbook*, Academic Press, 2000.
- 13 R. Giovannetti, in *Macro To Nano Spectroscopy*, InTech, 2012.
- 14 D. A. Skoog, F. J. Holler and S. R. Crouch, *Principles of instrumental analysis*, Belmonte, California, 6th edn., 2007.
- 15 J. R. Albani, *Principles and Applications of Fluorescence Spectroscopy*, Blackwell Publishing Ltd, Oxford, UK, 2007.
- 16 S. K. Mandal, N. Lequeux, B. Rotenberg, M. Tramier, J. Fattaccioli, J. Bibette and B. Dubertret, *Langmuir*, 2005, **21**, 4175-4179.
- 17 S. A. Corr, A. O' Byrne, Y. K. Gun'ko, S. Ghosh, D. F. Brougham, S. Mitchell, Y. Volkov and A. Prina-Mello, *Chem. Commun.*, 2006, **0**, 4474.
- 18 J. F. Lovell, T. W. B. Liu, J. Chen and G. Zheng, *Chem. Rev.*, 2010, **110**, 2839-2857.
- 19 T.-F. Liu, D. Feng, Y.-P. Chen, L. Zou, M. Bosch, S. Yuan, Z. Wei, S. Fordham, K. Wang and H.-C. Zhou, *J. Am. Chem. Soc.*, 2015, **137**, 413-419.
- 20 O. T. Wilcox, A. Fateeva, A. P. Katsoulidis, M. W. Smith, C. A. Stone and M. J.

- Rosseinsky, *Chem. Commun.*, 2015, **51**, 14989-14991.
- 21 J. Stetefeld, S. A. McKenna and T. R. Patel, *Biophys. Rev.*, 2016, **8**, 409-427.
- 22 B. H. Stuart, *Infrared Spectroscopy: Fundamentals and Applications*, John Wiley & Sons, Ltd, Chichester, UK, 2004.
- 23 C. V. Raman and K. S. Krishan, *Nature*, 1928, **121**, 501-502.
- 24 P. Gabbott, Ed., *Principles and Applications of Thermal Analysis*, Blackwell Publishing Ltd, Oxford, UK, 2008.
- 25 S. Vyazovkin, N. Koga and C. Schick, *Handbook of thermal analysis and calorimetry: recent advances, techniques and applications*, 2018.
- 26 B. Fernández, L. Lobo and R. Pereiro, in *Encyclopedia of Analytical Science*, eds. P. Worsfold, C. Poole, A. Townshend and M. Miro, Academic Press, 3rd edn., 2019, pp. 137-143.
- 27 J. D. Roberts, *Nuclear Magnetic Resonance: Applications to Organic Chemistry*, McGraw-Hill Book Company, Inc, New York, 1959.
- 28 J. Pople, H. J. Bernstein and W. G. Schneider, *High-Resolution Nuclear Magnetic Resonance*, New York, 1st edn., 1959.
- 29 I. Bilecka and M. Niederberger, *Nanoscale*, 2010, **2**, 1358.
- 30 D. M. P. Mingos and D. R. Baghurst, *Chem. Soc. Rev.*, , DOI:10.1039/cs9912000001.
- 31 S. A. McCarthy, G. L. Davies and Y. K. Gun'ko, *Nat. Protoc.*, 2012, **7**, 1667-1693.
- 32 T. E. Ashton, J. V. Laveda, D. A. MacLaren, P. J. Baker, A. Porch, M. O. Jones and S. A. Corr, *J. Mater. Chem. A*, 2014, **2**, 6238-6245.
- 33 M. Amores, T. E. Ashton, P. J. Baker, E. J. Cussen and S. A. Corr, *J. Mater. Chem. A*, 2016, **4**, 1729-1736.
- 34 M. J. Williams, E. Sánchez-Pérez, E. R. Aluri, F. J. Douglas, D. A. Maclaren, O. M. Collins, E. J. Cussen, J. D. Budge, L. C. Sanders, M. Michaelis, C. M. Smales, J. Cinatl, S. Lorrio, D. Krueger, R. T. M. De Rosales and S. A. Corr, *RSC Adv.*, 2016, **6**, 83520-83528.
- 35 J. A. Gerbec, D. Magana, A. Washington and G. F. Strouse, *J. Am. Chem. Soc.*, 2005, **127**, 15791-15800.
- 36 J. L. Vivero-Escoto and D. L. Vega, *RSC Adv.*, 2014, **4**, 14400-14407.
- 37 S. Hou, L. K. McCauley and P. X. Ma, *Macromol.*, 2007, **7**, 5, 620-628.
- 38 Y. Yong, Y. Bai, Y. Li, L. Lin, Y. Cui and C. Xia, *J. Magn. Magn. Mater.*, 2008, **320**, 2350-2355.
- 39 H. Yang, Y. Zhuang, Y. Sun, A. Dai, X. Shi, D. Wu, F. Li, H. Hu and S. Yang, *Biomaterials*, 2011, **32**, 4584-4593.
- 40 N. S. leong, K. Brebis, L. E. Daniel, R. K. O'Reilly and M. I. Gibson, *Chem. Commun.*, 2011, **47**, 11627.

- 41 N. S. Jeong, M. Hasan, D. J. Phillips, Y. Saaka, R. K. O'Reilly and M. I. Gibson, *Polym. Chem.*, 2012, **3**, 794.
- 42 H. Li, B. Yu, H. Matsushima, C. E. Hoyle and A. B. Lowe, *Macromolecules*, 2009, **42**, 6537-6542.
- 43 Y. Kotsuchibashi, M. Ebara, T. Aoyagi and R. Narain, *Polym. Chem.*, 2012, **3**, 2545.
- 44 D. P. Nair, M. Podgórski, S. Chatani, T. Gong, W. Xi, C. R. Fenoli and C. N. Bowman, *Chem. Mater.*, 2014, **26**, 724-744.

Chapter 3 - Porphyrin/PEG-functionalised magnetic nanoparticles

3.1 Introduction

In this chapter, the objective was to prepare a multifunctional nanocomposite for the removal of harmful iron ions from waterlogged archaeological wood. This nanocomposite should incorporate an iron chelating agent and should be easily applied and removed from the wood surface. To achieve this, the design was based on highly crystalline magnetite (Fe_3O_4) nanoparticles functionalised with Protoporphyrin IX (PPIX) and polyethylene glycol 200 (PEG 200, where 200 refers to the average molecular weight of the polymer chains). PPIX is a well-known chelating agent, with nitrogen donating groups capable of binding metal ions. PEG 200 was chosen as a surfactant because this polymer has been used to treat waterlogged wooden artefacts such as the *Mary Rose* and Swedish warship the *Vasa* for decades, increasing the likelihood of uptake of a nanocomposite incorporating this polymer.^{1,2} Adhering this moiety to the surface of magnetic iron oxide cores provides a convenient approach for the application of a treatment for the removal of harmful iron ions. The magnetic nature of the material opens up the possibility of removal of this treatment by means of an external magnetic field.

In this work, magnetite nanoparticles have been synthesised *via* a microwave-assisted co-precipitation method (MW co-precipitation), which allows for precise control over the crystallinity, size and shape of the nanoparticles, while maintaining short reaction times and low reaction temperatures. For comparison, magnetite was also prepared by a traditional and widely applied co-precipitation method. PPIX and PEG 200 were first linked to (3-Aminopropyl)triethoxysilane (APTES) *via* amide coupling in order to anchor these moieties to the magnetite nanoparticle surface. In the case of the PPIX, this coupling was performed between the carboxyl groups in PPIX and the amine end in APTES. In the case of PEG 200, an intermediate PEG-acid was prepared *via* esterification of the hydroxyl end groups, and an amide coupling reaction was carried out between the primary amine in APTES and one of the carboxyl groups in PEG-acid. APTES contains three ethoxy groups that are excellent leaving groups. This allows for the formation of a covalent bond between the 3-ethoxysilane end of APTES and the hydroxyl groups naturally present on the iron oxide surface.³ APTES also provides a separation between PPIX molecules which might otherwise aggregate *via* π - π interactions, leading to the deterioration of its chelating properties and quenching of its fluorescence. The schematic in **Figure 3.1** describes the structure of the designed nanocomposite, featuring a magnetite nanoparticle bearing equal amounts of PPIX and PEG 200 on its surface.

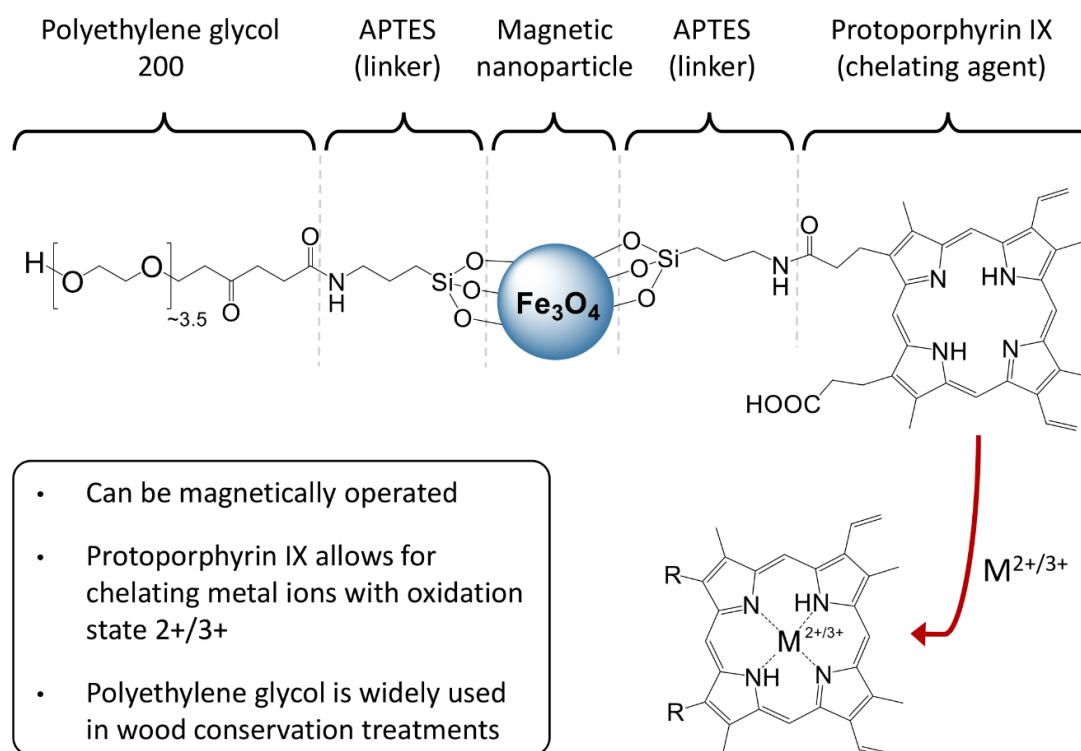


Figure 3.1. Schematic of the prepared nanocomposite. PPIX, a metal chelating agent, is anchored onto magnetite cores using APTES as a linker. Similarly, PEG 200 is also attached onto the nanoparticles. While PPIX can sequester harmful iron ions from the wood structure, the magnetic nature of the magnetite cores could play a key role in the handling and application of the nanocomposite to the artefact. PEG 200 may facilitate the diffusion of the nanocomposite into the archaeological wood, which has been treated with PEG for almost two decades.

This chapter describes the synthesis of APTES-PPIX and APTES-PEG 200, the preparation of magnetite nanoparticles, and further functionalisation of such particles with APTES-PPIX and APTES-PEG 200. The resulting nanocomposite has been characterised with a range of techniques to assess the successful attachment of PEG 200 and PPIX. Finally, the functionalised nanocomposite has been tested in aqueous and ethanolic iron solutions to evaluate the chelation performance of the PPIX attached to the surface of the magnetite nanoparticles in order to assess its potential as an artefact treatment.

3.2 Results and discussion

3.2.1 Synthesis of magnetic nanoparticles

Iron oxide nanoparticles were synthesised *via* a microwave-assisted co-precipitation method, as described by Williams *et al.*, (2016) Briefly, iron (III) and iron (II) chloride hydrated salts were dissolved in deoxygenated water in a 2:1 ratio, before addition of

ammonia to precipitate out the Fe_3O_4 nanoparticles. A short microwave treatment results in crystalline Fe_3O_4 nanoparticles. This additional microwave step has been reported to generate highly crystalline particles. This crystallinity has effects on the resulting magnetic properties, where less disorder at the surface results in better magnetic properties.⁴ This experimental process (described in **Section 2.3.1.1**) is summarised in the schematic in **Figure 3.2**. The black precipitate was washed several times with water, decanted magnetically, and dried under vacuum at 45 °C.

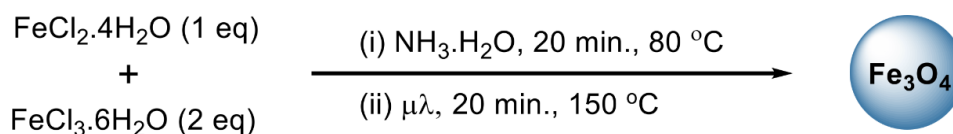


Figure 3.2. Reaction schematic for the MW co-precipitation of Fe_3O_4 nanoparticles in aqueous solution. The nucleation is initiated by the addition of ammonia, followed by a short ageing stage under microwave radiation, to finally obtain magnetite nanoparticles.

For comparison, magnetite nanoparticles were also prepared following a reported traditional co-precipitation method in aqueous media.⁵ **Figure 3.3** depicts a schematic of the traditional co-precipitation of iron oxide nanoparticles. Typically, iron (III) and iron (II) chloride hydrated salts were dissolved in a 2:1 ratio in HCl (0.4 M). This solution was added dropwise to a NaOH (0.5 M) solution at 40 °C under inert atmosphere to precipitate the Fe_3O_4 nanoparticles. The growth stage was carried out by stirring this solution at 80 °C for 1 hour. The black precipitate obtained was washed with water, magnetically decanted and dried under vacuum at 45 °C. Further details of this synthetic route can be found in **Section 2.3.1**.

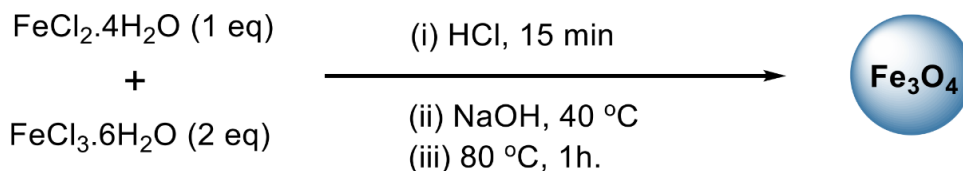


Figure 3.3. Schematic of the traditional co-precipitation of Fe_3O_4 nanoparticles in aqueous solution. The nucleation is initiated by adding dropwise an acidic solution of the iron chloride salts onto a solution of NaOH. The precipitated Fe_3O_4 nanoparticles were growth at 80 °C for 1 hour.

3.2.1.1 Characterisation of magnetic nanoparticles

The iron oxide nanoparticles prepared by these two routes have been characterised by powder XRD and electron microscopy to determine the phase purity, crystallinity, average size, and size distribution of the particles. XRD patterns obtained from both dry precipitates matched the standard of cubic spinel magnetite (Fe_3O_4 , JCPDS index card no. 19-629) in the $Fd\bar{3}m$ space group, with no evidence for the formation of any other phases. These data are plotted in **Figure 3.4**. The initial observation is the broad diffraction peaks, characteristic of nanostructured materials. The crystallite size was estimated for both samples using the Scherrer equation⁶ applied to the diffraction peak (311), and the results obtained are shown in **Table 3.1**.

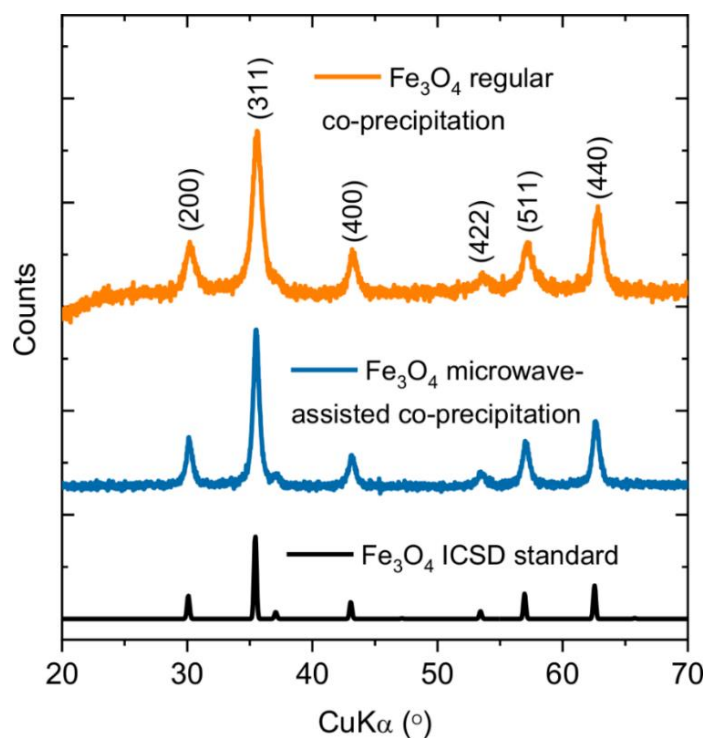


Figure 3.4. Powder XRD patterns of magnetite nanoparticles synthesised by MW co-precipitation and by traditional co-precipitation. **Orange:** Fe_3O_4 prepared by traditional co-precipitation⁵; **Blue:** Fe_3O_4 synthesised by MW co-precipitation⁴; **Black:** ICSD standard of Fe_3O_4 (cubic inverse spinel, space group: $Fd\bar{3}m$).

Table 3.1. Average crystallite sizes from Scherrer broadening for Fe₃O₄ nanoparticles synthesised by traditional and MW co-precipitation.

Sample	Size (nm)
Fe ₃ O ₄ (traditional co-precipitation)	11
Fe ₃ O ₄ (MW-assisted co-precipitation)	16

Calculations indicate that the average size of the crystalline domains is larger for the microwave-assisted synthesis than for the traditional co-precipitation method. Although this is not an accurate measure of the particle size, this indicates that larger crystallite sizes are obtained with the MW co-precipitation method.

The magnetite nanoparticles prepared by the MW co-precipitation method and by traditional co-precipitation were also characterised by high-resolution transmission electron microscopy (HR TEM) (**Figure 3.5**). The results of the analysis of 100 individual nanoparticle sizes are shown in **Table 3.2**. These calculations revealed a slightly larger average particle size for the sample prepared by MW co-precipitation (14.6 nm) compared to the traditional co-precipitation (11.3 nm), with monodisperse size distributions for both methods observed. Interestingly, the size distribution of the nanoparticles prepared by MW co-precipitation is lower than that obtained for the traditional co-precipitation. The polydispersity indices, obtained from 100 individual particles using ImageJ, are 0.21 and 0.31, respectively, consistent with the differences between the synthesis methods. In the method developed by Williams *et al.* the microwaves provide a homogeneous and stable heating of the reaction cavity, resulting in a better control of the ageing stage and, ultimately, a decrease in the polydispersity of the sample. The visible lattice fringes in **Figure 3.5** (C) and (D) confirmed the high crystallinity and the single domain nature of these iron oxide nanostructures, associated with superparamagnetism in nanoparticles with sizes under 20 nm.^{7,8,9}

Table 3.2. Nanoparticles average sizes and polydispersity index (PDI) values for iron oxide nanoparticles prepared by MW assisted co-precipitation and by traditional co-precipitation.

Sample	Average nanoparticle size (nm)	Polydispersity index
Fe ₃ O ₄ (traditional co-precipitation)	11.3	0.33
Fe ₃ O ₄ (MW assisted co-precipitation)	14.6	0.21

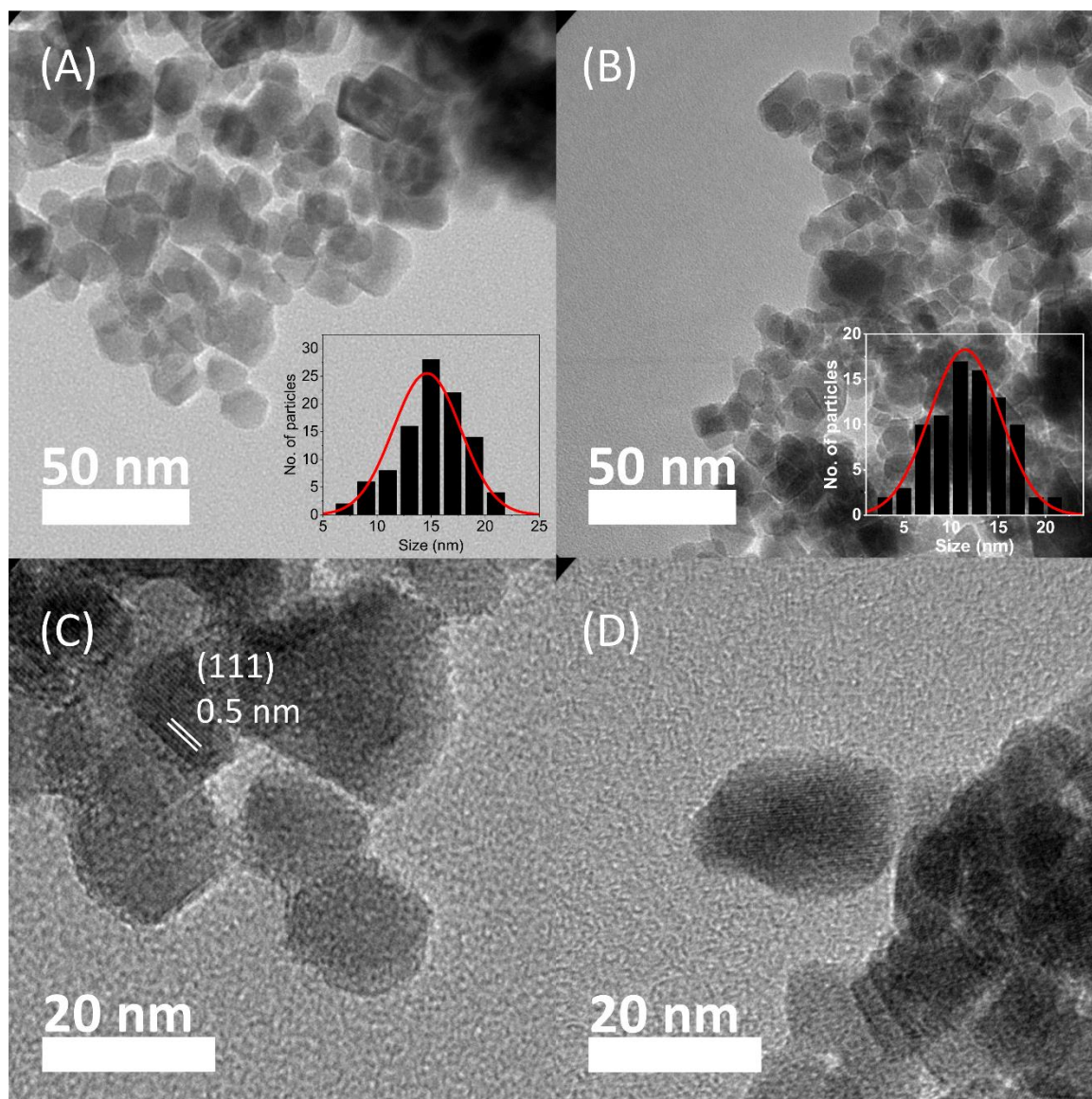


Figure 3.5. High-resolution TEM micrographs of Fe₃O₄ nanoparticles prepared by (A), (C) microwave-assisted co-precipitation and (B), (D) traditional co-precipitation. Insets in micrographs (A) and (B) show the size distribution histograms obtained for each method.

3.2.2 Functionalisation of Fe₃O₄ with PPIX and PEG 200

3.2.2.1 Strategies for functionalisation

A number of strategies were considered to attach PPIX and PEG 200 to the surface of the magnetite nanoparticles. Initially, the possibility of using PEG 200 as a linker between PPIX and the magnetite nanoparticles was explored. For this, magnetite nanoparticles were synthesised in the presence of PEG 200 following the traditional and MW co-precipitation methods, and also *via* a hydrothermal route. The aim was to obtain PEG 200-stabilised Fe₃O₄ nanoparticles onto which PPIX could be potentially attached *via*

electrostatic interactions between the carboxyl groups in PPIX and the ether groups in PEG 200. FTIR analyses revealed weak signals attributed to the PEG 200, with typical mass losses of 2-3 % observed in TGA. Subsequent attempts to incorporate PPIX onto the PEG 200 nanoparticles were unsuccessful. Therefore, another approach based on silane chemistry was investigated. In this case, an aminosilane (APTES) was employed to covalently attach PEG 200 and PPIX to the nanoparticle surface. The amine group in APTES was used to form an amide bond with the carboxylic groups in PPIX and one of the carboxylic groups in the intermediate PEG 200-acid. Furthermore, ethoxysilane is an excellent leaving group that favours the formation of a covalent bond to iron oxide surfaces.^{3,10} The syntheses of APTES-PPIX and APTES-PEG 200 *via* amide coupling are described below.

3.2.2.2 Synthesis of APTES-PPIX

The preparation of APTES-PPIX was performed in two stages.¹¹ Briefly, a solution of DCM:DMSO (1:1 volumetric ratio) was found to be optimal to dissolve PPIX at room temperature. The carboxylic groups in PPIX were initially activated by the coupling agent 1-Ethyl-3-(3-dimethylaminopropyl) carbodiimide (EDC), and N-Hydroxysuccinimide (NHS) was added to form a primary amine-specific intermediate, PPIX-succinimide. EDC was specifically selected since it is water soluble and therefore easy to remove after the reaction. The red-brown solid was filtered and purified by precipitation in an ethanolic solution, and lyophilised to remove the remaining water. PPIX-succinimide was dissolved in DMSO, and APTES was added dropwise in slightly alkaline conditions and reacted for 72h. The final product was again filtered and purified by precipitation in an ethanolic solution. Then it was lyophilised to remove the water, and stored at -20 °C to avoid the degradation of the PPIX. This synthesis was carried out in the dark to avoid the photodecomposition of PPIX, and in the absence of water or air to avoid the hydrolysis of the ethoxysilane groups and to guarantee the amide coupling. The detailed description of this process can be found in **Section 2.3.1.2.1**. The scheme in **Figure 3.6** describes the two-step reaction.

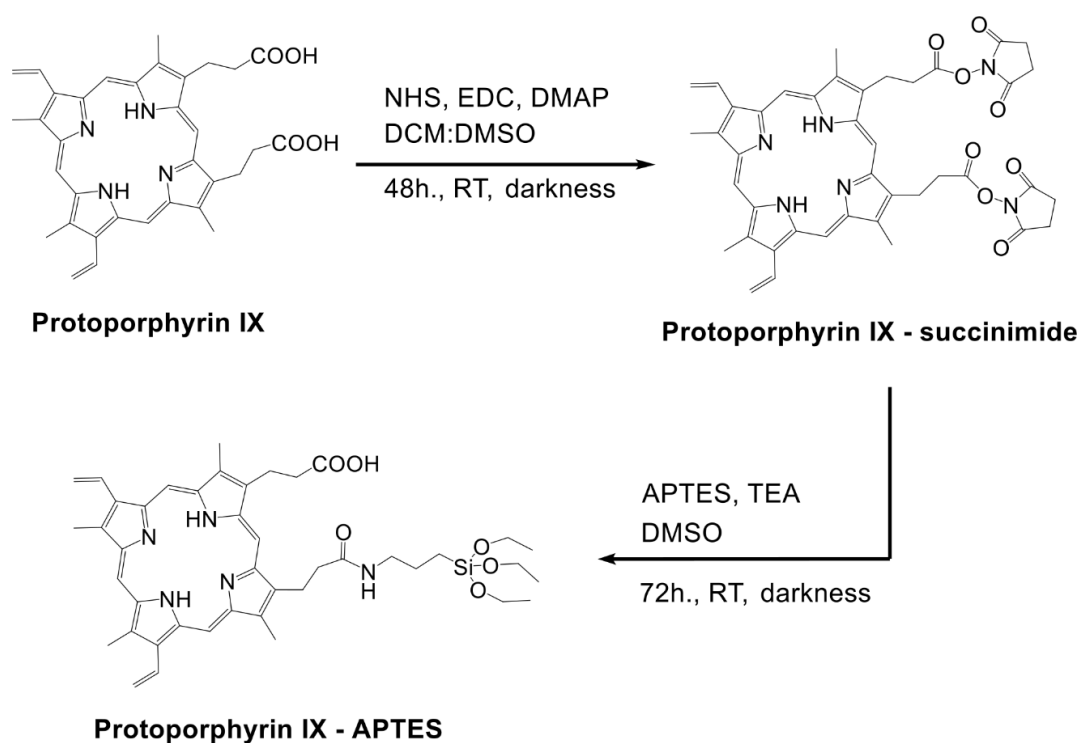


Figure 3.6. Preparation of the APTES-PPIX moiety by a two-step amide coupling reaction, carried out under inert atmosphere and in the dark. In the first step a carbodiimide and N-Hydroxysuccinimide were used to obtain an intermediate (PPIX-succinimide) that will readily react with a primary amine. In the second step the primary amine in APTES reacts with the succinimide groups to form PPIX-APTES.

3.2.2.2.1 Characterisation of APTES-PPIX

The APTES-PPIX moiety was characterised spectroscopically by FTIR in attenuated total reflectance (ATR) mode and ^1H NMR to confirm the formation of an amide bond between APTES and PPIX. **Figure 3.7** shows the FTIR spectra of APTES-PPIX alongside a standard of PPIX. Three characteristic bands can be observed in the spectrum of APTES-PPIX. The band at 1065 cm^{-1} is characteristic of the Si-O bond from APTES, while the bands at 1550 and 1639 cm^{-1} are the amide I and amide II bands associated with the newly formed amide bond between APTES and PPIX. The intense band at 1733 cm^{-1} in the spectrum of PPIX standard is attributed to the C=O stretches from the carboxyl group. The relative intensity of this band is reduced in the case of APTES-PPIX, compared to the band in the spectrum of PPIX, due to the use of one of the carboxyl groups in the amide coupling. Also, the slight shift to higher wavenumbers can be explained by the change in the surroundings of this carboxyl group.

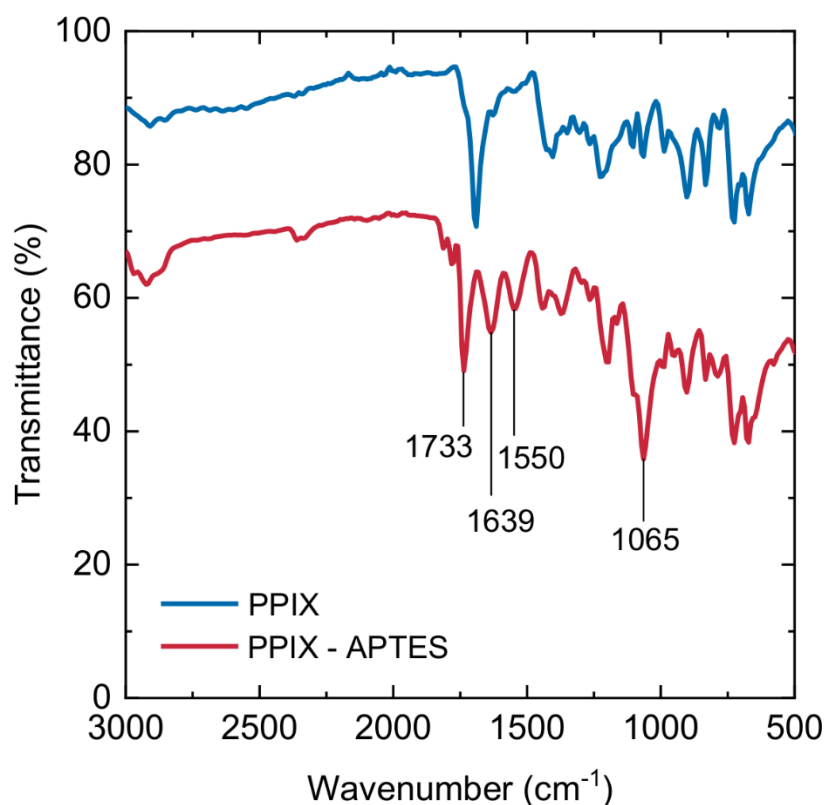


Figure 3.7. FTIR spectra of PPIX and APTES-PPIX. The band at 1065 cm^{-1} corresponds to the Si-O bond in APTES, while the peaks at 1550 and 1639 cm^{-1} are the amide I and amide II bands characteristic of amides. This suggests the successful formation of an amide bond between APTES and PPIX.

^1H NMR spectroscopy (**Figure 3.8**) was carried out in $\text{DMSO-}d_6$ to investigate the structure of the APTES-PPIX product obtained. Here, the double doublets at 6.25-6.5 ppm, the four singlets at 10.30-10.40 ppm, the singlet at -3.80 ppm and the quartet at 8.57 ppm correspond to the contributions of the $\text{CH}_2=$, $-\text{CH}=-$, $-\text{NH}-$, and $=\text{CH}-$ protons from PPIX, respectively, as labelled in the figure. The intense singlet at 3.34 ppm corresponds to the $-\text{CH}_2\text{COOH}$ proton in PPIX. The triplet at 0.89 ppm can be assigned to the contribution from the $-\text{SiOCH}_2\text{CH}_3$ proton in APTES. The multiplet at 3.40-3.46 ppm is attributed to contributions from the $-\text{SiOCH}_2\text{CH}_3$ proton in APTES. Signals from the $-\text{NH}-$ protons in amide groups usually do not couple with neighbouring protons and tend to be difficult to discern when using protic deuterated solvents, as is the case here. Additionally, the signals from the protons on the carbons adjacent to the amide group ($-\text{NHCO-CH}_2-$ and $-\text{CH}_2-\text{NHCO}-$) could not be distinguished from other $-\text{CH}_2-$ protons in this case. The ^1H NMR spectra from APTES and PPIX can be found in the Appendices (**Figures A3.1** and **A3.2**, respectively).

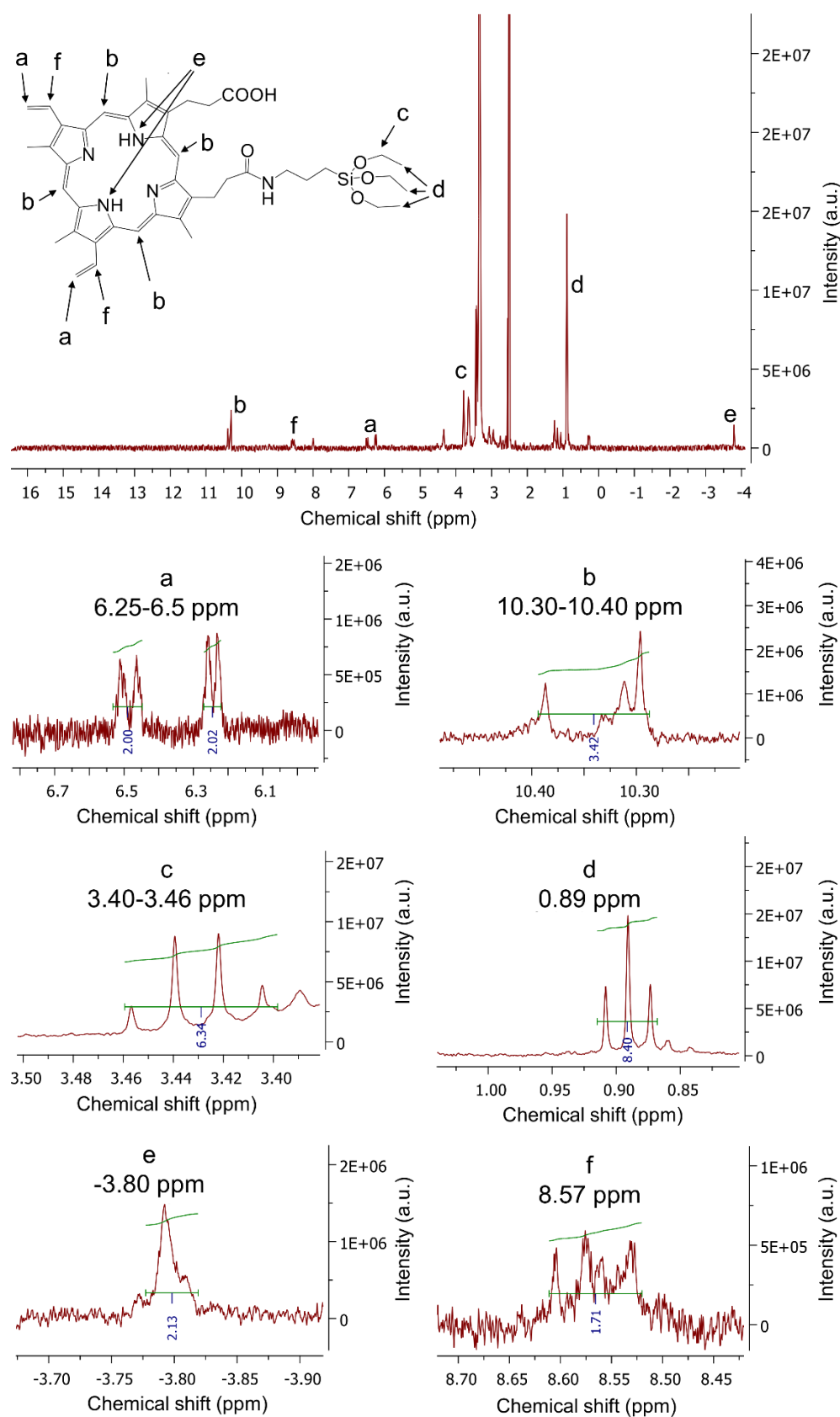


Figure 3.8. ^1H NMR spectra of APTES-PPIX obtained in $\text{DMSO-}d_6$. The signals **a**, **b**, **e** and **f** are contributions from PPIX, as described in the insets. The triplet **d** is attributed to the $-\text{SiOCH}_2\text{CH}_3$ protons in APTES. The multiplet **c** is a contribution from the $-\text{SiOCH}_2\text{CH}_3$ proton.

3.2.2.3 Synthesis of APTES-PEG 200

A similar strategy was followed for linking APTES to PEG 200. In this case a two-step process was performed inspired by the work of How *et al.*¹² In short, an excess of succinic anhydride was added to PEG 200 in the presence of a catalytic amount of 4-dimethylaminopyridine (DMAP) in alkaline conditions to form PEG 200-acid through an esterification reaction. The unreacted succinic anhydride and DMAP were removed by washing with 1 M HCl. The carboxylic groups in PEG 200-acid were activated by EDC, and NHS was added to form a primary amine-specific intermediate. Finally, APTES was added (1.2:1 to PEG 200-acid) to form APTES-PEG 200 *via* an amide coupling reaction. The solution obtained was washed several times with HCl 1 M to reverse the unreacted NHS ester, and the solvent was eliminated under vacuum. In order to avoid the hydrolysis of the ethoxysilane groups in APTES, this process was performed in the absence of water and air, and the product was stored at -20 °C. The details of this procedure are described in Section 2.3.1.2.1. Figure 3.9 depicts a schematic of the reaction.

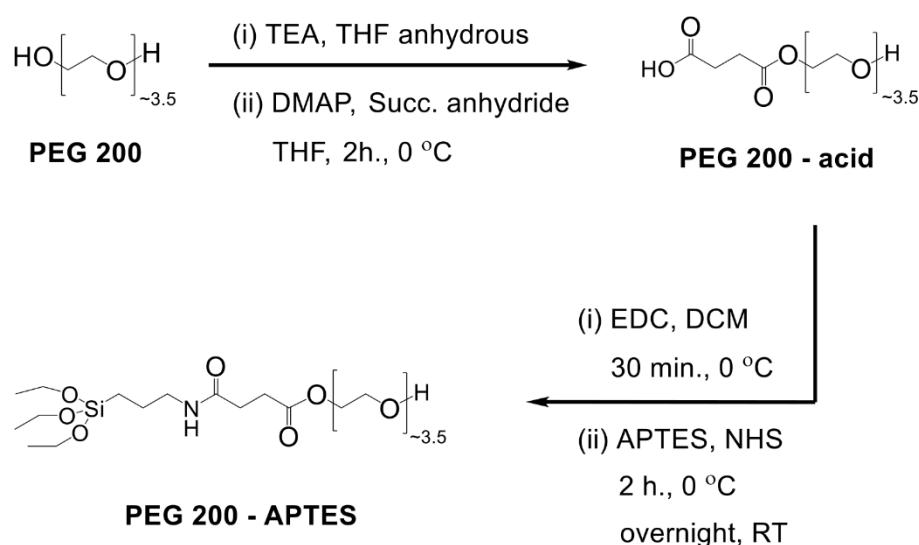


Figure 3.9. Preparation of the APTES-PEG 200 moiety *via* a two-step process under inert atmosphere. First, PEG 200 is reacted with succinic anhydride to form PEG 200-acid in alkaline medium. Then, an amide coupling between the primary amine in APTES and one of the carboxyl groups in PEG 200-acid yields APTES-PEG 200.

3.2.2.3.1 Characterisation of APTES-PEG 200

The FTIR spectrum of the solvent-free APTES-PEG 200 product is shown in **Figure 3.10** alongside a standard of PEG 200. The bands at 1070, 1200 and 1730 cm^{-1} correspond to the O-C-C stretch, the C-C-O stretch and C=O bond from the ester functional group in APTES-PEG 200. The bands at 1544 and 1649 cm^{-1} are the amide I and amide II bands corresponding to the C=O and C-N bonds resulting from the amide coupling between PEG 200-acid and APTES. The broad band observed at 2800 cm^{-1} may be attributed to aliphatic C-H stretches. Finally, the characteristic band from Si-O vibrations cannot be distinguished from the aforementioned O-C-C stretch band and the C-O stretches from PEG 200 as they are all found in the same region of 1040-1080 cm^{-1} . The signals of ester and amide groups are consistent with the structure of APTES-PEG 200.

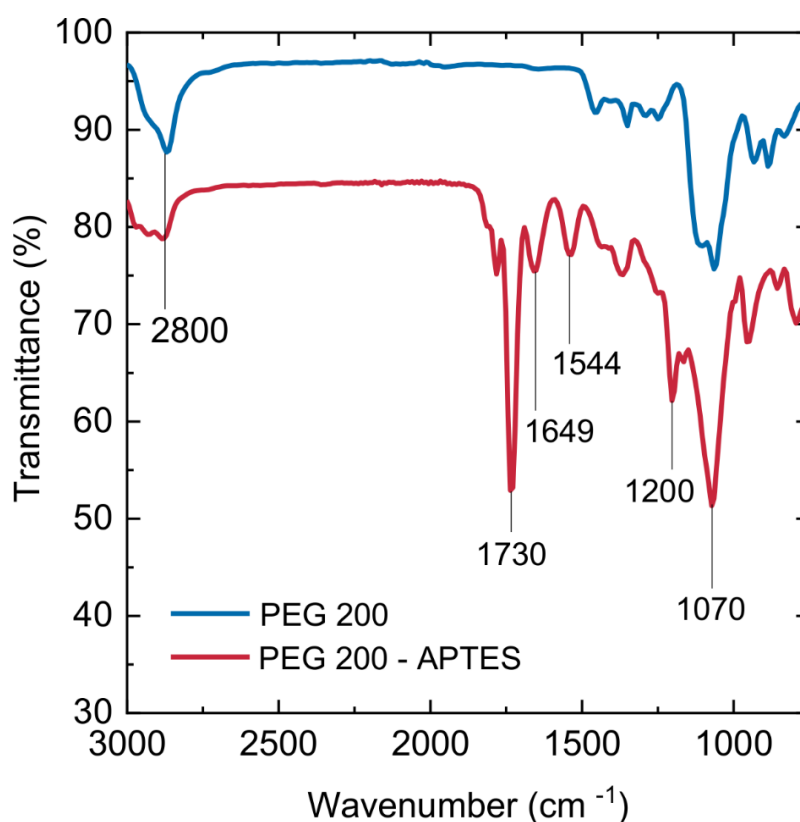


Figure 3.10. FTIR spectra of APTES-PEG 200 and a PEG 200 standard. The signals at 1070, 1200, and 1730 cm^{-1} can be attributed to the O-C-C stretch, the C-C-O stretch and the C=O stretch from the ester group. The band at 2800 cm^{-1} corresponds to aliphatic C-H stretches. The bands at 1544 and 1649 cm^{-1} are the amide I and amide II bands from the amide bond between APTES and PEG 200. The expected peak from Si-O in APTES is likely to be overlapped by the O-C-C and C-O stretches around 1070 cm^{-1} .

The prepared APTES-PEG 200 was analysed by ^1H NMR spectroscopy in CDCl_3 . The spectrum obtained is shown in **Figure 3.11**. The broad peak at 3.67 ppm is attributed to the contribution of the $-\text{[O-CH}_2\text{-CH}_2\text{]-}$ protons, and is the fingerprint of polyethylene glycols.¹³ The signals at 4.27 and 2.85 ppm may be attributed to the $-\text{COO-CH}_2\text{-}$ and $-\text{CH}_2\text{-COOH}$ protons, respectively. The intense signal at 1.23 ppm corresponds to the contribution of the $-\text{SiOCH}_2\text{CH}_3$ protons in APTES. Finally, the triplet at 2.71 ppm and the multiplet at 2.46 ppm are contributions from the $-\text{NHCO-CH}_2\text{-}$ and in $-\text{CH}_2\text{-NHCO-}$ protons, respectively, indicative of the presence of an amide bond. The ^1H NMR spectra from APTES and PEG 200 can be found in the Appendices (**Figures A3.1** and **A3.3**, respectively).

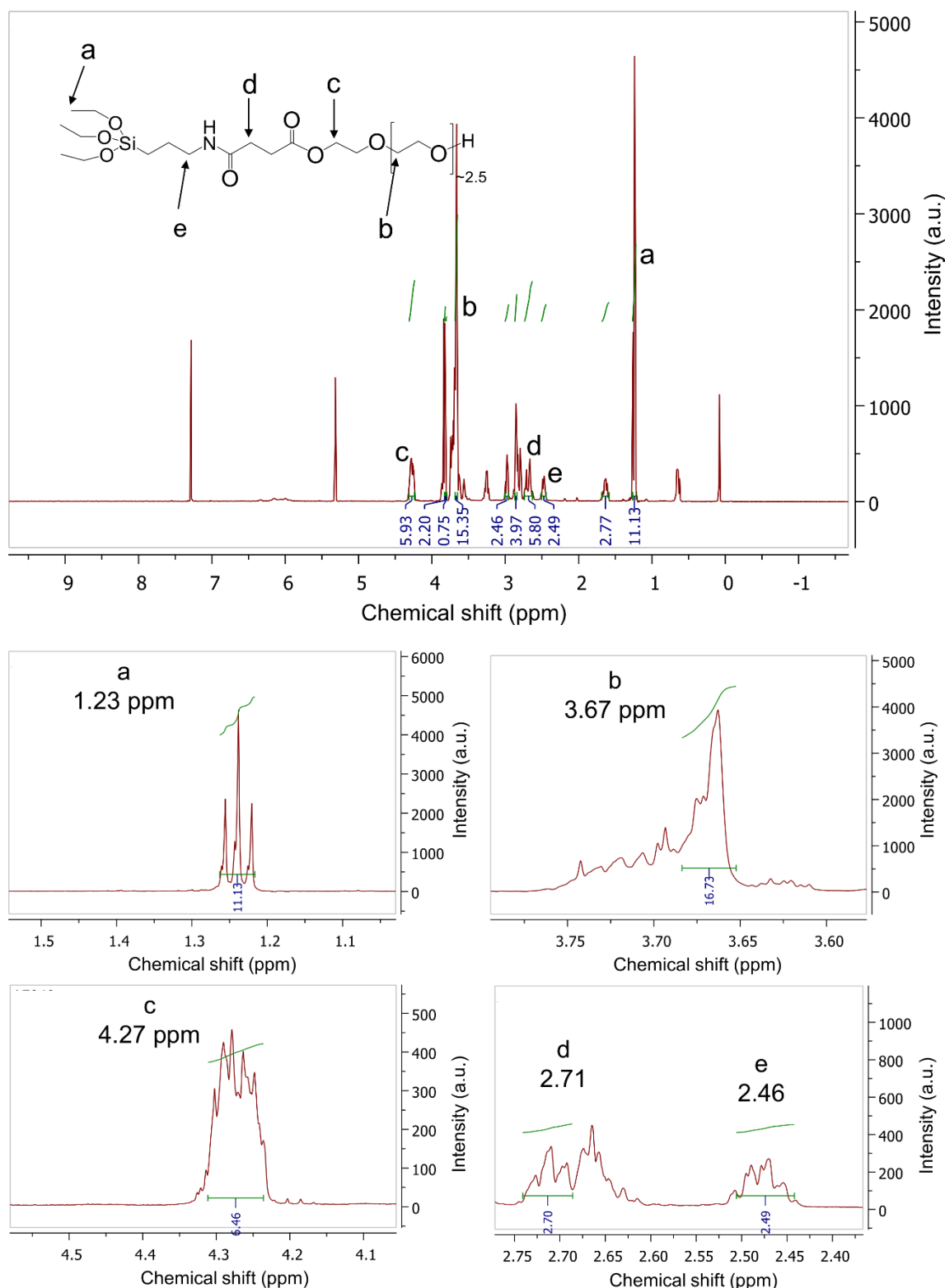


Figure 3.11. ^1H NMR spectrum from the synthesised APTES-PEG 200 obtained in CDCl_3 . The signals c is characteristic from $[\text{O}-\text{CH}_2-\text{CH}_2]$ - protons in the polyethylene glycol structure. Signals b and d correspond to contributions from the protons in in $-\text{COO}-\text{CH}_2-$ and CH_2-COOH , respectively. The peak a is attributed to the protons in $-\text{SiOCH}_2\text{CH}_3$, characteristic of APTES. The signals e and f result from the contribution of the $-\text{NHCO}-\text{CH}_2-$ and $-\text{CH}_2-\text{NHCO}-$ protons, respectively, and indicate the presence of an amide bond between APTES and PEG 200.

3.2.3 Coating magnetic nanoparticles with APTES-PPIX and APTES-PEG 200

Finally, the magnetite nanoparticles were coated with the previously synthesised APTES-PPIX and APTES-PEG 200. For this, the magnetite nanoparticles prepared by the MW co-precipitation method were used. The attachment of these moieties was achieved through the formation of covalent bonds between the hydroxyl groups, naturally present on the surface of iron oxide nanoparticles, and the siloxane groups present in APTES. APTES-PPIX was thoroughly dissolved in DMSO/EtOH (4:5), APTES-PEG 200 was dissolved in EtOH, and both solutions were added to a suspension of magnetite nanoparticles in ethanol. The reaction mixture was stirred for 48 hours at room temperature and in the dark, to avoid the degradation of the PPIX. This procedure is detailed in **Section 2.3.1.2.1**. **Figure 3.12** shows a schematic of the functionalisation process and the resulting nanocomposite.

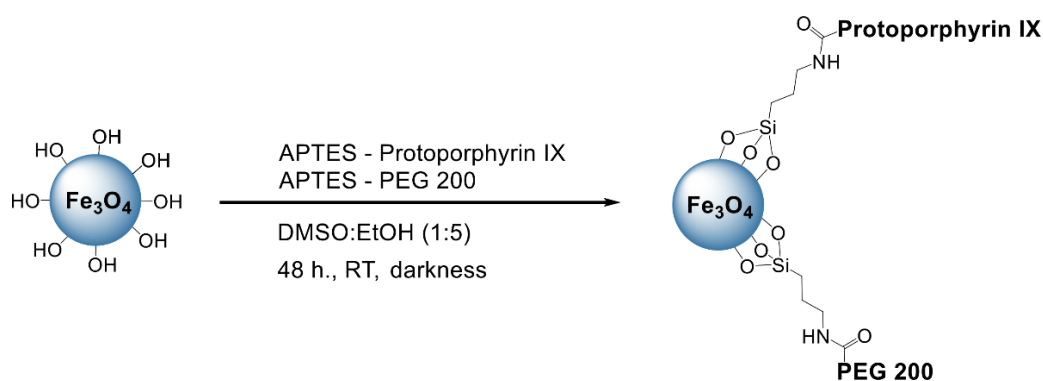


Figure 3.12. Coating of magnetite nanoparticles with APTES-PPIX and APTES-PEG 200, synthesised previously. Magnetite nanoparticles were dispersed in ethanol with the help of ultrasounds. Solutions of APTES-PPIX and APTES-PEG 200 were added to the nanoparticles dispersion, and reacted in the dark and at room temperature for 48 hours.

3.2.3.1 Characterisation of the nanocomposite Fe₃O₄-APTES-PEG 200/PPIX

FTIR spectroscopic studies of the iron oxide nanoparticles were performed before and after the coating stage, and the spectra obtained are shown in **Figure 3.13**. Magnetite shows one intense stretch at 550 cm⁻¹ corresponding to the Fe-O bond. In the spectrum of the nanocomposite, the vibrations at 1389 and 1730 cm⁻¹ correspond to the C-O stretch from the ester in PEG 200 and the carboxylic C=O stretch in PPIX and PEG 200, respectively. The band observed at 1070 cm⁻¹ is attributed to the Si-O bond in APTES. The stretches at 1545 and 1630 cm⁻¹ are the amide I and amide II bands, associated with the

C=O stretching vibration and the N-H bending, respectively, from the amide groups in APTES-PPIX and APTES-PEG 200.

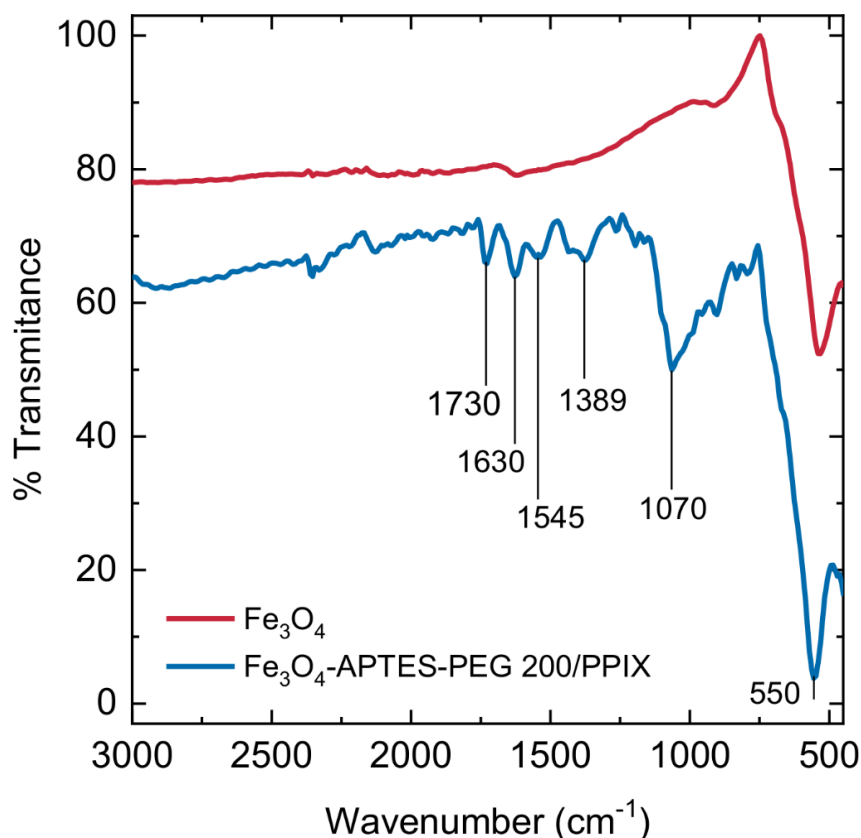


Figure 3.13. FTIR spectra of (red) bare Fe₃O₄ nanoparticles and (blue) iron Fe₃O₄ nanoparticles functionalised with APTES-PEG 200 and APTES-PPIX. The intense stretch at 550 cm⁻¹ is due to the Fe-O bond, and the broad band at 1070 cm⁻¹ is associated to the Si-O bond in APTES. The bands at 1389 and 1730 cm⁻¹ correspond to the C-O stretch from the ester in PEG 200, and the C=O stretch associated with PPIX and PEG 200. The stretches at 1545 and 1630 cm⁻¹ are the amide I (C=O) and amide II (C-N) bands from the amide in the APTES-PPIX and APTES-PEG 200 moieties.

The nanocomposite was also studied by UV-visible and fluorescence spectroscopy to investigate the optical properties the APTES-PPIX moiety immobilised onto the iron oxide nanoparticles. **Figure 3.14** shows the absorbance and emission spectra of an ethanolic suspension (0.33 mg/mL) of the nanocomposite, alongside a PPIX standard in ethanol. The absorbance peak of the magnetite nanoparticles coated in PPIX at 404 nm shows an intense inclined background, which is caused by the scattering of the light by the nanoparticles in suspension. The emission spectra were obtained from an excitation wavelength of 404 nm. The intense emission band of the nanocomposite at 632 nm

indicates that the PPIX retains its fluorescence after being attached onto the magnetite nanoparticles.

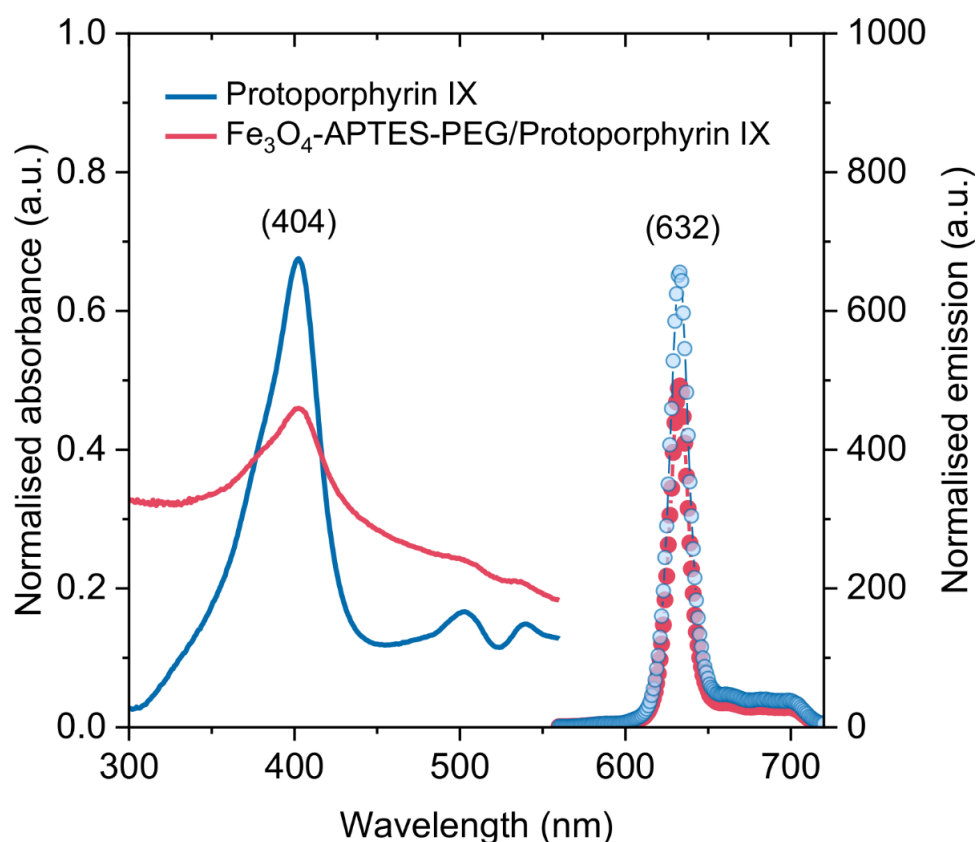


Figure 3.14. Absorbance and emission spectra of a colloidal suspension of PPIX-coated magnetite nanoparticles (0.33 mg/mL in ethanol) and a PPIX standard. The absorbance band at 404 nm confirms the presence of PPIX attached onto the iron oxide nanoparticles. The emission band at 632 nm ($\lambda_{exc}=404$ nm) also indicates that optical properties of the PPIX contained in the nanocomposite have been preserved, and its fluorescence has not been quenched.

Thermal gravimetric analyses (TGA) were performed to assess the organic content in the nanocomposite. Samples were analysed at temperature ramps of 10 °C/minute under nitrogen. **Figure 3.15** shows the thermogravimetric curves for bare magnetite nanoparticles and magnetite coated with APTES-PEG 200 and APTES-PPIX. The initial increase in mass of the bare magnetite can be explained by a brief initial oxidation of the Fe (III) in magnetite, followed by a slight mass loss due to physisorbed water molecules on the iron oxide surface. The curve corresponding to the nanocomposite shows a pronounced mass loss of about 30 % from 250 °C, which is associated to the presence of

organic species attached onto the surface the magnetic nanoparticles. This is indicative of an effective coating process, with a high density of functionalities per surface unit.

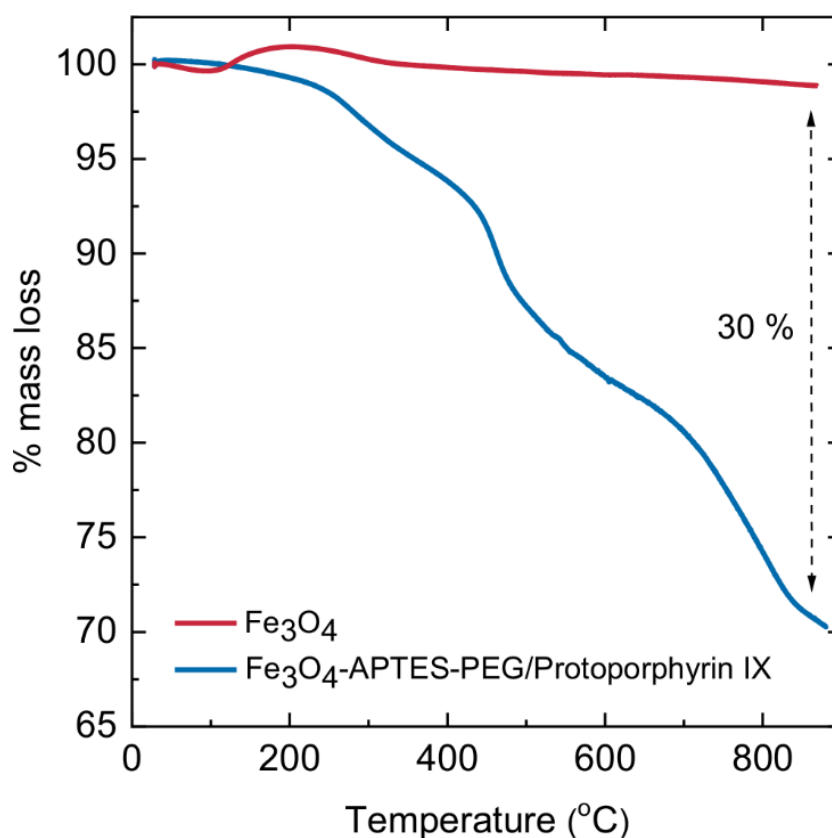


Figure 3.15. TGA curves of the bare iron oxide nanoparticles and the nanoparticles coated with APTES-PPIX and APTES-PEG 200. The marked mass loss of the nanocomposite of about 30 % confirms the presence of an organic coating attached to the magnetic cores.

Finally, the functionalised nanoparticles were studied once again by means of powder XRD to ensure the crystallinity of the magnetic cores was not affected by the functionalisation process. The diffraction patterns obtained from the dry precipitate of the nanocomposite matched the standard of cubic spinel magnetite (Fe₃O₄, JCPDS index card no. 19-629). This confirms that the Fe₃O₄ did not undergo any oxidation process during the functionalisation stage. The intense background observed on the diffraction pattern of the functionalised magnetite nanoparticles is associated with the amorphous nature of the coating. **Figure 3.16** shows the diffraction patterns obtained from bare magnetite nanoparticles and functionalised magnetite, alongside with the ICSD standard for Fe₃O₄. The average crystallite sizes for Fe₃O₄ nanoparticles functionalised with the APTES-PPIX and APTES-PEG 200 was estimated from the Scherrer equation applied to the

(311) diffraction peak. The results obtained are compared to the values for Fe_3O_4 synthesised by MW co-precipitation, and are shown in **Table 3.3**. These indicate that there is no significant variation of the crystallite size of the Fe_3O_4 nanoparticles before (16 nm) and after (17 nm) the functionalisation stage.

Table 3.3. Average crystallite sizes for magnetite nanoparticles synthesised by MW co-precipitation, and for magnetite functionalised with APTES-PPIX and APTES-PEG 200, estimated with the Scherrer equation.

Sample	Size (nm)
Bare Fe_3O_4	16
PEG 200/PPIX coated Fe_3O_4	17

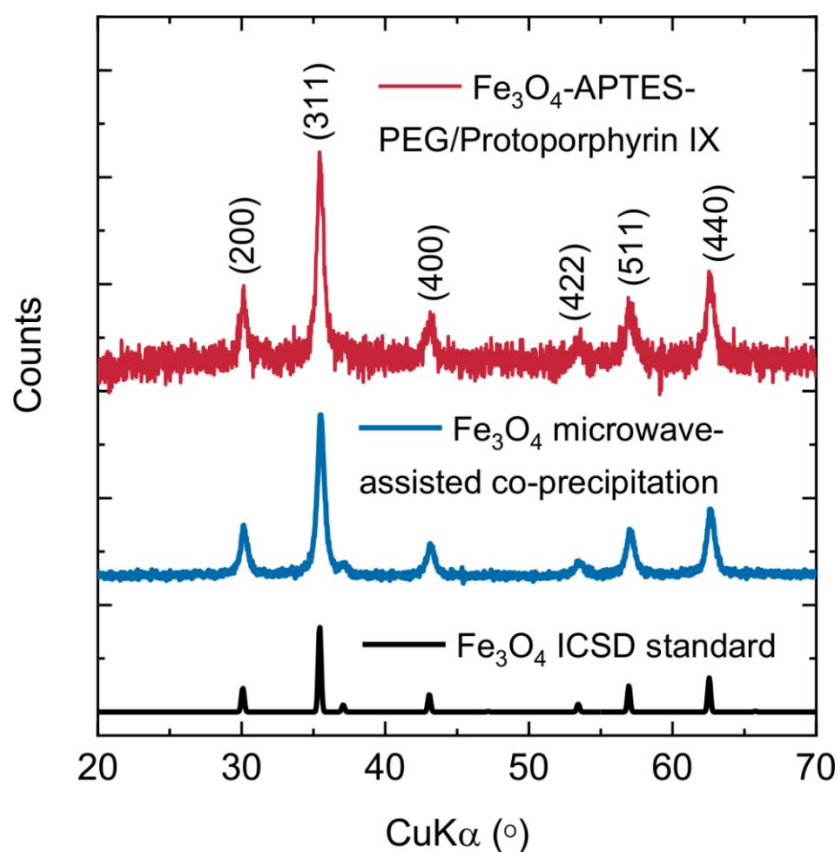


Figure 3.16. Powder XRD patterns of bare magnetite and magnetite coated with APTES-PPIX and APTES-PEG 200. **Red:** Fe_3O_4 functionalised with APTES-PPIX and APTES-PEG 200; **Blue:** bare Fe_3O_4 synthesised by MW co-precipitation; **Black:** ICSD standard of Fe_3O_4 (cubic inverse spinel, space group: $Fd\bar{3}m$)

3.2.4 Application of Fe₃O₄-APTES-PEG 200/PPIX for iron chelation

The iron chelating properties of the prepared nanocomposite were investigated against solutions of iron salts to determine whether the PPIX immobilised onto the magnetic nanoparticles was able to complex iron from aqueous solutions. This was designed as a proof-of-concept experiment as the eventual aim is to use such a nanocomposite to remove the iron ions from *Mary Rose* timbers which catalyse the formation of harmful acidic species. A series of UV-vis and atomic absorption spectroscopy (AAS) measurements were performed of ethanolic and aqueous solutions of various hydrated iron salts. UV-vis spectroscopy measurements were carried out in ethanolic solutions of FeCl₃·6H₂O. It was decided to use this salt and solvent as this combination provided the best absorbance. For AAS studies, water was used as a solvent due to instrument requirements. In this case, FeSO₄·7H₂O was found to dissolve better in water than other iron salts.

3.2.4.1 Evaluation of iron sequestration in aqueous solution

The ability of the nanocomposite to chelate iron ions in solution was studied by UV-visible spectroscopy. For this, 20 μL additions of an ethanolic suspension of the nanocomposite (0.6 mg/mL) were added in 10-minute intervals to an ethanolic solution of FeCl₃·6H₂O (0.2 mM, 2.5 mL). The magnetic nanocomposite was magnetically decanted for 5 minutes, and an absorption spectrum from the Fe (III) solution was recorded. **Figure 3.17 (A)** shows the decreasing absorption of a FeCl₃·6H₂O solution upon treatment with the magnetic nanocomposite. **Figure 3.17 (B)** shows the decrease in absorption intensity, with the number of additions of nanocomposite, recorded at 246 nm. This indicates a decrease in concentration of free Fe (III), further evidence that the iron chelating properties of the PPIX have been preserved once attached onto the magnetite nanoparticles.

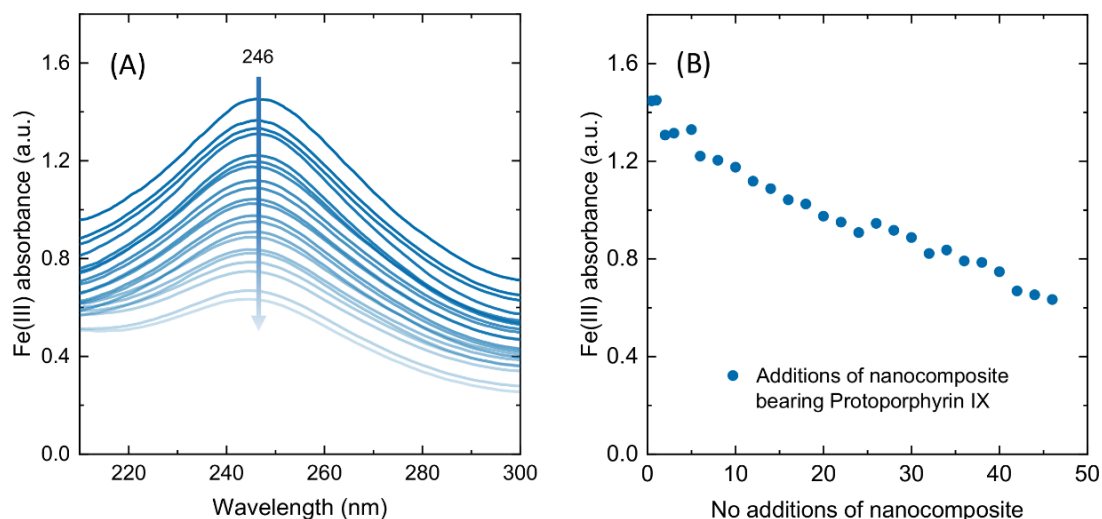


Figure 3.17. UV-vis spectroscopic studies of an ethanolic solution of $\text{FeCl}_3 \cdot 6\text{H}_2\text{O}$ (0.2 mM) treated with the nanocomposite (0.6 mg/mL, additions of 20 μL) to assess the chelation properties of the later. **(A)** Absorption spectra from an Fe (III) solution treated with the nanocomposite were recorded showing a progressive decrease in absorbance upon increase of nanocomposite concentration. **(B)** Absorption intensity of an ethanolic solution of Fe(III) recorded at 246 nm. The decrease of intensity upon addition of the nanocomposite indicates a decrease in the concentration of free Fe(III) due to the formation of the complex Fe-PPIX.

The iron uptake was also studied in solution by AAS. An aqueous solution of $\text{FeSO}_4 \cdot 7\text{H}_2\text{O}$ (0.048 mM) was treated once with the nanocomposite (0.6 mg/mL in the final solution) and stirred vigorously. Samples were taken periodically and, after magnetic decantation, the content of Fe(II) was determined by AAS. **Figure 3.18** shows the variation in concentration of Fe(II), initially 2.7 mg/L, over time during the treatment with the nanocomposite. A rapid decrease in the concentration of free Fe(II) during the first 6-7 hours was followed by a relatively stable plateau. This study shows that up to 85 % of the Fe(II) in aqueous solution, under these conditions, was chelated by the PPIX in the nanocomposite.

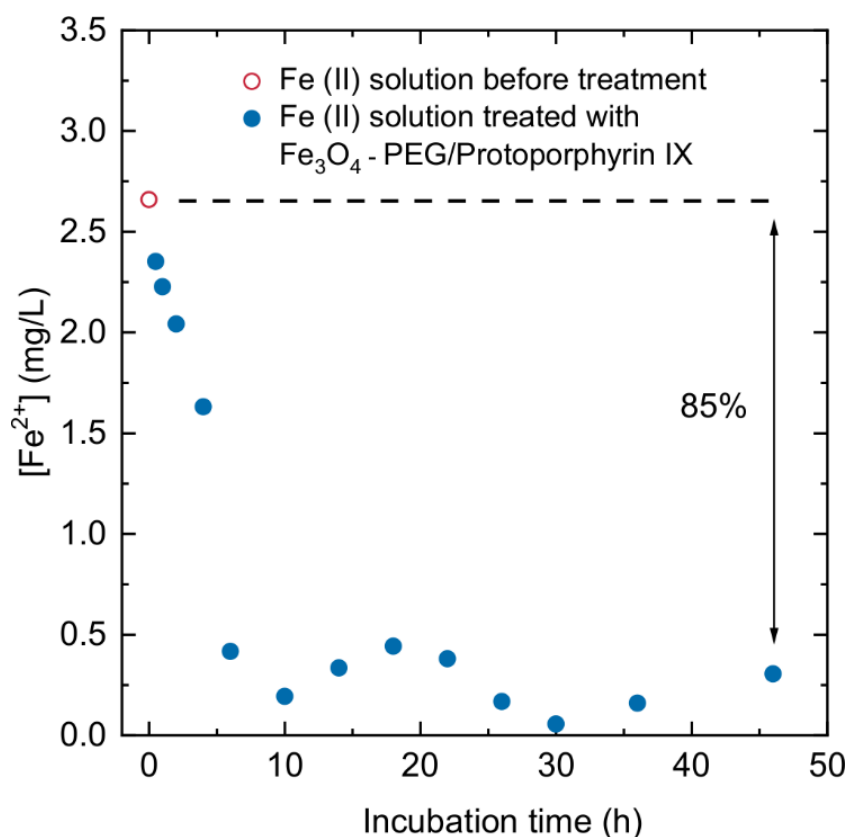


Figure 3.18. Variation of free Fe(II) in aqueous solution with time upon treatment with the magnetic nanocomposite, measured with atomic absorption spectroscopy. The treatment with the nanocomposite bearing PPIX was able to chelate up to 85 % of free iron from a solution in 6-7 hours.

3.3 Conclusions

In this chapter, the synthesis and characterisation of a magnetic nanocomposite based on magnetite nanoparticles functionalised with PEG 200 and PPIX have been described. Magnetite nanoparticles have been prepared following a microwave-assisted co-precipitation method, which yielded highly crystalline single phase (observed by powder XRD) Fe₃O₄ nanoparticles, with an average particle size of 14.60 nm and a polydispersity index (PDI) of 0.21. This synthetic approach shows an improvement in the polydispersity of the samples compared to the standard co-precipitation method, which yielded a PDI of 0.33.

APTES-PPIX and APTES-PEG 200 have been prepared and studied with a full range of characterisation techniques. The amide bonds formed between APTES and PEG 200, and

APTES and PPIX have been characterised by FTIR and ^1H NMR spectroscopies. The amide I and amide II bands observed in the region of $1540 - 1650\text{ cm}^{-1}$ in FTIR indicate the presence of an amide bond in both APTES-PPIX and APTES-PEG 200. ^1H NMR spectroscopy of APTES-PPIX revealed the fingerprint of both precursors, but the signals for the amide proton (-NH-) or the protons on the C_α (-NHCO-CH₂- and -CH₂-NHCO-) could not be observed. In the case of APTES-PEG 200, the ^1H NMR spectrum also shows a triplet system at 2.71 ppm and a multiplet at 2.46 ppm that can be assigned to contributions from the -NHCO-CH₂- and -CH₂-NHCO- protons, respectively.

These moieties have been successfully attached onto the surface of the magnetite nanoparticles by means of covalent bonds between the hydroxyl groups on the iron oxide surface and the siloxane groups in APTES. UV-vis spectroscopic studies of the nanocomposite revealed an absorbance peak at 404 nm and a corresponding emission band at 632 nm, proving the presence of PPIX onto the magnetic nanoparticles. As discussed previously, fluorescent species can suffer from quenching when anchored to a magnetic core due to a charge transfer process with the unpaired spin on the paramagnetic Fe(II) ions.¹⁴ This phenomenon is commonly avoided by coating the magnetic nanoparticle prior to the addition of the fluorescent species, or by introducing a molecular spacer between the particle and the fluorophore.^{15,16} In this work, the results indicate that the use of a spacer (APTES) has minimised the quenching of the PPIX, as the magnetic nanocomposite is active in Fluorescence spectroscopy. FTIR spectroscopy also confirms the amide bond formation in this nanocomposite, as well as the presence of PPIX and PEG 200 stretches. The formation of a coating on the surface of the particles is further confirmed by TGA, where a mass loss of 30 % is observed for the nanocomposite (compared with a ca. 2 % loss for bare nanoparticles) when heated to 850 °C.

Finally, the chelating properties of the nanocomposite were evaluated by UV-vis spectroscopy and atomic absorption spectroscopy and demonstrate the uptake of free iron (II) and iron (III) ions by the nanocomposite, respectively. The tests carried out to evaluate the chelating performance of the multifunctional nanocomposite are not intended to be quantitative. Rather they indicate the suitability of systems of this type for the uptake of iron ions, which demonstrates their potential as a targeted treatment for waterlogged archaeological wood samples such as those obtained from the hull of the *Mary Rose*.

The magnetic nature of this nanocomposite offers possibilities beyond current state-of-the-art conservation treatments where consolidants are applied to the wood and remain there after the treatment has ended. This nanocomposite is capable of sequestering iron ions, whose presence in archaeological wood has been proven to be

harmful; its magnetic nature provides a simple and practical way for their application into archaeological artefacts; the presence of the polyethylene glycol moiety may favour the diffusion of the nanocomposites through the wood structure. This nanocomposite is, therefore, a proof of concept to demonstrate the feasibility of a multifunctional tool that can be of great utility in the conservation of archaeological wooden artefacts. It can be considered the starting point of a new type of functional materials, highly tuneable to suit the necessities of final specific applications.

References

- 1 M. Jones and Mary Rose Trust, *For future generations: conservation of a Tudor maritime collection*, Mary Rose Trust, 2003.
- 2 E. Hocker, G. Almkvist and M. Sahlstedt, *J. Cult. Herit.* **13S**, 2012, 175-182.
- 3 M. Ma, Y. Zhang, W. Yu, H. Shen, H. Zheng and N. Gu, *Colloids Surfaces A Physicochem. Eng. Asp.*, 2003, **212**, 219-226.
- 4 M. J. Williams, E. Sánchez-Pérez, E. R. Aluri, F. J. Douglas, D. A. Maclaren, O. M. Collins, E. J. Cussen, J. D. Budge, L. C. Sanders, M. Michaelis, C. M. Smales, J. Cinatl, S. Lorrio, D. Krueger, R. T. M. De Rosales and S. A. Corr, *RSC Adv.*, 2016, **6**, 83520-83528.
- 5 S. A. McCarthy, G. L. Davies and Y. K. Gun'ko, *Nat. Protoc.*, 2012, **7**, 1667-1693.
- 6 A. L. Patterson, *Phys. Rev.*, 1939, **56**, 978-982.
- 7 H.-U. Worm, *Geophys. J. Int.*, 1998, **133**, 201-206.
- 8 C. T. Yavuz, J. T. Mayo, W. W. Yu, A. Prakash, J. C. Falkner, S. Yean, L. Cong, H. J. Shipley, A. Kan, M. Tomson, D. Natelson and V. L. Colvin, *Science*, 2006, **314**, 964-7.
- 9 Q. Li, C. W. Kartikowati, S. Horie, T. Ogi, T. Iwaki and K. Okuyama, *Sci. Rep.*, 2017, **7**, 9894.
- 10 B. Feng, R. Y. Hong, L. S. Wang, L. Guo, H. Z. Li, J. Ding, Y. Zheng and D. G. Wei, *Colloids Surfaces A Physicochem. Eng. Asp.*, 2008, **328**, 52-59.
- 11 J. L. Vivero-Escoto and D. L. Vega, *RSC Adv.*, 2014, **4**, 14400-14407.
- 12 S. Hou, L. K. McCauley and P. X. Ma, *Macromol. Biosci.*, 2007, **7**, 620-628.
- 13 J. M. Dust, Z.-H. Fang and J. M. Harris, *Macromolecules*, 1990, **23**, 3742-3746.
- 14 S. K. Mandal, N. Lequeux, B. Rotenberg, M. Tramier, J. Fattaccioli, J. Bibette and B. Dubertret, *Langmuir*, 2005, **21**, 4175-4179.
- 15 S. A. Corr, Y. P. Rakovich and Y. K. Gun'ko, *Nanoscale Res. Lett.*, 2008, **3**, 87-104.
- 16 S. A. Corr, A. O' Byrne, Y. K. Gun'ko, S. Ghosh, D. F. Brougham, S. Mitchell, Y. Volkov and A. Prina-Mello, *Chem. Commun.*, 2006, **0**, 4474.

Chapter 4 - Thermoresponsive magnetic nanocomposite for marine archaeological wood conservation

4.1 Application of Fe_3O_4 -APTES-PEG 200/PPIX nanocomposite on test wood samples

Mary Rose wood represents a highly heterogeneous system, with open vessels that could provide channels for the delivery of magnetic nanoparticles loaded with a treatment agent for the removal of potentially harmful iron ions. The magnetic nature of magnetite nanoparticles has indeed been exploited for use as drug delivery agents previously.^{1,2} To examine this opportunity in further detail, samples of *Mary Rose* timbers were taken to the I15 beamline at the ESRF for absorption tomography imaging, a non-destructive technique which allows imaging of the internal wood structure. **Figure 4.1** shows X-ray absorption tomography images obtained from (A) fresh oak, (B) and (C) wood samples from the *Mary Rose*. The fresh oak shows large vessels separated by thin walls, with denser areas where vessels are smaller. The archaeological wood in (B) and (C) shows a clear degree of degradation, where the rigid walls separating the vessels have broken down. The smaller vessels in denser areas appear to have further collapsed, leaving a less ordered and compact structure. This suggests that the functionalised nanoparticles should diffuse into the structure of degraded archaeological wood compared to fresh oak.

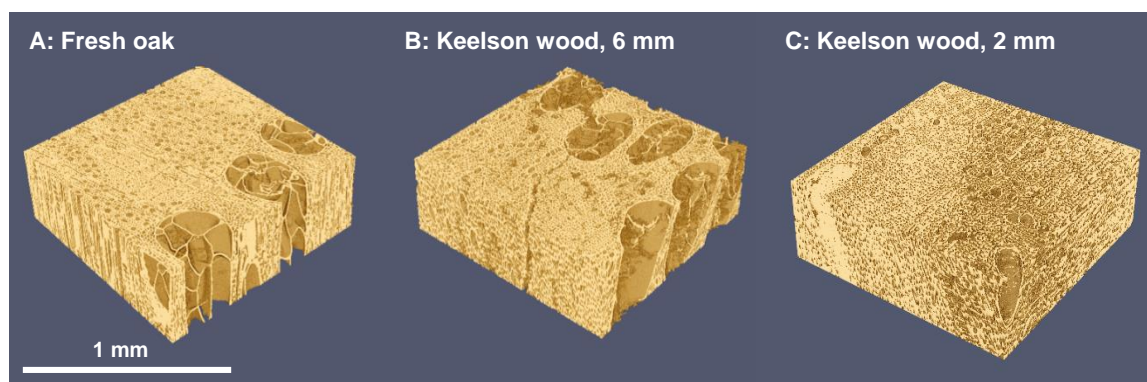


Figure 4.1. X-ray absorption tomography data for (A) fresh oak, cut across the grain of the wood; *Mary Rose* wood (B) 6 mm into the keelson plan and (C) 2 mm into the keelson wood (data collected by collaborator Prof. Kirsten M. Ø. Jensen). Image (A) displays large vessels separated by walls, and a denser area with smaller vessels. Images of degraded wood from the *Mary Rose* (B) and (C) show an increased amount of voids caused by the collapse of vessel walls.

The diffusion of bare and PPIX/PEG 200-functionalised magnetite nanoparticles in fresh wood was investigated under the influence of an applied external magnetic field. Aqueous suspensions (0.6 mg/mL) of bare nanoparticles and PPIX/PEG 200-functionalised

nanoparticles were applied to the surface of fresh oak samples with dimensions 1.5 x 1.5 x 1.5 cm. These wood samples were then incubated for 24 hours, in the dark, at room temperature, and under an external magnetic field (1.3 Tesla). Another set of wood samples were treated with the same suspensions, and were incubated in the same conditions but in the absence of a magnetic field. After incubation, the wood samples were sectioned along the wood grain and in the direction of diffusion of the applied suspensions. This procedure is detailed in **Section 2.3.4**. Representative cross sections of these samples were studied by SEM to determine the diffusion depth of the functionalised and bare magnetic nanoparticles under different conditions. **Figure 4.2** shows the backscattered SEM micrographs of fresh oak wood treated with bare Fe₃O₄ nanoparticles and incubated (Figure 4.2a) in the absence and (Figure 4.2b) in the presence of an external magnetic field. It also shows fresh oak wood samples treated with PPIX/PEG 200-functionalised nanoparticles and incubated (Figure 4.2c) in the absence and (Figure 4.2d) in the presence of a magnetic field. The bright areas are where the nanoparticles are in the wood. Figures 4.2a,c reveal that without the application of an external magnetic field, the magnetic materials only diffuse into the wood by less than one millimetre (the apparent diffusion of nanoparticles in Figure 4.2a is due to contamination with the scalpel used for the sectioning). Upon application of an external magnetic field, bare magnetite nanoparticles penetrate the wood by approximately 2.5 mm (Figure 4.2b). Under the same conditions, functionalised magnetic nanoparticles do not penetrate the wood structure as deeply. This may be due to the aggregated nature of these nanoparticles once functionalised. However, diffusion into the wood is observed and it should be noted that greater penetration depth into degraded *Mary Rose* timbers should be expected from absorption tomography observations.

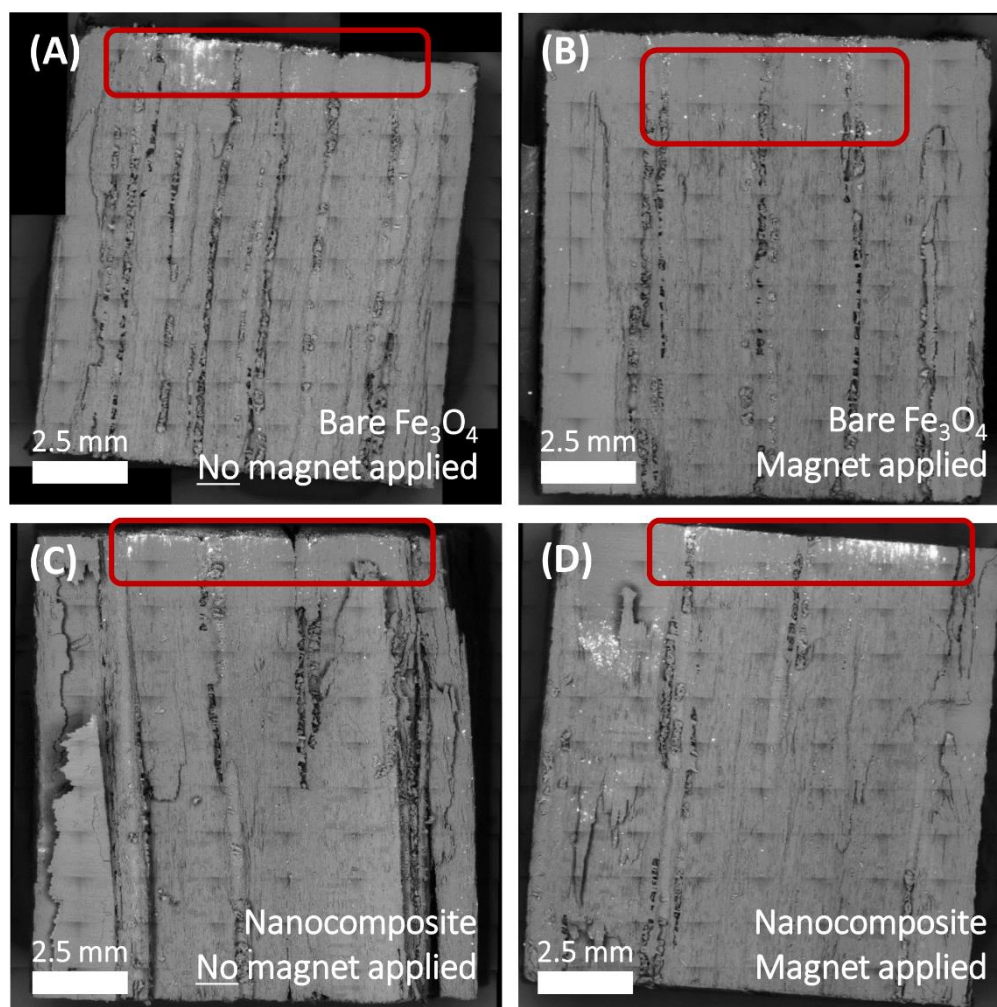


Figure 4.2. Backscattered SEM images of the cross-section of four fresh oak samples treated with 1 mL of an aqueous suspension of (A and B) bare Fe₃O₄ nanoparticles and (B and C) PPIX/PEG 200 - functionalised nanoparticles (0.6 mg/mL). The diffusion of bare and functionalised Fe₃O₄ within the wood structure was studied (A and C) in the absence and (B and D) in the presence of a 1.3 Tesla magnetic field. The bright areas indicate the depth reached by the nanoparticles under different conditions.

With the diffusion of magnetic nanoparticles into fresh oak samples demonstrated through the application of an external magnetic field, it is necessary to consider the most appropriate vector for applying and removing this treatment in a safe manner to artefacts. Embedding the functionalised magnetic nanoparticles in a polymer gel would provide a means for treating archaeological wood with precision and with minimal invasion. Polymer gels also present attractive possibilities in terms of tuning their functionality or employing polymers with additional functionalities, for example thermoresponsiveness. There is also a possibility of covalently attaching the polymer to

the surface of the magnetic nanoparticles, which may also aid in their removal and application to artefact pieces.

4.1.1 Development of a PEG-based thermoresponsive polymer

As the *Mary Rose* has been treated with the polymer PEG for three decades, it would be favourable to employ a polymer gel which contains PEG chains within it. As discussed in **Section 1.2**, the *Mary Rose* and most archaeological wooden findings have been extensively treated with PEGs of different grades. Hence, the use of PEG in the development of novel conservation treatments can guarantee minimal impact to the artefacts upon application and also find use in treatments beyond the *Mary Rose*. Additionally, a polymer capable of changing its physical properties under specific external stimuli could be a great advantage in the application and removal of the designed treatment, particularly where the safe removal of a treatment is paramount. PEG-methacrylate polymers display thermoreversible behaviour with a lower critical solution temperature (LCST), whose values depend on various factors such as molecular weight, concentration, or the chain transfer agent used.^{3,4,5} As discussed in **Section 1.6**, the LCST of copolymers containing PEG methacrylate can be also adjusted by the use of a hydrophobic comonomer. In particular, copolymers based on di(ethylene glycol) methyl ether methacrylate (DEGMA) and the more hydrophobic monomer methyl methacrylate (MMA) have been widely studied, showing narrow temperature windows and easily tuneable LCST.⁶

When p(DEGMA-co-MMA) is cooled below its LCST the DEGMA moieties imbibe water molecules *via* hydrogen bonding increasing the polymer's solubility. This leads to a "liquid-like" state that can facilitate the delivery of magnetic nanoparticles from the gel into the wood structure. When the temperature is raised above the LCST the hydrogen bonds with water molecules are cleaved, and the solubility of the polymer drops. This induces a "gel-like" state, which can facilitate the removal of the treatment by peeling the thermoresponsive nanocomposite off the surface of the wood. Therefore, the potential use of p(DEGMA-co-MMA) to develop a thermoresponsive functional nanocomposite for the removal of harmful substances from archaeological wood was investigated.

4.2 Synthesis and characterisation of thermoresponsive polymer p(DEGMA₄₅-co-MMA₅)

Poly(di(ethylene glycol) methyl ether methacrylate-co-methyl methacrylate), poly(DEGMA₄₅-co-MMA₅) was synthesised by reversible addition-fragmentation chain-transfer (RAFT) polymerisation.^{3,4,7} Ideally, conservation treatments should avoid major changes in temperature, since these could irreversibly damage the wood structure.⁸ Previous work on thermoresponsive polymers has been carried out in the group in search of an optimal LCST for this application. Different DEGMA:MMA molar ratios were explored by Dr Ester Rani Aluri in order to obtain a phase transition temperature close to that at which the *Mary Rose* is currently held (18-20 °C), and a 45:5 molar ratio (DEGMA:MMA) was found to show an optimal temperature window. Thus, in a typical RAFT mediated procedure, the monomers DEGMA and MMA were added to a Schlenk flask in a 45:5 ratio under inert atmosphere. Azobis(isobutyronitrile) (AIBN) and 4-cyano-4-(phenylcarbonothioylthio) pentanoic acid were chosen as initiator and charge transfer agent (CTA), respectively. In RAFT polymerisations, AIBN is commonly used as a radical source to start the reaction. It is a self-decomposing initiator and is often preferred over other initiators (benzoyl peroxide) due to its lower risk of explosion and lower initiation temperature.⁹ 4-cyano-4-(phenylcarbonothioylthio) pentanoic acid is a RAFT agent which provides a high degree of control in radical polymerisation, and is commonly used in the polymerisation of methacrylates. **Figure 4.3** shows a schematic of the reaction to obtain p(DEGMA₄₅-co-MMA₅). More detailed information about this procedure can be found in **Section 2.3.2**.

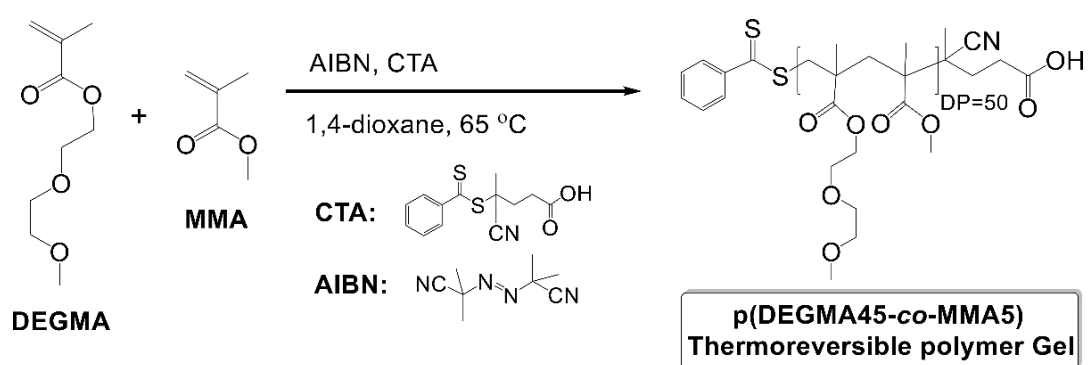


Figure 4.3. Preparation of the thermoresponsive polymer gel p(DEGMA₄₅-co-MMA₅) by RAFT polymerisation. Monomers DEGMA and MMA (45:5 molar ratio) were dissolved in 1,4-dioxane under inert atmosphere. AIBN and the CTA were added to the solution, and this was degassed by 4 freeze-thaw cycles. The mixture was stirred at 65 °C for 8 hours. The reaction was stopped by rapid cooling, the product was dialysed against deionised water for 5 days, and finally freeze dried for 24 hours to eliminate the residual water.

The product obtained was analysed by ^1H NMR and GPC. **Figure 4.4** shows the ^1H NMR spectrum of $p(\text{DEGMA}_{45}\text{-co-MMA}_5)$ carried out in CDCl_3 . The bands at 0.88-1.42 ppm are attributed to the $-\text{CH}_3$ protons in DEGMA and MMA monomers, and the multiplet at 1.81 ppm corresponds to the $-\text{CH}_2-$ protons on the backbone of the polymer. The three bands at 3.56-3.68 ppm correspond to the $-\text{OCH}_2-$ protons in DEGMA, while the intense signal at 3.40 ppm corresponds to the $-\text{OCH}_3$ protons in DEGMA and MMA monomers. The intense band at 4.11 ppm originates from the $-\text{COOCH}_2-$ protons in DEGMA. Finally, the three multiplets between 7.36-7.87 ppm correspond to the $=\text{CH}_2-$ protons in the phenyl end-group.^{4,7}

The integration ratios between the signals for the $=\text{CH}_2-$ protons in the phenyl group end and for the $-\text{CH}_3$ protons in DEGMA and MMA is 1:37, close to the expected value of 1:30. This indicates that the degree of polymerisation obtained is slightly higher than the expected of 50. Further, the degree of polymerisation was estimated by gel permeation chromatography (GPC). This revealed a number average molecular weight (M_n) of 5388 g/mol, a weight average molecular weight (M_w) of 6263 g/mol, and a good polydispersity (M_w/M_n) index of 1.16.

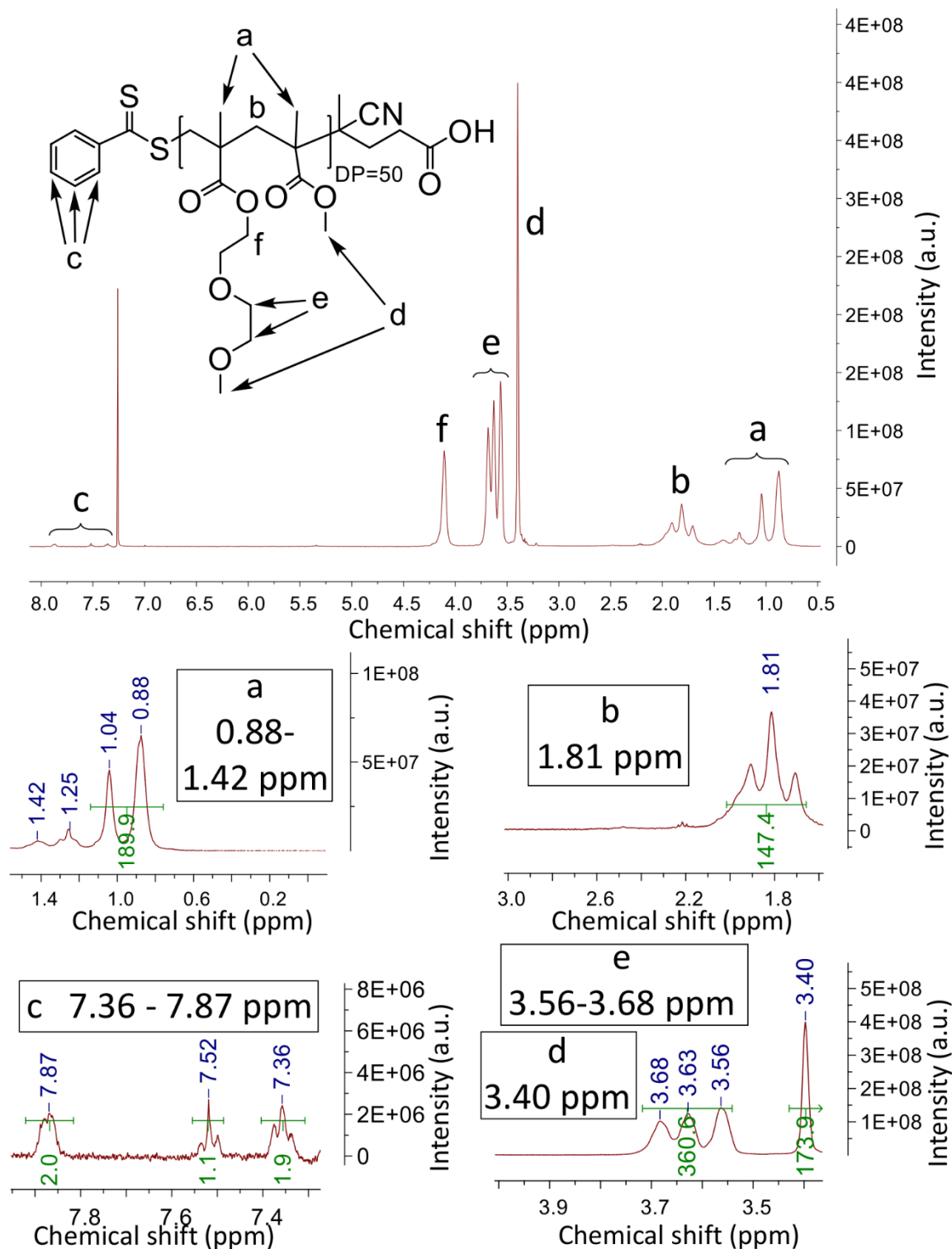


Figure 4.4. ¹H NMR spectrum of p(DEGMA₄₅-co-MMA₅) obtained in CDCl₃. The bands labelled a (0.88-1.42 ppm) and b (1.81 ppm) correspond to the -CH₃ and -CH₂- protons on the backbone of the polymer. The bands e (3.56-3.68 ppm) and d (3.40 ppm) are attributed to the -OCH₃ and -OCH₂- protons in DEGMA and MMA monomers. The triplets at 7.36, 7.52 and 7.87 ppm correspond to the *o*-, *p*- and *m*- =CH- protons, respectively, in the dithiobenzene end-group.

The thermoresponsive polymer was studied by variable-temperature UV-visible spectroscopy in order to determine its LCST. **Figure 4.5** shows the transmittance values obtained from an aqueous solution of p(DEGMA₄₅-co-MMA₅) measured between 10 and 40 °C. The abrupt change in transmittance at 26 °C indicates the LCST for this thermoresponsive polymer. Above the LCST, the polymer chains are able to imbibe water molecules as they become hydrophilic, yielding a clear solution. Upon an increase of the temperature, the polymeric chains become hydrophobic with leads to the water molecules being expelled, yielding a cloudy solution with low optical transmittance. This indicated that the polymer obtained is highly responsive to temperature changes within a narrow range of temperatures.

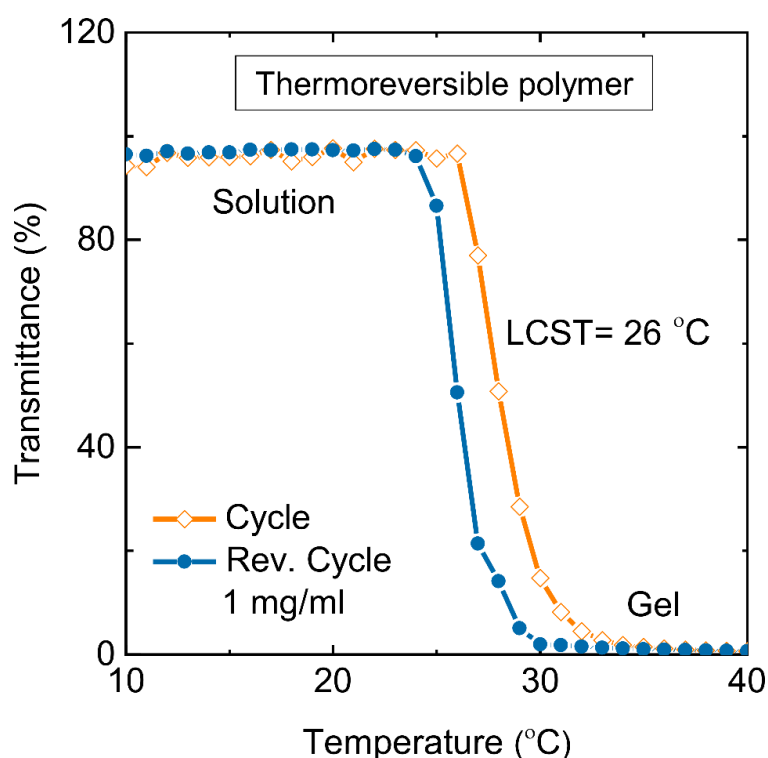


Figure 4.5. Variable-temperature UV-visible spectroscopy of p(DEGMA₄₅-co-MMA₅), showing its thermoresponsive behaviour. The abrupt transition in optical transmittance observed indicates that the value of the LCST is 26 °C. Below this temperature the polymer chains are hydrated and form a clear solution. Above the LCST the polymer chains expel the water molecules as they become gradually more hydrophobic, turning the solution opaque.

4.3 Preparation of polymer-mixed-nanocomposite

For the preparation of the polymer-mixed-nanocomposite, the Fe_3O_4 -APTES-PPIX/PEG 200 nanoparticles were physically mixed with the as synthesised thermoresponsive polymer. For this, p(DEGMA₄₅-co-MMA₅) was dissolved in a small amount of ethanol with the help of ultrasound. The PPIX/PEG 200 functionalised nanoparticles were added to the polymer solution in a 1:5 mass ratio, and this was sonicated until a homogeneous dispersion was obtained (1-2 minutes). The acetone was then removed under vacuum at room temperature for 30 minutes, and the flask was backfilled with argon. The product was stored at 5 °C in the dark to avoid the photodecomposition of the PPIX moieties on the nanoparticles. This procedure is described in detail in **Section 2.3.5**.

4.4 Treatment of artificial archaeological wood with polymer-mixed-nanocomposite and characterisation

4.4.1 Preparation of artificial archaeological wood samples

Artificial archaeological oak samples were prepared to simulate the conditions of archaeological wood in order to perform preliminary studies of iron removal without the need to use wood from the *Mary Rose*. Even though the artificial archaeological wood prepared cannot simulate the level of structural degradation of an archaeological wooden artefact, it is of great use for the study of iron removal from wood. For this, several cubic blocks of fresh oak, of approximately 1.5 cm per side, were soaked in a 100 mM solution of $\text{Fe}_2(\text{SO}_4)_3$ for four weeks, and finally allowed to dry for 3 days. The wood samples soaked in this solution turned into dark blue or black due to the presence of tannins in the wood.

4.4.2 Treatment of artificial archaeological wood with polymer-mixed-nanocomposite

The polymer-mixed-nanocomposite (approximately 20 mg) was applied on aged wood samples and fresh oak samples by cooling it down to 5 °C for 3 hours, and carefully spreading it with a plastic spatula. The wood samples were then placed atop a 1.3 Tesla permanent magnet and incubated at 5 °C for 6 months in the dark. After the incubation period, the wood samples were wrapped in transparent film and the permanent magnet was applied on the opposite direction for one week at 5 °C in the dark. **Figure 4.6** shows (A) a sample of artificial archaeological wood and (B) fresh oak being treated with polymer-mixed-nanocomposite and placed atop a permanent magnet, and (C) the polymer-mixed-nanocomposite removed from the wood after treatment.

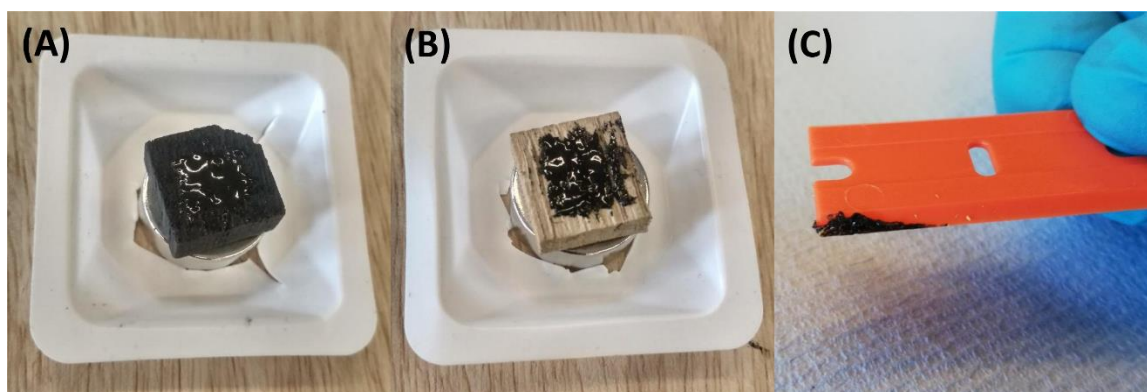


Figure 4.6. Images of (A) artificial archaeological wood and (B) fresh oak being treated with the polymer-mixed-nanocomposite placed onto a 1.3 Tesla permanent magnet. Image (C) shows a plastic spatula containing polymer-mixed-nanocomposite removed after the treatment.

4.4.3 Evaluation of the iron sequestration properties of polymer-mixed-nanocomposite

The capacity to sequester iron ions of the polymer-mixed-nanocomposite was evaluated qualitatively using far-IR spectroscopy. The aim was to detect bands originating from Fe–N vibrations, which would reveal the presence of iron ions chelated by the porphyrin ring. According to literature, signals due to metal–N vibrations can be expected in the lower and far-IR range. Specifically, bands attributed to Fe–N vibrations have been reported in the range $350\text{--}400\text{ cm}^{-1}$ on studying a variety of N-donor ligands. Signals at 390 cm^{-1} have been attributed to symmetric Fe–N vibrations, in Fe-imidazole complexes, by Paulat *et al.*¹⁰ Also, Fe–N vibrations from Fe(III)-octaethylporphyrin have been observed at 386 cm^{-1} by Mitchell *et al.*¹¹ Finally, Dörr *et al.* carried extensive studies on hemin and imidazole, and found bands corresponding to Fe–N vibrations at 350 cm^{-1} in the absence, and at 380 and 396 cm^{-1} in the presence of imidazole.¹² **Figure 4.7** shows the far IR spectra obtained from the polymer-mixed-nanocomposite applied onto (B) artificial archaeological oak and (C) fresh oak. The spectra obtained from (A) the thermoresponsive polymer and (D) the PPIX/PEG 200 functionalised nanoparticles are included for comparison. The broad band at 548 cm^{-1} , present in Figure 4.7d is attributed to the stretches of the Fe–O bond in magnetite, and the band at 438 cm^{-1} is associated with the rotation of the pyrrole ring in the PPIX. The peak at 363 cm^{-1} in Figure 4.7a,b,c could be assigned to the out-of-plane angle bend of the multiple C=O bonds in the thermoresponsive polymer.¹³ Finally, the band at 318 cm^{-1} in Figure 4.7b,c can be assigned

to the stretching of Fe-N₄ in the porphyrin moiety.^{14,15,16} This band is slightly more intense in the polymer-mixed-nanocomposite applied on artificial archaeological wood than in the one applied in fresh oak, suggesting the uptake of iron ions by the porphyrin ring present in the polymer-mixed-nanocomposite.

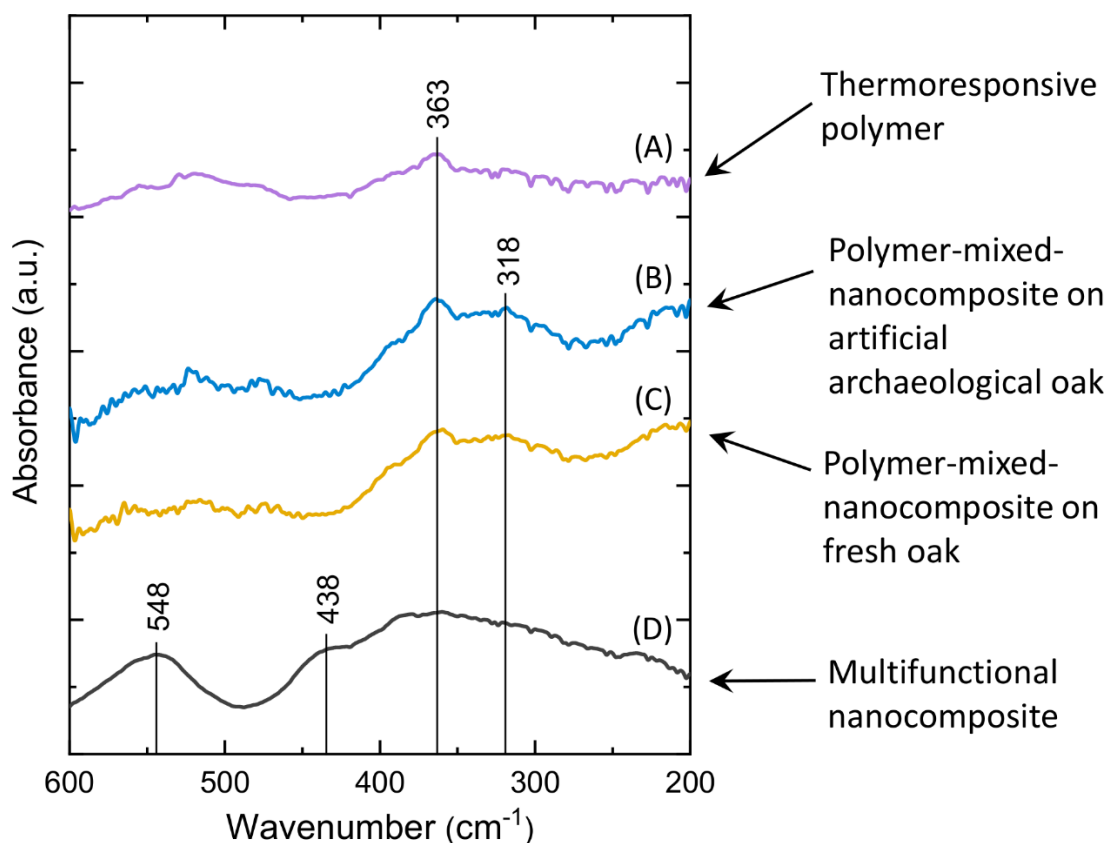


Figure 4.7. Far IR spectroscopy of polymer-mixed-nanocomposite after treating (B) artificial archaeological oak and (C) fresh oak. Also included are the spectra of (A) the thermoresponsive polymer and (D) the PPIX/PEG 200 functionalised nanoparticles. The bands observed at 548 and 438 cm⁻¹ are attributed to the stretches of Fe-O bonds in magnetite and to the rotation of the pyrrole rings in the porphyrin, respectively. The band at 363 cm⁻¹ can be assigned to the oop bending of C=O bonds in the thermoresponsive polymer. Finally, the weak peak at 318 cm⁻¹ in the polymer-mixed-nanocomposite applied on artificial archaeological oak could be assigned to the stretching of Fe-N bonds in the porphyrin moiety.

This polymer-mixed-nanocomposite is a proof of concept of this approach to employ thermoresponsive polymers as treatment vectors, which can be further developed in order to optimise its means of application and its iron chelation capacity.

4.5 Design of multifunctional nanocomposite Fe_3O_4 -p(DEGMA₄₅-co-MMA₅)-porphyrin (Fe_3O_4 -VTES-polymer-porphyrin)

Based on the concept of the PPIX/PEG 200 functionalised nanoparticles previously described, a number of modifications were devised in order to improve the iron chelation capability and ensure a better interaction of the nanoparticles with the thermoresponsive polymer which would provide greater control over the application and removal of the treatment.

The approach taken here was to apply the p(DEGMA₄₅-co-MMA₅) as a linker on the nanoparticle surface for the attachment of porphyrin. This would bring a series of advantages when encapsulating these nanoparticles in the thermoresponsive polymer. First, the nanoparticles containing p(DEGMA₄₅-co-MMA₅) chains would be encapsulated in a more stable manner in the thermoresponsive polymer. This is thanks to the convenient electrostatic interactions between the DEGMA monomers present both in the p(DEGMA₄₅-co-MMA₅) chains on the nanoparticles surface, and in the thermoresponsive polymer gel. Secondly, due to the presence of ethylene glycol moieties in p(DEGMA₄₅-co-MMA₅), the use of a second PEG functionality on the surface of the nanoparticles themselves would not be unnecessary. Therefore, the density of porphyrin units per nanoparticle would increase, potentially improving the chelating ability of the nanocomposite. **Figure 4.8** contains a schematic of the multifunctional nanocomposite, showing how a diethylene glycol based polymer is used to attach a porphyrin derivative to the surface of a Fe_3O_4 nanoparticle previously coated with a vinylsilane.

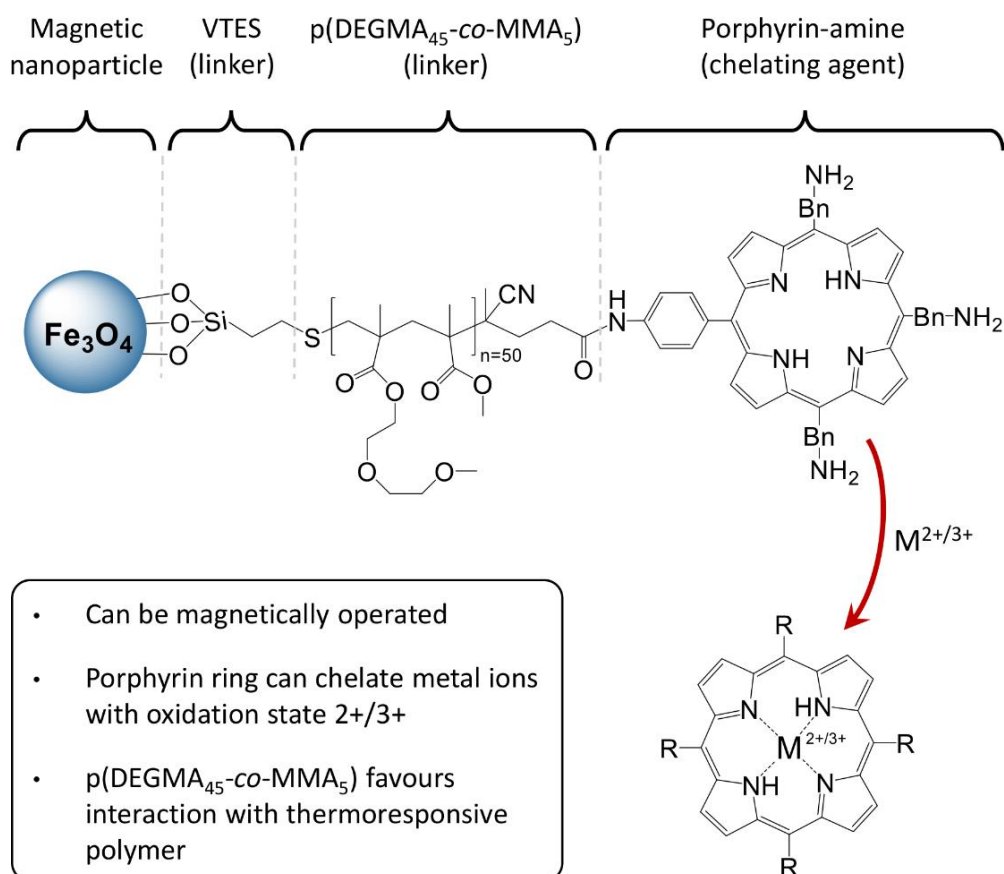


Figure 4.8. Schematic of Fe₃O₄-VTES-p(DEGMA₄₅-co-MMA₅)-porphyrin nanocomposite. Here, the role of p(DEGMA₄₅-co-MMA₅) is two-fold: linking the porphyrin-amine to the magnetic nanoparticle, and providing means for electrostatic interactions with the thermoresponsive polymer. Iron oxide nanoparticles are coated with VTES in order to anchor p(DEGMA₄₅-co-MMA₅)-porphyrin *via* a thiol-ene reaction.

4.5.1 Preparation and characterisation of Fe₃O₄-VTES-polymer-porphyrin multifunctional nanocomposite

4.5.1.1 Preparation and characterisation of Fe₃O₄-VTES

For this synthesis, the magnetite nanoparticles were first functionalised with vinyltriethoxysilane (VTES). The aim was to obtain a vinyl-functionalised surface onto which p(DEGMA₄₅-co-MMA₅) could be anchored *via* thiol-ene click chemistry. Highly crystalline iron oxide nanoparticles were prepared by microwave-assisted co-precipitation as described by Williams *et al.* and discussed in Section 3.2.1.¹⁷ The functionalisation with VTES was performed in a similar manner as described by Yong *et al.*¹⁸ Figure 4.9 (A) displays a schematic of the reaction. More detailed information can be found in Section 2.3.3.

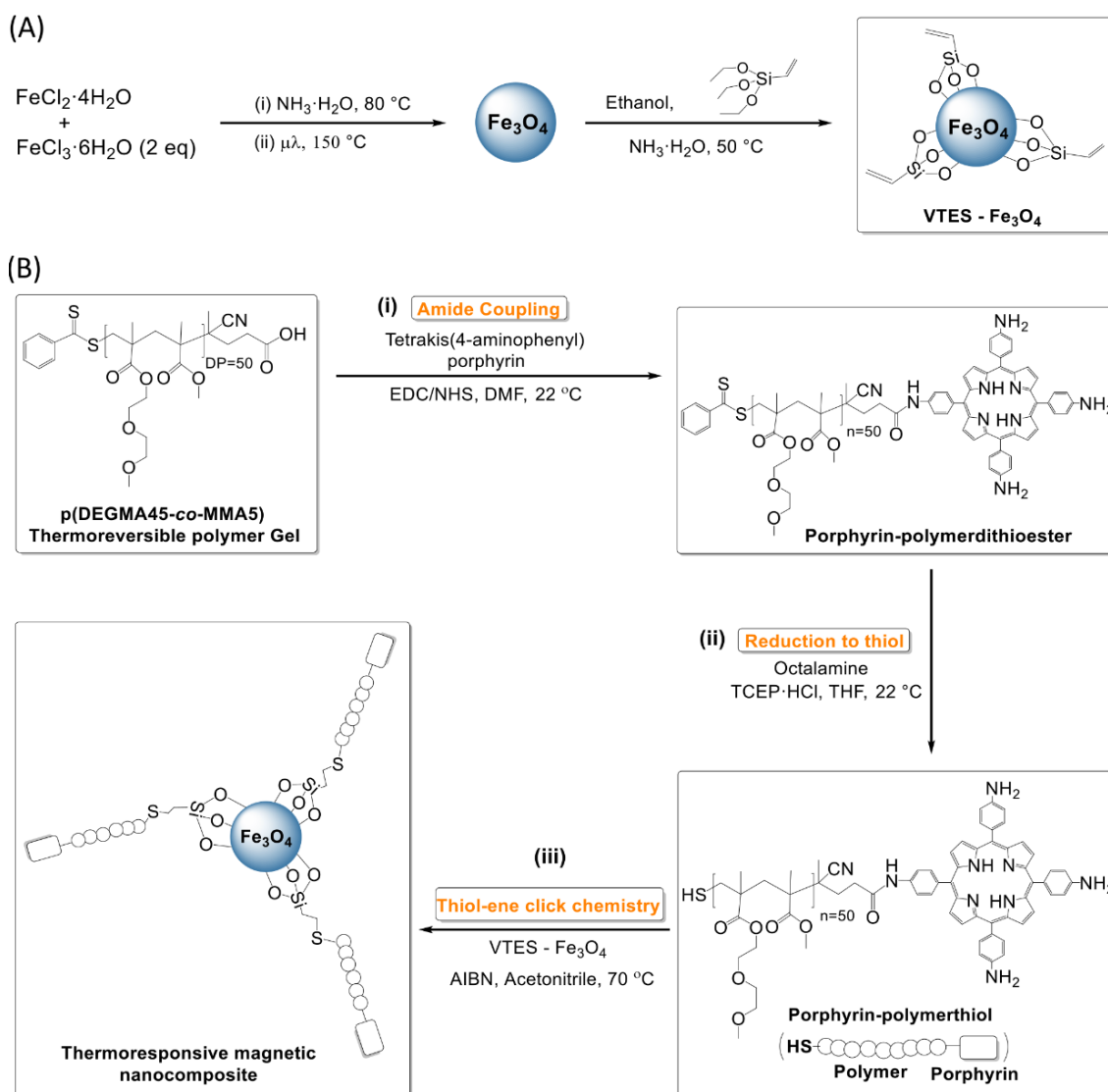


Figure 4.9. Schematic of the preparation of the multifunctional nanocomposite Fe₃O₄-VTES-p(DEGMA₄₅-co-MMA₅)-porphyrin. (A) Fe₃O₄ nanoparticles were synthesised by MW assisted co-precipitation, as described in Section 3.2.1, and further functionalised with vinyltriethoxysilane (VTES). (B)(i) Porphyrin-amine is anchored to the carboxylic group of p(DEGMA₄₅-co-MMA₅) *via* a conventional amide coupling. (ii) The porphyrin-polymerdithioester is reduced to porphyrin-polymerthiol, and (iii) this is anchored onto the VTES coated Fe₃O₄ nanoparticles *via* thiol-ene click chemistry.

4.5.1.2 Preparation of porphyrin-p(DEGMA₄₅-co-MMA₅) (porphyrin-polymerthiol)

Amide coupling of p(DEGMA₄₅-co-MMA₅) with 5,10,15,20-tetrakis(4-aminophenyl) porphyrin

In order to use p(DEGMA₄₅-co-MMA₅) as a linker between a porphyrin derivative and the magnetite nanoparticles, further modifications were made to its functional end

groups. For this purpose, 5,10,15,20-tetrakis(4-aminophenyl) porphyrin (porphyrin-amine), a porphyrin derivative with four primary amine groups, was selected. A regular amide coupling between the carboxylic end group of the polymer and one of the primary amines on the amino-porphyrin was performed to obtain a polymer-porphyrin moiety. Briefly, p(DEGMA₄₅-co-MMA₅) was dissolved in dimethylformamide (DMF) under inert atmosphere. EDC and NHS were added to the solution and stirred for 10 minutes, then DMAP was also added to the solution. Finally, porphyrin-amine was carefully dissolved in a small amount of DMF and added to the solution, followed by a catalytic amount of TEA. Once purified, the brown gel obtained was freeze-dried for 24 hours to remove any traces of water. **Figure 4.9(B)(i)** shows a schematic of this step. Further details about the procedure can be found in **Section 2.3.3**.

Figure 4.10 shows the ¹H spectrum for porphyrin-polymer obtained in DMSO-d₆. The intense bands at 0.8-1.45 ppm and the multiplet at 1.75 ppm correspond to the -CH₃ and the -CH₂- protons on the thermoresponsive polymer backbone. Also, the intense band at 3.33 ppm and the bands at 3.47-3.61 ppm are attributed to the -OCH₃ protons and the -OCH₂- protons in the DEGMA and MMA monomers, respectively.^{4,7} The singlet at 8.88 ppm and the two doublets at 7.86-6.99 ppm correspond to the -CH= protons in the pyrrole ring, and the and the -CH= protons in the aminophenyl groups in the porphyrin. The singlets at -2.73 ppm and 5.56 ppm correspond to the -NH= protons on the pyrrole rings, and to the -NH₂ protons in the three aminophenyl groups present in the porphyrin, respectively. The multiplets at 7.48 ppm and 7.64 ppm correspond to the -CH= protons in the dithiobenzene end of the polymer.¹⁹ Finally, the singlet at 8.45 ppm can be attributed to the -CONH- proton in the amide bond between the thermoresponsive polymer and the porphyrin-amine. The integration ratio between this proton and the signals for -NH₂ protons in porphyrin is 1:6.5, very close to the expected 1:6. Similarly, the ratio obtained between this signal and the one for -OCH₃ protons in DEGMA and MMA is 1:138, close to the expected 1:150. This confirms the successful formation of the moiety porphyrin-polymer *via* an amide coupling reaction.

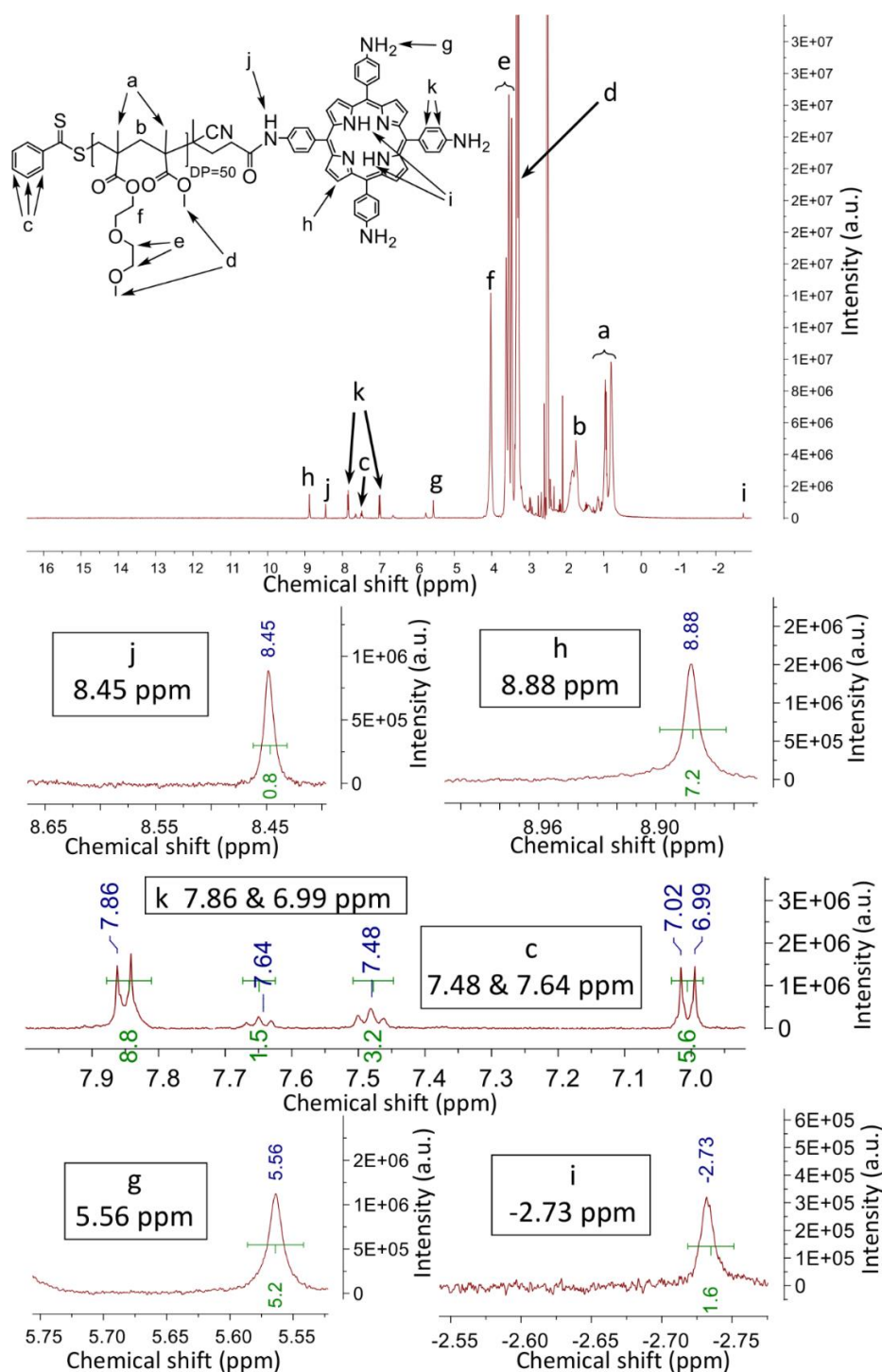


Figure 4.10. ¹H NMR spectra of porphyrin-p(DEGMA₄₅-co-MMA₅) obtained in DMSO-d₆. The signals a, b, d, e and f are contributions from the thermoresponsive polymer backbone. The signals h and k correspond to the -CH= protons in the pyrrole rings and the -CH= protons in amino phenyl groups in the porphyrin rings, respectively. The singlets g and i can be attributed to the -NH₂ protons in the aminophenyl groups, and the -NH- protons in the pyrrole rings of in the porphyrin, respectively. Finally, the singlet at 8.45 ppm (labelled as j) can be attributed to the -CONH- proton in the amide group, and the two triplets at 7.48 and 7.64 ppm (labelled as c) correspond to the -CH= protons in the dithiobenzene end of the polymer.

Reduction of porphyrin-polymerdithioester to porphyrin-polymerthiol

Next, the dithioester end on the porphyrin-polymer was reduced to a thiol. For this, the reducing agent tris(2-carboxyethyl)phosphine hydrochloride (TCEP-HCl), often used for cleaving sulphide bonds, was employed.²⁰ Briefly, the porphyrin-polymerdithioester was dissolved in octylamine under inert atmosphere. Then, a solution of TCEP-HCl in tetrahydrofuran was added to the mixture. The brown gel obtained was dried under vacuum and stored at 5 °C. A schematic of this step is shown in **Figure 4.9(B)(ii)**. More details about the procedure are discussed in **Section 2.3.3**.

The ¹H NMR spectrum obtained from the product in DMSO-d₆ is shown in **Figure 4.11**. The peaks at 0.79, 1.23, 3.27, 3.53 and 4.02 ppm are identified as the fingerprint of the thermoresponsive polymer p(DEGMA₄₅-co-MMA₅). These shifts correspond to the -CH₃, -CH₂-, -OCH₃, -OCH₂- and -COOCH₂- protons, respectively, in DEGMA and MMA monomers.^{4,7} The characteristic signals for the porphyrin-amine are at -2.75, 5.56, 7.01-7.85, and 8.87 ppm and are attributed to the -NH-, -NH₂, -CH= (aminophenyl group), and -CH= (pyrrole ring) protons, respectively.¹⁹ The singlet observed at 8.50 ppm corresponds to the -CONH- proton in the amide bond. The signals from -SH protons are typically found in the 1-3 ppm region, however, considering the relative amount of C-H and S-H bonds in the porphyrin-polymerthiol, the intensity of the signal originated from the latter is expected to be quite low. Thus, the singlet observed at 1.35 ppm could be attributed to the -SH proton, but due to the signal-to-noise ratio, this cannot be confirmed. Nonetheless, the signals for the -CH= protons in the dithiobenzene end of the polymer (7.40-7.70 ppm) observed in **Figure 4.10** are no longer visible in the same region of the spectrum in **Figure 4.11**, suggesting that the dithioester has been successfully reduced to thiol.

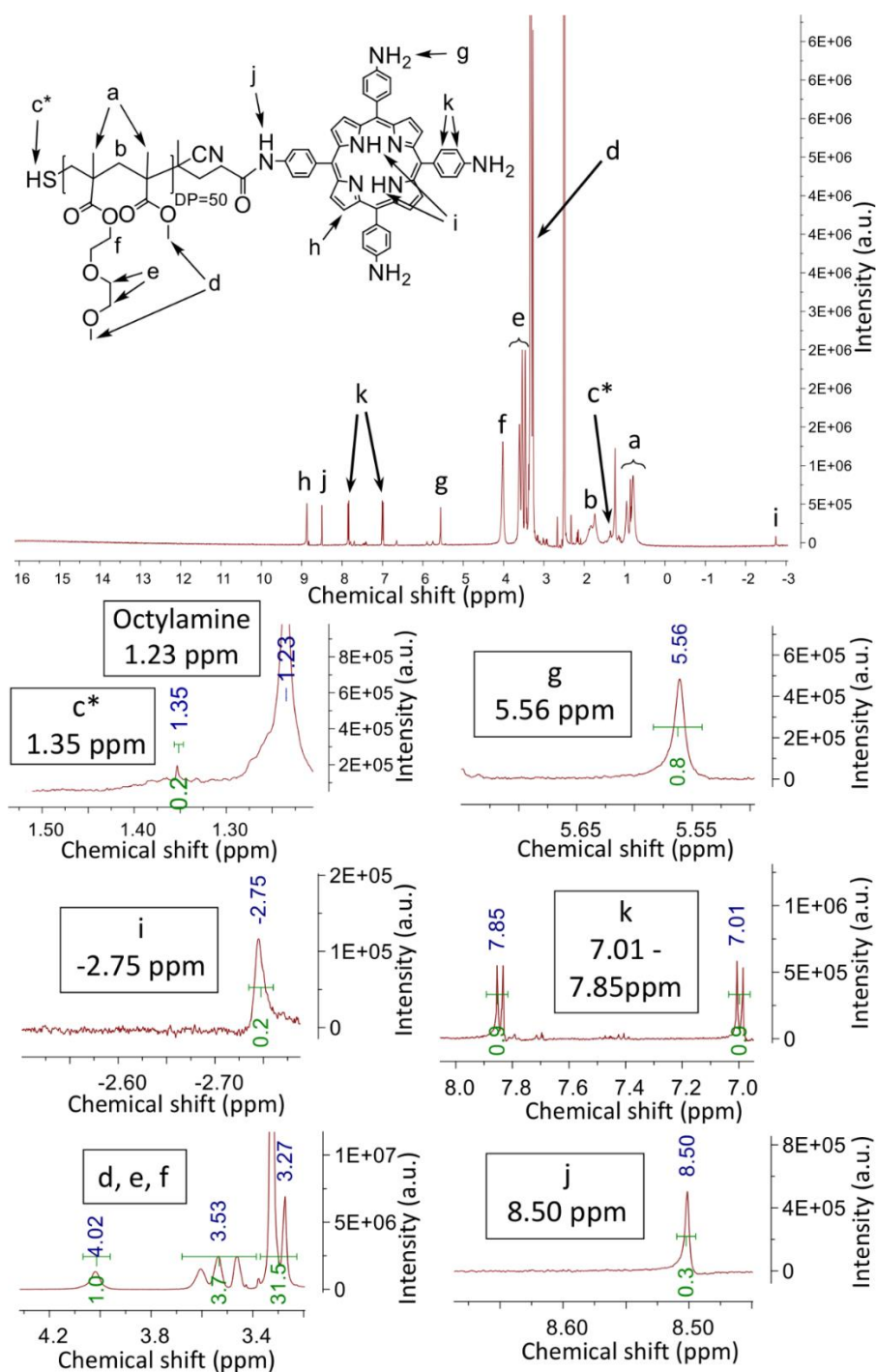


Figure 4.11. ¹H NMR spectrum of porphyrin-polymerthiol. The peaks labelled a, b, d, e and f are attributed to the -CH₃-, -CH₂-, -OCH₃-, -OCH₂- and -COOCH₂- protons, respectively, present in the backbone of p(DEGMA₄₅-co-MMA₅). The signals g, h, i, and k are the fingerprint of the porphyrin-amine, and correspond to the -NH₂-, -CH= (pyrrole ring), -NH- and -CH= (aminophenyl group), respectively. The singlet j (8.50 ppm) is attributed to the -CONH- proton in the amide bond. The signal c* could be attributed to the -SH proton. The absence of the doublets characteristic of -CH= protons in the dithiobenzene end group (7.4-7.6 ppm) suggests the reduction of this to a thiol.

4.5.1.3 Grafting porphyrin-polymerthiol onto Fe₃O₄-VTES

Finally, the attachment of the porphyrin-polymerthiol onto the magnetite nanoparticles was performed *via* thiol-ene click chemistry between the thiol end on the polymer and the vinyl functionalities on the nanoparticles.^{21,22,23} AIBN was used as a thermal initiator in spite of the slightly lower conversion rate associated to it, compared to photoinitiators.²⁴ However, due to the presence of a photosensitive porphyrin unit on the polymer, a photochemically initiated thiol-ene reaction was deemed incompatible. Thus, porphyrin-polymerthiol was dissolved in acetonitrile under inert atmosphere, and AIBN was added. Then, a suspension of vinyl functionalised nanoparticles in acetonitrile was added, and the reaction mixture was stirred for 18 hours at 70 °C under inert atmosphere. The obtained product was magnetically decanted, washed with ethanol and dried under vacuum. **Figure 4.9(B)(iii)** depicts a schematic of this reaction. Details of this procedure can be found in **Section 2.3.3**.

4.5.2 Characterisation of the multifunctional nanocomposite Fe₃O₄-VTES-polymer-porphyrin

The crystallinity and nature of the magnetite nanoparticles were studied throughout the synthesis process by powder XRD, while the successive functionalisation steps of the magnetite nanoparticles were monitored by thermal analysis and Fourier-transform IR spectroscopy. The optical and thermoresponsive properties of the polymeric coating and the multifunctional nanocomposite were studied by UV-visible and fluorescence spectroscopies, variable-temperature UV-visible spectroscopy, and dynamic light scattering. The thermal behaviour of the polymer was also studied by temperature-variable ¹H NMR by Dr Ester R. Aluri, and the results can be found in the Appendices (**Figure A4.1.**)

Powder XRD patterns collected from dry powders of magnetite, Fe₃O₄-VTES, and Fe₃O₄-VTES-polymer-porphyrin are shown in **Figure 4.12**. The patterns obtained matched the standard of cubic spinel magnetite (Fe₃O₄, JCPDS index card no. 19-629), revealing that Fe₃O₄ was obtained without any evidence for additional phases. Furthermore, this structure was retained during the subsequent functionalisation steps. The observed broad peaks are typical for nanoparticles and are consistent with the average crystallite size of 14 nm, obtained from the Scherrer equation. Since magnetite and other more oxidised forms of iron oxide such as maghemite (γ -Fe₂O₃) or haematite (α -Fe₂O₃) show similar XRD patterns, these samples were also studied by Raman spectroscopy by Dr Ester R. Aluri.

The Raman spectra obtained (shown in the Appendices, **Figure A4.2.**) revealed one intense peak at 671 cm^{-1} , characteristic of magnetite. No evidence of other phases was observed.

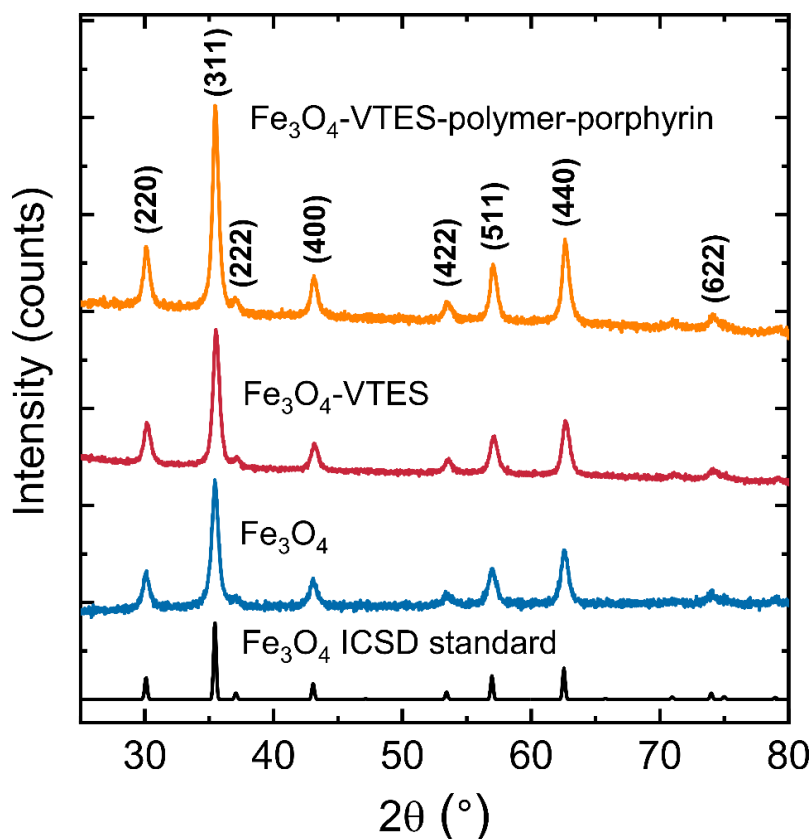


Figure 4.12. Powder XRD patterns from dry precipitates of Fe_3O_4 (blue), Fe_3O_4 -VTES (red) and Fe_3O_4 -VTES-polymer-porphyrin (orange). The three patterns are in excellent agreement with the standard of cubic inverse spinel magnetite (Fe_3O_4 , JCPDS index card no. 19-629), showing that the morphology of the magnetite nanoparticles does not change through the successive functionalisation steps. The broad diffraction peaks observed are typical from nanostructures, and the average crystallite size obtained with the Scherrer equation is in the order of 14 nm.

Thermal gravimetric analysis (TGA) was conducted to determine the loss of organic content from the surface of the magnetite nanoparticles at different stages of the synthesis. TGA curves of bare magnetite, Fe_3O_4 -VTES, and Fe_3O_4 -VTES-polymer-porphyrin are shown in **Figure 4.13**. The weight loss of bare Fe_3O_4 is around 0.5 %, likely due to the loss of water molecules physisorbed onto the nanoparticle's surface. The increased weight

loss for Fe_3O_4 -VTES (16.3 %), and Fe_3O_4 -VTES-polymer-porphyrin (20.6 %) indicates the successful attachment of VTES and porphyrin-polymer thiol on the nanoparticle surface.

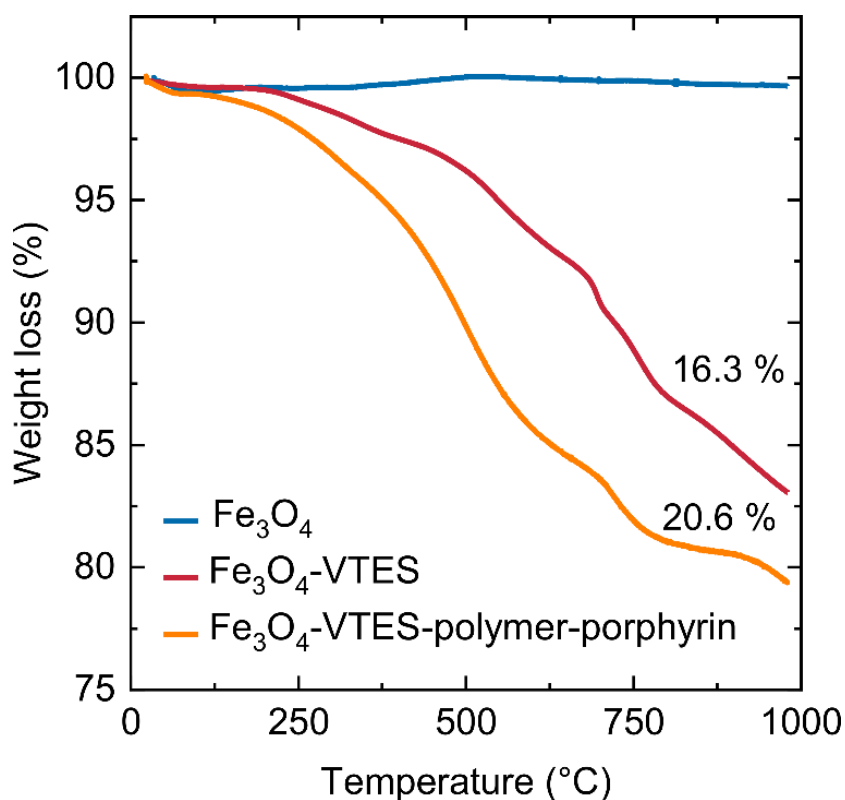


Figure 4.13. TGA curves of Fe_3O_4 , VTES functionalised Fe_3O_4 and Fe_3O_4 -VTES-polymer-porphyrin. While the mass loss of the bare Fe_3O_4 is 0.5 %, the mass loss of the particles coated with VTES and with VTES-polymer-porphyrin 16.3 % and 20.6 %, respectively. This confirms the presence of organic compounds successively grafted onto the Fe_3O_4 nanoparticles.

The presence of VTES, the porphyrin derivative, and the thermoresponsive polymer onto the magnetic nanoparticles was analysed by FTIR spectroscopy. IR spectra of bare Fe_3O_4 , and the successive functionalisation stages are shown in **Figure 4.14**. The intense band at 540 cm^{-1} , corresponding to the stretches of the Fe-O bond, can be seen in all three spectra. The bands at 754 , 1005 and 1099 cm^{-1} are attributed to the symmetric and asymmetric vibrations of the Si-O bond from the VTES attached onto the nanoparticles. The band at 959 cm^{-1} corresponds to the Si-O-Fe bond stretches, and indicates that the mode of binding of VTES to the nanoparticles is through the silane groups.²⁵ The stretches at 1597 and 1406 cm^{-1} correspond to the stretches from the C=C bond and the bending

vibration of the =CH₂ group in VTES. The bands at 1450 and 1720 cm⁻¹ correspond to the stretches of the C=O bond in the amide group, and to the stretching vibrations of the C=O bond in the ester groups in the DEGMA and MMA monomers, respectively. Also, a decrease in intensity of the bands at 1597 and 1406 cm⁻¹ (corresponding to stretching vibrations of C=C and =CH₂ bonds, respectively) can be observed. This is consequence of the hydrothiolation of the C=C bonds in VTES upon reaction with the porphyrin-polymerthiol via thiol-ene click reaction.^{22,25,26}

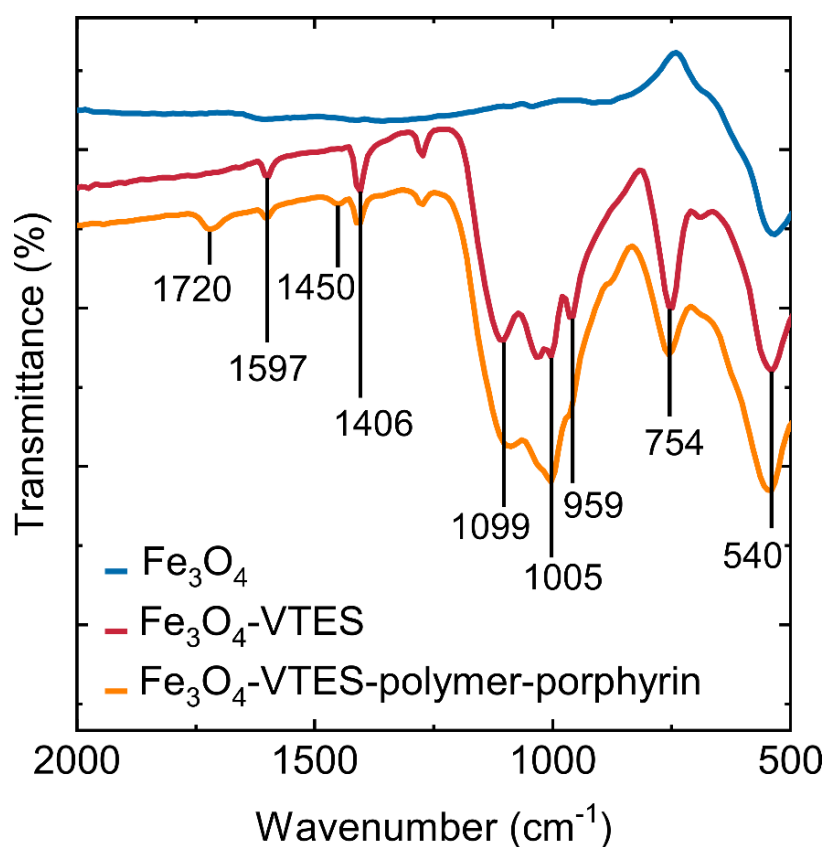


Figure 4.14. FTIR spectra of Fe₃O₄, Fe₃O₄-VTES and Fe₃O₄-VTES-polymer-porphyrin. The intense stretch at 540 cm⁻¹ is due to the Fe-O bond, the broad bands at 754, 1005 and 1099 cm⁻¹ are attributed to the vibrations of the Si-O bond, and the band at 959 cm⁻¹ is due to the Si-O-Fe stretches. Also, the bands at 1406 and 1597 cm⁻¹ correspond to the =CH₂ and C=C stretches, respectively in VTES. This confirms the successful binding of VTES onto the magnetite. The bands at 1450 and 1720 cm⁻¹ correspond to the stretches of the C=O bond in the amide and the C=O bond from the ester groups in the porphyrin-polymer, respectively, confirming its presence onto the Fe₃O₄ nanoparticles.

The optical properties of the multifunctional nanocomposite were studied by UV-visible and fluorescence spectroscopies in ethanol, and the spectra obtained for the porphyrin-polymerdithioester, the porphyrin-polymerthiol and the Fe₃O₄-VTES-polymer-porphyrin are shown in **Figure 4.15**. The characteristic absorbance band for porphyrin derivatives can be observed at 425 nm in all the three samples studied. The pronounced broadening and intense background observed in the spectra of Fe₃O₄-VTES-polymer-porphyrin is caused by the scattering of light by the nanoparticles in suspension. The emission band of the porphyrin moieties present in the three samples can be seen at 668 nm ($\lambda_{\text{exc}} = 425$ nm). These bands reveal the successful attachment of the porphyrin derivative to the thermoresponsive polymer, and the successful functionalisation of the magnetite nanoparticles with the porphyrin-polymer.²⁷ The small signal observed at 300 nm, in the spectrum from the porphyrin-polymerdithioester is due to the presence of the dithiobenzene end group. This signal disappears in the spectrum from the porphyrin-polymerthiol, confirming the successful reduction of the dithioester group to thiol.²⁸

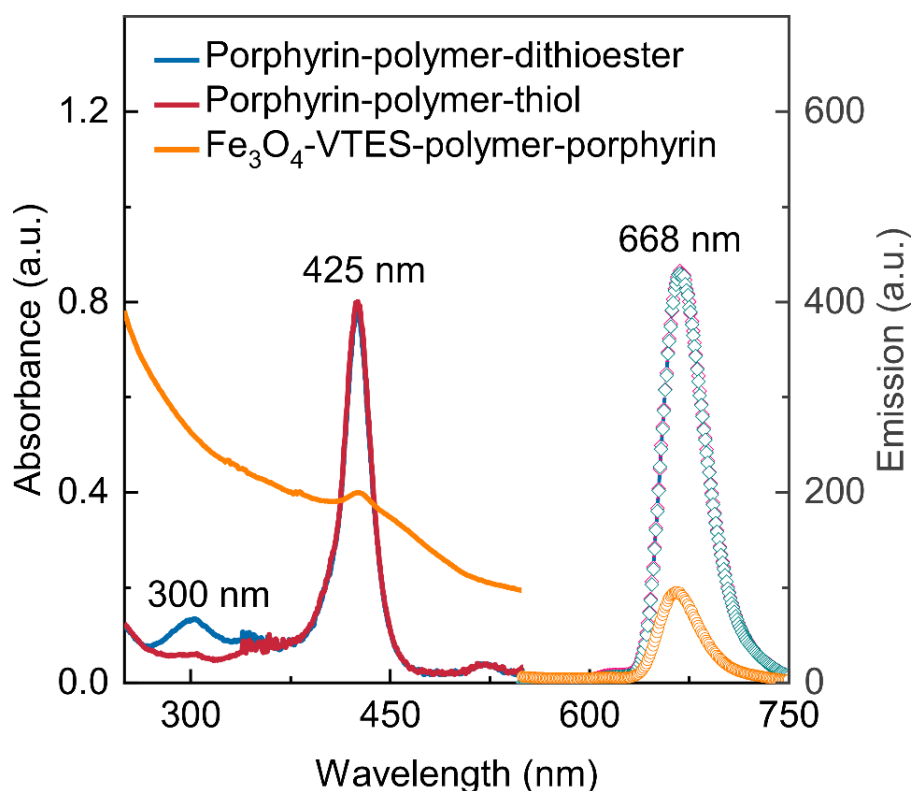


Figure 4.15. Absorbance and emission spectra of porphyrin-polymerdithioester, porphyrin-polymerthiol and Fe_3O_4 -VTES-polymer-porphyrin obtained in ethanol. The absorbance band at 425 nm, corresponding to the porphyrin moiety can be observed in the three stages of the synthesis. The intense background and incline in the Fe_3O_4 -VTES-polymer-porphyrin spectrum is due to the scattering of the light by the magnetic nanoparticles. The emission bands, obtained at $\lambda_{\text{exc}} = 425 \text{ nm}$, also confirm the presence of the fluorophore onto the Fe_3O_4 nanoparticles.

The thermoresponsive behaviour of porphyrin-polymerdithioester was studied by variable-temperature UV-visible spectroscopy. **Figure 4.16** shows the transmittance of the porphyrin-polymerdithioester in aqueous solution between 10 and 40 °C. The porphyrin-polymerdithioester shows a change in transmittance at approximately 23 °C. This change in transmittance is less pronounced than the one described for p(DEGMA₄₅-co-MMA₅) in **Section 4.1.1**. As discussed in **Section 1.6**, the LCST of a polymer can be tuned, among other things, by adjusting the hydrophobicity of the monomers within it. Thus, the addition of a bulky hydrophobic moiety, such as a porphyrin derivative, can have several effects. First, the LCST of the polymer may drop due to an increase of the overall hydrophobicity. Also, strong interchain hydrophobic interactions

between the porphyrin and the methacrylate backbone of the polymer can occur, leading to a slower sol-gel phase transition.²⁹

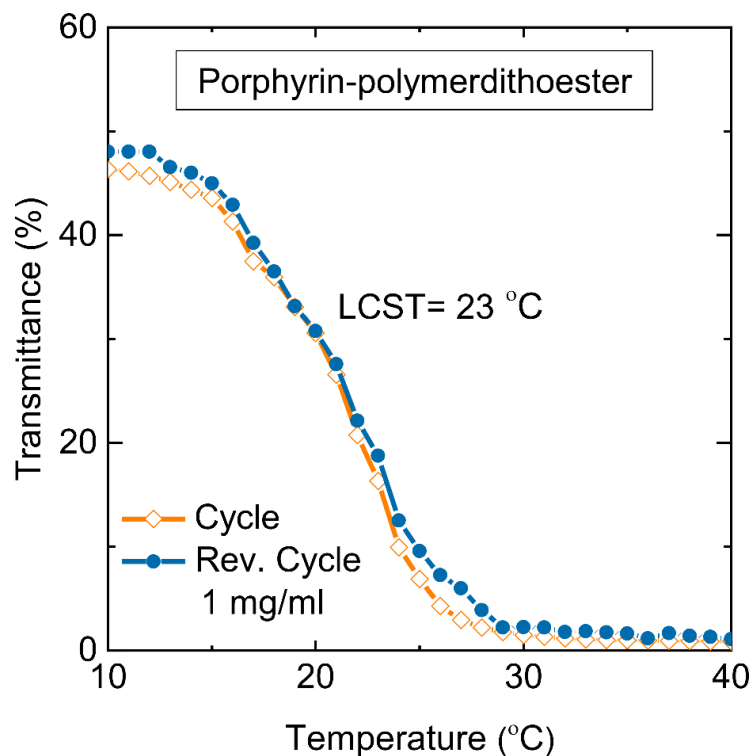


Figure 4.16. Variable-temperature UV-visible spectroscopy of porphyrin-polymerdithioester showing its thermoresponsive behaviour. The LCST observed (23 °C) is lower than the one obtained for the thermoresponsive polymer. This change in the LCST can be explained by the hydrophobic nature of the porphyrin moiety added.

The temperature-dependent hydrodynamic radius of the multifunctional nanocomposite was studied by dynamic light scattering. **Figure 4.17** shows (A) the variation of average hydrodynamic radius of the multifunctional nanocomposite with temperature in an aqueous suspension, and (B) a schematic depicting the potential changes of the thermoresponsive polymer chains on the nanoparticle with temperature. At 20 °C the porphyrin-polymer chains display hydrophilic behaviour, which causes them to be fully extended, yielding a hydrodynamic diameter of 210 nm. The porphyrin-polymer chains become gradually hydrophobic upon increasing the temperature and start to collapse. This evolves into a compact shell around the magnetite nanoparticle, showing a diameter of 170 nm at 40 °C.³⁰ The hydrodynamic size observed was significantly larger

than the primary particle diameter obtained from TEM. This difference is due to the solvated porphyrin-polymer chains in water.^{17,29}

For the multifunctional nanocomposite, the sol-gel phase transition occurs around 20 to 23 °C. This transition temperature window of 2-3 °C obtained is ideal for its application in archaeological wood conservation. This narrow window of temperature would allow the use of treatments without causing an undesirable stress to the wood structure by large changes in temperature.

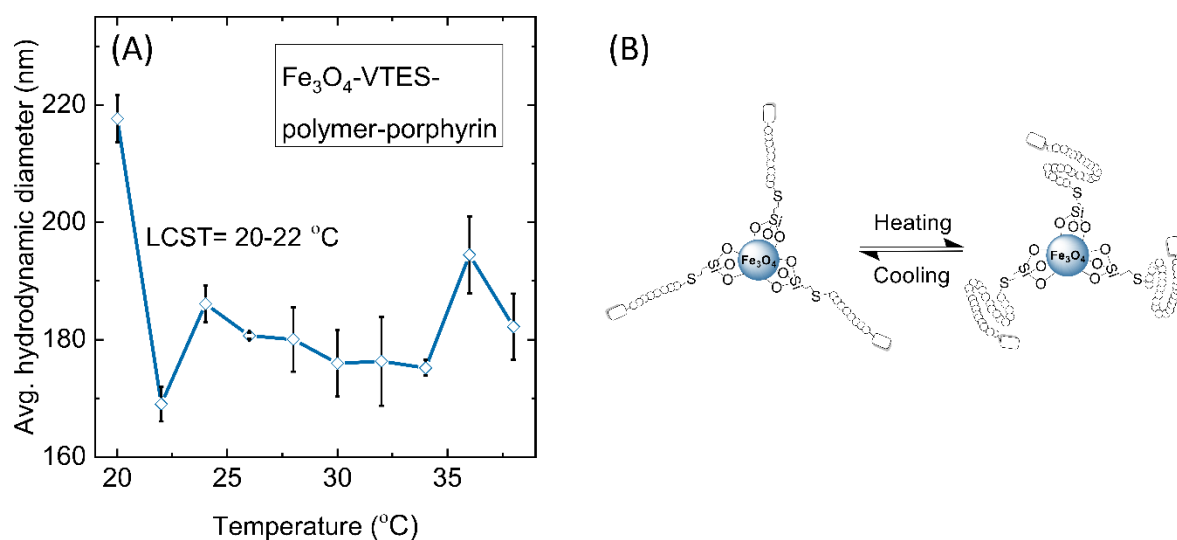


Figure 4.17. (A) Temperature-dependent dynamic light scattering of Fe_3O_4 -VTES-polymer-porphyrin obtained in aqueous suspension between 20 and 40 °C. The average hydrodynamic diameter of the multifunctional nanocomposite decreases from 220 nm to values between 170-180 nm when the temperature is raised above 20-22 °C. (B) Representation of the disposition of the polymer chains in Fe_3O_4 -VTES-polymer-porphyrin in aqueous suspension. Low temperatures favour the adsorption of water molecules and the unfurling of the polymer chains, while high temperatures lead to the cleavage of hydrogen bonds favouring a hydrophobic behaviour and the collapse of the polymer chains.

4.6 Evaluation of iron chelation of Fe_3O_4 -VTES-polymer-porphyrin

Prior to the application of the treatment on wood samples, the iron sequestering capability of Fe_3O_4 -VTES-polymer-porphyrin nanocomposite was studied in solution, under a controlled environment. For this, the multifunctional nanocomposite was incubated in ethanolic and aqueous solutions of iron salts, and the content in iron of these solutions was monitored over time by UV-visible spectroscopy and atomic absorption spectroscopy (AAS). Following these assessments, the treatment was applied to artificial archaeological

wood samples, previously treated with an aqueous solution of $\text{Fe}_2(\text{SO}_4)_3 \cdot 7\text{H}_2\text{O}$. Finally, a wood sample of the *Mary Rose* was treated with the multifunctional nanocomposite.

4.6.1 Evaluation of iron chelation in solution

The chelating ability of the multifunctional nanocomposite was studied using UV-visible spectroscopy, by monitoring changes in the intensity of the characteristic absorption band of Fe(III) at 283 nm in ethanol. For this, a 0.2 mM solution of $\text{Fe}_2(\text{SO}_4)_3 \cdot 7\text{H}_2\text{O}$ in ethanol (2.5 mL) was treated with consecutive additions (20 μL) of a suspension of the prepared multifunctional nanocomposites (0.25 mg/mL). The solution was stirred for 10 minutes at room temperature and in the dark, and the nanocomposite was decanted magnetically. The resulting solution of $\text{Fe}_2(\text{SO}_4)_3 \cdot 7\text{H}_2\text{O}$ was then measured by UV-visible spectroscopy. **Figure 4.18(A)** shows the spectra of the iron solution obtained during the treatment with the multifunctional nanocomposite. The intensity of the absorbance band at 283 nm, which corresponds to the free Fe(III) ion, decreases upon addition of the multifunctional nanocomposite.³¹ **Figure 4.18(B)** shows the absorbance values of a solution of $\text{Fe}_2(\text{SO}_4)_3 \cdot 7\text{H}_2\text{O}$ in ethanol, undergoing the same treatment and in similar conditions, measured at a fixed wavelength of 283 nm. This study shows, in a qualitative manner, the capacity of the prepared Fe_3O_4 -VTES-polymer-porphyrin composite to remove iron ions from solution.

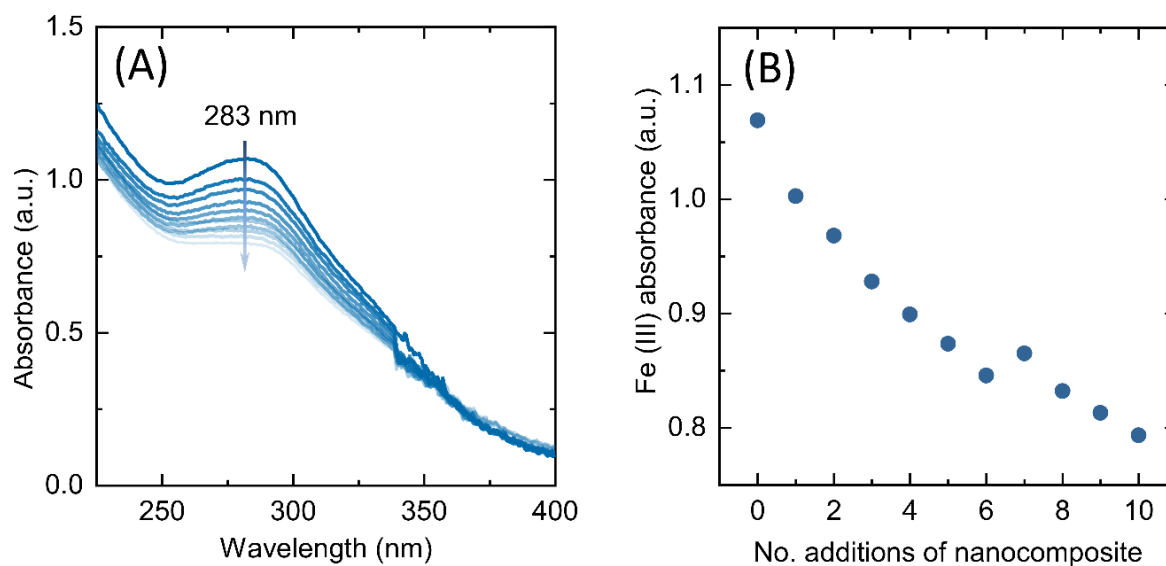


Figure 4.18. Performance tests on chelation of free iron ions solution. **(A)** UV-Visible absorption spectra of an ethanolic solution of $\text{Fe}_2(\text{SO}_4)_3 \cdot 7\text{H}_2\text{O}$ (0.2 mM) treated with consecutive additions of a suspension of Fe_3O_4 -VTES-polymer-porphyrin in ethanol (0.25 mg/ml, additions of 20 μL). A decrease in the intensity of the absorbance band is observed upon addition of porphyrin functionalised nanoparticles. **(B)** Absorption intensity of an ethanolic solution of $\text{Fe}_2(\text{SO}_4)_3 \cdot 7\text{H}_2\text{O}$ treated with functionalised nanoparticles recorded at 283 nm. Successive additions of functionalised nanoparticles lead to a decrease of the absorption intensity of Fe(III).

To complement these analyses, the iron sequestration capability of the multifunctional nanomaterial was tested by means of AAS. The studies performed consisted in monitoring the variation of the concentration of iron in a solution while being treated with a constant amount of the multifunctional nanocomposite. For this, an aqueous solution of $\text{Fe}_2(\text{SO}_4)_3 \cdot 7\text{H}_2\text{O}$ (25 mg/mL, 30 mL) was treated with the multifunctional nanocomposite (0.52 mg/mL) at room temperature and in the dark. Samples (0.4 mL) were periodically taken, prior magnetic decantation of the multifunctional nanocomposite, and diluted to 2 mL. The iron concentration in the samples was determined by AAS. **Figure 4.19** shows the variation of the concentration of iron in the solution monitored by AAS over 47 hours. An initial pronounced drop in the concentration of Fe(III) during the first 5-6 hours is followed by a gradual decrease over the next 40 hours. The concentration of iron in solution was reduced in 1.86 mg/mL, or by 39 %.

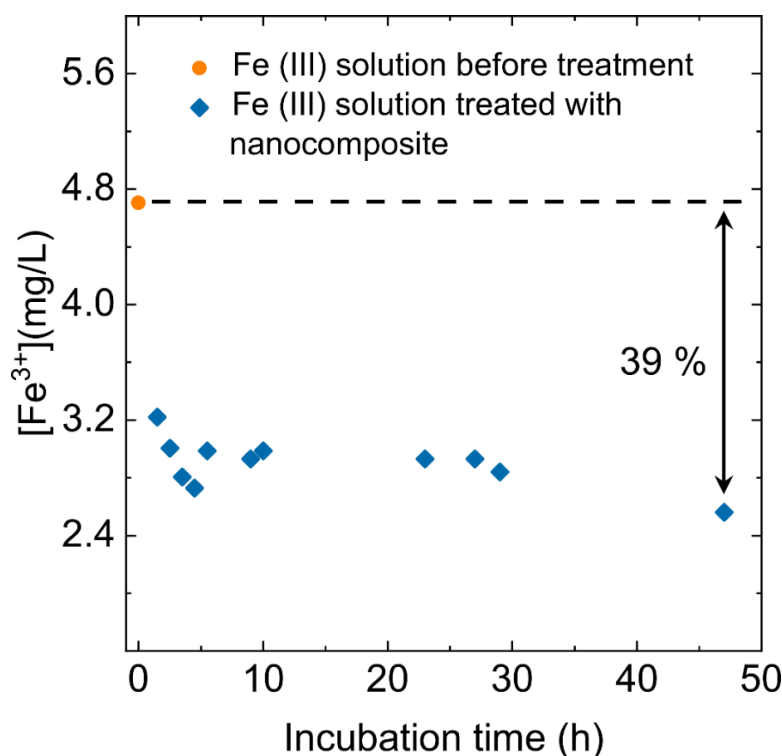


Figure 4.19. The concentration of Fe(III) in an aqueous solution of $\text{Fe}_2(\text{SO}_4)_3 \cdot 7\text{H}_2\text{O}$ was monitored by AAS during the treatment with Fe_3O_4 -VTES-polymer-porphyrin. The multifunctional nanocomposite was able to chelate 39 % of the free Fe(III) form solution after 5-6 hours.

4.6.2 Evaluation of iron chelation in artificial archaeological oak and *Mary Rose* wood

4.6.2.1 Preparation of the multifunctional nanocomposite-laden thermoresponsive polymer (nanocomposite-laden polymer)

The design of the treatment consisted in a matrix carrier into which the multifunctional nanocomposite was encapsulated for an optimised and safe application and removal from the wood. The vehicle chosen, as discussed in the introduction of this chapter, was the thermoresponsive polymer $p(\text{DEGMA}_{45}\text{-co-MMA}_5)$. The nanocomposite-laden polymer was prepared by adding the multifunctional nanocomposite to a solution of the thermoresponsive polymer in ethanol. The nanocomposite-to-polymer mass ratio used was 1:5. The solution was stirred briefly and then the solvent was evaporated under vacuum. **Figure 4.20** shows the stages of the preparation of the nanocomposite-laden polymer. The (A) multifunctional nanocomposite was embedded in an ethanolic solution of the thermoresponsive polymer, which is shown (B) below and (C) above the LCST. The

(D) nanocomposite-laden polymer obtained after removing the solvent was coloured dark brown.

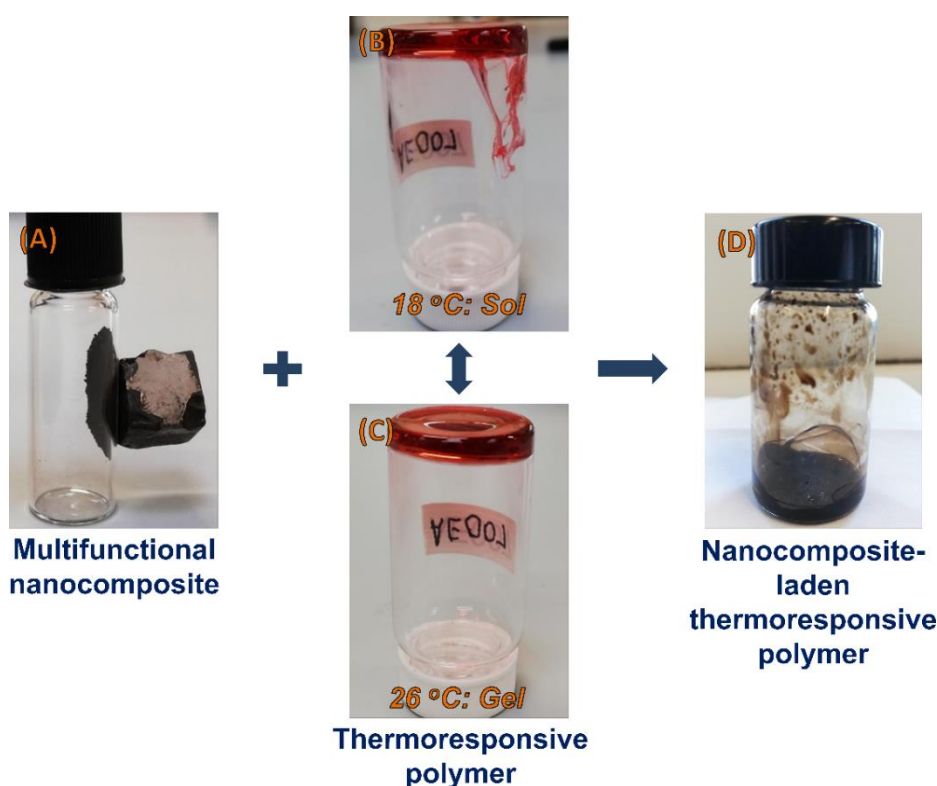


Figure 4.20. Stages of the preparation of the nanocomposite-laden polymer. The Fe_3O_4 -VTES-polymer-porphyrin (A) is added to an ethanolic solution of thermoresponsive polymer, yielding a dark gel (D). The thermoresponsive polymer gel is shown at temperatures (B) below and (C) above the LCST.

4.6.2.2 Application of the nanocomposite-laden polymer on artificial archaeological wood

The nanocomposite-laden polymer was applied onto artificial archaeological wood and fresh oak samples in order to study the feasibility of its application and removal, and its ability to chelate iron from wood. Thus, the nanocomposite-laden polymer was cooled down and approximately 20 mg were applied onto the wood samples with a plastic spatula. The wood samples were placed onto a 1.3 Tesla magnet and incubated at 5 °C in the dark for one month. After this, the wood samples were covered in transparent film and the magnet was applied on the treated face for one week at 5 °C. **Figure 4.21** shows samples of (A) fresh oak and (B) artificial archaeological wood sitting atop a 1.3 Tesla permanent magnet during the incubation of the treatment. After the one-month incubation, (C and D) the magnet was applied on the treated face, previously protected

by transparent film one week. The samples were brought to room temperature and the nanocomposite-laden polymer (E) was carefully removed from the wood surface with a plastic spatula.

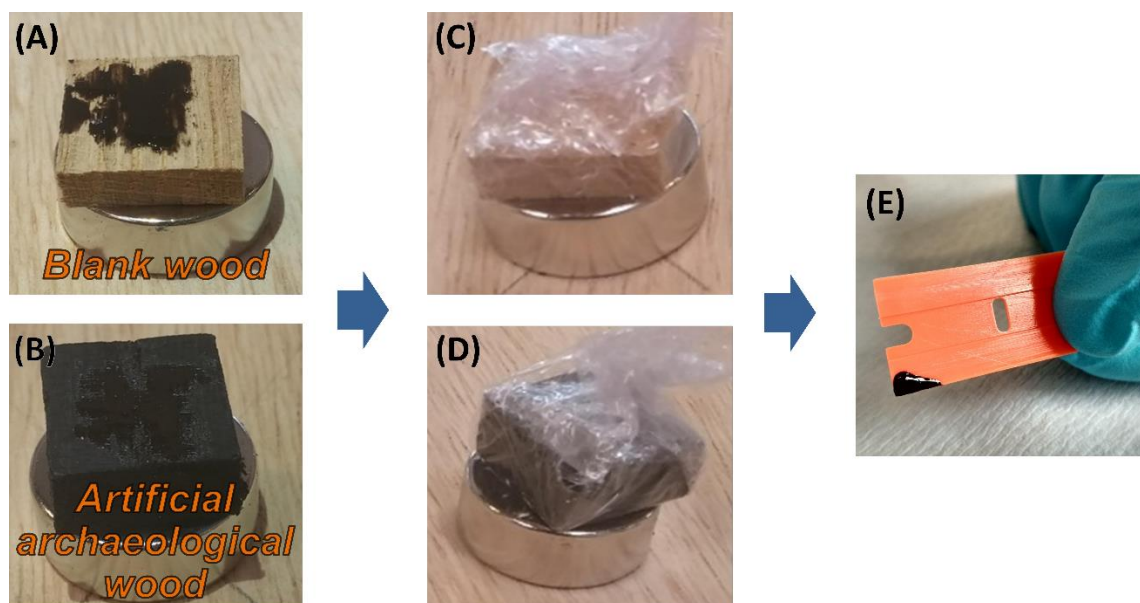


Figure 4.21. Multifunctional nanocomposite-laden polymer was applied on (A) Blank wood and (B) artificial archaeological wood, and incubated for 4 weeks at 5 °C atop a 1.3 Tesla neodymium magnet. After the incubation period the wood samples were wrapped in transparent film (C and D), and the magnetic field was applied in the opposite direction. (E) After a week the nanocomposite-laden polymer was peeled off the wood surface.

4.6.2.3 Application of the nanocomposite-laden polymer on *Mary Rose* wood and evaluation of its iron sequestration properties

A wood sample of the *Mary Rose* was treated with the nanocomposite-laden polymer in a similar manner to the fresh and artificial archaeological wood samples. The nanocomposite-laden polymer (approximately 20 mg) was carefully applied onto the side of a wood core obtained from the keel of the *Mary Rose*. The wood core was then protected with transparent film and fixed atop a permanent 1.3 Tesla magnet and incubated for one month in the dark, at 5 °C, in a similar manner to Section 4.6.2.1. As with the artificial archaeological wood samples, after the incubation period the magnetic field was applied in the opposite direction, and kept in the dark at 5 °C for one week. The wood core was then slowly brought to room temperature and the

nanocomposite-laden polymer was carefully peeled off its surface. **Figure 4.22** shows (A) the wood core from the *Mary Rose*, the dark region on the top end corresponds to the more degraded wood from the surface of the keel; (B) SEM micrograph of the wood core with an overlaid EDS map highlighting the areas where sulfur (red) and iron (green) are present; (C) a wood core from the *Mary Rose* sitting onto a permanent magnet while being treated with the nanocomposite-laden polymer.

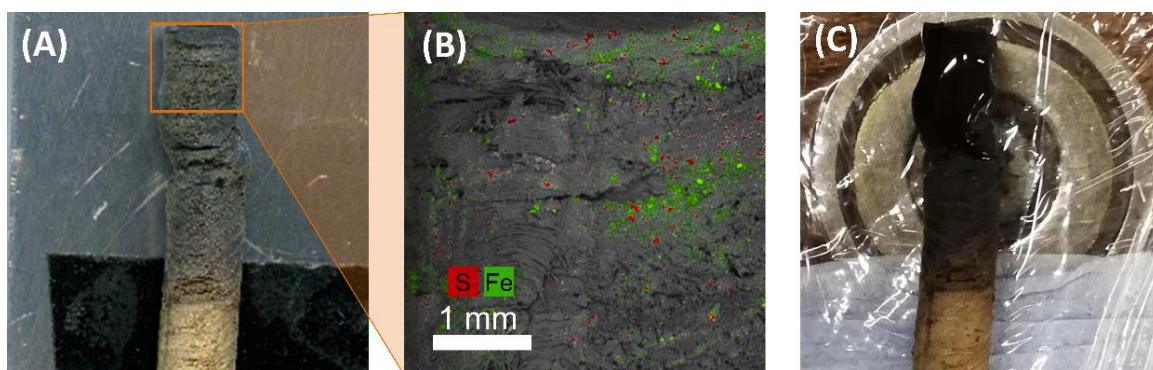


Figure 4.22. (A) Image of a core sample obtained from the keel of the *Mary Rose*. The more degraded, darker region corresponds to the section of the core close to the surface of the wood (B) SEM-EDS micrograph showing sulfur and iron present in the core, and (C) core sample being treated with a patch of polymer gel loaded with Fe_3O_4 -VTES-polymer-porphyrin.

4.6.2.4 Evaluation of the iron sequestration properties of the nanocomposite-laden polymer

Far IR spectroscopy was used to study the capacity of the nanocomposite-laden polymer to sequester and remove iron ions from wood. **Figure 4.23** displays the far IR spectra obtained from the nanocomposite-laden polymer after the treatment of (C) *Mary Rose* wood, (D) artificial archaeological oak and (E) fresh oak. For comparison, the spectra of (A) thermoresponsive polymer, (B) porphyrin amine and (F) multifunctional nanocomposite are included. The broad band at 552 cm^{-1} , present in the three treatments (C, D and E) and in the multifunctional nanocomposite (F), is attributed to the Fe-O stretches from magnetite. The band at 440 cm^{-1} , also observed in the nanocomposite-laden polymer (C, D and E) and multifunctional nanocomposite (F), can be attributed to the pyrrole ring rotation in the porphyrin.^{10,32} Two distinct features were observed at 316 and 393 cm^{-1} , and were particularly intense in the nanocomposite-laden polymer after the treatment of artificial archaeological wood (D) and *Mary Rose* wood (C). As discussed

previously in Section 4.4.3, the band at 316 cm^{-1} can be assigned to the stretching of Fe-N₄ bonds in the porphyrin moiety, and the band at 393 cm^{-1} can be attributed to Fe-N in plane vibrations of the porphyrin core.^{14,15,16} Also, the intense peak at 362 cm^{-1} can be associated to the out-of-plane angle bend of the C=O bonds in the thermoresponsive polymer.¹³ These signals indicate that the porphyrin moiety present in the nanocomposite-laden polymer was able to bind iron (III) ions lodged in the structure of the sample of artificial archaeological wood, and from the *Mary Rose* wood.

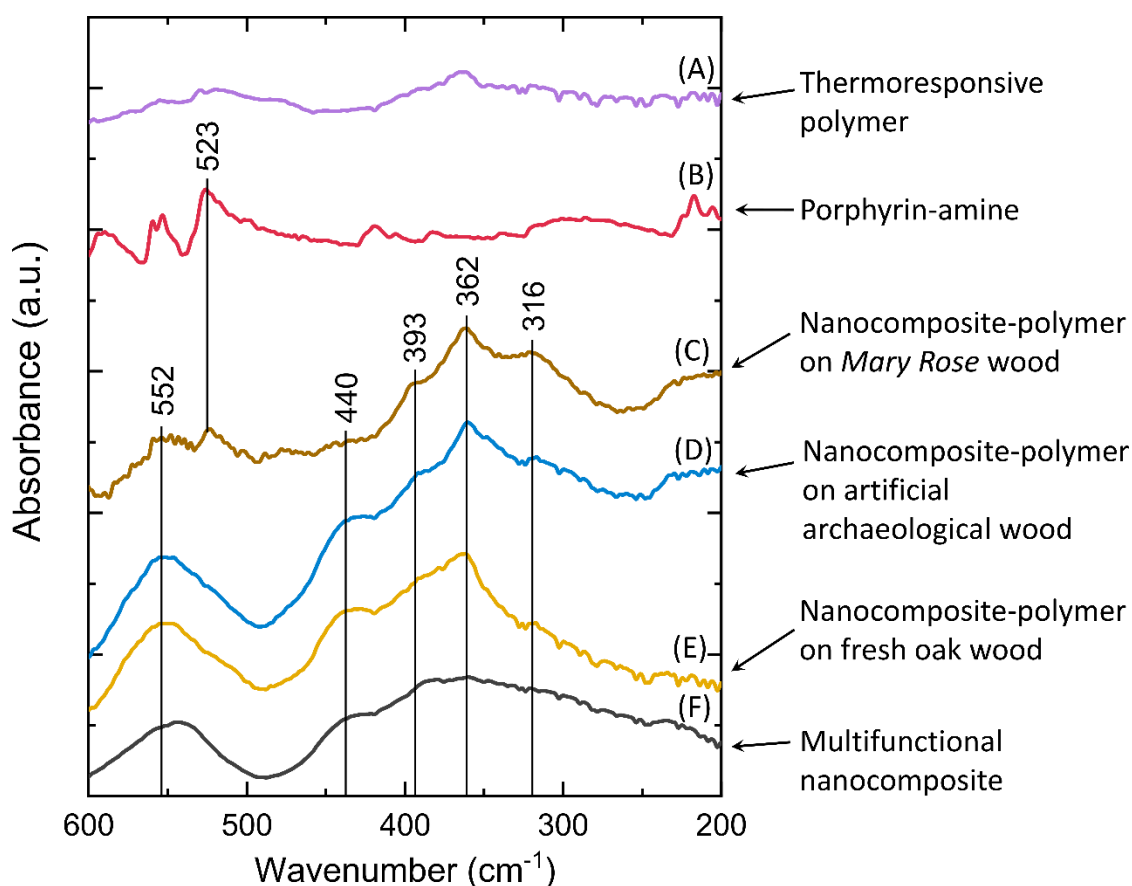


Figure 4.23. Far IR spectroscopy of nanocomposite-laden polymer after treating (C) *Mary Rose* wood, (D) artificial archaeological oak and (E) fresh oak. For comparison, the spectra of (A) thermoresponsive polymer, (B) porphyrin-amine and (F) multifunctional nanocomposite are included. The bands observed at 552 and 440 cm^{-1} correspond to the Fe-O stretches in magnetite, and the rotation of the pyrrole rings in the porphyrin moiety, respectively. The characteristic band at 362 cm^{-1} can be associated to the oop angle bends of the C=O bonds in the thermoresponsive polymer. The band at 393 cm^{-1} can be assigned to Fe-N in plane core vibrations, while the band at 316 cm^{-1} can be attributed to the stretching of Fe-N in the porphyrin moiety.

4.7 Conclusions

In this chapter, the diffusion and potential application routes for the PPIX/PEG 200 functionalised nanoparticles have been studied. Aqueous suspensions of these functionalised nanoparticles were applied on oak samples and its diffusion through the wood structure was studied under the effect of an external magnetic field. The diffusion of the functionalised nanoparticles was also compared to that of bare Fe_3O_4 . The diffusion of the functionalised nanoparticles under an external magnetic field was found to be only about 1.5 mm. A thermoresponsive polymer was then designed and synthesised for its use as a vehicle, with the aim of a more controlled application and removal of the functionalised nanoparticles. The polymer $\text{p}(\text{DEGMA}_{45}\text{-co-MMA}_5)$ was synthesised and its structure was confirmed by ^1H NMR. A LCST of 26 °C was estimated by variable-temperature UV-visible spectroscopy. The polymer-mixed-nanocomposite was tested on artificial archaeological oak to evaluate its abilities for iron removal. Far IR spectroscopy revealed a peak at 318 cm^{-1} , which could be attributed to the stretching of Fe-N bonds in the porphyrin moiety. This could indicate that iron ions have been chelated by the porphyrin moiety in the nanocomposite, however, the intensity of this signal is low.

Furthermore, another multifunctional nanocomposite ($\text{Fe}_3\text{O}_4\text{-VTES-p}(\text{DEGMA}_{45}\text{-co-MMA}_5)\text{-porphyrin}$) was devised and prepared. This multifunctional nanocomposite, and the thermoresponsive polymer constitute the two main building blocks of a conservation treatment designed for the removal of iron ions from archaeological wood. The prepared multifunctional nanocomposite ($\text{Fe}_3\text{O}_4\text{-VTES-p}(\text{DEGMA}_{45}\text{-co-MMA}_5)\text{-porphyrin}$) has been characterised by XRD, ^1H NMR, TGA, FTIR, UV-visible and fluorescence spectroscopies, variable-temperature UV-visible spectroscopy, and DLS. The magnetite nanoparticles were found to be Fe_3O_4 , and matched the standard of cubic spinel magnetite (Fe_3O_4 , JCPDS index card no. 19-629). The synthesis of the porphyrin-polymer was monitored by ^1H NMR, confirming that the final product contained a porphyrin unit and a thiol end group as expected. The LCST of the porphyrin-polymer was investigated by variable-temperature UV-visible spectroscopy, finding a transition temperature of 23 °C. The attachment of the porphyrin-polymer onto the magnetic nanoparticles was studied by TGA and FTIR. Thermal analyses showed the presence of an organic coating, and FTIR spectroscopy confirmed the nature of such coating. Variable-temperature UV-visible spectroscopy showed a LCST of 23 °C for the porphyrin-polymer. The temperature dependence of the hydroscopic diameter of the multifunctional nanocomposite was evaluated by DLS, showing a variation in diameter

between 210 and 170 nm. The transition temperature observed was 20-22 °C, similar to the LCST estimated by variable-temperature UV-visible spectroscopy.

Finally, the ability of the multifunctional nanocomposite to sequester iron ions was studied in solution and onto wood. Ethanolic and aqueous solutions of Fe(III) were treated with the multifunctional nanocomposite, and the concentration of free iron in solution was monitored over time with UV-visible spectroscopy and atomic absorption spectroscopy. The studies performed with UV-visible spectroscopy showed a decrease in the intensity of the band at 283 nm, characteristic of Fe(III), upon addition of functionalised nanoparticles over time. Likewise, an aqueous solution of Fe(III) was treated with the multifunctional nanocomposite, and the concentration of iron was monitored over time by atomic absorption spectroscopy. These measurements showed a marked decrease in concentration of 39 % over a period of 6-7 hours. Furthermore, the multifunctional nanocomposite was encapsulated into the thermoresponsive polymer for an optimal application on wood. The nanocomposite-laden polymer was used to treat artificial archaeological oak and *Mary Rose* wood, and it was later studied by far IR spectroscopy to assess its effectiveness in sequestering iron ions from the wood structure. Two characteristic bands were observed at 316 and 393 cm^{-1} . These can be attributed to the stretching of Fe-N₄ bonds and to the Fe-N in plane vibrations within the porphyrin core, respectively. This results indicate that iron has been chelated by the porphyrin in the nanocomposite-laden polymer, and successfully removed from the structure of artificial archaeological oak and *Mary Rose* wood. This is the first report of the targeted removal of iron from artificial archaeological wood and archaeological wood, in the frame of an archaeological conservation. This also has been done for the first time on already dry and conserved wooden artefacts. Moreover, this has been done in a non-invasive manner by exploiting the combination of the thermal responsiveness of the polymer and the magnetic nature of the Fe₃O₄ nanoparticles. While the thermoresponsive polymer allows a controlled manipulation and enhanced diffusion of the multifunctional nanocomposite with small variations in temperature (2-3 °C), the magnetic nature of the nanoparticles allows for a precise application of the treatment.

References

- 1 C. Corot, P. Robert, J.-M. Idée and M. Port, *Adv. Drug Deliv. Rev.*, 2006, **58**, 1471-1504.
- 2 M. Bonini, S. Lenz, E. Falletta, F. Ridi, E. Carretti, E. Fratini, A. Wiedenmann and P. Baglioni, *Langmuir*, 2008, **24**, 12644-12650.
- 3 N. S. leong, K. Brebis, L. E. Daniel, R. K. O'Reilly and M. I. Gibson, *Chem. Commun.*, 2011, **47**, 11627.
- 4 N. S. leong, M. Hasan, D. J. Phillips, Y. Saaka, R. K. O'Reilly and M. I. Gibson, *Polym. Chem.*, 2012, **3**, 794.
- 5 M. I. Gibson and R. K. O'Reilly, *Chem. Soc. Rev.*, 2013, **42**, 7204-13.
- 6 G. Gotzamanis and C. Tsitsilianis, *Polymer (Guildf.)*, 2007, **48**, 6226-6233.
- 7 M. I. Gibson, D. Paripovic and H.-A. Klok, *Adv. Mater.*, 2010, **22**, 4721-4725.
- 8 C. Pearson, *Conservation of marine archaeological objects*, Butterworths, 1987.
- 9 J. C. Bevington, *Makromol. Chemie. Macromol. Symp.*, 1987, **10-11**, 89-107.
- 10 Florian Paulat, V. K. K. Praneeth, and Christian Näther and N. Lehnert*, *Inorg. Chem.*, 2006, **45**, 2835-2856.
- 11 M. L. Mitchell, X. Y. Li, J. R. Kincaid and T. G. Spiro, *J. Phys. Chem.*, 1987, **91**, 4690-4696.
- 12 S. Dörr, U. Schade, P. Hellwig and M. Ortolani, *J. Phys. Chem. B*, 2007, **111**, 14418-14422.
- 13 J. F. Rabolt, W. H. Moore and S. Krimm, *Macromolecules*, **10**, 1065-74.
- 14 B. M. Leu, M. Z. Zgierski, G. R. A. Wyllie, W. R. Scheidt, W. Sturhahn, E. Ercan Alp, S. M. Durbin and J. T. Sage, *J. Am. Chem. Soc.*, 2004, **126**, 4211-4227.
- 15 B. K. Rai, S. M. Durbin, E. W. Prohofsky, J. Timothy Sage, G. R. A Wyllie, W. Robert Scheidt, W. Sturhahn and E. Ercan Alp, *Biophys. J.*, 2002, **82**, 2951-2963.
- 16 L. Marboutin, A. Desbois and C. Berthomieu, *J. Phys. Chem. B*, 2009, **113**, 4492-4499.
- 17 M. J. Williams, E. Sánchez-Pérez, E. R. Aluri, F. J. Douglas, D. A. Maclaren, O. M. Collins, E. J. Cussen, J. D. Budge, L. C. Sanders, M. Michaelis, C. M. Smales, J. Cinatl, S. Lorrio, D. Krueger, R. T. M. De Rosales and S. A. Corr, *RSC Adv.*, 2016, **6**, 83520-83528.
- 18 Y. Yong, Y. Bai, Y. Li, L. Lin, Y. Cui and C. Xia, *J. Magn. Magn. Mater.*, 2008, **320**, 2350-2355.
- 19 M. Araghi, V. Mirkhani, M. Moghadam, S. Tangestaninejad and I. Mohammdpoor-Baltork, *Dalt. Trans.*, 2012, **41**, 3087.
- 20 X.-P. Qiu and F. M. Winnik, *Macromol. Rapid Commun.*, 2006, **27**, 1648-1653.

- 21 H. Li, B. Yu, H. Matsushima, C. E. Hoyle and A. B. Lowe, *Macromolecules*, 2009, **42**, 6537-6542.
- 22 Y. Kotsuchibashi, M. Ebara, T. Aoyagi and R. Narain, *Polym. Chem.*, 2012, **3**, 2545.
- 23 D. P. Nair, M. Podgórski, S. Chatani, T. Gong, W. Xi, C. R. Fenoli and C. N. Bowman, *Chem. Mater.*, 2014, **26**, 724-744.
- 24 M. Uygun, M. A. Tasdelen and Y. Yagci, *Macromol. Chem. Phys.*, 2010, **211**, 103-110.
- 25 M. Nowostawska, S. A. Corr, S. J. Byrne, J. Conroy, Y. Volkov and Y. K. Gun'ko, *J. Nanobiotechnology*, 2011, **9**, 13.
- 26 E. Keleş, B. Hazer and F. B. Cömert, *Mater. Sci. Eng. C*, 2013, **33**, 1061-1066.
- 27 S. A. Corr, A. O' Byrne, Y. K. Gun'ko, S. Ghosh, D. F. Brougham, S. Mitchell, Y. Volkov and A. Prina-Mello, *Chem. Commun.*, 2006, **0**, 4474.
- 28 D. R. Lide and G. W. A. Milne, *Handbook of data on common organic compounds*, CRC Press, 1995.
- 29 J. Chen, M. Liu, C. Chen, H. Gong and C. Gao, *ACS Appl. Mater. Interfaces*, 2011, **3**, 3215-3223.
- 30 R. Liu, P. Zhang and H. Dai, *J. Polym. Res.*, 2016, **23**, 218.
- 31 G. Le Truong, T. Nguyen Ngoc, Q. T. Nguyen, J. De Laat and H. Y. Dao, *J. Adv. Oxid. Technol.*, 2014, **17**, 305-330.
- 32 S. Dörr, U. Schade and P. Hellwig, *Vib. Spectrosc.*, 2008, **47**, 59-65.

Chapter 5 - Thermoresponsive polymer-mixed DTPA-functionalised nanocomposite for marine archaeological wood conservation

5.1 Introduction

Thus far, various methods for the sequestration of iron ions from archaeological wood based in porphyrin derivatives have been devised, prepared, and fully characterised in this work. Due to the composite nature of the treatments designed, the logical step to follow on was to explore variations of the different components of this system. Thus, the next step was the investigation of alternative iron chelating agents. One of the main reasons to explore alternative chelating agents was the potential role of porphyrin derivatives in the degradation of the cellulose fibres of the treated wood. Porphyrins and metalloporphyrins are highly-valued photosensitizers with specific photocatalytic properties, for which they are used in a variety of fields like photocatalysis, solar energy conversion, photodynamic therapy, and photodegradation of organic pollutants.^{1,2,3,4} On absorption of radiation, these photosensitizers can relax *via* inter-system crossing to generate an excited triplet state. The energy of this state can be further transferred to molecular oxygen in the triplet ground state ($^3\text{O}_2$), generating a singlet excited state of molecular oxygen ($^1\text{O}_2$). Particularly, porphyrins and metalloporphyrins have a high photogenerated singlet oxygen yield and good electron donating properties due to their large π -electron system.⁵ Singlet oxygen is a powerful oxidant species, more reactive than ground state molecular oxygen. Therefore, there may be concerns regarding the potential threat of photodegradation of cellulose fibres in the wood by singlet oxygen generated by the porphyrin moieties used. It should be noted that all timbers and wooden artefacts recovered from the *Mary Rose* are kept under controlled temperature, humidity and dim light, which mitigates the risk of photodegradation of the cellulose. The exploration of alternatives to porphyrin-based iron chelating agents was then considered a priority in order to make a step forward in the development of efficient, safe and minimally invasive treatments for iron removal. In this regard, and as discussed in **Section 1.7**, the great variety of chelating agents available means that this is one of the areas in the design of these multifunctional nanocomposites where there is more potential for exploration and tunability. After careful considerations, the aminopolycarboxylic acid family was deemed interesting since these are well recognised chelating agents, used in a wide variety of applications and have also been used in the early stages of the conservation of the *Mary Rose* and *Vasa*.^{6,7}

Notably, diethylenetriamine pentaacetic acid (pentetic acid, DTPA) was found of particular interest. Unlike ethylenediaminetetraacetic acid (EDTA), DTPA consists of

three amine groups with lone pair electrons, and five carboxyl groups: eight available donor groups in total, making it a potential octadentate ligand. Iron ions can form stable coordination compounds with a variety of tetradentate and hexadentate ligands in octahedral geometries.^{8,9,10,11} The use of an octadentate ligand could provide the possibility of attaching it to other molecules or substrates while keeping at least six donor groups available for complexing iron ions in an octahedral environment. This is of importance in this work since the aim is to covalently bind the chelating agents to linkers, and this way DTPA would still have at least six donor groups available to form metal chelates.

Thus, a nanocomposite featuring DTPA molecules covalently bonded to the surface of magnetite nanoparticles was devised. In this case the DTPA functionalised nanoparticles (DTPA-nanocomposite) were prepared in a one-pot process, where the magnetite nanoparticles were synthesised by MW co-precipitation, and were functionalised with APTES and DTPA in subsequent steps. **Figure 5.1** describes the structure of the designed DTPA-nanocomposite, showing how DTPA is anchored to the magnetite nanoparticle *via* an APTES molecule. It also shows DTPA as a hexadentate ligand where the three amine and three carboxyl groups are forming a metal chelate, and two carboxyl groups are left unused.

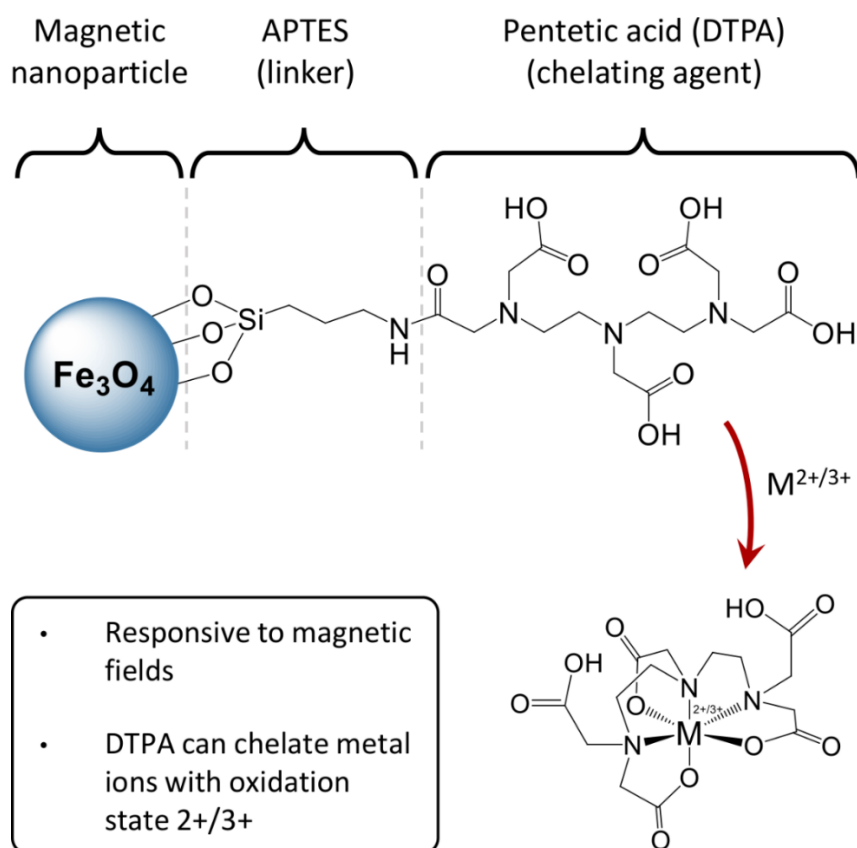


Figure 5.1. Schematic of the DTPA-nanocomposite. APTES is used to attach the chelating agent DTPA to the surface of the magnetic nanoparticles. This DTPA-nanocomposite has been devised to chelate iron ions by means of the DTPA moieties and to be manipulated with external magnetic fields. It can also be encapsulated in a thermoresponsive polymer for a magnetically and temperature controlled application.

This chapter describes the preparation of Fe₃O₄ nanoparticles functionalised with DTPA. These functionalised nanoparticles have also been fully characterised and its iron chelating properties have been evaluated in solution. Furthermore, this DTPA-nanocomposite has been encapsulated in a thermoresponsive polymer in order to study its potential application for the sequestration of iron ions from archaeological wood.

5.2 Results and discussion

5.2.1 Preparation of Fe₃O₄-APTES-DTPA (DTPA-nanocomposite)

5.2.1.1 Strategies for functionalisation

In this work, the attachment of several moieties onto the surface of magnetite nanoparticles *via* an alkoxysilane linker is described. Alkoxysilanes can form strong and stable covalent bonds with metal oxide surfaces, and thus are widely used for anchoring biological and organic functionalities on this type of substrates.^{12,13} In **Chapter 3**, the successful attachment of Protoporphyrin IX and PEG 200 onto iron oxide nanoparticles, using APTES as a linker, has been described. The amine end of APTES was used to react with the carboxyl functionalities present in both Protoporphyrin IX and PEG 200-acid, leading to the formation of an amide bond with each moiety. **Chapter 4** describes the successful functionalisation of magnetite nanoparticles with a polymeric moiety by means of VTES. The vinyl group in VTES and the thiol end-group of the polymer reacted *via* a thiol-ene click reaction. Due to the positive results obtained in the design of these nanocomposites, it was decided to follow a similar strategy in order to graft DTPA onto magnetite nanoparticles. Since DTPA features five carboxyl groups, an amine-terminated alkoxysilane was deemed the most suitable option in order to form an amide bond. The strategy followed also aimed to optimise the duration of the process. A one-pot process was devised in which the synthesis of iron oxide nanoparticles and the subsequent functionalisation stages were carried out in various steps within a single pot, optimising the use of solvents and the overall duration of the process.

5.2.1.2 Synthesis and characterisation of DTPA-nanocomposite

Unlike the synthetic methods used for the nanocomposites described in previous chapters, a bottom-up approach was used in this case. Here, the strategy adopted consisted of the initial MW co-precipitation of magnetite nanoparticles in aqueous media, followed by the functionalisation of the nanoparticle's surface with APTES, and the final attachment of DTPA to the amine group in APTES. This synthesis was carried out as a one-pot three-step process, where the reagents were added, reacted and washed in the same flask, in consecutive steps.

Iron oxide nanoparticles were prepared following a slight variation of the method developed by Williams *et al.*, described in **Section 2.3.2.1**.¹⁴ Briefly, stoichiometric amounts of iron (II) and iron (III) chloride hydrated salt were dissolved in deionised water and, on addition of ammonia, Fe₃O₄ nanoparticles were precipitated. Finally, a short

microwave treatment yielded highly crystalline and monodisperse Fe_3O_4 nanoparticles. The black precipitate obtained was washed with water and ethanol, and finally dispersed in 30 mL of dry ethanol by sonication during 30 minutes. Following a method adapted from Yong *et al.*¹⁵, ammonia was added under inert atmosphere and stirred briefly. Then, APTES was added to the suspension dropwise in order to favour the condensation onto the surface of nanoparticles, and to avoid the possible autocondensation due to a rapid increase of concentration of the silane. The mixture was stirred overnight at 50 °C and the product was magnetically decanted and washed with ethanol and deionised water. Lastly, the nanoparticles coated in APTES were dispersed in DMF by means of sonication for 10 minutes. Then, TEA was added, followed by diethylenetriamine pentaacetic acid dianhydride (DTPA-da). Here, the role of TEA was to avoid the protonation of the amide, favouring the forward reaction. DTPA-da was selected as the source of DTPA since in this compound the carboxyl groups are pre-activated, in the form of anhydrides, for the nucleophilic attack from the amine in APTES. The reaction mixture was stirred at 80 °C for 30 minutes and then at room temperature overnight under inert atmosphere. The product was magnetically decanted and washed with a diluted solution of TEA in DMF, deionised water and acetone, and finally dried under vacuum. **Figure 5.2** displays a schematic of the steps followed in the preparation of the DTPA functionalised nanoparticles. This synthesis is described in detail in **Section 2.3.1.2.2**.

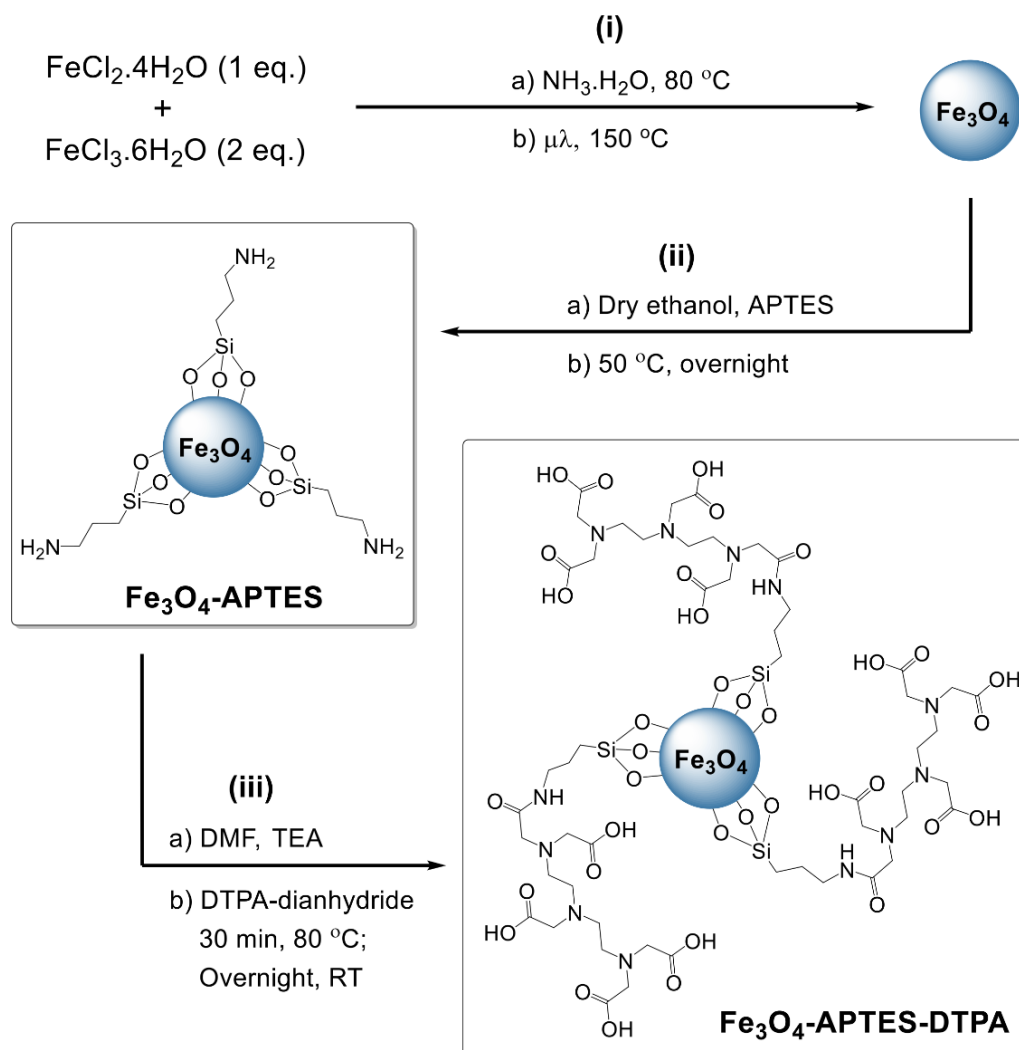


Figure 5.2. Schematic of the one-pot synthesis of DTPA-nanocomposite (Fe_3O_4 -APTES-DTPA). (i) Highly crystalline iron oxide nanoparticles were prepared by MW co-precipitation in aqueous media. (ii) The iron oxide nanoparticles were coated with (3-aminopropyl) triethoxysilane (APTES), which provided a convenient coating with amine groups. (iii) DTPA-da was finally anchored to the amino-coated nanoparticles *via* an amide bond between the amide and anhydride group.

The preparation of Fe_3O_4 -APTES-DTPA was monitored by various characterisation techniques to ensure the desired intermediate products were successfully obtained. **Figure 5.3** shows the XRD patterns obtained from dry precipitates of Fe_3O_4 , Fe_3O_4 -APTES, and Fe_3O_4 -APTES-DTPA alongside an ICSD cubic spinel magnetite standard (Fe_3O_4 , JCPDS index card no. 19-629). All three patterns show a very good concordance with the $Fd\bar{3}m$ space group, and matched the spinel magnetite standard, confirming Fe_3O_4 nanoparticles remained unaltered throughout the subsequent steps of the synthesis. The crystallite size of Fe_3O_4 was estimated with the Scherrer equation applied to the diffraction peak (311),

obtaining a value of 14 nm. This value did not show significant variations in the subsequent functionalisation stages of the synthesis. This indicates that the functionalisation steps, in which APTES and DTPA were anchored onto the surface, did not affect the crystallinity of the nanoparticle, and therefore its intrinsic magnetic properties.

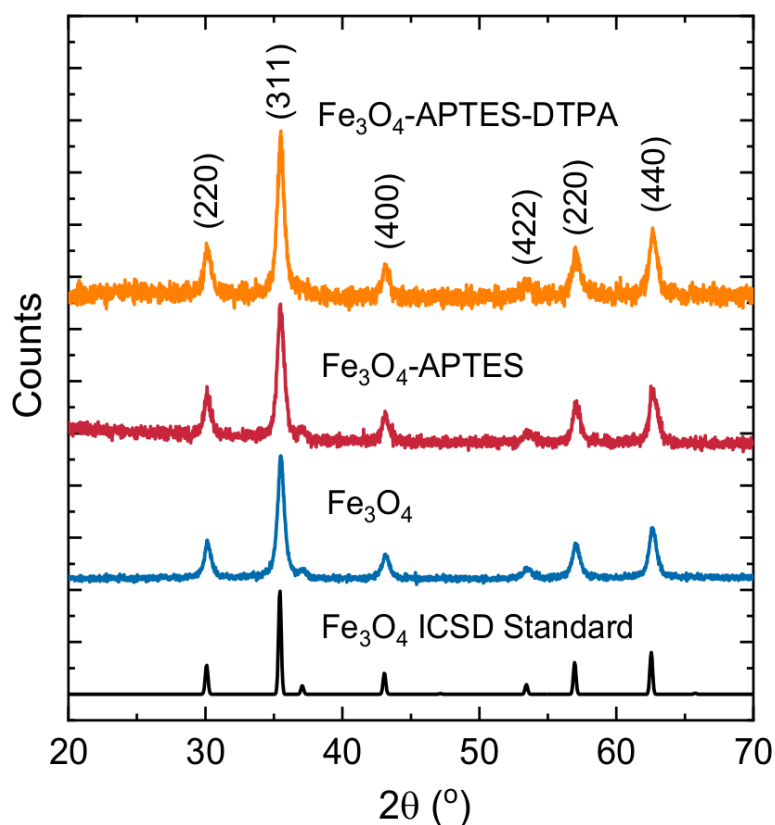


Figure 5.3. Powder XRD patterns obtained from Fe_3O_4 (blue), Fe_3O_4 -APTES (red) and Fe_3O_4 -APTES-DTPA (orange). The three patterns are in good agreement with the standard of inverse spinel magnetite (Fe_3O_4 , JCPDS index card no.19-629), plotted in black. This indicates that the morphology of the magnetite nanoparticles was not affected by the functionalisation with APTES and DTPA. The broad diffraction peaks observed are characteristic of nanostructured materials. The average crystallite size calculated with the Scherrer equation is 14 nm.

The nature of the coating layers attached to the nanoparticles was examined by FTIR spectroscopy in attenuated total reflectance mode (ATR). **Figure 5.4** shows the spectra obtained from bare Fe_3O_4 nanoparticles, Fe_3O_4 -APTES, and Fe_3O_4 -APTES-DTPA. The intense signal at 539 cm^{-1} is due to the stretches of the Fe-O bond in magnetite. The broad

peak at 991 cm^{-1} is attributed to the stretches of the Si-O-Fe bond originated from the attachment of APTES onto the magnetite nanoparticles. The band at 1632 cm^{-1} can be attributed to the vibrations of the C=O bonds present in the DTPA anchored onto the nanoparticles. Finally, the signal at 1389 cm^{-1} can be attributed to the amide II band, originated by the C-N stretching vibrations in combination with the N-H bending.

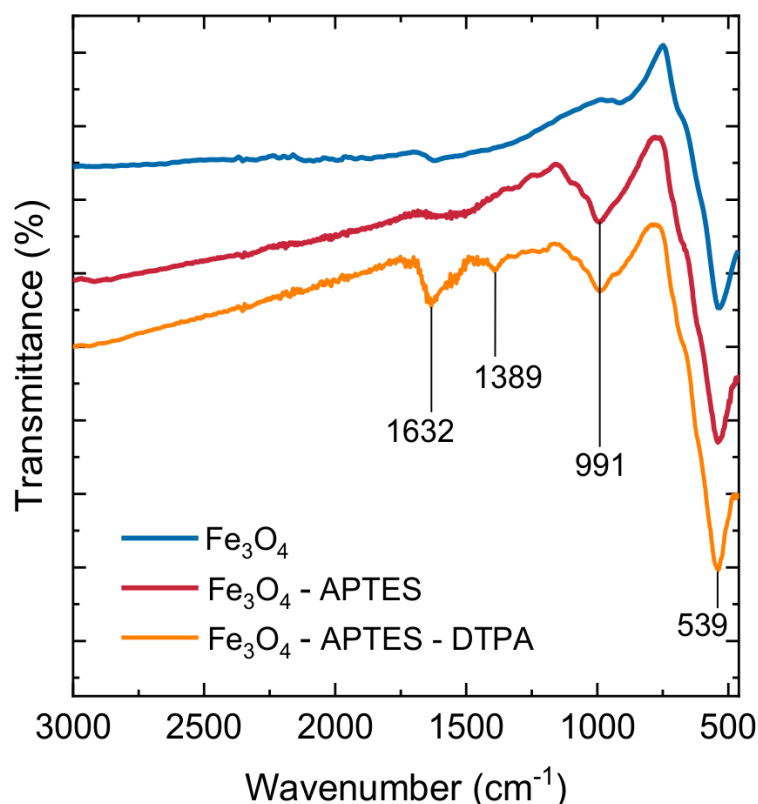


Figure 5.4. FTIR spectra of Fe₃O₄, Fe₃O₄-APTES and Fe₃O₄-APTES-DTPA. The intense band at 539 cm^{-1} corresponds to the stretches of the Fe-O bond. The broad band at 991 cm^{-1} is due to the stretches of the Si-O-Fe bond. The intense band at 1632 cm^{-1} is attributed to the vibrations of the C=O bonds present in the DTPA moiety. Finally, the weak band at 1389 cm^{-1} can be assigned to the amide II band. These signals confirm the successful attachment of APTES and DTPA onto the iron oxide nanoparticles.

The attachment of APTES and DTPA onto the nanoparticles was also studied by thermogravimetric analysis (TGA). Dry precipitates of Fe₃O₄, Fe₃O₄-APTES, and Fe₃O₄-APTES-DTPA were heated from room temperature up to $700\text{ }^{\circ}\text{C}$ under nitrogen, with a heating rate of $10\text{ }^{\circ}\text{C}/\text{minute}$, and the TGA curves obtained are shown in **Figure 5.5**. The Fe₃O₄ curve shows a slight mass loss of 1.5 %, most likely caused by the desorption of

water molecules physisorbed onto the surface of the nanoparticles. The curve corresponding to Fe_3O_4 -APTES shows a marked mass loss of 4 % starting at 250 °C, followed by a slight increase in mass at 550 °C. The decrease in mass corresponds to the loss of the APTES attached to the surface. The slight increase in weight is a common occurrence, and could be explained by the oxidation of the silane groups into silicon oxide. Finally, the curve corresponding to Fe_3O_4 -APTES-DTPA shows a greater mass loss of 10 %, revealing the presence of an extra organic layer onto the nanoparticles. For clarity, the mass loss of the three samples is compared at 550 °C, where Fe_3O_4 -APTES reaches the highest value in mass loss. These values are in reasonable good agreement with those reported in literature.^{16,17} TGA studies suggest that APTES and DTPA have been successfully grafted onto the magnetite nanoparticles.

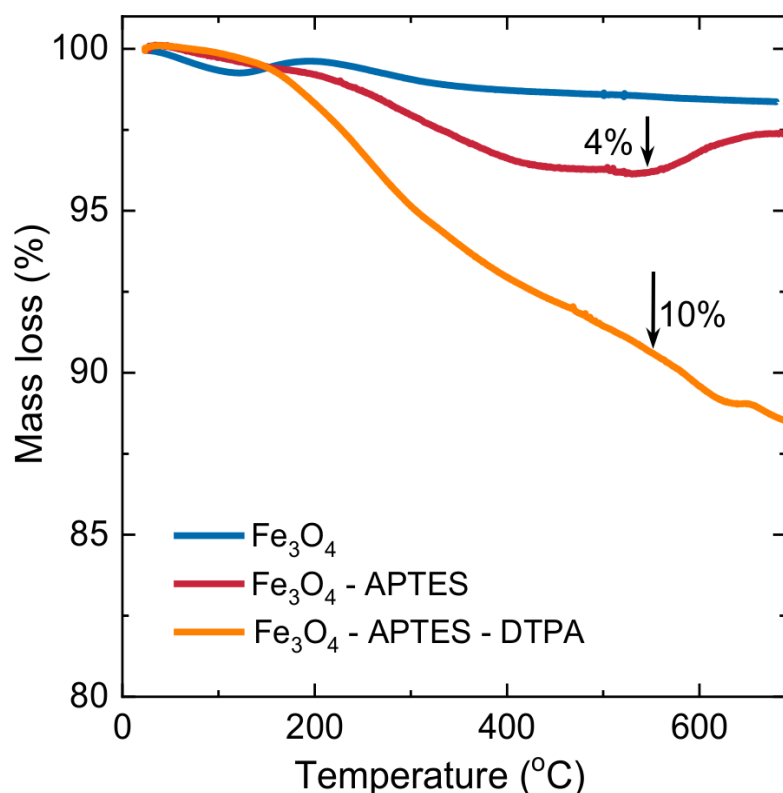


Figure 5.5. TGA curves of from Fe₃O₄ (blue), Fe₃O₄-APTES (red) and Fe₃O₄-APTES-DTPA (orange) obtained between 25 and 700 °C in N₂ atmosphere. The mass loss of 1.5 % in Fe₃O₄ can be explained by the loss of water molecules physisorbed and. Fe₃O₄-APTES and Fe₃O₄-APTES-DTPA show a mass loss of 4 % and 10 % at 550 °C, respectively, which indicates the attachment of the organic layers onto the magnetic nanoparticles. The slight gain in mass of Fe₃O₄-APTES after this temperature can be explained by the oxidation of the degraded silane.

5.2.2 Evaluation of iron chelation of the DTPA-nanocomposite

5.2.2.1 Evaluation of iron sequestration in solution

The next step in the development of the DTPA-nanocomposite is to study its ability to sequester iron ions. The performance tests were carried out in solution and analysed by UV-visible spectroscopy and atomic absorption spectroscopy (AAS), in a similar way to the nanocomposites described in previous chapters.

Thus, an ethanolic solution of Fe₂(SO₄)₃·7H₂O was treated with successive additions of a suspension of Fe₃O₄-APTES-DTPA, and UV-visible spectra were collected ten minutes after every addition of the nanoparticles. **Figure 5.7 (A)** shows the UV-visible spectra obtained during the treatment with the DTPA-functionalised nanoparticles. The band at 284 nm, corresponding to the free Fe(III) present in solution, decreases in intensity upon

addition of the DTPA functionalised nanoparticles. This suggests that the DTPA present in the nanoparticles is able to chelate iron ions from solution. Also, **Figure 5.6 (B)** shows the absorbance values from an ethanolic solution of $\text{Fe}_2(\text{SO}_4)_3 \cdot 7\text{H}_2\text{O}$ collected at a fixed wavelength of 284 nm during a similar treatment with the DTPA functionalised nanoparticles. The decrease in absorbance indicates a decrease of the concentration of Fe(III), proving the capacity of the DTPA-nanocomposite to remove iron ions form solution.

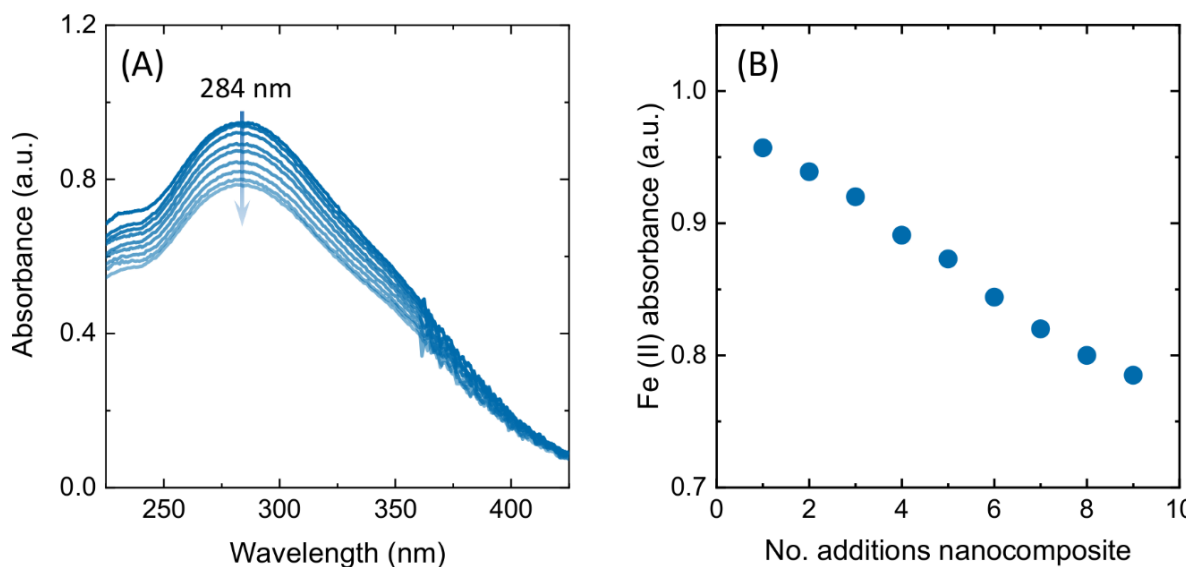


Figure 5.6. Evaluation of chelation of free iron in solution with UV-visible spectroscopy. (A) UV-visible absorption spectra of an ethanolic solution of $\text{Fe}_2(\text{SO}_4)_3 \cdot 7\text{H}_2\text{O}$ (0.2 mM) treated with a suspension of Fe_3O_4 -APTES-DTPA in ethanol (0.6 mg/mL, additions of 20 μL). The absorbance at 284 nm decreases upon addition of DTPA functionalised nanoparticles. (B) Absorbance of an ethanolic solution of $\text{Fe}_2(\text{SO}_4)_3 \cdot 7\text{H}_2\text{O}$, obtained at a fixed excitation wavelength ($\lambda_{\text{exc}} = 284 \text{ nm}$). The absorbance decreases upon addition of DTPA functionalised nanoparticles.

Further to these studies, the performance of the DTPA-nanocomposite was also studied by AAS. The concentration of iron in an aqueous solution was monitored over time while it was treated with the DTPA functionalised nanoparticles. A solution of $\text{FeSO}_4 \cdot 7\text{H}_2\text{O}$ (4.84 mg/mL) was treated with a suspension of Fe_3O_4 -APTES-DTPA (0.6 mg/L) over a period of 90 minutes. Periodically, the nanoparticles were magnetically decanted and a sample of the solution was taken and analysed with AAS. **Figure 5.7** shows the values of the atomic absorbance of the iron present in solution. The results obtained show a rapid decrease of concentration of iron in the first 5 minutes, and a subsequent stabilisation at 30 minutes. The amount of iron removed from solution under these conditions was 50 %,

and this was achieved after only 30 minutes of treatment. This study shows again the capacity of the DTPA-nanocomposite to sequester iron ions.

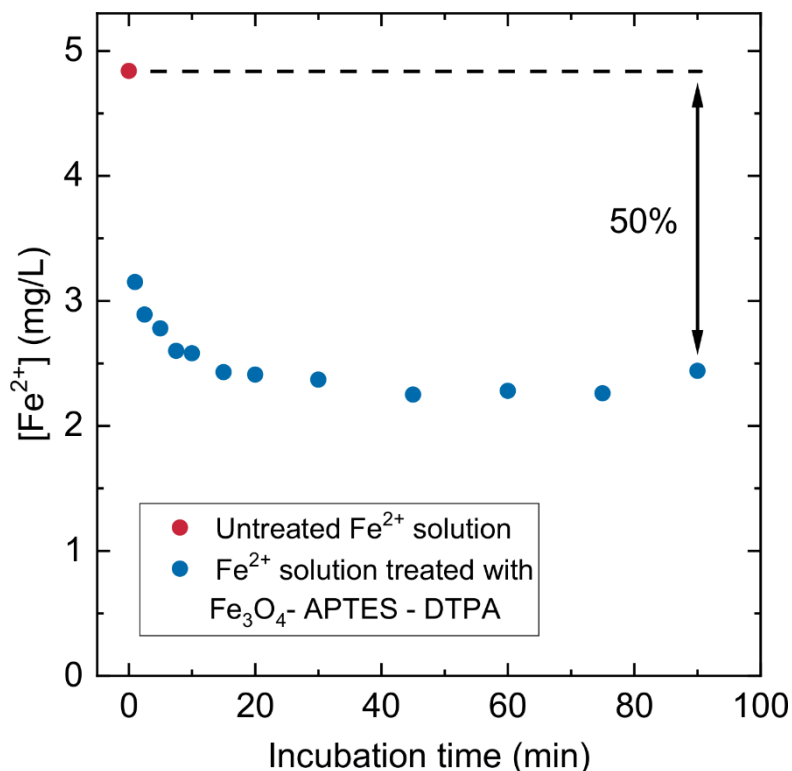


Figure 5.7. Atomic absorption spectroscopy was used to monitor the concentration of Fe(II) of an aqueous solution being treated with DTPA-functionalised nanoparticles. Results show that Fe₃O₄-APTES-DTPA was able to reduce the initial concentration of free Fe(II) (4.84 mg/mL) by 50 % within 30 minutes.

5.2.2.2 Evaluation of iron chelation in wood

5.2.2.2.1 Preparation of thermoresponsive polymer-mixed DTPA-functionalised nanocomposite (polymer-mixed DTPA-nanocomposite)

A similar strategy to the one described in Chapter 4 was followed for the application of the DTPA-nanocomposite onto the wood to be treated. A thermoresponsive polymer, p(DEGMA₄₅-co-MMA₅), prepared as described in Section 2.3.2, was used as a vehicle to apply and remove the nanoparticles in a safe and precise manner. Thus, for the preparation of the polymer-mixed DTPA-nanocomposite, the thermoresponsive polymer was first dissolved in a small amount of ethanol with the help of ultrasound. Then the

DTPA-nanocomposite was added to the solution and sonicated for better dispersion. The nanoparticles-to-polymer ratio employed was 1:5. Finally, the mixture was stirred for five minutes and put under vacuum to evaporate the solvent.

5.2.2.2.2 Application of polymer-mixed DTPA-nanocomposite on artificial archaeological oak

Fresh and artificial archaeological oak samples were treated with the polymer-mixed DTPA-nanocomposite in order to test its capability to remove iron ions from the wood matrix. For this, the polymer-mixed DTPA-nanocomposite was first cooled down and then portions of 20 mg were applied onto the oak samples with a plastic spatula. The samples were placed atop a permanent magnet (1.3 Tesla) and the treatment was run for four weeks at 5 °C. After this period, the samples were covered in transparent film and the magnetic field was applied in the reverse direction for one week at 5 °C. The polymer-mixed DTPA-nanocomposite was carefully removed with a soft plastic spatula to be examined by far IR spectroscopy. **Figure 5.8** shows images of the process described. Samples of (A) fresh oak and (B) artificial archaeological oak are sitting onto a permanent magnet while being treated with the polymer-mixed DTPA-nanocomposite. Once the treatment period is finished, the samples (C and D) are wrapped in a transparent film and flipped over the permanent magnet. The treatment (E) is finally removed with a plastic spatula.

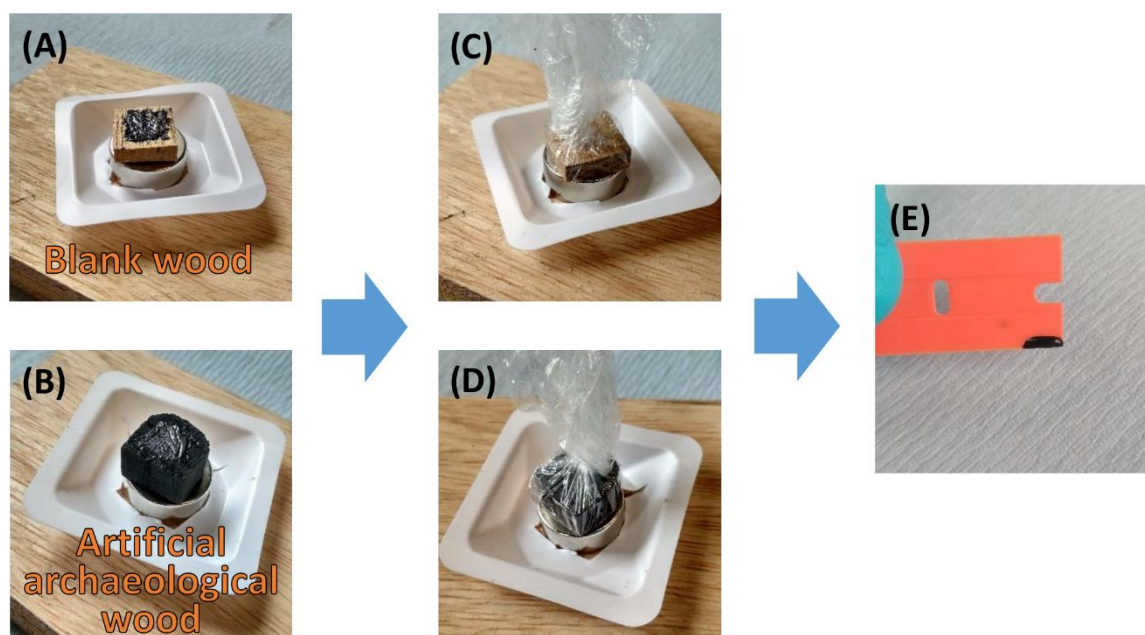


Figure 5.8. Polymer-mixed DTPA-nanocomposite was applied onto (A) fresh oak and (B) artificial archaeological oak. These samples were placed atop a 1.3 Tesla permanent magnet, and incubated for 4 weeks at 5 °C. After the incubation period, the treated wood samples (C and D) were protected by transparent film and placed upside down onto the permanent magnet for one week at 5 °C. Finally, the samples were brought to room temperature and the polymer mixed DTPA-nanocomposite was peeled off the surface of the oak samples.

5.2.2.2.3 Evaluation of the iron sequestration properties of polymer-mixed DTPA-nanocomposite

The performance of this treatment based on DTPA as the iron sequestering agent was studied with far IR spectroscopy. **Figure 5.9** shows the far IR spectra collected from the treatments applied onto fresh oak and artificial archaeological oak. The spectrum of the thermoresponsive polymer is included for comparison. The broad signal observed at 560 cm^{-1} is associated with the stretches of the Fe-O bond in magnetite. The band at 362 cm^{-1} can be attributed to the C=O bonds in the thermoresponsive polymer.¹⁸ Bands found at $390\text{-}394$ and $316\text{-}320\text{ cm}^{-1}$ can be normally assigned to the in plane vibrations and stretchings of the Fe-N bonds, respectively.^{19,20,21} Weak signals are found at 392 and 318 cm^{-1} in the spectrum of the treatment applied to artificial archaeological oak, which are only slightly more intense than those observed in the fresh oak treatment. Weaker intensities might be expected in the case of the DTPA-composite, as the mode of binding to iron here includes both Fe-O and Fe-N binding. It is difficult to ascertain from these spectra the contribution of Fe-O binding in DTPA, since these bands would overlap with

those from the iron oxide particles themselves. There may also be some competing steric hindrance for iron binding to the DTPA and future work would include optimising the binding capability of this treatment.

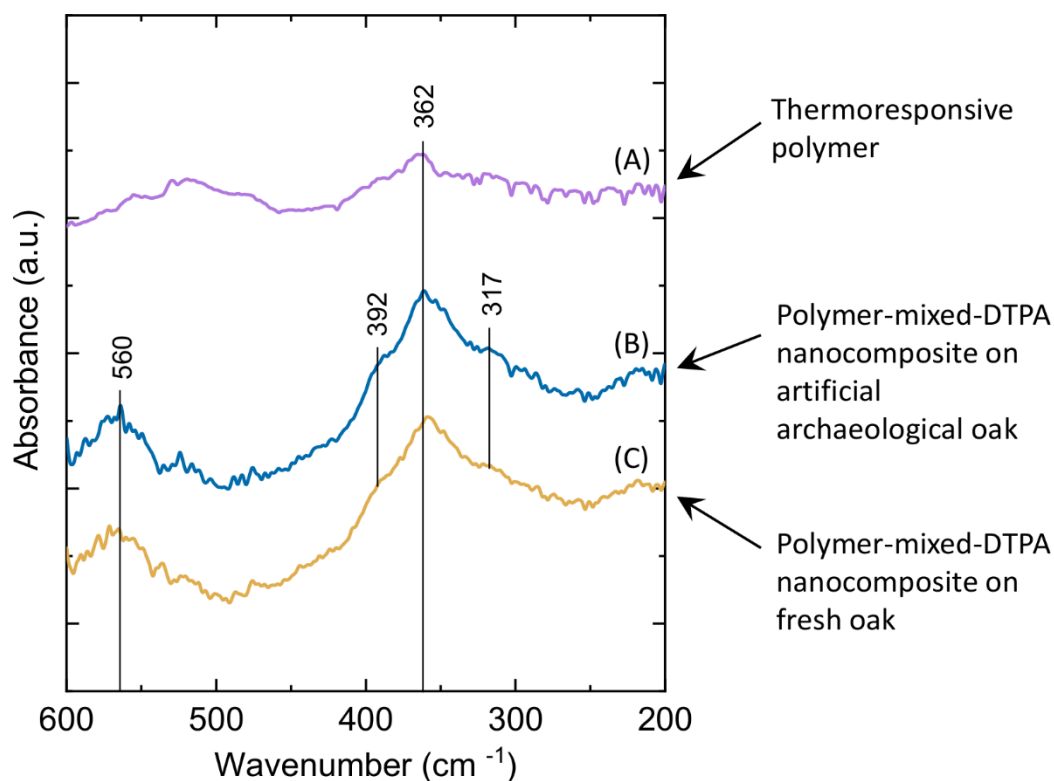


Figure 5.9. Far IR spectroscopy of polymer-mixed-DTPA nanocomposite after treating (B) artificial archaeological and (C) fresh oak. The spectrum of (A) the thermoresponsive polymer is also included for comparison. The broad band at 560 cm⁻¹ is attributed to the stretches of the Fe-O bonds in the iron oxide nanoparticles, and the band at 362 cm⁻¹ can be assigned to the C=O bonds in the thermoresponsive polymer. Bands at 393 and 317 cm⁻¹ have been previously related to the stretching and out-of-plane vibrations of Fe-N bonds. In this case, however, the intensity of those signals is not significantly different between the blank sample and the artificial archaeological wood. Bands around 316-320 cm⁻¹ could be related to the three Fe-N bonds in DTPA-Fe.

5.3 Conclusions

In this chapter, the preparation and characterisation of Fe₃O₄-APTES-DTPA has been described. Some interesting variations have now been introduced in the design and preparation of this family of nanocomposites. An aminopolycarboxylic acid derivative, DTPA, has been used in this second generation of wood conservation treatments, in substitution of the porphyrin-based treatments. In part, this change was motivated by the

concerns of the potential degradation of the cellulose by the singlet oxygen photogenerated by the porphyrin moieties. The use of DTPA as an iron chelating agent has been widely documented. Furthermore, the precursor used in the synthesis, DTPA-da, is relatively inexpensive, not toxic and not light sensitive. The DTPA-nanocomposite presented here has been prepared *via* a simple three-step, one-pot procedure, which has allowed to optimise the overall preparation time and the use of solvents.

XRD showed that the functionalisation steps with APTES and DTPA did not affect the crystallinity of the Fe₃O₄ nanoparticles. FTIR spectroscopy confirmed the presence of APTES and DTPA on the magnetite nanoparticle surface. Furthermore, the stretch at 1389 cm⁻¹ can be assigned to the amide II band, originated from the bond between APTES and DTPA, indication the success in attaching DTPA to the nanoparticles. TGA also confirms the loss of organic components from the surface of the functionalised iron oxide nanoparticles. UV-visible spectroscopy studies on an ethanolic solution of Fe(III) showed a gradual decrease of the intensity of the signal upon addition of the DTPA-nanocomposite. Also, an aqueous solution of Fe(III) treated with the DTPA-nanocomposite was studied by atomic absorption spectroscopy showing that the concentration of free iron in solution was reduced by 50 %. Furthermore, the DTPA-nanocomposite was encapsulated in the thermoresponsive polymer p(DEGMA₄₅-co-MMA₅), forming polymer-mixed DTPA-nanocomposite, and was used to treat fresh and artificial archaeological oak samples. However, far IR spectroscopy studies did not allow to identify the stretchings and bends of the Fe-N bonds in the hypothetical Fe-DTPA coordination complex.

References

- 1 P. Liao, Y. Hu, Z. Liang, J. Zhang, H. Yang, L.-Q. He, Y.-X. Tong, J.-M. Liu, L. Chen and C.-Y. Su, *J. Mater. Chem. A*, 2018, **6**, 3195–3201.
- 2 N. Aratani and A. Osuka, *Macromol. Rapid Commun.*, 2001, **22**, 725–740.
- 3 J. Jin, Y. Zhu, Z. Zhang and W. Zhang, *Angew. Chemie Int. Ed.*, 2018, **57**, 16354–16358.
- 4 L. Fernández, V. I. Esteves, Â. Cunha, R. J. Schneider and J. P. C. Tomé, *J. Porphyr. Phthalocyanines*, 2016, **20**, 150–166.
- 5 M. Neamțu, C. Nădejde, V.-D. Hodoroaba, R. J. Schneider and U. Panne, *Appl. Catal. B Environ.*, 2018, **232**, 553–561.
- 6 A. Berko, A. D. Smith, A. M. Jones, E. J. Schofield, J. F. W. Mosselmans and A. V Chadwick, *J. Phys. Conf. Ser.*, 2009, **190**, 012147.
- 7 G. Almkvist and I. Persson, *Holzforschung*, 2006, **60**, 678–684.
- 8 M. Sooriyaarachchi and J. Gailer, *Dalt. Trans.*, 2010, **39**, 7466.
- 9 F. A. Walker and U. Simonis, in *Encyclopedia of Inorganic Chemistry*, John Wiley & Sons, Ltd, Chichester, UK, 2006.
- 10 B. E. Douglas and D. J. Radanović, *Coord. Chem. Rev.*, 1993, **128**, 139–165.
- 11 A. J. Sillanpää, R. Aksela and K. Laasonen, *Phys. Chem. Chem. Phys.*, 2003, **5**, 3382–3393.
- 12 M. Ma, Y. Zhang, W. Yu, H. Shen, H. Zheng and N. Gu, *Colloids Surfaces A Physicochem. Eng. Asp.*, 2003, **212**, 219–226.
- 13 B. Feng, R. Y. Hong, L. S. Wang, L. Guo, H. Z. Li, J. Ding, Y. Zheng and D. G. Wei, *Colloids Surfaces A Physicochem. Eng. Asp.*, 2008, **328**, 52–59.
- 14 M. J. Williams, E. Sánchez-Pérez, E. R. Aluri, F. J. Douglas, D. A. Maclaren, O. M. Collins, E. J. Cussen, J. D. Budge, L. C. Sanders, M. Michaelis, C. M. Smales, J. Cinatl, S. Lorrio, D. Krueger, R. T. M. De Rosales and S. A. Corr, *RSC Adv.*, 2016, **6**, 83520–83528.
- 15 Y. Yong, Y. Bai, Y. Li, L. Lin, Y. Cui and C. Xia, *J. Magn. Magn. Mater.*, 2008, **320**, 2350–2355.
- 16 S. Villa, P. Riani, F. Locardi and F. Canepa, *Materials*, 2016, **9**, 10, 826–840.
- 17 Y. Huang, Y. Wang, Y. Wang, Q. Pan, X. Ding, K. Xu, N. Li and Q. Wen, *RSC Adv.*, 2016, **6**, 5718–5728.
- 18 J. F. Rabolt, W. H. Moore and S. Krimm, *Macromolecules*, **10**, 1065–74.
- 19 B. M. Leu, M. Z. Zgierski, G. R. A. Wyllie, W. R. Scheidt, W. Sturhahn, | E Ercan Alp, S. M. Durbin and J. T. Sage, *J. Am. Chem. Soc.*, 2004, **126**, 4211–4227.
- 20 B. K. Rai, S. M. Durbin, E. W. Prohofskey, J. Timothy Sage, G. R. A Wyllie, W. Robert Scheidt, W. Sturhahn and E. Ercan Alp, *Biophys. J.*, 2002, **82**, 2951–2963.
- 21 L. Marboutin, A. Desbois and C. Berthomieu, *J. Phys. Chem. B*, 2009, **113**, 4492–4499.

Chapter 6 - Conclusions and future work

6.1 Conclusions

In this work, a novel strategy to address the acidification problem of marine archaeological wood has been proposed. A family of multifunctional nanocomposites capable of removing harmful iron ions from the wood in a safe and controlled manner have been devised. These multifunctional nanocomposites are composed by magnetite nanoparticles functionalised with metal chelating molecules, which are encapsulated in a thermoresponsive polymer. The magnetic nature of the magnetite nanoparticles has been found to help in the penetration of the nanocomposite into the wood structure upon application of a 1.3 Tesla external magnetic field. Furthermore, the thermoresponsive polymer allowed for a precise and safe application of the treatment. Bringing the nanocomposite-laden polymer to a fluid-like state facilitated the application and the penetration of the magnetic cores into the wood. After the treatment, the nanocomposite was brought to a gel state, allowing for the safe removal from the surface of the wood. Two chelating agents have been studied (DTPA and Porphyrin), and various ways to incorporate them into the nanocomposite have been explored.

Initially, the nanocomposite Fe_3O_4 -APTES-PPIX/PEG 200 was prepared to study the feasibility of attaching a porphyrin moiety to a magnetic core while keeping the fluorescent properties. In this design, APTES was used as a spacer and proved to minimise the quenching of the fluorescence of Protoporphyrin IX commonly observed in the presence of the paramagnetic Fe(II) ions in magnetite. The Protoporphyrin IX anchored to the magnetic cores also retained its iron chelating properties as shown by spectroscopic measurements (AAS and UV-vis) in aqueous and ethanolic solutions, where 85 % of iron in solution was sequestered.

In order to achieve a high degree of control over the application of these nanocomposites on wood, a thermoresponsive polymer has been devised and prepared. This polymer, $p(\text{DEGMA}_{45}\text{-co-MMA}_5)$, showed a liquid-gel temperature window of 2-3 degrees at 26 °C, and has also been employed as a spacer between the magnetic nanoparticles and a porphyrin moiety. In its role as spacer, the porphyrin-polymerdithioester showed a liquid-gel temperature window of 5-6 degrees at 23 °C. The fluorescence of the porphyrin moiety in the multifunctional nanocomposite Fe_3O_4 -VTES-polymer-porphyrin was mildly quenched, and its iron chelating properties were retained, showing up to 39 % of iron removal from aqueous and ethanolic solutions. Both nanocomposites, Fe_3O_4 -APTES-PPIX/PEG 200 and Fe_3O_4 -VTES-polymer-porphyrin, were encapsulated in the thermoresponsive polymer, $p(\text{DEGMA}_{45}\text{-co-MMA}_5)$, and applied

as a treatment on artificial archaeological oak and *Mary Rose* wood. Subsequent far-IR analysis has revealed that iron ions can be removed from *Mary Rose* timbers, where the nanocomposite displays Fe-N bond stretches and Fe-N in plane vibrations indicating iron uptake by the attached porphyrin.

Finally, in order to explore the tunability of the designed treatment, the chelating agent DTPA was anchored to the magnetite nanoparticles in place of Protoporphyrin IX. This new design, Fe₃O₄-APTES-DTPA, demonstrated to be effective in sequestering iron ions from aqueous and ethanolic solutions, removing up to 50 % of iron ions in only 20 minutes. Fe₃O₄-APTES-DTPA was also encapsulated in p(DEGMA₄₅-co-MMA₅) and applied on artificial archaeological oak, however, far-IR studies could not ascertain whether iron ions were removed from the wood. This can be explained since, in DTPA, the modes of binding with iron ions is through Fe-N and Fe-O bonds. Therefore, a weaker signal for Fe-N bonds is expected, and the contribution from the Fe-O bonds is very likely to overlap with the signal from the iron oxide nanoparticles.

Various combinations of chelating agents, linkers and synthetic methods have been studied in order to explore the potential of this design. The systems developed here are a step forward from previous treatments designed for the removal of iron from waterlogged wood. While previous strategies were designed to penetrate the wood and neutralise the iron ions, none of these were tuned to physically remove these harmful substances from the wood structure. The multifunctional nanocomposites-laden polymers described in this thesis are a series of tools capable of neutralising removing iron ions lodged in the wood structure. This is possible due to the magnetic nature of the nanoparticles, which can be directed into and out of the wood upon application of an external magnetic field. The thermoresponsiveness of the polymer allows for the safe and controlled application of the treatment. The liquid-gel transition temperature window of 2-3 °C permits the application of the treatment with minimal temperature changes, thus avoiding damage to wooden waterlogged artefacts. Furthermore, these treatments can be easily tuned for specific applications. Thus, parameters like the concentration and nature of the metal chelator used, and the temperature window of the polymer can be adjusted at will in order to adapt the treatment to the needs of a particular material.

Given the nature of these multifunctional nanocomposites designed and prepared in this thesis, and the degree of complexity of their synthesis, scaling up the production for the treatment of large artefacts can be challenging. Consequently, this system would be better aimed to treat localised areas where iron is located a few millimetres below the surface, perhaps complementing other superficial, larger scaled treatments.

Even though this family of multifunctional nanocomposites-laden polymers have been designed and prepared focusing exclusively on the treatment of marine archaeological wood, these systems could be used on other archaeological and non-archaeological materials. The ability to easily replace the chelating agent by other functionalities and to fine-tune the thermoresponsive properties of the polymer opens up a range of possibilities for the application of these nanocomposites for the treatment of a variety of porous materials such as stone, paintings, fabric or leather. In this sense, the combination of the magnetic and thermoresponsive properties would have a key role in the design of next generation non-invasive treatments.

6.2 Future work

The natural continuation of this project should follow two main ideas: firstly, the use of p(DEGMA₄₅-co-MMA₅) as a linker between DTPA and the magnetite nanoparticles should be explored. This would provide a better interaction between the functionalised nanoparticles and the thermoresponsive polymer, ensuring greater control over the application and removal of the DTPA-based treatment. Secondly, the design of the thermoresponsive polymer could be optimised in order to obtain a temperature window even closer to that of the *Mary Rose* current storage conditions. This would save energy and time in the application and removal of the treatment and further reduce the thermal stress caused to the artefacts. The introduction of p(DEGMA₄₅-co-MMA₅) into the design of the DTPA functionalised nanoparticles could be just a small step within this project, however, the optimisation of the design of a thermoresponsive polymer for its use on wood treatment could be a separate project in itself due to its complexity.

Besides the optimisation of the thermal properties of the polymer, other interesting changes could be made to its design. For instance, the chelating agent attached in the nanoparticles could be also included in the structure of the thermoresponsive polymer. This way, the number of molecules of chelating agent present in the multifunctional nanocomposite and in the polymer combined would be greater and therefore, the iron removal efficiency would be presumably enhanced. This would especially affect to the removal of the iron located on the very surface of the artefact, since the functionalised magnetic nanoparticles would be operating a few millimetres within the wood structure.

Another aspect of the design of the treatment that is worth pursuing is the nanocomposite-to-polymer mass ratio used. This has not been studied in this work, but it certainly is a parameter that can provide another degree of tunability to the treatment.

Last, but not least, it is crucial to find a means to characterise and evaluate quantitatively the iron removal from wood. Far IR spectroscopy has been used in this

thesis, and although proved useful in showing the iron uptake by the chelating agents, these measurements had only a qualitative nature. For the full evaluation of the efficiency of such treatments, the quantitative evaluation of the iron removal would be essential. XAS studies of artificial archaeological wood and *Mary Rose* wood cores, before and after treatment, would allow evaluating the extent of the iron removal. This technique would also allow detecting possible changes in the iron and sulfur species present in the wood induced by the treatment.

Appendices

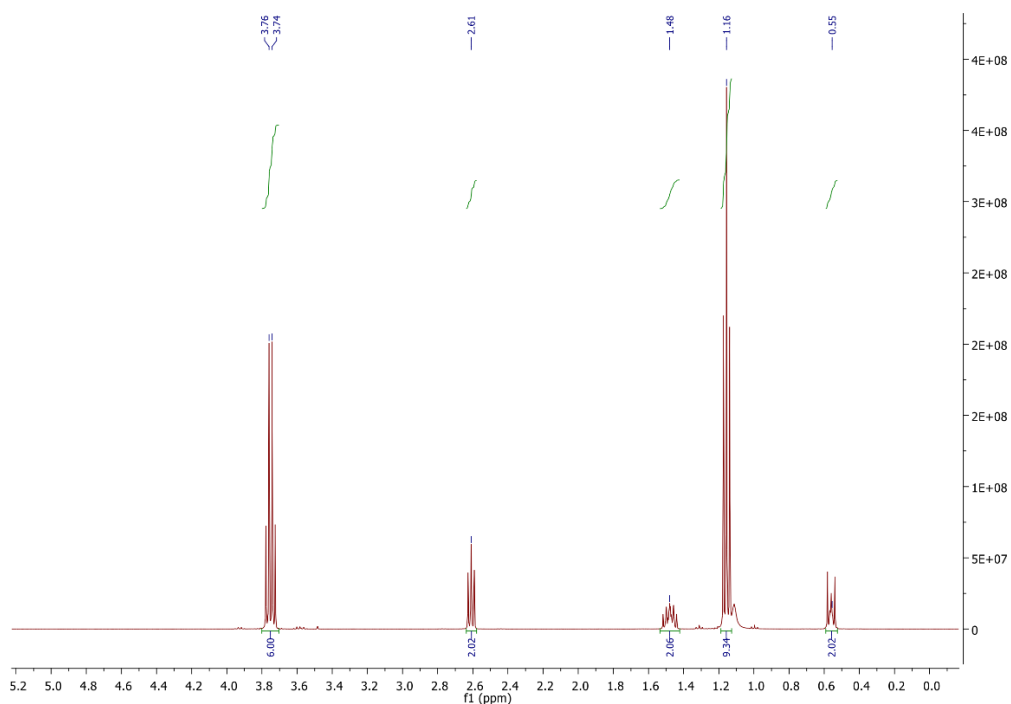


Figure A3.1. ^1H NMR spectrum of APTES obtained in $\text{DMSO-}d_6$

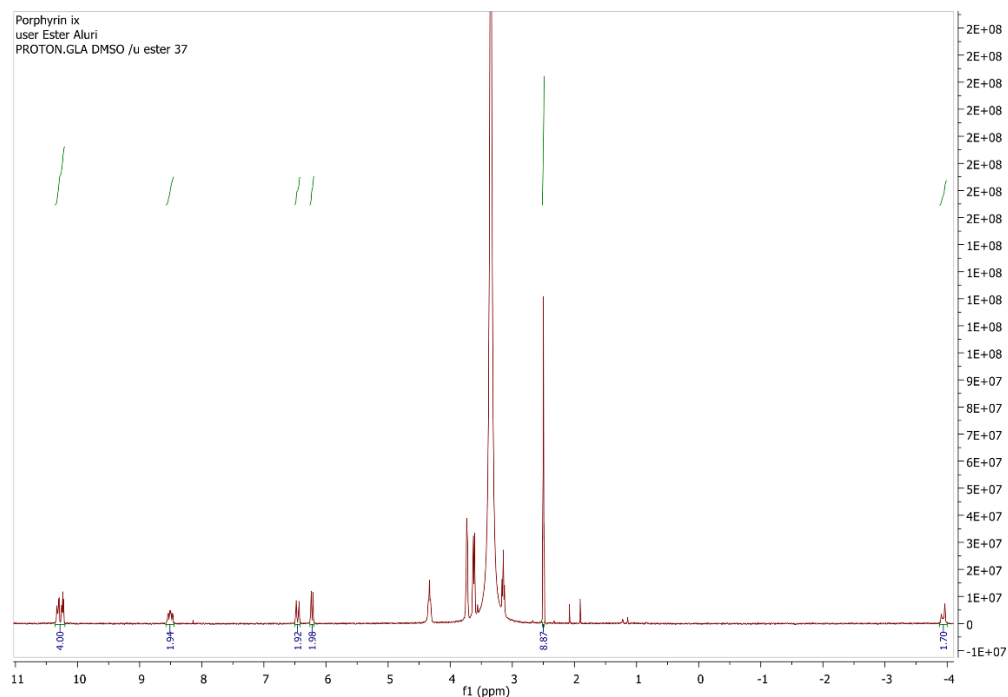


Figure A3.2. ^1H NMR spectrum of PPIX obtained in $\text{DMSO-}d_6$

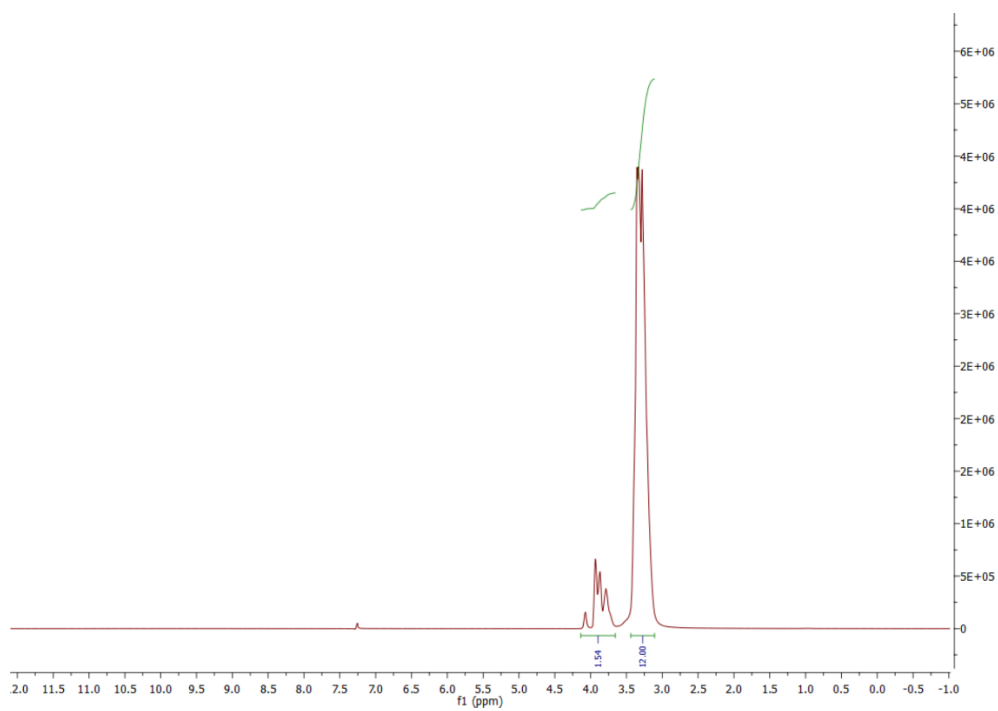


Figure A3.3. ^1H NMR spectrum of PEG obtained in CDCl_3

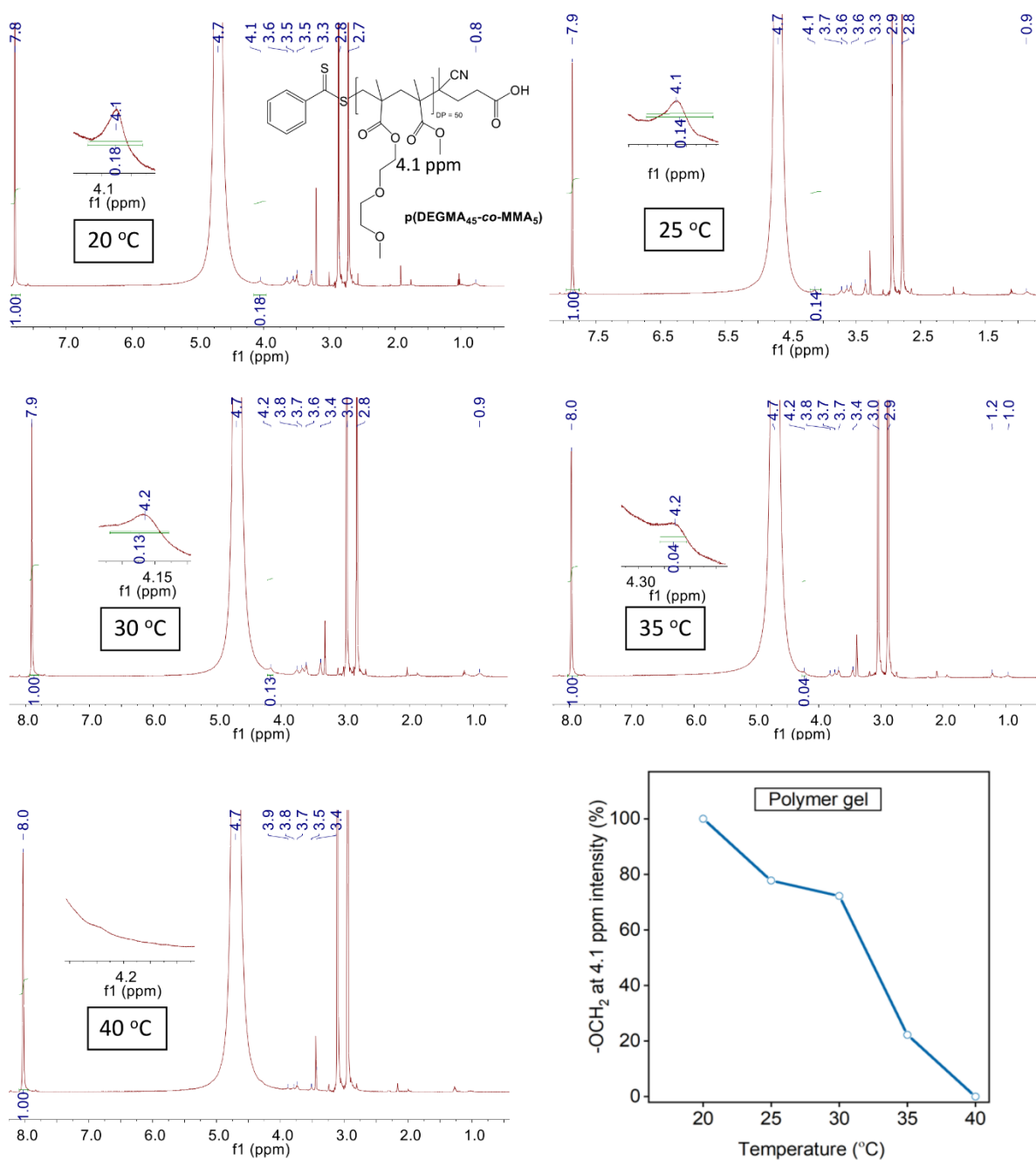


Figure A4.1. Temperature variable ¹H NMR spectra of p(DEGMA₄₅-co-MMA₅) obtained between 20 and 40 °C. The figure on the bottom-right corner shows the variation of relative intensity with temperature, measured for the -OCH₂- proton.

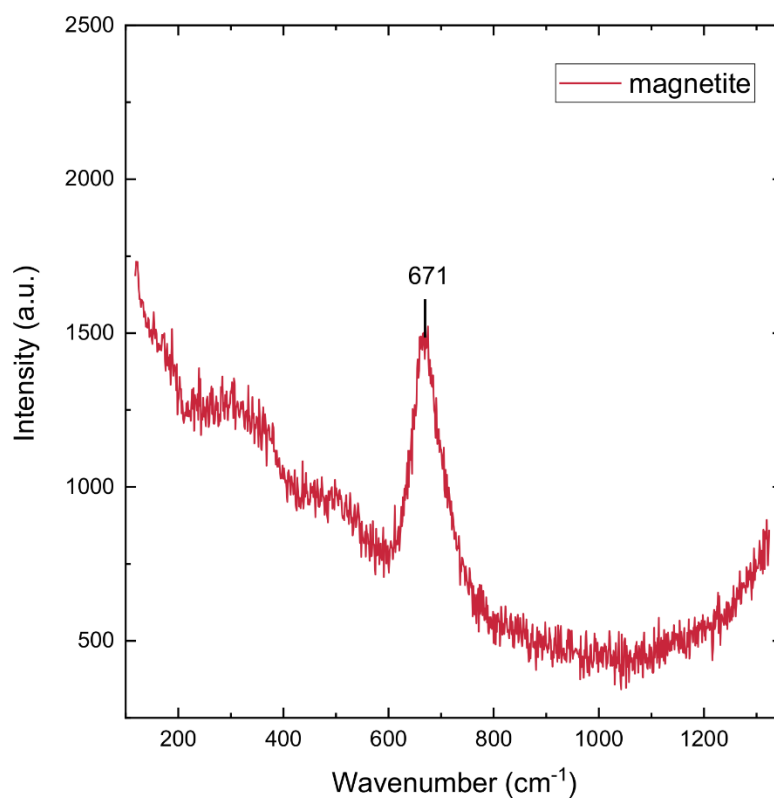


Figure A4.2. Raman spectrum obtained from magnetite nanoparticles. The peak at 670 cm⁻¹ is characteristic of magnetite. No evidence of other phases such as maghemite (γ -Fe₂O₃) or haematite (α -Fe₂O₃) is observed.